



UNIVERSITAT POLITÈCNICA
DE CATALUNYA
BARCELONATECH

Computational fluid dynamics techniques for fixed-bed biofilm systems modelin : numerical simulations and experimental characterization

Lledó Prades Martell

ADVERTIMENT La consulta d'aquesta tesi queda condicionada a l'acceptació de les següents condicions d'ús: La difusió d'aquesta tesi per mitjà del repositori institucional UPCommons (<http://upcommons.upc.edu/tesis>) i el repositori cooperatiu TDX (<http://www.tdx.cat/>) ha estat autoritzada pels titulars dels drets de propietat intel·lectual **únicament per a usos privats** emmarcats en activitats d'investigació i docència. No s'autoritza la seva reproducció amb finalitats de lucre ni la seva difusió i posada a disposició des d'un lloc aliè al servei UPCommons o TDX. No s'autoritza la presentació del seu contingut en una finestra o marc aliè a UPCommons (*framing*). Aquesta reserva de drets afecta tant al resum de presentació de la tesi com als seus continguts. En la utilització o cita de parts de la tesi és obligat indicar el nom de la persona autora.

ADVERTENCIA La consulta de esta tesis queda condicionada a la aceptación de las siguientes condiciones de uso: La difusión de esta tesis por medio del repositorio institucional UPCommons (<http://upcommons.upc.edu/tesis>) y el repositorio cooperativo TDR (<http://www.tdx.cat/?locale-attribute=es>) ha sido autorizada por los titulares de los derechos de propiedad intelectual **únicamente para usos privados enmarcados** en actividades de investigación y docencia. No se autoriza su reproducción con finalidades de lucro ni su difusión y puesta a disposición desde un sitio ajeno al servicio UPCommons No se autoriza la presentación de su contenido en una ventana o marco ajeno a UPCommons (*framing*). Esta reserva de derechos afecta tanto al resumen de presentación de la tesis como a sus contenidos. En la utilización o cita de partes de la tesis es obligado indicar el nombre de la persona autora.

WARNING On having consulted this thesis you're accepting the following use conditions: Spreading this thesis by the institutional repository UPCommons (<http://upcommons.upc.edu/tesis>) and the cooperative repository TDX (<http://www.tdx.cat/?locale-attribute=en>) has been authorized by the titular of the intellectual property rights **only for private uses** placed in investigation and teaching activities. Reproduction with lucrative aims is not authorized neither its spreading nor availability from a site foreign to the UPCommons service. Introducing its content in a window or frame foreign to the UPCommons service is not authorized (*framing*). These rights affect to the presentation summary of the thesis as well as to its contents. In the using or citation of parts of the thesis it's obliged to indicate the name of the author.



**UNIVERSITAT POLITÈCNICA
DE CATALUNYA
BARCELONATECH**

**Department of Mining, Industrial and ICT Engineering
Natural Resources and Environment Doctoral Program**

Doctoral Thesis

**COMPUTATIONAL FLUID DYNAMICS TECHNIQUES FOR
FIXED-BED BIOFILM SYSTEMS MODELING: NUMERICAL
SIMULATIONS AND EXPERIMENTAL CHARACTERIZATION**

Lledó Prades Martell

A thesis submitted for the degree of Doctor of Philosophy
at the Universitat Politècnica de Catalunya

Supervised by:

Dr. Xavier Gamisans Noguera

Dr. Antonio D. Dorado Castaño

Manresa, October 2018

***“The important thing is not to stop questioning;
curiosity has its own reason for existing”***

Albert Einstein

AGRAÏMENTS/ACKNOWLEDGEMENTS

Després de més quatre anys, mirar enrere quasi que em dona una mica de vertigen. Realment tots aquests anys de tesi han estat com un viatge ple d'experiències, vivències i kilòmetres, i sempre envoltada de moltes persones que m'han dirigit (i redigit), aconsellat i ajudat per anar en la direcció correcta. Sense tots vosaltres no hauria sigut capaç de tancar aquesta etapa, i el resultat tampoc hages estat el mateix.

En primer lloc vull agrair als meus directors de tesi, Xavier i Toni, tot el que m'han ensenyat durant els darrers anys. Moltes gràcies per confiar en mi per a la FPI, per formar-me en tots els àmbits que desconeixia, i també per les nombroses reunions (presencials i virtuals). Gràcies per sempre respondre als meus dubtes, i per escoltar les meves (llargues) divagacions. Gràcies per donar-me llibertat per poder gestionar les meves visites al laboratori de fluids (i a casa). Com a doctoranda espero haver estat a l'alçada, tot i que sé que algunes vegades m'ha costat gestionar les emocions. Però, sobretot, gràcies per haver-me proposat un tema de tesi tant enriquidor. Si quan vaig cursar l'assignatura d'introducció a la simulació al màster (any 2010) m'haguessin dit que acabaria fent una tesi amb CFD, mai m'ho hages cregut.

També voldria agrair a la resta dels membres del grup BIOGAP les seves aportacions. Gràcies Anna, Conxita, F. Xavier i Montse per la vostra ajuda sempre que ho he necessitat, i merci per l'afecte amb el que ho heu fet. A la resta d'investigadors que van formar part del grup durant els meus anys de tesi, i també companys de despatx (Dani, Eloi, Eva i Xavi), gràcies per totes les estones que hem compartit junts, i ajudar-me sempre que us he demanat. Dani, merci per ajudar-me en les mostres de biomassa, en el cultiu del biopel·lícules, i en tot allò relacionat amb el laboratori. Eloi, gràcies per les converses disteses d'arduino i programació, i per ensenyar-me tant, per seure al meu costat a mirar els colorines del CFD, i intentar trobar-li la lògica als meus resultats, però sobretot merci per sempre escoltar-me amb tanta atenció, seguida d'un bon consell. Eva, merci infinitament, per tot, no em puc posar a detallar-ho, ja saps que és moltíssim tot el que has fet per mi tant a nivell personal com professional (i fins al darrer dia de tesi!), gràcies per totes les experiències que hem compartit juntes i merci per sempre estar al meu costat. Xavi merci per ajudar-me a integrar-me quan vaig començar, per explicar-me tantíssimes coses, per fer els perfils que necessitava per presentar els treballs als congressos, per preparar-me mostres, i per sempre estar disposat a donar-me un cop de mà en tot i més del que t'he demanat.

Merci també a tot el personal administratiu de l'escola, en especial a Llúcia, Xesca i Manel per la seva ajuda inestimable en diferents tasques al llarg d'aquests anys, i també a tots els membres del centre del càlcul per resoldre ràpidament les nombroses incidències al meu PC (instrument essencial per al desenvolupament de la tesi). Gràcies en general a tots els membres de la UPC-Manresa pel vostre afecte i caliu, realment vau fer que em sentís pràcticament com a casa.

Als companys de la UAB també els voldria agrair la seva ajuda i suport. Al David agrair-li totes les seves aportacions en les nombroses reunions del BTP-GO, i tots els suggeriments per a encaminar les tasques de la tesi. Gràcies al Javier pels seus comentaris quan vaig començar amb el CFD. Gràcies Gemma i Mireia per la interacció en les reunions i les vostres aportacions. També voldria agrair a Juan Antonio la seva ajuda en l'automatització de la bureta, i a Julio per posar-nos en contacte amb Cristian. A la Mabel i l'Eva, merci per totes les converses i ànims, sobre tot en l'etapa final. Gràcies Mabel per tots els teus consells quan tenia que anar a Delft, i gràcies Eva per la convivència els dies que vas estar allí. Gràcies Luis, Enric i David Cueto per tot el temps compartit als congressos, reunions, i en altres ocasions.

Part de la investigació presentada en aquesta tesi ha estat desenvolupada en col·laboració amb altres grups de recerca, on he tingut l'oportunitat de realitzar estades de llarga duració. Al grup de fluids multifàsics de la UJI, gràcies Sergio per donar-me l'oportunitat de treballar amb vosaltres, gràcies per la teua supervisió durant la meua estada, i per totes les aportacions a les diferents col·laboracions que hem anat desenvolupant. També moltes gràcies per ensenyar-me tant de CFD i per donar-me bones directrius i consells sempre que ens hem reunit. A més, agrair a tots el membres del grup la seua ajuda durant les meues nombroses visites, i el suport via mail/telèfon. Gràcies Jose i Rosario per deixar-me els vostres PCs per a simular. També gràcies a Rosario per tolerar totes les meues

discussions i dubtes random sobre Fluent, i a Jose per l'assessorament en temes de malles. Gràcies Salva per ajudar-me quan he estat trastejant pel taller. Gràcies Carlos i Raúl per les explicacions més tècniques de CFD, i gràcies Javi i Rubén per les tantes discussions sobre reologia i models. Gràcies Guillem per ajudar-me des del primer dia en la tesi i ser la consciència de la mateixa. Gràcies per sempre treure temps per comentar-ho tot, i per resoldre molts dels meus dubtes. Gràcies per tots els cafès i les infinites cridaes, i gràcies per tota la feina del Capítol 8 (menció especial a la pàg. 178), que fa patent que una part d'aquesta tesi siga teua.

De la UJI también quiero mencionar a Yolanda Bautista y a Vicente Sanz por abrirme las puertas del ITC, y ayudarme a analizar la reología de la biomasa. Gracias Yolanda por toda tu dedicación, y por explicarme tanto sobre reología.

My second stay was at Environmental Biotechnology group in TU Delft. I would like to thank Mark and Cristian for giving me the opportunity to perform my stay at EBT. I think that joining EBT was an excellent chance to improve my skills and to broaden my research field, and I really felt that I grew as a researcher. Cristian, I have no words to thank you for everything you have done for this thesis, I guess sometimes without knowing it, but you have taught me so much. I really appreciate all the time that you spent working with me, all our meetings and our discussions about modeling, and it was a pleasure to assist to your lessons in the course. Thank you also for the time that we spent together, not only working, as in the Eurobiofilms congress or the dinner with your family, I really enjoyed those days. Thank you so much for pushing me when I needed, for all your explanations and advice, and for making me a more critical individual. Thank you so much David, Geert-Jan, Mark, Robbert and Yuemei for sharing your time with me and discussing various topics. I really appreciate all your explanations and contributions (Yuemei many thanks for your comments to my rheological work!). Morez, thanks for all, for pushing me when it was a "bad" day, for the talks (not only about modeling), for all your comments about biofilm mechanics, for all the advice, for taking care of me and accommodating at your home. I really enjoyed the time that I spent with you and Donya. Thanks to all other EBTeans (Aina, Ana Maria, Andrés, Ben, Danny, Diana, Emma, Eveline, Hugo, Ingrid, Joe, Jules, Jure, Marissa, Mahsa, Marta, Michele, Mónica, Rhody, Simon, Viktor, Wladimir...) for the time that we shared together, and for the random conversations during the lunch, coffees breaks or in botanical garden. I also would like to thank Miranda and Kawieta for helping me my first days, and getting all my paperwork in order. I am glad to have met you all.

También quisiera tener un recuerdo para investigadores de otros grupos con los que he tenido la oportunidad de compartir jornadas/congresos: Domingo Cantero, Martín Ramírez, Raúl Muñoz, Guillermo Quijano, Carmen Gabaldón, Javier Álvarez, Pau San-Valero y Jorge Rodríguez. Gracias por vuestros comentarios y aportaciones constructivas a mi trabajo.

A més, agrair el suport incondicional dels meus amics de la terreta. A la mini-comi, gracias por preguntar siempre por la tesis, por los ánimos y por hacerme aparcarla a ratos. Menció especial a Belén por esos "dale rubia", e incitarme a ir a verla (ya sabes que volveré unas cuantas veces más!). Gràcies als Hugo's coffe per sempre animar-me, i gràcies bonicos pels molts bon ratets que hem passat al Teapot. Gràcies també als del Regne Unit (Pepe, Mariola) per pensar en mi, i per tots els vostres consells (Mariola quanta raó tenies en la muntanya russa d'emocions!). I gràcies als ex-companys de la UJI (Silvana, Victor, Dani, Pati, Julio, David, Pilar...) per recordar-me i demanar-me de tant en tant; Dani por fin se acabaron los bichos-holónicos!

I finalment, moltíssimes gràcies a tota la meua família. Heu sigut el major suport que he tingut tots aquests anys. Gràcies per tot, per les visites i per acoblar-vos a les meues anades i vingudes. Gràcies als meus pares per ensenyar-me tant, i demostrar-me que els límits sols els trobes quant tu mateix te'ls poses. Gràcies germanets (Eneko i Neus) i cunyaets (Neleta i Jorge) pels vostres consells i per sempre donar-me suport en tot (i gràcies pels vostres nombrosos suggeriments en quan a formats i tonalitats en la tesi!). Gràcies a tots per ajudar-me, animar-me i fer-me riure sempre!

This doctoral thesis has been carried out thanks to the financial support provided by:

- FPI doctoral grant (BES-2013-066873).
- Research project “Monitoring, modelling and control towards the optimization of anoxic and aerobic desulfurizing biotrickling filters” (CTM2012-37927-C03-02), financed by the Ministerio de Economía y Competitividad (Spain).
- Research project “Development of a selective absorption process of SO_x and NO_x from flue gases and biofilms monitoring of biological process for recovery” (CTQ2015-69802-C2-2-R), financed by the Ministerio de Economía y Competitividad (Spain), FEDER funds.

Additionally, part of the work developed in this thesis has been done in collaboration with Multiphase Fluids research group (Universitat Jaume I, Spain) and Environmental Biotechnology research group (Delft University of Technology, Netherlands), financed by mobility grants EEBB-I-15-09717 and EEBB-I-17-12181 respectively, both financed by the Ministerio de Economía y Competitividad (Spain).

CONTENTS

Summary v

Resumen vii

CHAPTER 1. MOTIVATIONS AND THESIS OVERVIEW

1.1. MOTIVATIONS..... 3

1.2. THESIS OVERVIEW 4

CHAPTER 2. INTRODUCTION

2.1. BIOFILMS 9

2.1.1. Biofilm systems, biofilm processes, and biofilm reactors

2.1.2. Biofilm activity

2.1.3. Biofilm-fluid interaction

2.1.4. Biofilm structure

2.1.5. Key parameters in biofilm control strategies

2.2. BIOFILMS AND BIOSYSTEMS MODELING 14

2.2.1. Modeling biofilms development and structure

2.2.2. Biosystems modeling

2.3. BIOFILMS AND BIOSYSTEMS CHARACTERIZATION 20

2.3.1. Hydrodynamic characterization techniques

2.3.2. Structural characterization techniques

2.3.3. Mechanical characterization techniques

2.3.4. Biomass activity monitoring

2.4. COMPUTATIONAL FLUID DYNAMICS TECHNIQUES..... 23

2.4.1. Computational fluid dynamics models

CHAPTER 3. OBJECTIVES

3.1. GENERAL AND SPECIFIC OBJECTIVES 35

CHAPTER 4. ONE PHASE CFD MODELING FOR COUPLING HYDRODYNAMICS AND BIODYNAMICS IN A FIXED-BED BIOFILM REACTOR

Abstract 38

4.1. INTRODUCTION 39

4.2. MATERIALS AND METHODS	40
4.2.1. Bioreactor operation and DO microprofiles recording	
4.2.2. Biofilm parameters characterization	
4.2.3. Bioreactor hydrodynamic characterization	
4.3. MODELS DEVELOPMENT	43
4.3.1 Microbial kinetic model	
4.3.2 General assumptions in bioreactor models	
4.3.3 Description of bioreactor models	
4.4. RESULTS AND DISCUSSION	50
4.4.1. Experimental measurements in the FPB	
4.4.2. Simulation results	
4.5. CONCLUSIONS	61

CHAPTER 5. DETAILED RHEOLOGICAL CHARACTERIZATION OF FIXED AND SUSPENDED HETEROTROPHIC BIOMASS

Abstract	64
5.1. INTRODUCTION	65
5.2. MATERIALS AND METHODS	66
5.2.1. Cultivation and preparation of the samples	
5.2.2. Rheological characterization	
5.3. RESULTS AND DISCUSSION	70
5.3.1. Steady shear flow test results	
5.3.2. Oscillatory shear flow tests results	
5.3.3. Transient shear flow test results	
5.4. CONCLUSIONS	85

CHAPTER 6. MULTIPHASE CFD MODELING OF FIXED-BED BIOFILMS BIOCHEMICAL PHENOMENA AND MECHANICAL BEHAVIOR UNDER LAMINAR FLOW CONDITIONS

Abstract	88
6.1. INTRODUCTION	89
6.2. MATERIALS AND METHODS	90
6.2.1. Bioreactor operation and dissolved oxygen (DO) microprofiles recording	
6.2.2. Biofilm modeling: biological kinetics and rheological parameters	

6.2.3. Mass transfer model (liquid-biofilm)	
6.3. MODELS DEVELOPMENT	93
6.3.1. Two-phase CFD models	
6.3.2. Implementation of the rheological model into CFD codes	
6.3.3. Customizing CFD code: implementation of expressions and correlations	
6.4. RESULTS AND DISCUSSION	104
6.4.1. Model verification: comparison of simulated results with experimental data	
6.4.2. Model capabilities testing	
6.5. CONCLUSIONS	124

CHAPTER 7. MULTIPHASE CFD MODELING OF TURBULENT FLOWS OVER FIXED-BED BIOFILMS

Abstract	126
7.1. INTRODUCTION	127
7.2. MATERIALS AND METHODS	128
7.2.1. Inoculum and culture media for biofilm growth	
7.2.2. Experimental set-up	
7.2.3. Confocal microscope analysis	
7.2.4. Data post-processing	
7.3. MATHEMATICAL MODEL	129
7.3.1. Assumptions	
7.3.2. Governing equations	
7.3.3. Biofilm thickness measurements	
7.3.4. Numerical simulations	
7.4. RESULTS AND DISCUSSION	137
7.4.1. Biofilm characterization	
7.4.2. Model verification: simulated and experimental data comparison	
7.4.3. Parametric study	
7.5. CONCLUSIONS	157

CHAPTER 8. STUDY ON THE APPLICATION OF LOCAL CAPACITANCE NEEDLE-PROBES FOR IN-SITU BIOFILM LAYER CHARACTERIZATION AND INTERFACE DETECTION

Abstract	160
8.1. INTRODUCTION	161
8.2. MATERIALS AND METHODS	163
8.2.1. Experimental set-up	
8.2.2. Biofilm growth and samples preparation	
8.2.3. Sensor development and set-up overview	
8.2.4. Motion system and control program	
8.3. PRELIMINARY RESULTS AND MEASUREMENT PRINCIPLE	170
8.4. RESULTS AND DISCUSSION	173
8.4.1. Experimental results of two-phase biosystems	
8.4.2. Experimental results of three-phase biosystems	
8.5. CONCLUSIONS	182

CHAPTER 9. GENERAL CONCLUSIONS AND FUTURE WORK

9.1. GENERAL CONCLUSIONS	187
9.1.1. Rheological properties characterization of fixed and suspended biomass	
9.1.2. CFD models developed to study biosystems performance under laminar flow conditions	
9.1.3. CFD models developed to study biosystems performance under turbulent flow conditions	
9.1.4. Application of needle-probes to characterize fluid interfaces in biosystems	
9.2. FUTURE WORK	190
<i>Nomenclature</i>	193
<i>References</i>	201

SUMMARY

The study and modeling of biosystems remains a challenge that requires exploring the physical and bio-chemical phenomena from different spatial and temporal resolution levels. The fluid-biofilm interactions should be investigated in detail even for the simplest laminar flow regime. Computational fluid dynamics (CFD) is a widespread and promising tool for rigorously modeling hydrodynamic in reactors, which recently has been emerge as an alternative approach to bioreactors model. Nevertheless, the complicated interactions between biofilm and fluid flow phases (gas and liquid), have not been described using this type of techniques.

In this thesis, one-phase and multiphase models using CFD commercial codes were designed and developed to analyze biosystems behavior at mesoscale level. In the first part, the operation of a fixed-bed biofilm reactor was simulated using Eulerian one-phase models, coupling fluid flow dynamics with biokinetics, and implementing a hydraulic pressure loss model to consider biofilm physical characteristics. This technique allowed obtaining accurate results related to the bioreactor performance, experimentally verifying hydrodynamics and species transport. However, these models needed to be improved in order to reproduce real scenarios where biofilm motion can play an important role.

On further consideration, this thesis suggested the development of Eulerian two-phase models using volume of fluid (VOF) method, where the biofilm was defined as an independent fluid phase. To develop these models, the experimental characterization of biofilm properties become essential to acquire in-depth knowledge of the phenomena involved, especially for accurately reproducing the fluid interaction over the biofilm, which has a direct effect on its structure. As a result, a comprehensive rheological analysis was developed under steady, oscillatory and transient shear flows, to obtain macroscopic mechanical properties and to analyze binding mechanisms between the structural components at microscale. Experimental results pointed out that biofilms exhibited gel-like character, showing shear-thinning behavior with yield stress, thus defining the biofilm as a non-Newtonian fluid, which parameters were strongly dependent on the density.

In the second part of this thesis, a novel continuum approach for biosystems modeling was proposed, implemented and tested. This included the biofilm definition as a non-Newtonian fluid phase, and other implementations to reproduce the species transfer at the interface (liquid-biofilm), and to link the possible growth of the biofilm phase with the transported and transferred species, among others. This new approach coupled fluid dynamics under laminar conditions with biochemical phenomena and/or biofilm mechanical behavior, tracking accurately the volume fraction of the phases across the domain, so being able to reproduce fluid-biofilm interaction in case of biofilm motion. The simulated results were experimentally verified evaluating transport mechanisms under different hydrodynamic conditions. Additionally, the model capability to reproduce shear-induced deformation and detachment, and recoil (or recovery) in biofilms was shown, being the simulated results in qualitative agreement with experimental observations.

In order to reproduce wide range of hydrodynamic conditions to which biosystems can be exposed, the capacities of the new approach of continuum model were further tested. Particularly, Eulerian multiphase models were developed and solved to characterize turbulent gas flows behavior over biofilms attached to walls, using a coupled method of VOF and level set and shear stress transport (SST) $k-\omega$ model, in order to accurately reproduce gas-biofilm interactions, turbulence and near-wall treatment. The simulated results were experimentally verified to confer identity to developed CFD approach, correctly describing the interfacial instabilities on the fixed-bed biofilm, such as a ripples formation, and biofilm displacement and removal from its original position. The results also revealed that biofilm fluidization was the mechanisms behind the impact of turbulent air flows.

Finally, in the last part of this thesis, the work was focused on the accurate analysis of fluid-biofilm interface, and on the necessity of acquiring local experimental data to verify models, as discussed in the previous chapters. The applicability of needle-probes as an innovative technique for in-situ biofilm layer and fluids interfaces detection was examined. The probes performance was calibrated and verified in multiphase systems, revealing its practicability for interface detection, depth measuring, and surface reconstruction. So, a feasible tool for the experimental characterization of biosystems and models verification at mesoscale was provided.

Therefore, the Eulerian multiphase approach proposed in this thesis, together with the experimental analyses, revealed the potential of CFD techniques as an alternative tool to model fixed-bed biofilm systems, allowing to reproduce simultaneous spatial and temporal physical and biochemical phenomena under different operating conditions and biosystems configurations. The proposed approach helped to address key aspects of the biofilm modeling such as its deformation and detachment under laminar and turbulent conditions.

RESUMEN

El estudio y modelización de los sistemas biológicos o biosistemas sigue siendo un reto que requiere explorar los fenómenos físicos y bioquímicos desde diferentes niveles de resolución espacial y temporal. Incluso para el régimen de flujo laminar más simple, las interacciones fluido- biopelícula deben ser investigadas en detalle. La dinámica de fluidos computacional (CFD, del inglés computational fluid dynamics) es una herramienta prometedora y extendida para modelar rigurosamente la hidrodinámica en reactores, la cual recientemente ha surgido como un enfoque alternativo para el modelo de biorreactores. Sin embargo, las complicadas interacciones entre la biopelícula y las fases fluidas (gas y líquido), aún no han sido descritas utilizando este tipo de técnicas.

En esta tesis, se diseñaron y desarrollaron modelos monofásicos y multifásicos utilizando códigos comerciales CFD para analizar el comportamiento de los biosistemas a nivel de mesoescala. En la primera parte, se simuló la operación de un reactor de biopelícula de lecho fijo utilizando modelos monofásicos Eulerianos, acoplando la dinámica del flujo de fluido con la biocinética, e implementando un modelo de pérdidas de presión hidráulica para considerar las características físicas de la biopelícula. Esta técnica permitió obtener resultados precisos relacionados con el rendimiento del bioreactor, verificando experimentalmente la hidrodinámica y el transporte de las especies. Sin embargo, estos modelos necesitaron ser mejorados para poder reproducir escenarios reales donde el movimiento de la biopelícula puede jugar un papel importante.

Por ello, se sugirió el desarrollo de modelos Eulerianos de dos fases utilizando el método de volumen de fluido (VOF, del inglés volume of fluid), donde la biopelícula se definió como una fase líquida independiente. Para desarrollar estos modelos, la caracterización experimental de las propiedades de la biopelícula fue imprescindible para adquirir un conocimiento profundo de los fenómenos implicados, especialmente para reproducir con precisión la interacción fluida sobre la biopelícula, ya que tiene un efecto directo sobre la estructura de la biopelícula. Como resultado, se desarrolló un análisis reológico integral bajo flujos de cizallamiento estables, oscilatorios y transitorios, para obtener las propiedades mecánicas macroscópicas y analizar los mecanismos de unión entre los componentes estructurales a microescala. Los resultados experimentales señalaron que las biopelículas mostraban un carácter gelatinoso, y teniendo un comportamiento de adelgazamiento del cizallamiento con una tensión de fluencia. Así, la biopelícula se caracterizó como un fluido no Newtoniano, cuyos parámetros dependían en gran medida de la densidad de la biopelícula estudiada.

En la segunda parte de esta tesis, se propuso, implementó y probó un nuevo enfoque continuo para el modelado de biosistemas. Esto incluyó la definición de biopelícula como una fase fluida no Newtoniana, y otras implementaciones para reproducir la transferencia de especies en la interfaz (líquido-biopelícula), y para vincular el posible crecimiento de la fase de biopelícula con las especies transportadas y transferidas, entre otras consideraciones. Este nuevo enfoque combinó la dinámica de fluidos en condiciones laminares con

fenómenos bioquímicos y/o comportamiento mecánico de la biopelícula, calculando con precisión la fracción volumétrica de las fases a lo largo del dominio, pudiendo así reproducir la interacción fluido-biopelícula en caso de movimiento de la biopelícula. Los resultados simulados fueron verificados experimentalmente evaluando los mecanismos de transporte bajo diferentes condiciones hidrodinámicas. Adicionalmente, se mostró la capacidad del modelo desarrollado para reproducir deformaciones y desprendimientos inducidos por cizallamiento y el retroceso (o recuperación) en las biopelículas, estando los resultados simulados en concordancia cualitativa con las observaciones experimentales.

Con el fin de reproducir una amplia gama de condiciones hidrodinámicas a las que pueden estar expuestos los biosistemas, las capacidades del nuevo enfoque del modelo continuo se probaron más a fondo. En particular, se desarrollaron y resolvieron modelos Eulerianos multifásicos para caracterizar el comportamiento de los flujos de gas turbulento sobre biopelículas adheridas a la pared, utilizando un método acoplado de VOF y de conjunto de nivel (en inglés level-set) y el modelo SST $k-\omega$, con el fin de reproducir con precisión las interacciones gas-biopelícula, la turbulencia y el tratamiento cercano a la pared. Los resultados simulados fueron verificados experimentalmente para conferir identidad al enfoque de CFD desarrollado, describiendo correctamente las inestabilidades interfaciales en la biopelícula de lecho fijo, tales como la formación de ondulaciones, y el desplazamiento y desprendimiento de la biopelícula de su posición original. Los resultados también revelaron que la fluidización del biopelícula era el mecanismo que se encontraba detrás del impacto de flujos de aire turbulentos.

Finalmente, en la última parte de esta tesis, el trabajo se centró en el análisis preciso de la interfase fluido-biopelícula, y en la necesidad de adquirir datos experimentales locales para verificar modelos, como se había comentado en los capítulos anteriores. Se examinó la aplicabilidad de las sondas de aguja como técnica innovadora para la detección *in-situ* de la capa de biopelícula y de las interfases de los fluidos. El comportamiento de las sondas fue calibrado y verificado en sistemas multifásicos, mostrando su practicidad para la detección de interfases, medición de profundidad y reconstrucción de superficies. Así pues, se proporcionó una herramienta viable para la caracterización experimental de biosistemas y la verificación de modelos a mesoescala.

Por lo tanto, el enfoque multifase Euleriano propuesto en esta tesis, junto con los análisis experimentales, reveló el potencial de las técnicas CFD como una herramienta alternativa al modelo de sistemas de biopelícula de lecho fijo, permitiendo reproducir simultáneamente fenómenos físicos y bioquímicos en espacio y tiempo, y bajo diferentes condiciones de operación y configuraciones de los biosistemas. El enfoque propuesto ayudó a abordar aspectos clave del modelado de biopelículas como su deformación y desprendimiento bajo condiciones laminares y turbulentas.



MOTIVATIONS AND THESIS OVERVIEW

1.1. MOTIVATIONS

Biosystems modeling is required to control and optimize the operation of biofilm-based technologies, which have emerged as promising techniques for waste abatement and water treatment during last years. Considering biofilm mechanics and its implications in biosystems behavior for biofilm-fluid interaction scenarios is an emerging research in biofilm modeling field (Fabbri and Stoodley, 2016).

The fluid flowing around biofilms can have an effect on the biosystems performance, since such fluid flow influences the microbial activity and its development in several important ways: the transport of dissolved solutes into and out of the biofilm, and the application of shear forces to the biofilm which could cause biofilm deformation and detachment (Stewart, 2012). In the fluids flowing over the biofilm, the transport of substrates is governed mainly by advection (Lewandowski and Beyenal, 2007). This implies that the biochemical processes and biofilm dynamics can be affected by biosystem fluid conditions, which may even cause limitations in bioreactors efficiency operated for pollutants removal (Liotta et al., 2014). In addition, the external mass transfer is also determined by flow patterns, i.e. higher fluid velocities produce higher mass transfer rate (Zhang and Bishop, 1994). Finally, the fluid flow applies shear forces at the biofilm surface, which can produce structural modifications. Slow fluid flow can produce deformations on biofilm structure due to the low shear forces, whereas fast fluid flow implies substantial shear forces, stretching the biofilm structure and being able to form streamers, for finally detaching it from the rest of biofilm structure (Stoodley et al., 1999a). In addition, sudden changes or stoppages of the biosystem fluid flow can produce a viscoelastic behavior showing biofilm time-dependent creep or recoil respectively (Klapper et al., 2002; Fabbri et al., 2016b). Thus, it is clearly demonstrated that fluid flows in biosystems have an effect on biofilm structure formation, being essential to contemplate processes such as fluid flow, substrate transport by convection and diffusion, substrate consumption, biomass growth and biomass detachment, in any model aiming to represent biosystems evolution as a response to environmental conditions (Picioreanu, 1999).

In order to consider the described processes, it is required to characterize the biofilm properties, explaining the way in which the biofilm matrix behaves dependent on the external shear stress produced by the fluid flowing over it. Different experimental analyses have been performed examining it, proposing various models to describe it. Some of these models view the biofilm matrix as a viscoelastic structure and others as a non-Newtonian fluid (Rittmann and Lapidou, 2001). For the first type of models, experimental analyses have been widely performed for characterizing parameters (e.g. Young's modulus, elastic modulus, etc) and the models have been implemented using fluid-structure interactions approaches, focusing in the simulation of biofilm deformation induced by the liquid flow (Mattei et al., 2017). Nevertheless, little attention has been paid to the second type of models, since only few works in the literature related to characterization and modeling of biofilms as non-Newtonian

fluid can be found. The main reference is the pioneering analysis performed by Ohashi and Harada (1994), where the biofilm was characterized as a Bingham fluid. Therefore, the perspective of exploring novel modeling approaches, such as computational fluid dynamics (CFD) techniques, that are able to couple the biochemical part (substrate transport/consumption and biomass growth/distribution) with mechanical characteristics and biofilm behavior (deformation and detachment) is very encouraging.

The present thesis has been developed in the Department of Mining, Industrial and ICT Engineering of the UPC, in the research group Biological Treatment of Odours and Gaseous Pollutants (BIOGAP) within the project “Monitorización, modelización y control para la optimización de biofiltros percoladores de desulfuración anóxicos y aerobios” (MICROBIOFIN) funded by the Spanish Ministerio de Economía y Competitividad. The project proposes the use of a variety of techniques for monitoring the biofiltration process, including biofilms characterization with microsensors, and obtaining biodegradation mechanisms and kinetics of the process. The experimental data obtained from the rigorous monitoring allowed the development of models to describe biofilms and biosystems performance, which will provide tools for their behavior prediction in different situations. Among the abovementioned research topics, this thesis is focused particularly in the development of accurate models of the described biosystems, trying to reproduce mostly phenomena present in biofilms behavior. It must be pointed out that this thesis directly drives to a further knowledge and optimization of biofilm systems.

1.2. THESIS OVERVIEW

The thesis is divided into nine chapters, each one focusing on specific aspects of biofilms behavior and its effects on biosystems performance.

In this **first Chapter**, the motivations and the thesis overview are presented. In **Chapter 2**, the relevant background information about biosystems and computational fluid dynamics (CFD) techniques is given, describing in detail biofilm and biosystems modeling, which include CFD models for describing bioreactors performance, and the techniques for biofilms and biosystems characterization. In **Chapter 3** the general and the specific objectives of the thesis are stated.

Chapters 4, 5, 6, 7 and 8 contain the results obtained during the thesis. In **Chapter 4** the development of a methodology to model accurately bioreactor performance is presented, coupling the biological behavior with the systems hydrodynamics by means of using CFD techniques. The operation of a fixed-bed bioreactor is simulated using one-phase model and validated with experimental data measured in liquid and biofilm phases. In **Chapter 5** a complete rheological characterization of fixed and suspended heterotrophic biomass is given, examining their macroscopic mechanical properties and microstructure. Analysis under steady, oscillatory and transient shear flows conditions are performed focusing mainly on the

description of the biofilm as a non-Newtonian fluid. These experimental data together with the methodology developed in Chapter 4 are further used in Chapters 6 and 7 to develop multiphase models (liquid-biofilm and gas-biofilm, respectively). The fluid dynamics are coupled with the biochemical phenomena (substrate transport/consumption and biomass growth) and/or the biofilm mechanical behavior (deformation and detachment), examining biosystems performance under laminar and turbulent conditions. Specifically, in **Chapter 6** the experimental data which characterize the biological system as a non-Newtonian fluid are used to define the biofilm into the CFD code, allowing to define multiphase models (liquid-biofilm). Models are solved using the volume of fluid (VOF) method, tracking accurately interfacial area to consider mass transfer processes, thus presenting a novel continuum approach for biosystems modeling. In addition, microbial growth kinetics are considered as a mass source for the non-Newtonian fluid phase, i.e. the biofilm. The implemented models are subsequently used to estimate bioreactor system performance, studying the effect of fluid dynamics of laminar flow over biomass growth and mass transport/transfer mechanisms. Additionally, capabilities of this new approach modeling were tested for reproducing the biofilm growth and the biofilm-flow interaction in various geometries and laminar flow conditions, obtaining promising results. The knowledge obtained from the previous chapters is applied and extended in **Chapter 7**, in order to examine the influence of turbulent regimes on biosystems performance. The models proposed in Chapter 6 are adapted to reproduce how gas phases on turbulent regimes can disrupt the biological system attached to the substratum (gas-biofilm models). Also, in this chapter high-speed camera image-processing technique is applied to capture the biofilm-fluid interactions when the fluid phase impacts over the biofilm. As a result, multiphase models for analyzing turbulence effect on displacement/detachment of the biological system are developed and experimentally verified, establishing the use of the new continuum modeling approach for reproducing biofilm behavior under turbulent conditions. Moreover, the predominant parameters influencing in the biofilm disruption and removal under gaseous and high-speed flows are estimated. **Chapter 8** is focused on the experimental characterization of fluid-biofilm interface. A novel local capacitance needle-probe for in-situ biofilm layer and fluid interfaces detection is presented. The probe performance is calibrated and verified in multiphase systems, providing an additional tool for the experimental characterization of biosystems at mesoscale. In addition, the sensor capabilities for interface detection, depth measuring, and surface reconstruction are discussed.

In **Chapter 9** the conclusions extracted from the results obtained in previous chapters are exposed and future research topics are recommended.



INTRODUCTION

2.1. BIOFILMS

Although there is no commonly accepted definition of the term *biofilm*, “a biofilm is considered to be an aggregate of microorganisms embedded in a matrix composed of microbially produced extracellular polymeric substances (EPS) and attached to a surface” (Lewandowski and Beyenal, 2007).

Depending on where the biofilms have growth and what their microbial compositions are, the effects of biofilms can be desirable, undesirable or even disastrous from the human point of view. Biofilms have a desirable effect when they remove pollutants in wastewater treatment plants, e.g. biofilms present in wetlands and biotrickling filters (BTF). Biofilms have an undesirable effect when they produce alterations in processes, e.g. biofilms accumulated increase heat transfer resistance in cooling towers or heat exchangers, or they can reduce flow capacity in pipelines. In addition, biofilms can have a harmful effect when they colonize implants or prosthesis in the human body, e.g. heart valves, dental implants, contact lenses, which can lead to serious infections.

2.1.1. Biofilm systems, biofilm processes, and biofilm reactors

Besides the biofilm term, it is required to introduce the term *biofilm system* or *biosystem*, which includes the components affecting biofilm formation, activity and structure. A biosystem is defined as a group of compartments and their components (IWA Task Group on Biofilm Modeling, 2006). Usually, biosystems are composed of four compartments:

- The biofilm (formed by the microorganisms and the EPS matrix)
- The surface to which the biofilm is attached, i.e. substratum
- The liquid phase, which usually supplies nutrients solution and lies over the biofilm
- The gas phase (if present)

Figure 2.1 depicts a characteristic biosystem with the described compartments.

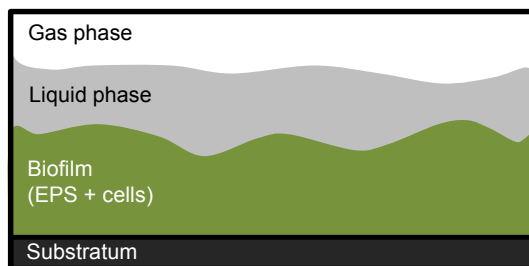


Figure 2.1. Biofilm compartments: gas phase, liquid phase, biofilm (microorganisms and EPS) and substratum (adapted from Lewandowski and Beyenal (2007)).

Therefore, the compartments previously listed can describe the following biofilm system with diverse components: the biofilm is formed by a gel-like aggregation of microorganisms

and water, all embedded by the EPS, being this biofilm anchored to a substratum and in contact with the liquid phase on the other side, which also interacts with the gas phase.

The components present in the biofilm systems can undergo transformation, transport, and transfer processes, i.e. *biofilm processes*, which includes all physical, chemical, and biological processes that affect or are affected by the rate microbial activity in biofilms. For instance, substrate utilization is a transformation process and diffusion is a transport process.

The biofilm processes are quantified in *biofilm reactors*, thus biofilm reactors and biofilm systems have the same meaning colloquially. The subtle difference between them is that the biofilm systems exist with or without human intervention, whereas biofilm reactors are created by human actions. Therefore, a biofilm reactor is defined as a biofilm system in which biofilm processes are produced and controlled (Lewandowski and Beyenal, 2007). Examples of engineered biofilm reactors are constructed wetlands, packed-bed reactors such as biotrickling filters (BTF), or membrane and moving bed biofilm reactors used in wastewater treatment plants (Henze et al., 2008). The BTF for waste gas abatement is taken as an example for illustrating the different process that can take place in a bioreactor. In a BTF, the polluted gas flows through a biomass immobilized over the surface of an inert packing material, which is continuously irrigated with a liquid phase containing the nutrients required by the biological system. Then the fixed biomass degrades the pollutant previously absorbed in a continuously circulating liquid phase (Delhom nie and Heitz, 2005). Figure 2.2 shows the processes typically occurring in biotrickling filters bioreactor, which is formed by four compartments listed above (substratum or support medium, biofilm, liquid phase, and gas phase).

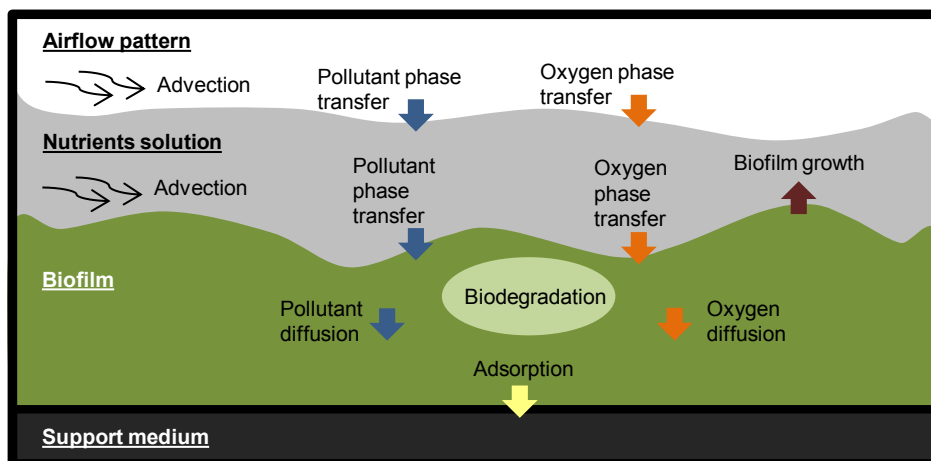


Figure 2.2. Phenomena involved in the operation of biotrickling filters (adapted from Devigny and Ramesh (2005)).

As can be seen, pollutants are carried into the biotrickling filters by the gas phase at presumably laminar flow rates, although dispersion occurs because of the tortuosity of the

pores in the packed beds. As the gas phase passes through the packing material, pollutants are transferred from the gas phase to the liquid phase, and then to the biofilm. The pollutants diffuse into the biofilm, and microorganisms in the biofilm absorb the pollutants and biodegrade them. Usually, aerobic bioreactors are used, so that oxygen and nutrients are also dissolved in the water and diffuse to the biofilm, which produces its enrichment and growth (Devinny and Ramesh, 2005).

2.1.2. Biofilm activity

Biofilm activity is defined as the rate of nutrient utilization per unit of biofilm, being conventionally evaluated analyzing the utilization rate of the growth-limiting nutrient, or the product concentration. The concept of biofilm activity is especially important in the biosystems study for waste abatement, since it is related to the rate of pollutants degradation and biosystem effectiveness. In order to characterize biokinetic models in this type of biosystems, the activity is evaluated based on the utilization rate of the pollutants or, if this is not possible, it is based on the utilization rate of the main electron acceptor in the respiration of selected groups of microorganisms (Lewandowski and Beyenal, 2007).

The utilization rate of nutrients and pollutants is defined from the kinetic models of growth. Expressions 2.1 and 2.2 are used to estimate the temporal evolution of the concentration of substrates (dC/dt) from the growth rate of microorganisms. The endogenous metabolism of microorganisms is considered in Expression 2.2, thus allowing to include the utilization rate for the maintenance of microorganisms in the global substrate utilization rate.

$$-\frac{dC}{dt} = \frac{1}{Y_{X/S}} \frac{dX}{dt} \quad (2.1)$$

$$-\frac{dC}{dt} = \frac{1}{Y_{X/S}} \frac{dX}{dt} + k_d X \quad (2.2)$$

Where C is the concentration of nutrient or pollutant in the biofilm (kg m^{-3}), t is the time (s), $Y_{X/S}$ is the relationship between the consumed nutrient (S) concentration and the produced microorganisms concentration (kg X kg S^{-1}), k_d is maintenance factor for the compound (s^{-1}), and X is the biomass concentration (kg m^{-3}), being dX/dt the microbial growth rate.

The microbial growth rate is defined as the temporal change in microbial cell concentration, which is characterized by the specific growth rate (μ) (s^{-1}) by means of Expression 2.3.

$$\frac{dX}{dt} = \mu X \quad (2.3)$$

Microbial growth kinetics define the relationship between the specific growth rate of a microorganism and the nutrient or pollutant concentration. The Monod equation for one limiting nutrient or pollutant (Expression 2.4) is widely used for correlating these two parameters (Devinny and Ramesh, 2005; IWA Task Group on Biofilm Modeling, 2006).

$$\mu = \mu_{\max} \frac{C}{K_{S,M} + C} \quad (2.4)$$

Where μ_{\max} is the maximum growth rate when the growth-limiting nutrient concentration is not limiting (s^{-1}), and $K_{S,M}$ is the Monod half-saturation constant ($kg\ m^{-3}$).

Further information about other single-nutrient-limited growth kinetic models and multiple-nutrient-limited growth kinetic models can be found elsewhere (Lewandowski and Beyenal, 2007).

2.1.3. Biofilm-fluid interaction

Fluid around biofilms can influence biosystems performance, having an effect on biofilm development and activity. In particular, there are two important ways that fluid flow influences microbial biofilm formation and maturity: (1) the transport of dissolved solutes into and out of the biofilm, and (2) the application of shear forces to the biofilm which could cause biofilm deformation and detachment (Stewart, 2012).

In the fluids which are flowing over the biofilm, the transport of substrates is governed mainly by advection, having the diffusion a more participative role in the concentration boundary layer (CBL) (Wäsche et al., 2002; Lewandowski and Beyenal, 2007; Guimerà et al., 2016). This implies that the biochemical processes and biofilm dynamics can be affected by biosystem fluid conditions, which may even cause problems in biofilm growth limited by the amount of nutrient available and/or limitations in bioreactors efficiency operated for pollutants removal (Iliuta and Larachi, 2004; Liotta et al., 2014). In addition, the external mass transfer is also determined by flow patterns: higher fluid velocities produce higher mass transfer rate, i.e. higher biofilm accumulation rate (Zhang and Bishop, 1994; Horn and Hempel, 1995). Finally, the fluid flow applies shear forces at the biofilm surface, which can produce structural modifications. Slow fluid flow can produce deformations, i.e. short stretching, on biofilm structure due to the low shear forces; whereas fast fluid flow implies substantial shear forces, stretching the biofilm structure, being able to form streamers, and finally detaching it from the rest of biofilm structure (Stoodley et al., 1999a). In addition, sudden changes or stoppages of the biosystem fluid flow can produce a viscoelastic behavior showing biofilm time-dependent creep or recoil respectively (Klapper et al., 2002; Towler et al., 2003; Fabbri et al., 2016b).

From the stated above, it is clearly demonstrated the direct influence that the fluid flows around the biofilms have in all the processes which regulate biofilms behavior, and thus, in the biosystems performance. In addition, bioreactors hydrodynamics and the rest of the factors previously described have also an effect on biofilm structure formation. Therefore, processes, such as fluid flow, substrate transport by convection and diffusion, substrate consumption, biomass growth and biomass detachment, are essential in any model aiming to represent biosystems evolution as a response to environmental conditions (Picioreanu, 1999).

2.1.4. Biofilm structure

During last decades, the view of biofilm structure has changed due to the development of tools, such as confocal microscopy and microelectrodes sensing, for directly probing the biofilm environment with high spatial resolution (Lewandowski and Beyenal, 2007). Firstly, it was assumed that the biofilms were more or less homogeneous, being the microorganisms uniformly distributed in the biofilms matrix. Later, analytical tools revealed a more complex view of biofilm morphology, by finding heterogeneous structures, which could contain cell clusters, discrete aggregates of microbial cells in an EPS matrix, interstitial voids, and open channels connected to the bulk liquid (De Beer et al., 1994).

Variations on diverse parameters, such as microbial species, biomass density, substrate concentration, biofilm porosity, diffusivity, pH, etc, have been widely reported, thus many forms of heterogeneity in biofilms can be considered. Piciooreanu (1999) summarized the most usual cases of possible biofilm heterogeneity: (1) geometrical heterogeneity (e.g. biofilm thickness, surface roughness and porosity); (2) chemical heterogeneity (e.g. diversity of chemical solutes, pH variations, diversity of reactions); (3) biological heterogeneity (e.g. microbial diversity of species and their spatial distribution, differences in activity); (4) physical heterogeneity (e.g. biofilm density, permeability and viscoelasticity, EPS properties, solute concentration and diffusivity).

In the last decade, most of the researchers have focused on the study of biofilm physical heterogeneity, since EPS matrix has been pointed as a key parameter in the determination of biofilm architecture and mechanical properties (Hall-Stoodley and Stoodley, 2002). The EPS network present in biofilms provide them stability, and specific mechanical properties (Sheng et al., 2010; Wilking et al., 2011; Peterson et al., 2015), making biofilms to behave typically as a viscoelastic structure if shear forces are applied over them (Ohashi and Harada, 1994; Stoodley et al., 1999a; Klapper et al., 2002). Biofilm mechanics is an emerging field in the study of biosystems, which may provide new insights into the development, mechanical disruption or stabilization methods for biofilms (Fabbri and Stoodley, 2016).

2.1.5. Key parameters in biofilm control strategies

Control strategies are used to promote the growth of desired biofilms or to eradicate undesired biofilms. In industrial or medical applications, it is usual to use strategies to eradicate biofilms, but there are also cases in which it is necessary to control the biofilm and its growth, for example in fixed-bed reactors. In the case of biotrickling filters, both strategies are needed during bioreactor operation. In such systems, it is required an initial stage for the inoculation, attachment and biofilm growth, and then maintaining the required operating conditions to avoid damaging the biofilm attached to the packed bed, but allowing its growth. After some time of operation, the major drawback limiting BTFs use is the formation of an excessive amount of biomass, i.e. packed bed clogging (Iliuta and Larachi, 2004). This

phenomenon leads to the progressive obstruction of the bed, which is accompanied with a rise in pressure drop and, eventually, flow channeling, needing the application of strategies to remove biomass excess (Mendoza et al., 2004), and being a key operational step to optimize the performance of this type of biosystems (Liu et al., 2016). Therefore, appropriate control strategies are essential to achieving the efficient performance of biosystems for long-term operations.

Several techniques to remove biofilms can be applied to a particular system, including mechanical methods (e.g. backwashing or scrubbing); chemical methods (e.g. use of disinfectants agents); stopping biofilm growth by removing essential nutrients; and inhibition of microbial attachment to a surface (Chen and Stewart, 2000; Evans, 2000; Meyer, 2003; Thormann et al., 2005). All these methods are clearly promoting biomass detachment, being mechanical and chemical strategies the most-used methods (Srinivasan et al., 1995; Xavier et al., 2005a).

In most of these strategies, fluid flow plays an important role in the efficiency of the removal method, e.g. when mechanical backwash is applied or an antimicrobial is fed up in the liquid phase, since the fluid acts as a major medium to biofilm-environment interaction (Stewart, 2012). Even further, it has been reported that the efficacy of biofilm removal agents can depend on the action of fluid shear (Simões et al., 2005). At the same time, as discussed above, biofilm structural changes can be produced depending on fluid conditions. Additionally, the viscoelastic biofilms properties have been recently pointed as a pivotal element for the way in which biofilms response to mechanical and chemical challenges (Hall-Stoodley and Stoodley, 2002; Jones et al., 2011; Peterson et al., 2015). Reviews on biofilm mechanics showed that changes in EPS composition significantly modify biofilm mechanical behavior or increase/decrease biofilm detachment (Fabbri and Stoodley, 2016).

From the stated above, fluid flow dynamics, biofilm viscoelastic behavior, and biofilm deformation and detachment are some fundamental parameters in biofilm control strategies. Therefore, the recent emerging generation of models, i.e. multi-physic and mechanical models in which biofilm physics interacts with the adjacent fluid, considering viscoelastic properties biofilm-fluid interaction will help to open new approaches in the design of effective strategies to remove biofilms, and to control and prevent the excessive biofilm growth (Fabbri and Stoodley, 2016).

2.2. BIOFILMS AND BIOSYSTEMS MODELING

2.2.1. Modeling biofilms development and structure

Over the last decades, several biofilms models have been developed, reaching a high level of complexity and progressively incorporating a huge number of physico-chemical and biological processes (IWA Task Group on Biofilm Modeling, 2006). The first-generation of

models described mass flux into the biofilm and concentration profiles within the biofilm of one rate-limiting substrate, assuming a simple geometry (one-dimensional) and uniform biomass distribution. The second-generation models were aimed to evaluate the overall flux of substrates and metabolic products through the biofilm surface. Finally, in the third-generation mathematical models, all components can vary in multi-dimensional space, as well as time, and they can generate complex physical and ecological structures. In general, the developed models can be classified in two different approaches based on the representation of the microbial community (Böl et al., 2012; Storck et al., 2014; Mattei et al., 2017):

- Continuum models: biofilm is defined as a single material based on population-averaged behavior of different functional groups, i.e. averaged properties for concentration, density, etc, in the whole domain.
- Discrete models: biofilm is defined as a collection of cells with different properties (i.e. mass, size, etc), taking into account the behavior of an individual microorganism, i.e. actions and interactions of the biomass units with each other and the environment.

Additionally, models combining both approaches, i.e. individual or discrete cells for microbial in a continuum EPS, have also been developed (e.g. Alpkvist et al. (2006)). Figure 2.3 shows a schematic representation of continuum, discrete and combined approaches.

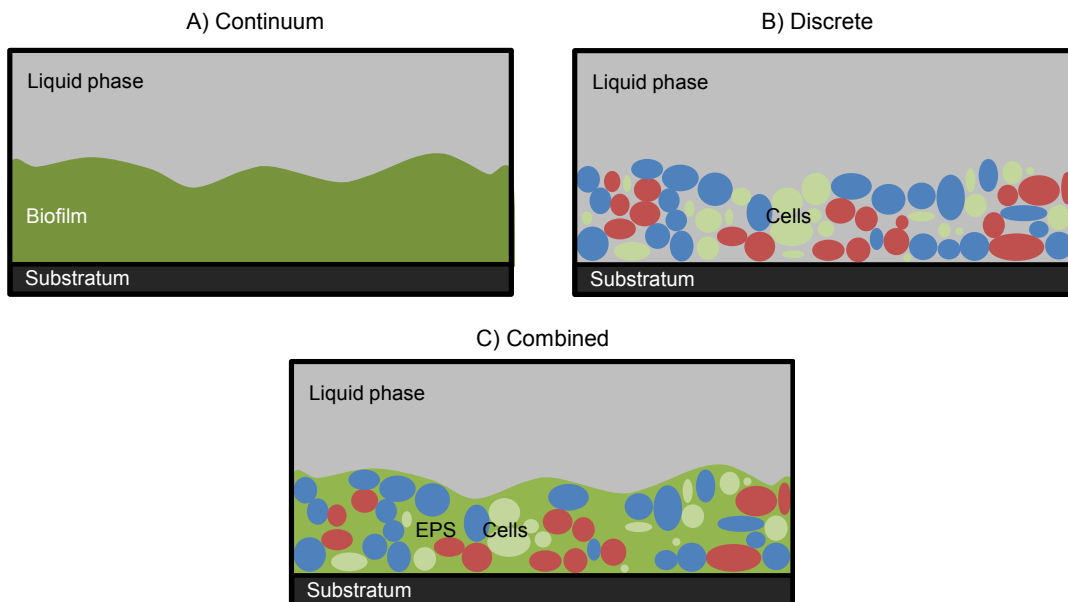


Figure 2.3. Schematic representation of biofilms modeling approaches: continuum, discrete and combined (adapted from Picioreanu (2018)).

Continuum models treat the dynamics of biomass spreading, i.e. biomass transport, by volume-averaged balances using, in general, partial differential equations. The continuum models are usually implemented and solved in powerful commercial solvers, allowing to

compute large-scale cases. In discrete models, biomass spreading is computed by forces balances resolving ordinary differential equations, mainly in user-defined codes. The discrete approach allows the implementation of small-scale models (Picioreanu, 2018).

In the continuum approach, two-dimensional and three-dimensional models have been developed, considering multispecies in a heterogeneous biofilm development (Alpkvist and Klapper, 2007a), fluid flow and shear stress on biofilm growth (Duddu et al., 2009), and biofilm-flow interaction to describe deformation and detachment (Zhang et al., 2008; Tierra et al., 2015). Using the discrete approach, modeling biomass growth, spreading and activity has been widely performed by using a cellular automata (CA) approach (Picioreanu et al., 1998a; Picioreanu et al., 2001) and individual-based models (IbM) (Picioreanu et al., 2004; Xavier et al., 2005b, 2005c; Storck et al., 2014). In addition, other authors applied the immersed boundary (IB) method in a discrete approach based on particles connected by springs, in order to simulate biofilm deformation and/or detachment (Alpkvist and Klapper, 2007b; Stotsky et al., 2014, 2016; Sudarsan et al., 2016). For further details of biofilm modeling, comprehensive reviews can be found in literature (Wang and Zhang, 2010; Horn and Lackner, 2014; Mattei et al., 2017).

Most of the models listed above aimed at describing biofilm formation defining it as a rigid material, i.e. non-deformable. As stated above, biofilms modeling is now focused on a new generation of models, where biofilm-fluid interactions are reproduced considering biofilm mechanical properties. Therefore, this new generation of biofilm models is aiming to couple fluid dynamics with biofilm structure to reproduce the physical movement produced when the biofilm is deformed or even detached by external forces. Table 2.1 summarized the main features of the biofilm models for both discrete and continuum approaches, describing fluid-structure interaction due to applied tangential forces.

In the discrete approach, one of the first contributions without assuming a rigid biofilm was the ball-spring model applied in the immersed boundary (IB) method (Alpkvist and Klapper, 2007b), where the fluid-driven mechanical response of biofilms and their detachment were described, considering biofilms as elastic materials. Recently, Stotsky and coworkers (Stotsky et al., 2016) extended the work of Alpkvist and Klapper (2007) including the viscoelastic behavior of biofilms, by means of implementing Maxwell and Zener models. These authors simulated different scenarios showing the deformations produced over biofilm matrix, whereas detachment conditions were not considered. Interestingly, these authors also reported that the viscous nature of the IB produced that the biofilm still behaved visco-elastically, even when it was defined using an elastic constitutive relation (Hooke's law) due to its immersion in a viscous fluid. Although very promising results were obtained applying IB method, still there is a lack of information in how to relate biofilm material properties at macroscale (e.g. elastic modulus and Poisson ratio) to parameters at microscale (e.g. spring coefficient and length).

Table 2.1. Relevant models describing biofilm-fluid interactions sorted by the modeling approach type.

Modeling approach	Reference	Dimension and scale	Biofilm definition	Flow conditions	Biofilm movement
Immersed boundary (IB)	Alpkvist and Klapper (2007b)	2D (300 x 250 μm) 3D (500 x 250 x 250 μm)	Elastic material	Laminar	Deformation and detachment
	Stotsky et al. (2016)	3D (30 x 30 x 30 μm)	Viscoelastic material (Maxwell and Zener models)	Laminar	Deformation
Phase field	Zhang et al. (2008)	2D (1 x 1 mm)	Two-phase: two viscous fluids	Laminar	Deformation, rippling and detachment
	Tierra et al. (2015)	2D (1 x 1 mm)	Two-phase: viscous and viscoelastic (Oldroyd-B model) fluids	Laminar	Deformation and detachment
Finite element method (FEM)	Towler et al. (2007)	2D (40 x 3 mm)	Viscoelastic material (Burger model)	Turbulent	Deformation
	Böl et al. (2009)	3D (0.462 x 0.330 x 1 mm)	Elastic (St. Venant-Kirchhoff model) Hyperelastic (Arruda-Boyce model) material	Laminar	Deformation and detachment (dropping out elements)
	Taherzadeh et al. (2010, 2012)	2D (12 x 3.2 mm) (1.492 mm streamer length)	Elastic material (St. Venant-Kirchhoff model)	Laminar	Streamer oscillations
	Piciooreanu et al. (2018)	2D (3 x 1 mm)	Poroelastic material	Laminar	Deformation

In the continuum approach, an example of a two-dimensional biofilm model was presented by Zhang et al. (2008). In that work, the phase field approach was used to reproduce several biofilm-fluid interaction scenarios, and being able to simulate deformations, detachment phenomena and rippling. The same approach was used by Tierra and coworkers (Tierra et al., 2015) but the biofilm viscoelastic behavior experimentally observed was implemented in the model. The biofilm was defined as a two-phase mixture, in which bacteria behave like a Newtonian fluid and EPS like a viscoelastic substance (Oldroyd-B model), correctly reproducing biofilm deformation and detachment. Towler and coworkers (Towler et al., 2007) used a finite element method (FEM) to simulate the response of a hemispherical biofilm structure to a turbulence flow (velocity of 1 m s^{-1}), defining the biofilm cluster as a viscoelastic material by means of Burger model. In a similar work, Böl et al. (2009) combined confocal laser scanning microscopy (CLSM) with FEM, reproducing the deformation in a real biofilm structure reconstructed from stacks of CLSM images. Biofilm detachment was also considered, dropping out of the simulation the elements in which the critical strength was exceeded, due to the difficulty of dealing with breaking and colliding objects in this method. FEM approach has been also used to describe the influence of flow

velocity on the oscillation of a biofilm streamer, showing how the streamer oscillation reduced the forces induced by the moving fluid and the streamer movement clearly led to improved mass transfer (Taherzadeh et al., 2010, 2012). Recently, Piciooreanu et al. (2018) combined FEM approach with optical coherence tomography (OCT), a non-invasive imaging technique. In this study, the biofilm elastic properties were determined by modeling the biofilm deformation recorded by OCT imaging under defined flow conditions. In the developed fluid-structure model, the biofilm was defined as a poroelastic material to consider the pressure of water in the biofilm pores.

Despite the high computational requirements, more advances have been done using the continuum approach, which provides models at mesoscale (e.g. millimeters scale). Thus, the multidimensional continuum models seem to be more convenient than discrete approaches when applied to mechanical problems which necessarily imply flow field calculations (Mattei et al., 2017). The perspective of exploring new continuum approaches able to couple the biosystems biochemical part with mechanical characteristics and fluid behavior is very promising (Horn and Lackner, 2014).

2.2.2. Biosystems modeling

In an effort to include the fluid flow influence on biosystems in a large scale modeling, different hydrodynamic models have been considered when bioreactor performance is modeled. Table 2.2 summarizes the hydrodynamic models used to simulate the performance of the most common aerobic bioreactors configurations (activated sludge reactors, fluidized bed reactors, biofilters, and biotrickling filters) (Liotta et al., 2014). The considered hydrodynamic models include: ideal plug flow reactor (PFR), ideal continuously stirred tank reactor (CSTR), tank-in-series (TIS) model, dispersion model, and computational fluid dynamics (CFD) model; where C is reactant concentration, t is time, U is flow velocity, x is the spatial variable coordinate, i is the subscript denoting influent, e is the subscript denoting effluent, τ is hydraulic retention time, N_R is the number of reactor in series, and D_N is the dispersion number.

In the bioreactor case above presented, i.e. biotrickling filters (Figure 2.2), several phenomena are involved in its modeling (Kim and Deshusses, 2003; Ahmed et al., 2013; Rodriguez, 2013; López et al., 2016; San-Valero et al., 2018): mass balances of the pollutants, oxygen and products resulting from pollutant degradation, and biomass generation, in all phases present in the reactor (usually gas, liquid, biofilm and solid). Moreover, depending on the objectives for which the model is developed, the resulting equations may include terms for the dispersion effects in gas phase, mass transfer between the phases, diffusional mass transfer in the biofilm, consumption due to biological reactions, adsorption onto solid media and biomass growth. In an effort to facilitate the mathematical solutions, the complexity of the models is often substantially reduced using assumptions, such as: plug flow for gas phase; ideal mixing in liquid phase; equilibrium between

biofilm/liquid interface; constant biofilm thickness and biomass density; negligible biomass growth; steady-state conditions (Deshusses and Shareefdeen, 2005). Thus, most of the published biotrickling models consider that the liquid movement through a porous bed occurs by an ideal plug flow pattern, because the effect of axial dispersion can be neglected under certain conditions (Hodge and Devinny, 1997). The assumptions make that the solutions are less arduous. However, in some cases, simplifying assumptions make models unrealistic and may lead to errors in estimating design parameters and in model extrapolation.

Table 2.2. Modeling approach used in the hydrodynamic modeling of the most common aerobic bioreactors (adapted from Liotta et al. (2014)).

Modeling approach	Basic concept	Equation
Ideal PFR	No longitudinal mixing occurs between adjacent fluid elements	$\frac{\partial C}{\partial t} = -U \cdot \frac{\partial C}{\partial x}$
Ideal CSTR	Concentration is assumed to be homogenous in the reactor	$\frac{C_{ex}}{C_{in}} = e^{-\frac{t}{\tau}}$
TIS model	The flow is discretized into a series of hypothetical CSTRs	$\frac{C_{ex}}{C_{in}} = \frac{N_R^{N_R}}{(N_R - 1)!} \left(\frac{t}{\tau}\right)^{N_R-1} e^{-\frac{N_R t}{\tau}}$
Dispersion model	Set of differential equations including longitudinal diffusion and advection terms	$\frac{\partial C}{\partial t} = D_N \cdot \frac{\partial^2 C}{\partial x^2} - U \cdot \frac{\partial C}{\partial x}$
CFD model	Technique applied to solve fluid dynamics models	Discretizes the reactor using a computational grid and including fundamental mass, momentum, and energy conservation equations

Liotta and coworkers (Liotta et al., 2014) compared performance-prediction models of the biotrickling filters, considering the different flow models listed in Table 2.2. They concluded that CFD models are the most complete describing space-time evolution of physical and biological phenomena. Recently, CFD techniques have been stated as a useful tool for describing hydrodynamics and biochemical reactions in the wastewater treatment field with promising results. Specifically, models of airlift loop reactors (Feng et al., 2007; Jia et al., 2009; Wang et al., 2011), activated sludge reactors (Glover et al., 2006; Le Moullec et al., 2010; Climent et al., 2018), and biotrickling filters (Liotta and Larachi, 2005) have been developed. In these CFD models, the bioprocess behavior is usually associated with the liquid phase dynamics.

In addition, IWA Task Group on Biofilm Modeling (Noguera and Morgenroth, 2004) defined a set of benchmark problems to evaluate model responsiveness under established scenarios. Particularly, the Benchmark problem 2 (BM2) is focused on estimating hydrodynamics influence over mass transfer in heterogeneous biofilms, considering diffusive and advection mass transport in the fluid phase and concluding that 2D and 3D models should be applied when a detailed resolution inside the biofilm is required (Eberl et al., 2004;

IWA Task Group on Biofilm Modeling, 2006). In fact, other works have demonstrated the suitability of 3D CFD models to study biofouling phenomenon coupled with hydrodynamics variables in membrane bioreactors (Picioreanu et al., 2009; Vrouwenvelder et al., 2010).

To the author's knowledge, so far, there has not been a study regarding the application of computational fluid dynamics to the simulation of biofilm-fluid interactions in biosystems. The works mentioned above provide confidence to develop CFD simulations in fixed-bed biofilms, considering the biochemical and physical phenomena in the biosystem.

2.3. BIOFILMS AND BIOSYSTEMS CHARACTERIZATION

Biofilms and biosystems characterization is generally focused on the study of structural, operational and ecological aspects. These aspects include the fluid conditions, the development and growth of biofilms, biofilm structure, and biodegradation processes. In the following sections, the most used analytical methods in the study of biosystems are presented.

2.3.1. Hydrodynamic characterization techniques

Hydrodynamic in biosystems has been mainly studied using techniques for determining the fluid flow, and techniques for measuring velocity patterns.

2.3.1.1. Residence time distribution (RTD) characterization

In order to characterize fluid flow patterns, residence time distribution (RTD) analyses have been used at different biosystems scales (Picioreanu et al., 2009; Climent et al., 2018). RTD is experimentally determined by injecting an inert substance, i.e. tracer, at the initial time. The concentration of the tracer is then measured along time in the effluent zone, usually at the outlet. To perform the RTD analysis, the concentration-time and the residence time distribution curves should be obtained from the experimental data, linking mass and volumetric flow rate of the tracer along the experiment, and allowing to calculate the mean residence time. Further RTD details can be found elsewhere (Levenspiel, 1999).

2.3.1.2. Velocity characterization

Various methods have been used to measure velocity patterns in biosystems: laser Doppler anemometry (LDA) in airlift bioreactors (Feng et al., 2007), acoustic Doppler velocimeter (ADV) in activated sludge reactors (Ramin et al., 2014; Climent et al., 2018), and high-speed camera in jet impacts on fixed-bed biofilms for biomedical applications (Fabbri et al., 2016b, 2017). Further details of measurements procedures can be found in the works beforehand cited.

2.3.2. Structural characterization techniques

The biofilms structural characterization techniques offer qualitative and quantitative information on their superficial characteristics, as well as helping to determine their composition. The most commonly used methods are described below.

Confocal laser scanning microscopy (CLSM) has been widely used in the study of biofilms (De Beer et al., 1994; Evans, 2000; Vinogradov et al., 2004; Böl et al., 2009). The results obtained using CLSM offer high-resolution images and three-dimension reconstructions of biofilms structures. Using fluorescence techniques allow the identification of the different components present in the biofilm (Evans, 2000). Results from CSLM have shown cell clusters, discrete aggregates of microbial cells in an EPS matrix, interstitial voids, and open channels connected to the bulk liquid (De Beer et al., 1994; Lewandowski and Beyenal, 2007). Another powerful technique to describe biofilm morphology on the microscale is atomic force microscopy (AFM), obtaining images of the biofilms surfaces at nanometer resolution. The technique has been often used to map the topography of the biofilm surface, and to investigate single bacteria cells (Lewandowski and Beyenal, 2007).

To investigate the mesoscale biofilm structure, other methods such as magnetic resonance microscopy (MRM) and optical coherence tomography (OCT) need to be applied (Wagner et al., 2010). MRM-based techniques for the non-invasive analysis of living biofilms have been employed to measure fluid properties. Nuclear magnetic resonance (NMR) have enabled three-dimensional mapping of structure and fluid velocities in biofilm systems (Lewandowski et al., 1993; Stewart, 2012). Furthermore, NMR methods have been used to obtain the imaging of biofilms in porous media, and to determine molecular mobility and chemical composition of biofilm EPS (Denkhaus et al., 2007). Recent progress in two and three-dimensional in-situ non-destructive biofilm imaging has been achieved by OCT (Wagner and Horn, 2017). This technique has been used to investigate biofilm formation and development under operational conditions. Datasets were obtained of the overall biofilm structure at mesoscale, containing a representative description of processes dependent on time, such as growth or deformation (Wagner et al., 2010; Blauert et al., 2015). In addition, the structural description provided by OCT was related to biofilm mechanical properties by numerical models (Jafari et al., 2018; Picioreanu et al., 2018)

2.3.2.1. Biofilm thickness measurement

Biofilm thickness is a parameter obtained from the biofilm structural characterization, which should be monitored in-situ during biosystem operation, since it plays a key role in mass transfer processes (Bakke and Olsson, 1986). In addition, biofilm thickness is directly related to diffusion phenomenon and biofilm growth and development (Hoehn et al., 1973).

Non-destructive methods based on optical and laser technologies have been used to measure biofilm thickness in biofilm fixed-bed systems, using light microscopy (Bakke and

Olsson, 1986; Bakke et al., 2001), confocal laser scanning microscopy (CLSM) (Stoodley et al., 1999b; Heydorn et al., 2000), a laser triangulation sensor (Okkerse et al., 2000), a scanner with an image acquisition system (Milferstedt et al., 2006), or recently OCT technique (Wagner et al., 2010; Wagner and Horn, 2017). In addition, a mechanical method based on uniaxial compression (Paramonova et al., 2007) and magnetic resonance imaging (Manz et al., 2003) are other non-destructive techniques proposed for adequately measuring biofilm thickness, and other more affordable techniques such as optical methods and impedance probes (Janknecht and Melo, 2003).

2.3.3. Mechanical characterization techniques

Mechanical biofilm properties are also determined, as these are directly connected with the internal structural organization of the biofilm. Rheological analyses can characterize mechanical properties under various shear flow conditions, providing information on how the material reacts both in regard to time-scale and applied stress. Rheology can be divided into two main groups: macrorheology and microrheology methods (Billings et al., 2015; Fabbri and Stoodley, 2016).

2.3.3.1. Macrorheology measurements

Macrorheological studies give insights on the biofilm mechanical properties at a macroscopic scale. These measurements are commonly performed on rheometers (Towler et al., 2003; Vinogradov et al., 2004; Wloka et al., 2005; Di Stefano et al., 2009), or flow cells (Stoodley et al., 1999a; Klapper et al., 2002), involving the application of a controlled external force. The rheological experimental data provided a wide range of insight into biofilms properties, including their shear-thinning (or pseudo-plastic) nature, and parameters such as the elastic moduli, complex viscosity and relaxation times. Even, macrorheology has been used to assess the effect of different chemical and antimicrobial treatments on biofilm viscoelastic properties (Jones et al., 2011; Lieleg et al., 2011). Recent reviews (Böl et al., 2012; Billings et al., 2015; Fabbri and Stoodley, 2016) are recommended to consult for a comprehensive analysis of measured properties, and additional discussion of techniques used.

2.3.3.2. Microrheology measurements

Microrheology is used to determine the same properties as macrorheology through the use of microscale probes, allowing to monitor the system over small length scales, and being applied without severe invasion of the biosystem state. The most common techniques used in microrheology are AFM (in this case for measuring force response), magnetic tweezers, microindenters, micro-cantilevers, microfluidics chambers and particle-tracking microrheology (PTM). Measurements with these techniques have revealed the spatial distribution of biofilm viscoelastic parameters at the microscale (Fabbri and Stoodley, 2016). Microrheological studies have also allowed measurements of biofilm adhesive and cohesive

strengths, essential parameters for assessing biofilm detachment (Ohashi and Harada, 1994). For a deeper description of microrheology instruments and measurements, the following recent reviews are suggested (Böl et al., 2012; Billings et al., 2015; Fabbri and Stoodley, 2016)

2.3.4. Biomass activity monitoring

Biofilm accumulation and its activity have been in-situ monitored in biosystems by means of microsensors, and optical and capacitance probes (Vojinović et al., 2006; Denkhaus et al., 2007).

Microsensors suitable in biofilm analysis, which small tip size providing a high spatial resolution, are applied in the study of biofilm formation, influx and efflux of substances and nutrients (e.g. rates of nutrient consumption, depth of nutrient penetration, mass-transport rates and diffusivity), and microprofiling of dissolved substances (Denkhaus et al., 2007). Microsensors can be used for measurements of oxygen, sulphide, hydrogen, chlorine, hydrogen peroxide, ammonia, nitrate, sulfide and pH among others (Lewandowski and Beyenal, 2007; Guimerà, 2016). They have also been used to characterize mass-transport dynamics and nutrients biodegradation processes inside the biofilms (Lewandowski et al., 1993; Zhang and Bishop, 1994; Horn and Hempel, 1995; Guimerà et al., 2015, 2016).

Optical and capacitance probes have also been applied for in situ biofilm monitoring of biosystems (Janknecht and Melo, 2003; Ferreira et al., 2005; Vojinović et al., 2006; Lewandowski and Beyenal, 2007). Optical density and biofilm capacitance parameters have been used as measurements to indicate biofilm activity and growth, since they are related to biomass density and cell concentration.

2.4. COMPUTATIONAL FLUID DYNAMICS TECHNIQUES

Computational fluid dynamics (CFD) is the analysis of systems involving fluid flow, and associated phenomena such as heat transfer and chemical reactions by means of computer-based simulation solving equations for mass, momentum, energy, turbulence and scalars with specified conditions on the boundary of that region. In CFD codes one of the most commonly used solution methods is known as the finite volume technique. In this technique, the region of interest is divided into small sub-regions, called control volumes. The equations are discretized and solved iteratively for each control volume. As a result, an approximation of the value of each variable at specific points throughout the domain can be obtained (ANSYS Inc, 2015, 2016). Therefore, CFD codes are based on conservation equations for mass, momentum and energy, which represents balances of accumulation (i.e. net inflow by convection and diffusion) as well as production within a defined control volume.

CFD codes are structured around the numerical algorithms that can tackle fluid flow problems. The typical steps in a CFD code workflow can be subdivided into pre-processing,

processing and post-processing (see Figure 2.4). The first step, i.e. pre-processing, involves building the geometry model and its mesh. The geometry of the study region, i.e. the computational domain, should be defined, and the grid should be generated, thus performing the sub-division of the domain into a number of smaller cells (or control volumes or elements). After mesh generation, the boundaries over the geometry faces required to be defined. Moreover, the specification of the fluid properties, and initial and boundary conditions should be done. In the same way, the physical models and the solution algorithms should be selected. Secondly, the processing step is mainly performed by the CFD code. The governing equations of fluid flow are integrated over all control volumes of the computational domain. The partial differential equations are discretized. The solution is parallelized and solved by an iterative method. Finally, the post-processing step involves the simulated data visualization and interpretation by means of vectors, contours or path lines plots, and planes or volumes weighted with minimum and maximum values of variables. Once the results are evaluated, they should be verified with experimental data. These steps are implemented in the most common CFD codes, such as ANSYS Fluent, ANSYS CFX, POLYFLOW, PHOENICS, STAR-CD and OpenFOAM (Versteeg and Malalasekera, 2007; Kaiser et al., 2014).

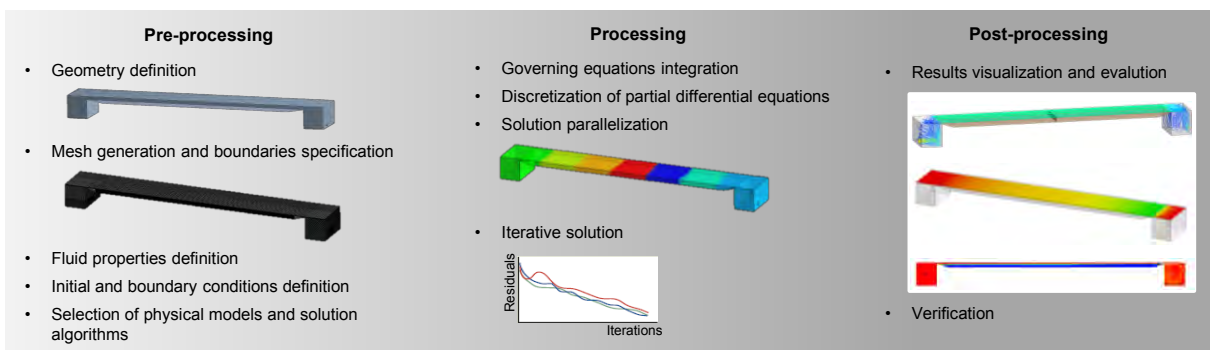


Figure 2.4. CFD codes workflow (adapted from Kaiser et al. (2014)).

In this thesis, ANSYS codes, i.e. Fluent and CFX, were used to implement and solve different CFD models. Focusing on the processing step, these programs utilize the finite volume method to solve the governing integral equations for the conservation of mass and momentum, and for scalars (when appropriate). During the solution procedures, a segregated solver was used in ANSYS Fluent whereas ANSYS CFX applied a coupled solver. Figure 2.5 depicts schematically the solution algorithms applied in each code in this thesis, showing the differences between both algorithms. The coupled solver applied by ANSYS CFX solves the momentum and continuity equations as a single system, thus the pressure-velocity coupling is inherent in the solution procedure. This solution algorithm uses a fully implicit discretization of the equations at any given time step. In the uncoupled (or segregated) solvers used in ANSYS Fluent, i.e. SIMPLE, SIMPLEC and PISO, the governing equations are solved sequentially, i.e. segregated from one another. Then using the updated

velocity field, the pressure correction equation is calculated for continuity, repeating these steps until convergence. The segregated algorithm is memory-efficient since the discretized equations need only be stored in the memory one at a time. However, the solution convergence is relatively slow, inasmuch as the equations are solved in a decoupled manner. In coupled solvers, the rate of solution convergence significantly improves, since hydrodynamics equations are solved in a closely coupled manner. Nevertheless, the memory requirement increases by almost two times that of the segregated algorithm since the discrete system of all momentum and pressure-based continuity equations need to be stored (ANSYS Inc, 2015, 2016).

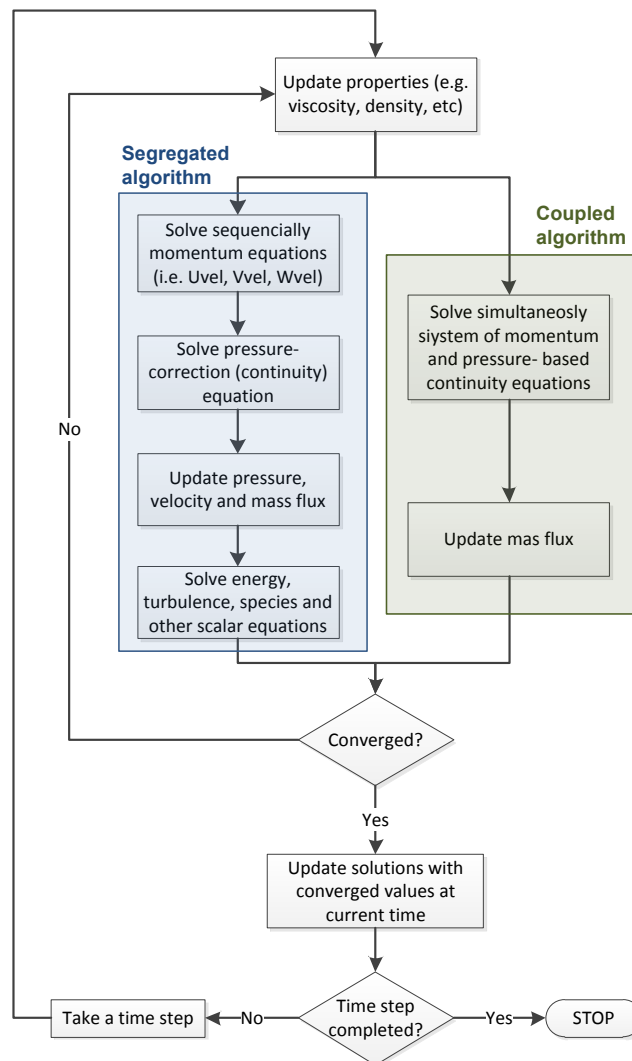


Figure 2.5. Solution procedures applied in ANSYS CFX and Fluent codes in this thesis (adapted from ANSYS Inc (2015, 2016)).

In Chapters 4, 6 and 7, further details of the adapted solution algorithms used to compute the developed CFD models are described. A detailed description of CFD solution algorithms can be found in several reference books (Ferziger and Perić, 1996; Wilcox, 1998; Versteeg and Malalasekera, 2007), which describe CFD theoretical background.

2.4.1. Computational fluid dynamics models

Computational fluid dynamics (CFD) models can be classified according to various criteria depending upon the analysis type and solver requirements. In general, CFD models are grouped attending the following features: two-dimensional (2D) and three-dimensional (3D) geometries, meshes or computational domains; laminar and turbulent flow conditions; Newtonian and non-Newtonian fluids; steady and unsteady flows; and one-phase and multi-phase models.

2.4.1.1. 2D and 3D domains

Once the computational domain is identified, it should be taken into account the assumptions considered in the model (i.e. symmetry), and the accuracy degree and the computation time required to obtain the results, in order to decide whether the model could be simplified or approximated as 2D or axi-symmetric computational domain.

For a 2D or axi-symmetric domain, geometry and all the elements of the mesh, i.e. 2D cells and their nodes, lie in a given plane. Thus, a two-dimensional flow is the one in which the velocity vector depends on only two spatial variables. An example is a plane flow, which its velocity vector depends on two spatial coordinates, x and y , but not z , i.e., $U = U(x, y)$. In an axisymmetric flow, the velocity vector would depend on the radii (r) and angle (θ), i.e., $U = U(r, \theta)$.

3D models do not lie in a single plane, allowing a more realistic description of the modeled system but, conversely, increasing the computational time compared to 2D models. In a three-dimensional flow, the velocity vector depends on three space coordinates, being the velocity components, U_u , U_v , and U_w depend on x , y and z ; that is, $U_u = U_u(x, y, z)$, $U_v = U_v(x, y, z)$ and $U_w = U_w(x, y, z)$.

Specifically, in biofilm modeling, the Benchmark problem 2 (BM2 from IWA task group) (Eberl et al., 2004) was focused on estimating hydrodynamics influence over mass transfer processes in heterogeneous biofilms. In BM2 the need to define 2D or 3D models to reproduce in detail the phenomena associated with biosystems behavior is extensively discussed.

2.4.1.2. Newtonian and non-Newtonian fluid

A Newtonian fluid is one which exhibits a linear relationship between fluid shear and strain (Expression 2.5).

$$\sigma = \eta \frac{\partial u}{\partial y} \quad (2.5)$$

Where σ is the fluid shear stress, η is the shear viscosity coefficient, and $\frac{\partial u}{\partial y}$ is the shear rate or the velocity gradient perpendicular to the plane of shear ($\dot{\gamma}$). For Newtonian fluids, the

viscosity is either constant or a function of temperature. Many common fluids, such as air, water, and diluted aqueous solutions, are Newtonian.

For non-Newtonian fluids, the shear stress is a non-linear function of the strain rate because the viscosity is also a function of the strain rate (Expression 2.6).

$$\eta = f\left(\frac{\partial u}{\partial y}\right) \quad (2.6)$$

Due to their inherent complex molecular composition, non-Newtonian fluids can have different types of behavior. Dilatants or shear-thickening, such as slurries, become more resistant to motion as the strain rate increases, whereas pseudoplastic or shear thinning, such as paint, become less resistant to motion with increased strain rate. Ideal plastics or Bingham fluids require a minimum shear stress to cause motion. For instance, toothpaste requires a minimum shear to cause motion, but they do not have a linear stress-strain rate relationship (Potter et al., 2012). The shear stress versus strain rate relationships of Newtonian and Non-Newtonian fluids are depicted in Figure 2.6.

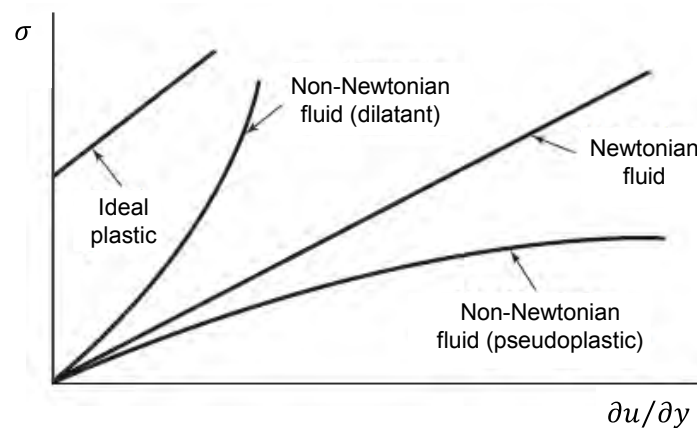


Figure 2.6. Newtonian and non-Newtonian fluids (adapted from Potter et al. (2012)).

For a non-Newtonian fluid, the power law or Ostwald–de Waele model for the shear stress is expressed as:

$$\sigma = K \frac{\partial u}{\partial y}^n \quad (2.7)$$

Where K is the consistency index and n is the flow behavior index. In terms of viscosity, Expression 2.7 can be written as Expression 2.8.

$$\eta = K \frac{\partial u}{\partial y}^{n-1} \quad (2.8)$$

Several models have been defined to describe the non-Newtonian fluid character, such as Ostwald-de Waele, Carreau-Yasuda and Herschel-Bulkley, reproducing both shear thinning and shear thickening flow behavior (Mezger, 2006).

The non-Newtonian character of biosystems has been observed in experimental works, being further investigated and characterized in sludge (Eshtiaghi et al., 2013; Ratkovich et al., 2013) than in fixed biofilms (Ohashi and Harada, 1994; Stoodley et al., 1999a).

2.4.1.3. Steady and unsteady flows

Steady flow is defined as that in which the flow properties at any given point in space do not change with time, i.e. properties are invariant. Flow in which properties are changing with time is termed unsteady, non-steady or transient. In practice, the great majority of flows may be analyzed assuming the fluid motion is steady. Nevertheless, there are three cases where unsteady effects are important: waves formed on free surfaces displaying oscillatory effects; liquid flows rapidly brought to rest; and cases where the boundary conditions of the flow may be steady, but the flow itself is inherently unstable (e.g. the classical case in which the flow of fluid dodges a circular cylinder obstacle, where although the velocity is steady and uniform, large eddies, i.e. Karman vortex, are formed for certain range of Reynolds numbers) (Massey and Ward-Smith, 1998).

2.4.1.4. Laminar and turbulent flows

Laminar flow is characterized by smooth, steady fluid motion, i.e. no substantial mixing of fluid occurs, whereas turbulent flow is fluctuating and agitated motion with significant fluids mixing. The velocity and all other flow properties vary in a random and chaotic way in turbulent flows. The reason why a flow can be laminar or turbulent has to do with what happens to flow disturbance, i.e. a perturbation to the velocity components, which can either increase or decrease in size. If a flow disturbance in a laminar flow increases, the flow may become turbulent, whereas if the disturbance decreases, the flow remains laminar. The dimensionless number which is used to classify a flow as either laminar or turbulent is the Reynolds number (Expression 2.9):

$$Re = \frac{U \cdot L}{\nu} \quad (2.9)$$

Where U is the fluid velocity ($m \ s^{-1}$), L is the characteristic length of the flow field (m), and ν is the kinematic viscosity of the fluid ($m^2 \ s^{-1}$). For instance, in a pipe flow, U would be the average velocity and L would be the pipe diameter.

The flow is laminar if the Reynolds number is relatively small, whereas the flow is turbulent if it is large. This is more precisely described by defining a critical Reynolds number, Re_{crit} , so that the flow is laminar if $Re < Re_{crit}$. For example, in a flow inside a rough-walled pipe it is found that $Re_{crit} \approx 2000$. The critical Reynolds number is different for every geometry, e.g., $Re_{crit} \approx 1500$ for a flow between parallel plates using for U the average velocity and for L the distance between the plates (Potter et al., 2012). In open-channel flat plate bioreactors, the flow in a conduit is characterized as laminar if Re_{crit} is below 2000 and as turbulent if it is above 4000, being L equal to liquid phase height (Lewandowski and Beyenal, 2007).

The transitional flow occurs between the laminar and turbulent flow regimes. In this flow regime, the flow goes through several stages of non-linear behavior before becoming fully turbulent. The common features which can be found in transition processes are: the amplification of initially small disturbances; the development of areas with concentrated rotational structures; the formation of intense small-scale motions and, finally, the growth and merging of these areas of small-scale motions into fully turbulent flows (Versteeg and Malalasekera, 2007). The described stages are highly unstable, being able to rapidly change the flow from one type of behavior to another (e.g. from turbulent spots to vortex breakdown and back again).

1. CFD modeling of turbulent flows

The numerical methods developed to capture the effects due to turbulence can be grouped into the following three categories (Versteeg and Malalasekera, 2007):

- Turbulence models for Reynolds-averaged Navier–Stokes (RANS) equations: these methods are focused on the mean flow and the effects of turbulence on mean flow properties. First, the Navier–Stokes equations are time-averaged and, then, the numerical methods are applied. Extra terms appear in the time-averaged (or Reynolds averaged) flow equations due to the interactions between various turbulent fluctuations. These extra terms are modeled with classical turbulence models (see Table 2.3), which form the basis of standard turbulence calculation procedures in currently available commercial CFD codes.

Table 2.3. The most common RANS turbulence models are classified on the basis of the number of additional transport equations that need to be solved along with the RANS flow equations (adapted from Versteeg and Malalasekera (2007)).

Number of extra transport equations	RANS model name
Zero	Mixing length mode
One	Spalart–Allmaras model
Two	k– ϵ model k– ω model k– ω shear stress transport (SST) Algebraic stress model
Seven	Reynolds stress model (RSM)

- Large eddy simulation (LES): this is an intermediate form of turbulence calculations which tracks the behavior of the larger eddies. Prior to the computations, this method involves space filtering of the unsteady Navier–Stokes equations, which passes the larger eddies and rejects the smaller ones. The effects on the resolved flow due to the smallest unresolved eddies, i.e. mean flow plus large eddies, are included by means of a so-called sub-grid scale model.

- Direct numerical simulation (DNS): this method computes the mean flow and all turbulent velocity fluctuations. The unsteady Navier–Stokes equations are solved on spatial grids that are sufficiently fine for resolving the Kolmogorov length scales (Wilcox, 1998) at which energy dissipation takes place, and using time steps sufficiently small to resolve the period of the fastest fluctuations.

It should be considered that RANS turbulence models, such as k – ϵ and k – ω models, are valued for their robustness, requiring modest computing resources and being still widely preferred in internal flow computations. Nevertheless, LES and DNS methods are highly costly in terms of computing resources, being still under study and development for full application in an industrial general-purpose.

Regarding biosystems modeling, RANS methods are the turbulence models used in wastewater treatment CFD modeling for reproducing bioreactors performance, being k – ϵ the most widely used model in general (Karpinska and Bridgeman, 2016; Samstag et al., 2016). In biofilm-fluid interaction modeling, works considering turbulent flow over biofilms have been rarely reported (Towler et al., 2007), being the flow dynamics usually computed without considering classical turbulence models.

2.4.1.5. Single phase and multiphase flow

In a single phase flow or model, there is only one fluid present in the domain, whereas in a multiphase model various phases are present in the flow field. In a multiphase model, the fluid present in the domain can be different substances (e.g. oil and water) or different phases of the same substance (e.g. water and steam). In order to differentiate it, the key is to know how the two fluids are mixed: if they are mixed at a molecular level, it is a multi-species flow, being a common example when two gases are present (e.g. methane and air); in contrast, it is a multiphase flow if the mixing is at macroscopic level. Thus, multi-phase flows imply the simultaneous presence of two or more phases, i.e. liquid, gaseous and/or solid. The most common class of multiphase flows are the two-phase flows, which include: gas-liquid flow, gas-solid flow, liquid-liquid flow and liquid-solid flow. The particular case of liquid-liquid flow should be classified as a multifluid flow, since although it is formed of two immiscible liquids, both fluids are the same type of phase.

1. CFD modeling of multiphase flows

Currently, there are two approaches for the numerical calculations of multiphase flows: Eulerian–Lagrangian and Eulerian–Eulerian, being the second one the most general multiphase flow model. In the Eulerian–Lagrangian approach, the fluid phase (usually liquid) is treated as a continuum by solving the time-averaged Navier–Stokes equations, whereas the dispersed or discrete phase (usually gas) is solved by tracking solid particles (i.e. droplets or bubbles) through the calculated flow field. The dispersed phase can exchange momentum, mass, and energy with the fluid phase. The trajectory of discrete phase particles

is obtained by integrating the force balance (inertia, gravity, drag, etc.) on a particle, which is written in the Lagrangian reference frame. Particle trajectories are computed at specified intervals during the fluid-phase calculation. In the Eulerian–Eulerian approach, the different phases are mathematically treated as interpenetrating continuous media. In this approach, the concept of phasic volume fraction is introduced since the volume of one phase cannot be occupied by the volume of other phases. The volume fractions of the phases are assumed to be continuous functions of space and time, and their sum is equal to one. Conservation equations for each phase are derived to contain a set of equations, which are closed by providing constitutive equations typically obtained from empirical information, and solved in the Eulerian frame of reference (ANSYS Inc, 2016).

In the Eulerian–Eulerian approach, different numerical techniques can be used. The volume of fluid (VOF) model (Hirt and Nichols, 1981) is a surface-tracking technique applied to a fixed Eulerian mesh, useful when the position of the interface between two or more immiscible fluids is of interest. Thus, the volume fraction of each of the fluids in each computational cell is tracked throughout the domain, and a single set of momentum equations is shared by the fluids. Another numerical technique in the Eulerian approach for tracking interfaces is the level-set method (Osher and Sethian, 1988), which can perform numerical computations on a fixed grid without having to parameterize the interface. The interface is captured and tracked by the level-set function, defined as a signed distance from the interface. The spatial gradients can be rigorously calculated, since the level-set function is smooth and continuous, producing accurate estimates of interface curvature and surface tension force caused by the curvature. However, the level-set method is found to have a deficiency in preserving volume conservation (ANSYS Inc, 2016). On the other hand, the VOF method is naturally volume-conserved, but its weakness lies in the calculation of its spatial derivatives, since the VOF function is discontinuous across the interface. Therefore, a robust interface-tracking solution can be provided by coupling VOF and level-set methods (ANSYS Inc, 2016).

In addition, two more Euler-Euler multiphase models are available in commercial codes, such as ANSYS Fluent (ANSYS Inc, 2016): the mixture model, and the Eulerian model. The mixture model is designed for two or more phases (fluid or particulate). As in the Eulerian approach, the phases are treated as interpenetrating continua, solving the mixture momentum equation and prescribing relative velocities to describe the dispersed phases. Applications of the mixture model include particle-laden flows with low loading, bubbly flows, and sedimentation. The mixture model can also be used without relative velocities for the dispersed phases to model homogeneous multiphase flow. The Eulerian model is the most complex of the multiphase models, solving a set of momentum and continuity equations for each phase. Coupling is achieved through the pressure and interphase exchange coefficients. Momentum exchange between the phases is dependent upon the type of

mixture being modeled. Applications of the Eulerian multiphase model include bubble columns, risers, particle suspension, and fluidized beds.

Regarding to biosystems modeling, both Eulerian–Eulerian and Euler-Lagrangian approaches have been typically used in wastewater treatment CFD modeling for reproducing bioreactors performance at large scale (Naessens et al., 2012; Karpinska and Bridgeman, 2016; Samstag et al., 2016), being the bioreaction behavior generally associated to the liquid phase dynamics. Specifically, models of airlift loop reactors (Feng et al., 2007; Jia et al., 2009; Wang et al., 2011), activated sludge reactors (Glover et al., 2006; Le Moullec et al., 2010; Climent et al., 2018), and membrane bioractors (Naessens et al., 2012) have been developed using the Euler-Euler approach (mixture and Eulerian models); whereas the Euler-Lagrangian approach has been mainly used for modeling ultraviolet reactors (Samstag et al., 2016). Finally, in biofilm-fluid interaction modeling, VOF method has also been used to predict the wall shear stress produced by turbulent flows over biofilms (Rmaile et al., 2015), and to characterize the removal of biofilm by impinging water droplets (Cense et al., 2006).



OBJECTIVES

3.1. GENERAL AND SPECIFIC OBJECTIVES

The general objective of this thesis was **modeling the performance of fixed-bed biosystems at mesoscale using computational fluid dynamics (CFD) techniques**, including substrate transport/consumption, biomass growth, deformation and detachment phenomena, through the characterization of physical, biochemical and mechanical properties of biofilms.

For the achievement of the general goal, it is essential to consider a number of specific objectives which are defined below:

- To determine procedures for the implementation of biochemical processes coupled with fluid dynamics into CFD codes, in order to implement one-phase and multiphase models reproducing biosystems performance.
- To verify the described methodologies with experimental data under different operating conditions in fixed-bed biofilm reactors.
- To characterize viscous and elastic biofilms response to various shear flows, to link the rheological and physical macroscopic properties of biofilms to their shear-induced microscopic structures.
- To propose a new continuum model approach to reproduce the biofilm physical movement in different biofilm-fluid interactions scenarios (various geometries and laminar flow conditions), by means of CFD multiphase models.
- To implement and verify experimentally the new approach for continuum modeling to model the fixed-bed biofilm response to interaction with gaseous and turbulent fluids.
- To elucidate the mechanisms involved in the biofilm disruption processes studied under different geometrical and physical properties, in order to contribute to the existing knowledge in biosystems control strategies.
- To advance in biosystems characterization and model verification, by presenting a new local capacitance needle-probe for in-situ biofilm layer and fluids interfaces detection.



ONE PHASE CFD MODELING FOR COUPLING HYDRODYNAMIC AND BIOKINETICS IN A FIXED- BED BIOFILM REACTOR

The main motivation of this chapter was to define a procedure to develop accurate models of fixed-bed biofilm reactors using computational fluid dynamics (CFD) techniques, coupling the hydrodynamic effects with the behavior of the biological system. Since the performance of this type of bioreactors is mainly governed by mass transport and transfer phenomena, an adequate characterization of the flow patterns is required to predict correctly the operation of real systems. The first approach was the implementation of a one-phase model using CFD codes, considering the biological system as a pseudo-porous media. After validating the model performance, this methodology was used in this chapter and in the following chapters in order to develop new biosystems models, examining how the fluid circulation and the associated phenomena affected bioreactors operation.

Abstract

In this chapter, a methodology was developed and applied to investigate the effect of integrating fluid flow dynamics in the modeling of biological systems. Specifically, the hydrodynamics and behavior of biofiltration systems were mimicked in a fixed-bed biofilm reactor simulating the common operation of a biotrickling filter. Several models using 2D and 3D geometries and diverse approaches were developed. In the case of 2D bioreactor models, three different well-established tools for modeling bioreactors (AQUASIM, MATLAB, and CFD) were used, in order to consider from ideal flow patterns to more complex fluid dynamics. A detailed comparison was performed, taking into account the simulation of dissolved oxygen profiles in the liquid phase, inside the biofilm and in the concentration boundary layer along the simulated bioreactor. These models were validated by comparing the simulations with direct measurements obtained by means of dissolved oxygen microsensors at high spatial resolution. In all cases, deviations were below 6%, nevertheless, CFD predictions obtained the lowest deviations among the approaches (below 3.5%). The results underlined that CFD techniques represent more accurately the performance of fixed-bed biofilm reactors, allowing the study in detail of all the hydrodynamics-related variables involved in the process. In addition, a 3D CFD model was developed, combining hydrodynamics and biological reactions. The model was solved to simulate local transient flow and dynamic behaviors of oxygen consumption in the bioreactor, validating its hydrodynamic behavior by means of a residence time distribution test. Results of CFD simulations were analyzed by characterizing hydrodynamics (advection and diffusion), in order to determine the effect of mass transport phenomena on the operation and, finally, to predict the oxygen degradation along the bioreactor.

A modified version of this chapter has been published as:

L. Prades, A.D. Dorado, J. Climent, X. Guimerà, S. Chiva, X. Gamisans, 2017. **CFD modeling of a fixed-bed biofilm reactor coupling hydrodynamics and biokinetics**, *Chem. Eng. J.*, 313, 680-692

4.1. INTRODUCTION

Microorganisms are an essential element in the operation of biofilm-based technologies, such as biofilters, biotrickling filters, integrated fixed-film activated sludge and moving bed biofilm reactors. In these bioreactors, the microorganisms grow as fixed-films while interacting with the environment through the gas/liquid phase that flows over them. This fluid flow influences biofilm development and activity by the transport of dissolved solutes into and out, and the application of shear forces to the biofilm (Stewart, 2012). An adequate characterization of this fluid flow is required in order to represent accurately the biological behavior (Eberl et al., 2004).

Several mathematical models have been used to describe hydrodynamics for modeling liquid-phase bioreactors performance, from plug flow or complete mixed ideal models to computational fluid dynamic (CFD) models. Specifically, Liotta and coworkers (Liotta et al., 2014) have compared performance-prediction models of the most common aerobic bioreactors, considering ideal and non-ideal flows, and have concluded that CFD models are the most complete, i.e. they let to describe space-time evolution of physical and biological phenomena. Therefore, CFD techniques have been employed as a useful tool for understanding hydrodynamics and biochemical reactions in the wastewater treatment field (Feng et al., 2007; Le Moullec et al., 2010; Wang et al., 2011; Liotta et al., 2014; Climent et al., 2018), where the bioprocess is influenced by the liquid phase dynamics. Biofilms mathematical modeling has been well-established by IWA Task Group on Biofilm Modeling (Noguera and Morgenroth, 2004), describing the basic features to model biofilms, developing numerous mathematical models in different dimensions and defining a set of benchmark problems to evaluate model responsiveness under established scenarios (IWA Task Group on Biofilm Modeling, 2006). Particularly, the Benchmark problem 2 (BM2) is focused on estimating hydrodynamics influence over mass transfer mechanics in heterogeneous biofilms, considering diffusion and advection mass transport in the fluid phase and concluding that 2D and 3D models should be applied when a detailed resolution inside the biofilm is required. Moreover, other works have demonstrated the suitability of 3D CFD models to study biofouling phenomenon coupled with hydrodynamics variables in membrane bioreactors (Picioreanu et al., 2009; Vrouwenvelder et al., 2010).

Regarding to gas-phase biofiltration, most of published models consider that the liquid movement through a porous bed occurs by an ideal plug flow pattern (Kim and Deshusses, 2003; Baquerizo et al., 2007; Álvarez-Hornos et al., 2009; Ahmed et al., 2013; López et al., 2016), since axial dispersion effect is generally neglected for the conditions on which such bioreactors are operated (Hodge and Devinny, 1997). Nonetheless, residence time distribution techniques (RTD) have been used for characterizing the hydrodynamics in biotrickling filters (Trejo-Aguilar et al., 2005; Sharvelle et al., 2008), measuring the liquid dispersion of circulating fluids in packed beds. These experimental analyses allowed

detecting axial dispersion, due to the formation of some preferential flow channels or stagnant regions as a consequence of packing structure and biofilm growth. Hence, mathematical models based on generally accepted assumptions seem not suitable for developing rigorous dynamic models, since hydrodynamics might critically influence the biofilm dynamics of the system (Horn and Lackner, 2014). In addition, adopted procedures for validating these bioreactor models are commonly based on experimental data measured in the liquid phase, despite the biological activity is mainly located at the biofilm.

Over the last decades, microelectrodes have demonstrated a notable potential in characterizing biofilms, allowing for spatial measurement of species, such as dissolved oxygen (DO), at the liquid phase, the bulk liquid/biofilm interface, and in the biofilm (Horn and Hempel, 1997a). Determination and modeling of oxygen profiles in biofilm reactors at laboratory scale have been previously addressed (Horn and Hempel, 1995, 1997b; Masić et al., 2010), showing that the concentration profiles in the biofilm are considerably influenced by boundary layers and flow characteristics of the liquid phase. Accurate experimental measurements and hydrodynamics description coupled with the biological reactions should be considered to develop rigorous models (Eberl et al., 2004). In contrast, models present in the literature neither take into account the simulation of the species gradients at the liquid phase nor describes in detail concentration boundary layer (CBL) profiles.

According to the stated above, the aim of this chapter was to contribute to the existing knowledge of how considering fluid flow dynamics could aid to develop more rigorous models for biological systems. In particular, a bioreactor model was developed employing CFD techniques and its performance was validated with experimental measurements inside the biofilm recorded using DO microsensors. A fixed-bed biofilm reactor was used to characterize the biodegradation phenomena inside an aerobic heterotrophic biofilm, reproducing at laboratory-scale the operating conditions of an industrial biotrickling filter, and studying in detail the relevant phenomena in both liquid and biofilm phases. Additionally, to confer a coherent identity model, the CFD simulation results were compared qualitatively with those results obtained from a well-established modeling tool such as AQUASIM, and from using traditional diffusion-reaction models. The developed 3D CFD model was used to study the influence of hydrodynamic over mass transport and to predict species presence anywhere in the bioreactor.

4.2. MATERIALS AND METHODS

4.2.1. Bioreactor operation and DO microprofiles recording

Experimental measurements were conducted through an aerobic heterotrophic biofilm grown on a flat plate bioreactor (FPB). The bioreactor was manufactured in methacrylate and in accordance with the suggestions described by Lewandowski and Beyenal (2007). The flat plate, i.e. the surface for the biofilm development, was 18 cm long, 3.5 cm wide and 0.3 cm

tall. The reactor included two reservoirs, located at the inlet and the outlet of the flat plate, which were 2 cm long, 3.5 cm wide and 2.8 cm tall.

Aerobic heterotrophic biofilms were grown on the FPB. After sterilizing the FPB, it was seeded with 40 ml of a sludge (4 g of volatile suspended solids (VSS) L⁻¹) obtained from the WWTP of Manresa (Barcelona, Spain). The remaining volume of the FPB was filled with a nutrient solution, and it was operated in batch mode for 24 hours to promote the bacteria immobilization. Then, the FPB was operated continuously. Oxygen saturation conditions, taking into account salinity and temperature, were achieved aerating solutions with standard air. Glucose, fed in excess to avoid biomass growth limitation, was used as the sole carbon source. During biofilm growth and DO profiles recording, operating conditions were set up reproducing those typical of a conventional biotrickling filter (liquid phase velocity and hydraulic residence time were adjusted to approximately 1 m h⁻¹ and 12 hours respectively by using a peristaltic pump to recirculate the phase through the FPB). Further details about reactor setup and operation can be found in Guimerà et al. (2015).

In the FPB, DO profiles were recorded at different regions along bioreactor. Specifically, P1 and P2 profiles were measured in zones close to the inlet (at 6 and 9 cm from the beginning of the flat plate respectively), while P3 and P4 profiles were recorded in regions near the outlet (at 15 and 18 cm from the beginning of the flat plate, respectively). Experimental data were recorded in less than one hour, in order to avoid the biofilm dynamic effect on the profile. These profiles were recorded using a commercial Clark-type microsensor (OX-25, Unisense, Denmark). The electrodes were connected to a 4-channel amplifier (Microsensor Multimeter, Unisense, Denmark) and polarized at -0.80V (vs Ag/AgCl). Data acquisition was performed using specific data acquisition software (Sensor Trace Basic, Unisense, Denmark). Linear two-point calibrations were performed in the measurement medium solution. The sensor positioning within the biofilm was possible through the use of a three-dimensional micromanipulator (MM33-2, Unisense, Denmark), with a precision in the z-axis of 10 µm, and in the x-/y-axis of 100 µm. Biofilm density was monitored along the flat plate using protein analysis (Bradford, 1976). These measurements were related to the volatile suspended solids (VSS) concentration according to the correlation described by Guimerà and coworkers (Guimerà et al., 2016). Further details about the recorded profiles and the applied procedure can be found in Guimerà (2016).

4.2.2. Biofilm parameters characterization

Experimental DO profiles, recorded during both endogenous and substrate consumption conditions, were used to estimate the microbial consortium kinetic parameters. In this way, the evaluation of the recorded microsensor profiles was performed using the methodology proposed by Wäsche et al. (2002), obtaining the concentration boundary layer thickness and the dissolved oxygen profiles inside the biofilm, thus locating liquid and biofilm interfaces.

Moreover, the effective diffusivity was estimated using the correlation described in Guimerà et al. (2016), in which the diffusion coefficient of n-compound in biofilm phase (D_{Bn}) is quantified depending on biomass density and Reynolds number (Expression 4.1):

$$D_r = D_{Bn} \cdot D_{Ln}^{-1} = 0.93 - 0.023 \cdot X + 1.17 \cdot 10^{-2} \cdot Re^2 + 1.1 \cdot 10^{-4} \cdot X^2 \quad (4.1)$$

Where D_r is the relative diffusivity, D_{Ln} is the diffusion coefficient of n-compound in the liquid phase in ($m^2 s^{-1}$), X is biomass density ($kg m^{-3}$) and Re is Reynolds number (-).

Finally, the parameters of the biological kinetics expressions were fitted from recorded DO oxygen profiles following the procedure defined by Zhou et al. (2012), where a dynamic model is developed to estimate oxygen evolution using one-dimensional diffusion-reaction equation.

Fitting goodness between the predicted values and the reference data was analyzed calculating the normalized root mean square error (NRMSE). The NRMSE (Expression 4.3) is a non-dimensional form of the root mean square error (RMSE), which is defined as the square root of the mean squared error (Expression 4.2).

$$RMSE = \sqrt{\frac{\sum_{i=1}^N [x_e(t) - x_p(t)]^2}{N}} \quad (4.2)$$

$$NRMSE = \frac{RMSE}{x_{e,max} - x_{e,min}} \quad (4.3)$$

Where $X_e(t)$ is the measured value for $i = 1$ to N data points obtained along the experimental time, $X_p(t)$ is the predicted value according to the model and $X_{e,max}$ and $X_{e,min}$ are the maximum and minimum measured value for the experimental data recorded, respectively.

4.2.3. Bioreactor hydrodynamic characterization

The residence time distribution (RTD) was obtained in order to validate models hydraulic behavior, performing the experimental tracer technique in the FPB. The measuring control point was located at the outlet of the bioreactor, taking samples at a 60 seconds frequency. Methylene blue was used as a dye tracer following a pulse as the injection method. After a sampling period of 3000 seconds, tracer sorption studies were carried out processing the samples analytically with an ultraviolet/visible spectrometer (UV/Vis Lambda 25, Perkin-Elmer, United States).

To perform the RTD analysis, the concentration-time ($C(t)$) and the residence time distribution ($E(t)$) curves (Expressions 4.4 and 4.5 respectively) were obtained, linking mass and volumetric flow rate of the tracer along the experiment, and allowing to calculate the mean residence time (t_m) according to the Expression 4.6.

$$\frac{M}{q} = \int_0^{\infty} C(t)dt \quad (4.4) \quad E(t) = \frac{C(t)}{\int_0^{\infty} C(t)dt} \quad (4.5) \quad t_m = \int_0^{\infty} E(t) \cdot t dt \quad (4.6)$$

Where M is the tracer mass (kg), q is the volumetric flow rate of the tracer ($m^3 s^{-1}$), $C(t)$ is the concentration-time function of the tracer ($kg m^{-3} s$), t_m is the mean residence time (s), $E(t)$ is the residence time distribution function of the tracer (-), and t is the time (s).

4.3. MODELS DEVELOPMENT

The developed models were built coupling the description of the physical transport phenomena and the biological processes occurring along this type of biofilm reactors, considering the most relevant phenomena (i.e. advection, diffusion, and biodegradation). Two phases were considered: bulk solution and biofilm. The liquid phase (composed of water, mineral salts, glucose and dissolved oxygen) was circulated from the inlet to the outlet of the bioreactor, passing over the biofilm, which remains immobile inside the bioreactor. Oxygen and glucose were transferred from the liquid phase to the biofilm phase, where the aerobic glucose biodegradation takes place.

4.3.1 Microbial kinetic model

Aerobic heterotrophic bacteria can use dissolved oxygen (DO) and glucose (S) as electron acceptor and carbon source, respectively. The biological reaction rates for the DO and S were described by Monod type kinetic expressions, depending on the concentrations of dissolved oxygen and dissolved glucose inside the biofilm. These consumption rates are related to microbial growth limited by oxygen, also considering an endogenous term, and glucose in excess (Expressions 4.7 and 4.8). This last assumption was verified experimentally, measuring glucose concentration through the bioreactor far superior to the half-saturation coefficient for glucose ($K_{S,G}$), i.e. glucose concentration greater than $10 g L^{-1}$ and $K_{S,G}$ less than $1 mg L^{-1}$ (Guimerà, 2016).

$$R_{BDO}(i, j) \left| \begin{array}{l} i=n_L \\ j=n_B \\ i=1 \\ j=1 \end{array} \right. = q_{max,DO} \cdot \frac{C_{BDO}(i,j)}{K_{S,DO} + C_{BDO}(i,j)} \cdot X(i, j) + k_d \cdot X(i, j) \quad (4.7)$$

$$R_{BS}(i, j) \left| \begin{array}{l} i=n_L \\ j=n_B \\ i=1 \\ j=1 \end{array} \right. = \frac{1}{Y_{DO/S}} \cdot q_{max,DO} \cdot \frac{C_{BDO}(i,j)}{K_{S,DO} + C_{BDO}(i,j)} \cdot X(i, j) \quad (4.8)$$

Where R_{Bn} is the biological reaction rate of n-compound ($kg m^{-3} s^{-1}$), X is the biomass concentration ($kg m^{-3}$), $q_{max,DO}$ is the maximum specific growth rate ($kg DO kg VSS^{-1} s^{-1}$), C_{BDO} is the concentration of oxygen in the biofilm phase ($kg DO m^{-3}$), $K_{S,DO}$ is the Monod half-saturation coefficient for oxygen ($kg DO m^{-3}$), k_d is the maintenance factor for oxygen ($kg DO kg VSS^{-1} s^{-1}$), and $Y_{DO/S}$ is the oxygen-glucose yield ($kg DO kg S^{-1}$).

Values of kinetic and stoichiometric parameters are summarized in the subsection 4.4.1.

4.3.2 General assumptions in bioreactor models

The general assumptions of the models, based on consolidated models reported in the literature (Baquerizo et al., 2007; Dorado et al., 2008; IWA Task Group on Biofilm Modeling, 2006), are:

1. The biofilm is considered as a flat surface with a constant thickness, according to bioreactor design.
2. The biofilm is covered by a liquid film of constant thickness.
3. The heterogeneous character in the biomass is considered since it has been observed in previous studies for this type of bioreactors (Guimerà et al., 2015). Therefore, a biomass density gradient has been defined along the biofilm.
4. Degradation kinetics within the biofilm is described by the Monod-type equation.
5. The biofilm system is at pseudo-steady state.
6. Liquid phase circulation regime in the flat plate is described as plug flow pattern.
7. No reaction is considered in the liquid phase (i.e. there is a negligible amount of biomass in the liquid phase).
8. The concentration at the inlet for dissolved oxygen is kept constant at saturation concentration and glucose is supplied in excess.
9. Mass transport from the liquid phase to the biofilm and throughout the biofilm occurs by diffusion, following Fick's law. The diffusion coefficients for the substrate and dissolved oxygen in the biofilm were calculated by Expression 4.1. In the liquid phase, the diffusion coefficients are equal to those in pure water (Table 4.1).
10. Mass-transfer resistance at the interface between the biofilm and the bulk fluid is considered.

4.3.3 Description of bioreactor models

Three different models were developed and tested in order to evaluate the effect of considering hydrodynamic when the bioreactor model is defined. The models were used to evaluate pseudo steady-state glucose degradation and oxygen consumption within the biofilm at different positions in the flat plate bioreactor. All modeling approaches consider several mechanisms occurring in the bioreactor, schematized in Figure 4.1C, such as mass transport by advective flow in the liquid phase, mass transfer by diffusion at the liquid-biofilm interface, internal diffusion in the biofilm phase and biological reaction in the biofilm.

Table 4.1. Main parameters for the bioreactor models formulation.

Parameter	Symbol	Value	Units	Determination method /Reference
Volumetric flow rate (bioreactor inlet)	Q	$4.37 \cdot 10^{-8}$	$\text{m}^3 \text{s}^{-1}$	Operating conditions
Liquid phase volume in the flat plate	V_L	$4.46 \cdot 10^{-6}$	m^3	Bioreactor design
Interfacial area liquid-biofilm	A_i	$5.94 \cdot 10^{-3}$	m^2	Bioreactor design
Boundary layer thickness	δ_C	0.0002	m	Indirectly determined from experimental data (Wäsche et al., 2002)
Biofilm thickness	th	0.003	m	Bioreactor design
Substrate influent concentration	C_{LG0}	13	kg m^{-3}	Operating conditions
Oxygen influent concentration	C_{LO0}	0.00685	kg m^{-3}	Operating conditions
Number of discretizations in liquid phase	n_L	8	-	Determined by sensitivity study to n_L
Number of discretizations in biofilm phase	n_B	30	-	Determined by sensitivity study to n_B
Glucose diffusivity in liquid phase	D_{LG}	$6.73 \cdot 10^{-10}$	$\text{m}^2 \text{s}^{-1}$	Perry and Green (1997)
O ₂ diffusivity in liquid phase	D_{LO}	$1.88 \cdot 10^{-9}$	$\text{m}^2 \text{s}^{-1}$	Nguyen et al. (2014)
Glucose diffusivity in biofilm phase	D_{BG}	Expression 4.1	$\text{m}^2 \text{s}^{-1}$	Guimerà et al. (2016)
O ₂ diffusivity in biofilm phase	D_{BO}	Expression 4.1	$\text{m}^2 \text{s}^{-1}$	Guimerà et al. (2016)

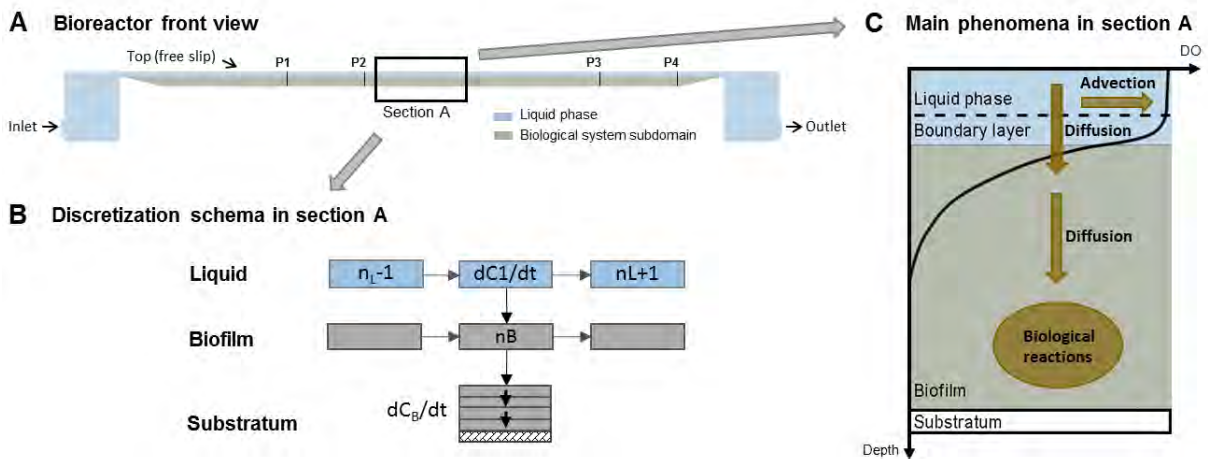


Figure 4.1. Discretization and schematic of the main phenomena considered in the model. (A) Bioreactor front view, (B) Bioreactor discretization considering n_L horizontal layers along the flat plate and n_B subdivisions in the biofilm section, (C) schematic of the main phenomena considered in the model.

Regarding the computing solution methodologies, two of the models were solved as nodal models defining mass balances equations in the phases, and the third one was worked out using CFD techniques. The first nodal model is defined as a traditional diffusion-reaction model, discretizing the set of partial differential equations in space along the bioreactor height and biofilm thickness and solving them using MATLAB. The second nodal model was implemented using a well-established tool such as AQUASIM simulation package. In the third model, which is developed using a CFD software, the biological reactions are introduced into the CFD code, coupling them with system hydrodynamic.

A mesh sensitivity analysis was performed to find an optimal discretization of the bioreactor models, using dissolved oxygen variable as the optimization criterion. As a result, a minimum of eight mesh points was used for discretizing the reactor length, while thirty nodes more to discretize the biofilm thickness (for more details see subsection 4.4.2).

The main parameters characterizing the bioreactor performance in all the models are shown in Table 4.1.

4.3.3.1. Conventional Diffusion-Reaction model

The theoretical model describing the aerobic glucose biodegradation in the bioreactor was based on mass balances in the liquid and biofilm phases. Model equations were established according to the mechanisms and assumptions mentioned above. Mass transport throughout the liquid phase was modeled as a sequence of single continuous stirred tank reactors (CSTR's) in order to simulate a plug flow. As can be seen in Figure 4.1B, horizontal layers (n_L) were defined from the bioreactor inlet to the outlet. Similarly, the biofilm layers were also divided into several layers (n_B) starting from the biofilm surface to the biofilm layer in contact with the substratum. Then, the set of partial differential equations was discretized in space along the bioreactor length and biofilm thickness, i.e. two-dimensional area. The resulting set of simultaneous ordinary differential equations was solved in MATLAB® Release 2015a, using a variable order method based on the numerical differentiation formulas (NDFs) to solve stiff differential equations. Mass balances in liquid and biofilm phases are described below.

1. Mass balance for the liquid phase

Components considered in the liquid phase were oxygen and glucose. In this phase, the dynamic mass balance for a compound n , $C_L n$, in a segment i was represented by two expressions, i.e. Expression 4.9 is for the first segment ($i=1$), which bear boundary constraints, and Expression 4.10 is from the second segment ($i=2$) to the last bioreactor segment ($i= n_L$).

$$\left. \frac{dC_L n(i)}{dt} \right|_{i=1}^{i=1} = \frac{Q}{(V_L/n_L)} \cdot (C_L n_0 - C_L n(i)) - \frac{D_{Ln} \cdot A_I}{\delta_c \cdot V_L} \cdot (C_L n(i) - C_B n(i, 1)) \quad (4.9)$$

$$\left. \frac{dC_{Ln}(i)}{dt} \right|_{i=2}^{i=n_L} = \frac{Q}{(V_L/n_L)} \cdot (C_{Ln}(i-1) - C_{Ln}(i)) - \frac{D_{Ln} \cdot A_i}{\delta_c \cdot V_L} \cdot (C_{Ln}(i) - C_{Bn}(i,1)) \quad (4.10)$$

Where V_L is the liquid phase volume (m^3), n_L is the number of discretizations in the liquid phase (-), C_{Ln} is the concentration of compound n in the liquid phase ($kg\ m^{-3}$), Q is the volumetric flow rate in the inlet bioreactor ($m^3\ s^{-1}$), C_{Ln0} is the concentration of compound n in the inlet liquid phase ($kg\ m^{-3}$), D_{Ln} is the diffusion coefficient of n -compound in the liquid phase ($m^2\ s^{-1}$), A_i is the available surface area between the entire biofilm and the liquid phase (m^2), δ_c is the concentration boundary layer thickness (m), and $C_{Bn}(i,1)$ is the concentration of n -compound in the first layer of biofilm ($kg\ m^{-3}$).

II. Mass balance for the biofilm

In the biofilm phase, the same compounds as in the liquid phase were considered (oxygen and glucose). The dynamic mass balance for a compound n , C_{Bn} , in a segment i of the liquid phase and in the j layer of the biofilm depth is expressed by Expression 4.11, except for the first layer near the interface ($j=1$) and the last before the substratum ($j=n_B$), which bear boundary constraints (Expressions 4.12 and 4.13 respectively).

$$\left. \frac{dC_{Bn}(i,j)}{dt} \right|_{i=1}^{i=n_L} \left. \right|_{j=2}^{j=n_B-1} = \frac{D_{Bn}}{(th/n_B)^2} \cdot (C_{Bn}(i,j-1) - 2 \cdot C_{Bn}(i,j) + C_{Bn}(i,j+1)) - R_{Bn}(i,j) \quad (4.11)$$

$$\left. \frac{dC_{Bn}(i,j)}{dt} \right|_{i=1}^{i=n_L} \left. \right|_{j=1} = \frac{D_{Ln}}{\delta_c \cdot (th/n_B)} \cdot (C_{Ln}(i) - C_{Bn}(i,j)) - \frac{D_{Bn}}{(th/n_B)^2} \cdot (C_{Bn}(i,j) - C_{Bn}(i,j+1)) - R_{Bn}(i,j) \quad (4.12)$$

$$\left. \frac{dC_{Bn}(i,j)}{dt} \right|_{i=1}^{i=n_L} \left. \right|_{j=n_B} = \frac{D_{Bn}}{(th/n_B)^2} \cdot (C_{Bn}(i,j-1) - C_{Bn}(i,j)) - R_{Bn}(i,j) \quad (4.13)$$

Where C_{Bn} is the concentration of n -compound in the biofilm phase ($kg\ m^{-3}$), D_{Bn} is the diffusion coefficient of n -compound in the biofilm phase ($m^2\ s^{-1}$), th is the biofilm thickness (m), n_B is the number of discretizations in the biofilm phase (-), R_{Bn} is the biological reaction rate of n -compound ($kg\ m^{-3}\ s^{-1}$) (see Expressions 4.7 and 4.8 for more details).

4.3.3.2. AQUASIM model

The heterotrophic biofilm model was simulated using AQUASIM 2.1 (Reichert, 1998). Using this package a pseudo-2D bioreactors modeling can be solved, i.e. mass transfer in the flow direction occurs only between the compartments zones whereas transport in the biofilm occurs only in the substratum perpendicular direction (IWA Task Group on Biofilm Modeling, 2006). The mathematical model was established in accordance with the

assumptions stated above, and considering that oxygen and glucose diffuse from the liquid phase to the biofilm phase, where the biological reaction occurs. The model was developed using a set of biofilm reactor compartments (n_L), in which mass transport in the biofilm occurs in the direction perpendicular to the substratum and the biofilm evolution is calculated independently in each compartment. These compartments are combined through advective links between the bulk fluid zones, so that mass transfer occurs in the flow direction (IWA Task Group on Biofilm Modeling, 2006).

Biofilm reactor compartments were configured following the guidelines suggested by Wanner and Morgenroth (2004). The reactor type was chosen as unconfined to model free-surface flow over the biofilm and the pore volume contains only liquid phase and dissolved substances. Oxygen and glucose were introduced as dissolved variables. The biofilm matrix was assumed to be rigid and the particulate variable of the system, biomass (X), was specified. Moreover, the bioreactor parameters were introduced in the variables section and Expressions 4.7 and 4.8 were implemented as processes. In addition, the number of grid points was defined as $n_B + 2$, since AQUASIM keeps 2 boundary points (Reichert, 1994). The properties of particulate and dissolved variables were defined and initial conditions and influent value were also provided.

4.3.3.3. CFD model

The commercial CFD software ANSYS® Academic Research, Release 16.2, was used to solve the equations of continuity and momentum. In particular, the finite-volume ANSYS CFX solver was used, employing body-fitted grids. ANSYS CFX uses a co-located (non-staggered) grid layout and all variables are evaluated at the cell centers. An improved version of the Rhie–Chow algorithm was used to calculate the velocity at the cell faces. The code makes use of a high order advection scheme, with a numerical advection correction term. A multigrid accelerated incomplete lower-upper factorization technique was selected for solving the discrete system of linearized equations.

A single-phase model was implemented to characterize the bioreactor performance, following the general assumption previously discussed. The bioreactor was defined by a single domain, and the region of the biological system was introduced as a subdomain in the lower part of the flat plate. The boundary conditions of inlet, outlet, and free slip were defined in the respective areas of the bioreactor, and the remaining surfaces are bounded by walls (see Figure 4.1A). A hydraulic pressure loss model was introduced into the momentum equation in order to model the physical characteristics of biomass.

The implementation of biological reactions in the CFD software was performed using the methodology described by Climent et al. (2018), derived from bioreactors modeling in wastewater treatment field (Glover et al., 2006; Le Moullec et al., 2010). Variables on kinetic expressions (oxygen, glucose, and biomass) were defined as additional variables or scalars in the computational space, including an extra transport equation for each of them:

$$\frac{\partial(\rho\varphi)}{\partial t} + \nabla \cdot (\rho \mathbf{U} \varphi) = \nabla \cdot (\rho D \nabla \varphi) + S_{\varphi} \quad (4.14)$$

Where \mathbf{U} is the fluid velocity (m s^{-1}), ρ is the fluid density (kg m^{-3}), C_n is the concentration of the n variable (kg m^{-3}), i.e. C_{Ln} in liquid phase and C_{Bn} in the biofilm phase, $\varphi = C_n/\rho$ is the conserved quantity of n variable per unit mass of fluid (-), S_{φ} is a volumetric source term ($\text{kg m}^{-3} \text{ s}^{-1}$), and D is the kinematic diffusivity for the n variable ($\text{m}^2 \text{ s}^{-1}$), i.e. D_{Ln} in liquid phase and D_{Bn} in biofilm phase. The left-hand side includes the temporal and the convective terms, while in the right-hand side the diffusion and the term for the sources appears. All terms in Expression 4.14 are considered for oxygen and glucose, whereas the diffusive term was neglected for the biomass additional variable. In addition, the expressions for the biodegradation kinetics (Expressions 4.7 and 4.8) were included as source terms. Moreover, a new transport equation was introduced in order to calculate RTD. Then, a further additional variable was created to obtain the residence time distribution in the transient state. The source term for the tracer additional variable was considered equal to the unit (Climent et al., 2018). Moreover, tracer (methylene blue) was defined as a new additional variable and the tracer pulse was specified into the CFD model.

During the meshing procedure, the guidelines detailed in *CFX Best Practices Guide for Numerical Accuracy* (ANSYS Inc, 2015) were taken into account, testing mesh dependence and discretization schemes. Then, a sensitivity analysis of the mesh confirmed the null impact of the mesh size element on the simulation results (for more details see subsection 4.4.2). In the 3D model, a multi-block geometry was designed to give flexibility in the meshing, saving computational cells but defining regular meshes of high quality at the same time.

Finally, simulations were calculated either in the transient and steady state. In both states, the laminar flow regime was defined since operating conditions were characterized by low Reynolds numbers, and a time step of 0.1 seconds was defined, fulfilling the condition of the Courant number. Moreover, in order to reduce computing time, the simulation results were obtained after following two steps (Climent et al., 2018). First, a converged steady-state solution for the fluid was calculated. Secondly, the resulting hydrodynamic variables were kept constant for the transient simulation, and only the transport equations for the additional variables were solved, since biochemical reactions do not affect the hydrodynamic calculation. Convergence was assumed when the maximum normalized root mean square in each cell for all the equations (momentum, mass, and additional variables) reached a value less than $1 \cdot 10^{-4}$ and additional variables residuals were kept at a constant value.

4.4. RESULTS AND DISCUSSION

4.4.1. Experimental measurements in the FPB

4.4.1.1. DO microprofiles recording and biokinetics parameters estimation

DO microsensors measurements were performed in order to characterize the biological activity within the biofilm under both endogenous and substrate consumption conditions and to study biofilm heterogeneous character, as it has been reported in previous works (Guimerà et al., 2015). Several oxygen concentration profiles were measured at six different regions along the bioreactor during both endogenous and substrate consumption conditions (Guimerà, 2016). Four representative profiles during substrate operating conditions (P1, P2, P3, and P4) are shown in Figure 4.2. The locations where the profiles were recorded are depicted in Figure 4.1.

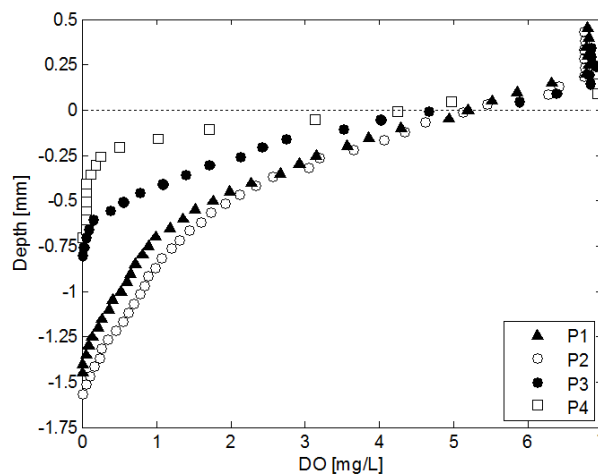


Figure 4.2. DO profiles recorded at different positions along the bioreactor (from inlet P1 to outlet P4) during substrate consumption conditions. P1 (\blacktriangle) and P2 (\circ) profiles were measured at 6 and 9 cm from the beginning of the flat plate, respectively, and P3 (\bullet) and P4 (\square) profiles were recorded at 15 and 18 cm from the beginning of the flat plate, respectively.

Using the methodology proposed by Wäsche et al. (2002), the characterization of these profiles allowed to distinguish three phases (see Figure 4.1): the liquid phase, in which DO concentration can be assumed to be constant; the boundary layer (liquid-biofilm interface), in which DO mass transfer from liquid to biofilm occurs; and the biofilm, in which DO is diffused and consumed by the microbial activity.

Since the interface between the concentration boundary layer (CBL) and the biofilm is located at the inflection point in which the profile changes the curvature from convex to concave, the profiles were presented positioning the inflection point as the zero of axis coordinate. Then, positive values in Figure 4.2 are measurements in the bulk and the concentration boundary layer, while the negative ones correspond to measurements inside the biofilm. As can be seen, the profiles showed the characteristic shape for substrate

profiles diffusing into a matrix where it is consumed (Lewandowski and Beyenal, 2007). In general, the experimental data registered along the bioreactor (from the inlet P1 to the outlet P4) exhibit a tendency to increase the oxygen profile slope, indicating higher oxygen consumption rate, since biomass concentration increases along the reactor (Table 4.2). In all cases, dissolved oxygen was completely exhausted before reaching the substratum, being oxygen penetration depths in the biofilm between 500–1500 μm . Besides, the concentration boundary layer thickness ranged from approximately 100–200 μm , which is close to the values measured in other biofilm systems (Wäsche et al., 2002).

Table 4.2. Kinetic and stoichiometric parameters for bioreactor model.

	X (kg VSS m^{-3})	k_d (kg DO kg VSS $^{-1}$ s^{-1})	$K_{S,O}$ (kg DO m^{-3})	q_{\max} (kg DO kg VSS $^{-1}$ s^{-1})
P1	9.30	$1.60 \cdot 10^{-7}$	$2.46 \cdot 10^{-4}$	$1.27 \cdot 10^{-6}$
P2	13.25	$1.72 \cdot 10^{-7}$	$2.32 \cdot 10^{-4}$	$4.47 \cdot 10^{-7}$
P3	18.20	$5.66 \cdot 10^{-7}$	$1.42 \cdot 10^{-4}$	$7.01 \cdot 10^{-7}$
P4	25.60	$3.02 \cdot 10^{-7}$	$3.02 \cdot 10^{-4}$	$4.82 \cdot 10^{-6}$

In addition, to determine biokinetic parameters of Expressions 4.7 and 4.8, biofilm density was measured using protein analysis at bioreactor regions where profiles were recorded, obtaining a biomass density gradient as is shown in Table 4.2. Oxygen-glucose yield was calculated from the oxidation reaction of glucose, obtaining a value of 1.07 kg DO kg S^{-1} . The effective diffusivities within the biofilm were estimated by Expression 4.1. Consequently, using one-dimensional diffusion-reaction equations (Zhou et al., 2012), different sets of the biological kinetics parameters (the maximum specific oxygen uptake rate, q_{\max} ; the Monod half saturation coefficient of oxygen, $K_{S,O}$; and the maintenance-decay coefficient for oxygen, k_d) were fitted from the DO profiles, reflecting the heterogeneous character along the bioreactor. Values of these parameters are summarized in Table 4.2.

The maintenance coefficient for oxygen and growth parameters varied in a considerable range, which is a consequence of the differences observed in profiles of Figure 4.2. Despite these variations, fitted parameters were in the ranges that other authors have reported for biokinetic parameters of immobilized biofilms (Zhou et al., 2012; Guimerà et al., 2015).

4.4.1.2. Fluid flow characterization

The concentration-time $C(t)$ and the residence time distribution $E(t)$ were obtained in the RTD analysis according to Expressions 4.4 and 4.5 respectively (Figure 4.3 represents the experimental $E(t)$ curve). RTD shows an exponential curve displaced in time. The initial time (240 seconds) was related to plug-flow behavior in the flat plate region, while the two reservoirs (located at the inlet and the outlet of the flat plate) corresponded to the CSTR in series, contributing to obtain mixed flux. The maximum concentration was obtained at 420

seconds and its value was used to calculate the number of reactor in series (Levenspiel, 1999). From this, it was possible to develop a hydrodynamic study on the bioreactor by means of a non-ideal hydraulic model, concluding that the bioreactor configuration was equivalent to a plug-flow reactor with a CSTR in series model.

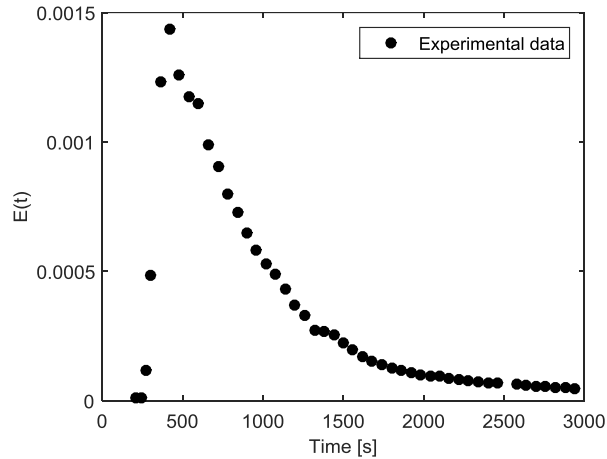


Figure 4.3. Residence time distribution curve $E(t)$ obtained in the experimental RTD analysis.

4.4.2. Simulations results

4.4.2.1. Mesh sensitivity analysis

Since the procedures to solve the developed models are either finite differences or finite volumes methods, it is necessary to select the number of grid points used for discretizing the bioreactor length (n_L) and the biofilm thickness (n_B). The number of discretizations is an essential parameter which influences in the resolution of the numerical calculation and, additionally, has direct effect on the accurate reproduction of the experimentally observed gradients within and outside the biofilm.

A wide range of values for mesh grid points can be found in the literature of biofiltration modeling, from lower values below 10 (Deshusses et al., 1995; Zarook and Ansar, 1996; Dorado et al., 2008) to larger ones over 50 (Shareefdeen et al., 1993; Spigno et al., 2004; Álvarez-Hornos et al., 2009), without indicating a standard criterion to select this number of divisions. In addition, a systematic evaluation of biofilm reactor models (Boltz et al., 2011) has shown that the number of discretizations in the concentration boundary layer (CBL) and the biofilm are highly sensitive parameters. These authors have examined the impact of the discretization points on predicted values and have recommended choosing a number of layers appropriate to represent the substrate and biomass gradients.

As shown in Figure 4.2, the biological activity varies along the bioreactor, being essential to examine the suitability of the mesh size in order to determine whether it can be used for

capturing in detail dissolved oxygen transport and consumption inside and outside the biofilm.

Predicted values from three different values of mesh element size were compared, considering a fine mesh (element size of 0.05 mm, $n_B=60$), a medium mesh (element size of 0.1 mm, $n_B=30$) and a coarse mesh (element size of 0.2 mm, $n_B=15$). All the three meshes presented a well-behaved convergence. The sensitivity of n_B with respect dissolved oxygen variable is depicted in Figure 4.4A for two profiles with different depths. As can be seen, the oxygen profiles reproduce adequately the expected behavior and follow the same trend for fine and medium meshes, but they have significantly change for the coarse mesh. In order to compare the fine mesh with the medium and coarse meshes, the normalized root mean square errors (NRMSE) (Expression 4.3) was calculated, obtaining deviations for P1 of 0.17% and 1.45% respectively; and for P3 are 0.29% and 1.21%. Therefore, the improvements between fine and medium meshes did not justify the increase in computational time. Hence, the medium mesh (with $n_B=30$ discretizations points or defining an element size of 0.1 mm for CFD meshes) was used as the base case for the simulations presented herein.

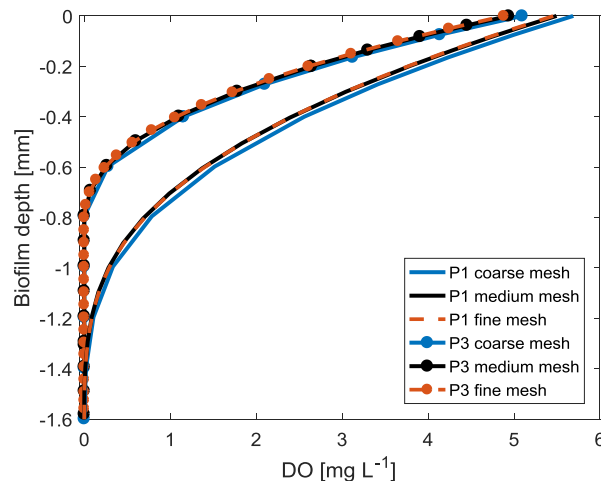


Figure 4.4. Simulated DO profiles in depth using coarse, medium and fine mesh densities for P1 (solid lines) and P3 (solid lines with symbols) profiles.

From the results of n_B analysis, it was possible to perform a sensitivity analysis of n_L to know the effect of the biomass density gradient along the bioreactor. Figure 4.5 depicts the variation of dissolved oxygen concentration along the reactor at the interface level using the medium mesh. These results showed that a minimum of 7 discretizations was needed in order to reproduce correctly the DO gradients along the bioreactor in the nodal models.

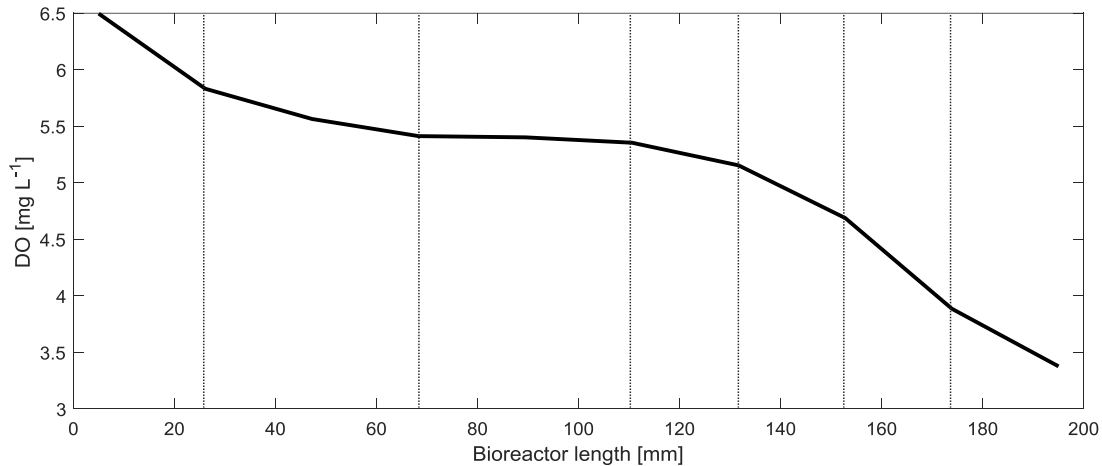


Figure 4.5. Simulated DO profile along the bioreactor at the interface using the medium mesh.

Finally, for the defined meshes for the CFD simulations with an element size of 0.1 mm, the mesh quality parameters (orthogonal quality and skewness) was checked. An orthogonal quality average of 0.9902 and a skewness average of 0.0209 were obtained in the active section of the bioreactor, being both inside the range of recommended values (0.95-1 and 0-0.25 respectively). A detail of the developed mesh for the 3D bioreactor geometry is shown in Figure 4.6, which was composed of approximately 505000 cells.

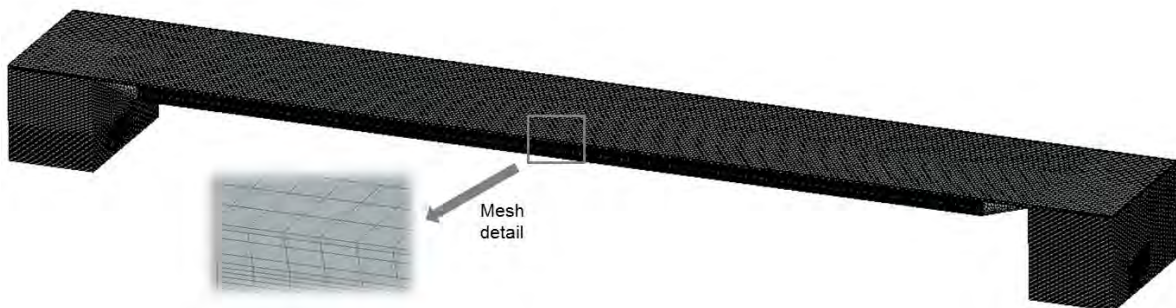


Figure 4.6. Mesh developed for the 3D bioreactor geometry.

4.4.2.2. Comparison and verification of the bioreactor models performance

Three different modeling tools (AQUASIM, MATLAB, and ANSYS CFX) were used for bioreactor performance modeling. The first set of simulations was carried out using 2D steady-state models, which were implemented as indicated in subsection 4.3.3 and according to the operating conditions specified in Table 4.1. In order to compare models performance and to validate the implementation of biological expressions into the CFD code, the results of the simulations performed are presented in Figure 4.7. The results of simulating the bioreactor performance in AQUASIM, MATLAB, and ANSYS CFX were compared with the corresponding experimental DO profiles, obtained along the bioreactor for four different biofilm densities (9.3, 13.5, 18.2 and 25.6 g VSS L⁻¹).

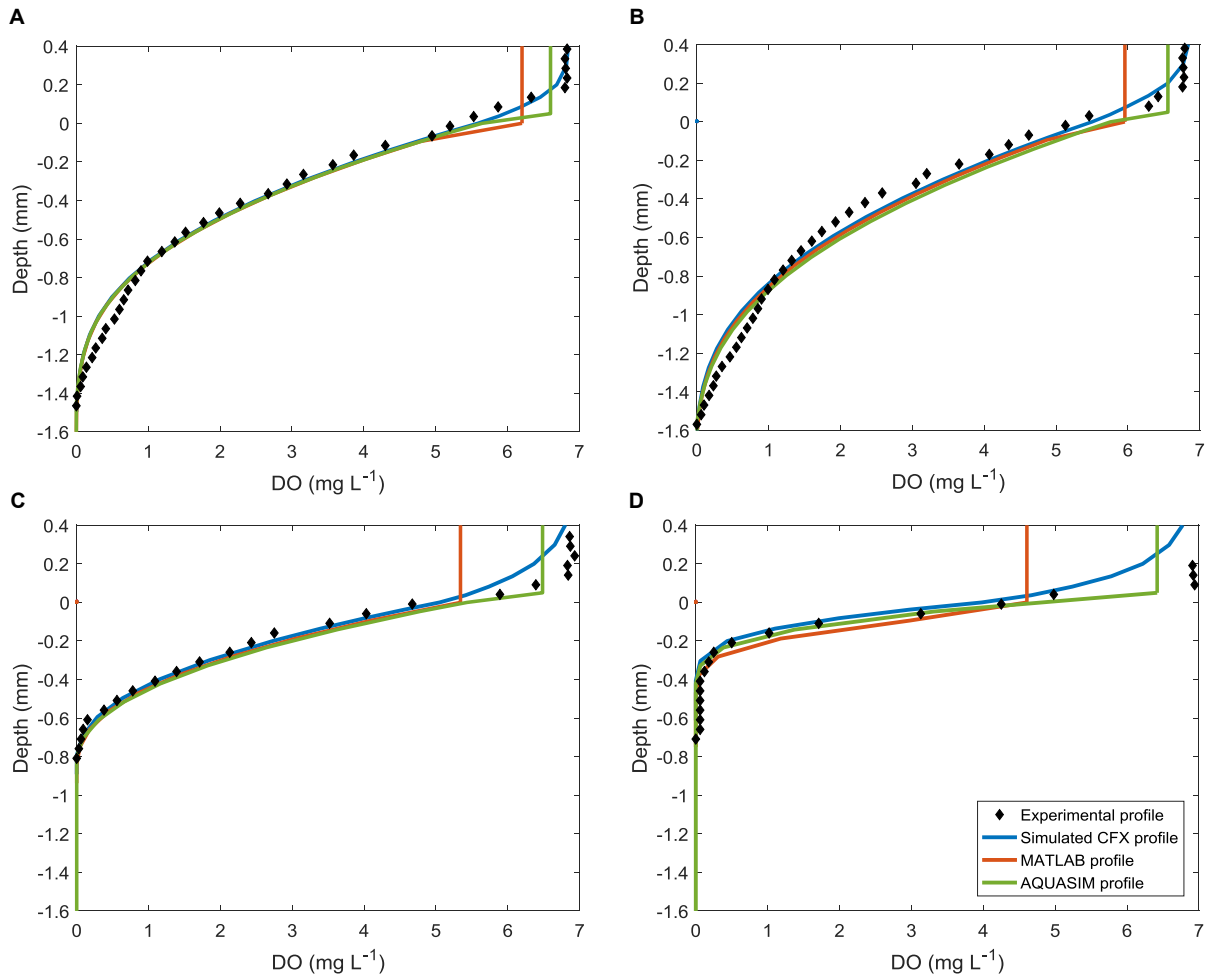


Figure 4.7. Experimental DO profiles (symbols) and simulated DO profiles (solid lines) inside the biofilm under substrate consumption conditions at different biofilm densities: (A) 9.3 g VSS L⁻¹, (B) 13.5 g VSS L⁻¹, (C) 18.2 g VSS L⁻¹, and (D) 25.6 g VSS L⁻¹.

Qualitatively, AQUASIM, MATLAB and CFD simulated profiles present the same behavior and the same trend throughout the biofilm, reaching the anaerobic limit at similar depths for all the studied biofilm densities. Therefore, fitting the kinetic constants and their implementation into CFD software can be stated as successful. However, the characterization of the liquid phase using these three techniques shows marked differences. MATLAB and AQUASIM models considered each element of the liquid phase as a CSTR, and they did not explicitly simulate the external concentration gradients to the biofilm surface, thus modeling the reduction in concentration as a mass-transfer resistance in the CBL. Consequently, the concentration value remained constant in the liquid phase. In the CFD model, several discretizations were performed across the liquid phase, and the transport of oxygen was defined with numerical hydrodynamic models so, more accurate results were obtained with this technique.

For a more quantitative comparison with the experimental results, the NRMSE (Expression 4.3) between the experimental DO profiles and the DO simulated profiles for the

different biofilm densities were determined (Table 4.3). The deviations obtained using any of the three techniques for modeling the bioreactor are below 6%, reproducing with great accuracy the biological behavior. Although the deviations obtained with nodal models are the largest, AQUASIM program described with exactitude the mean value of the oxygen concentration in the liquid phase. MATLAB model also simulated biofilm profiles with lower deviations, but the profile along the liquid phase is steeper, reducing excessively the concentration in the zones near the bioreactor outlet. CFD results obtained the lowest deviations, reproducing the DO values at the liquid-biofilm interface with high accuracy, despite they required more computing time. Hence, comparing AQUASIM and MATLAB simulated profiles with the CFD ones, in which a detailed simulation of mass transport phenomena in the liquid has been considered, the fact of including hydrodynamic models and accurate discretization in the liquid phase improved the simulations results, reducing the NRMSE around 2% for the studied conditions. It should be noted that P1 profile had the minor deviations in all simulated results, since the convective term affected in a lesser extent in that region.

Table 4.3. Normalized root mean square errors (NRMSE) between the experimental DO profiles and the DO simulated profiles.

	P1 (9.3 g VSS L ⁻¹)	P2 (13.5 g VSS L ⁻¹)	P3 (18.2 g VSS L ⁻¹)	P4 (25.6 g VSS L ⁻¹)
AQUASIM	3.04%	5.36%	4.96%	4.48%
MATLAB	3.47%	4.35%	4.48%	5.13%
CFD	2.35%	3.47%	2.65%	3.34%

Depending on the purpose for which the bioreactor model is developed, the results obtained with the three techniques will have advantages and disadvantages. In brief, when a bioreactor model is developed, it should be taken into account that AQUASIM is easy and quick to configure, MATLAB allows to define 'tailored' used-defined models, and CFD allows to couple the biological equations with hydrodynamic models easily, but it introduces computational intensity and increases simulation time. Even so, it should be pointed out that the use of CFD techniques allows a much more realistic description of hydrodynamic effects over the transport of substrates in the bulk phases, which directly affects the model accuracy on the mass transfer at the concentration boundary layer (Boltz et al., 2010).

As shown in Figure 4.7, oxygen and concentration gradients external to the biofilm surface can be simulated using the developed CFD model, also reproducing the behavior in the concentration boundary layer (CBL). Therefore, the developed CFD model can be used to determine the effective biofilm thickness and CBL and to differentiate between aerobic and anaerobic zones in the bioreactor. Nevertheless, resulted prediction should be improved at the boundary layer in the cases near the outlet (Figures 4.7C and 4.7D). The reason for having less accurately fitting in these areas was because of the thicker and denser biofilm

sections that were found at the bioreactor outlet, as it was observed experimentally in these cases and in a previous work (Guimerà et al., 2015). These phenomena cause a reduction of the liquid layer thickness in these zones, thus raising the liquid velocity with the consequent increase in the slope of the measured oxygen profile. Therefore, these phenomena should be considered to improve the present model. In spite of that, the developed CFD model allows to simulate adequately the DO concentration trend throughout the CBL, permitting to study in detail mass transfer phenomena in this type of bioreactors.

4.4.2.3. Bioreactor performance under transient conditions

A new set of CFD simulations was carried out, describing the bioreactor performance using the 3D model in transient conditions. From the results, the fluid flow characteristics, mass transport mechanism and biodegradation phenomena along the bioreactor in the unsteady state were analyzed.

The hydrodynamic characterization of the bioreactor was described from RTD analysis, streamlines and velocity profiles. CFD hydrodynamic model was validated using the RTD test. Both experimental and simulated the residence time distribution ($E(t)$) curves are represented in Figure 4.8. As can be seen, the designed CFD model reproduced correctly the experimental data obtained in the control point. Specifically, a mean residence time (Expression 4.6) of 812 seconds was obtained for the complete bioreactor, being this value close to the theoretical with a deviation of 2.7%.

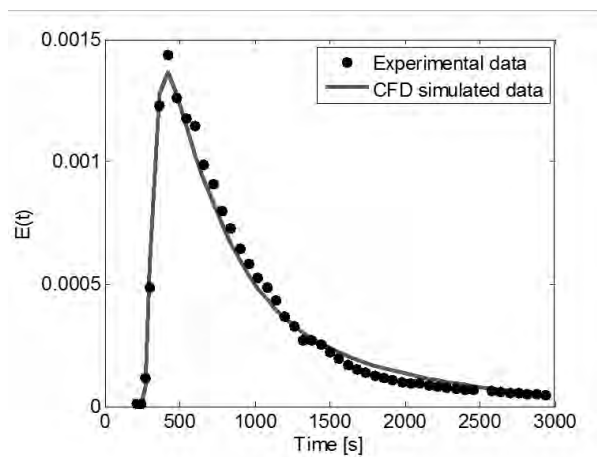


Figure 4.8. Comparison between experimental (symbols) and simulated results (solid line) of RTD analysis.

Streamlines and velocity profiles along the bioreactor are shown in Figure 4.9. The streamlines (Figure 4.9A) show that the liquid phase was correctly distributed over the bioreactor, contacting the whole of the biomass (specified in grey color). Moreover, the velocity profiles (Figure 4.9B) identify bioreactor zones which support the highest and lowest velocities. The bioreactor zones which supported lower velocities were mainly in the biofilm section, thus the diffusive phenomena were predominant over the mass transport in these

zones, as it was indicated by Lewandowski and Beyenal (2007). Finally, the velocity profiles in the liquid phase (represented by L1 line in the cross-section of the bioreactor in Figure 4.9B) match satisfactorily the velocity distribution of a laminar flow regime (Figure 4.9D).

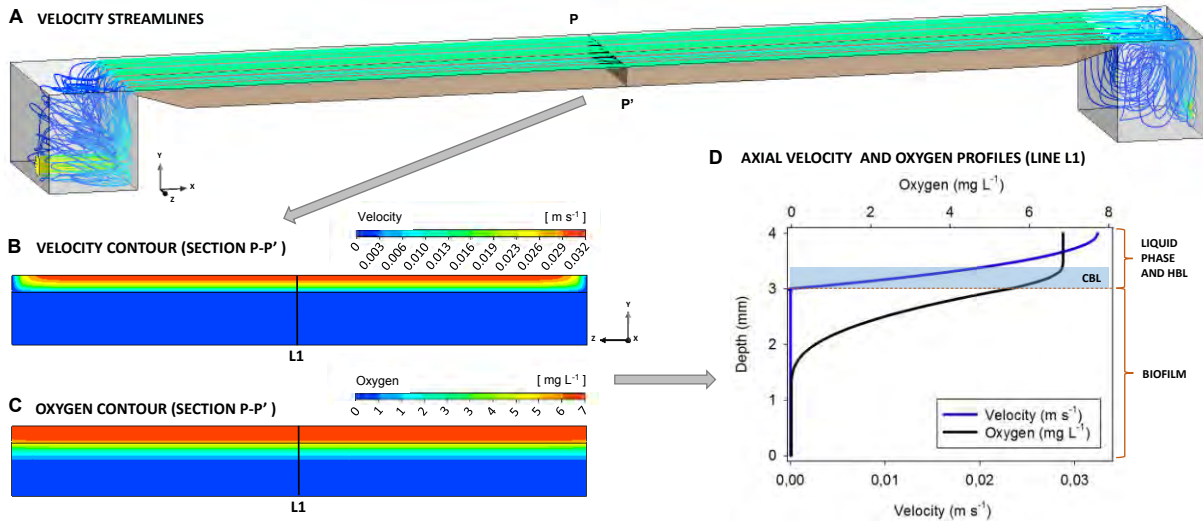


Figure 4.9. Velocity and oxygen profiles in different zones of the bioreactor. (A) Velocity streamlines inside the bioreactor, (B) velocity contours in section P-P', (C) oxygen contours in section P-P', and (D) axial velocity and oxygen profiles in line L1.

An accurate global behavior of the bioreactor was reproduced since the hydrodynamics in the reactor were precisely reproduced and validated. So, variables involved in bioreactor mass transfer mechanics can be analyzed from the results of this simulation to contribute to the existing knowledge of this type of processes in the liquid phase, concentration boundary layer, and biofilm.

Then, oxygen and velocity contours are both depicted in a transverse plane to the direction of the liquid phase in Figures 4.9B and 4.9C. Also, Figure 4.9D shows axial profiles of these variables in the line L1 of the transverse plane. In these figures, DO concentration profiles and velocity distributions describe the behavior of the studied biofilm with a uniform structure. The flow velocity in the liquid phase forms a profile which is called the hydrodynamic boundary layer (HBL), decreasing from the maximum value when is in contact with the gas phase (free-slip condition) to zero at the surface biofilm (non-slip condition). It is noted that, as described in other studies (Lewandowski and Beyenal, 2007), this velocity profile had a direct consequence in the formation of the concentration boundary layer (CBL) in the oxygen profile above the biofilm. At the interface, where velocity distribution reaches zero, the oxygen profile changes the curvature from convex to concave due to the effect of combining microbial activity and diffusion within the biofilm. So, the CBL is formed within the HBL, existing a relationship between the thicknesses of both layers and being the HBL thickness (δ_H) higher than CBL thickness (δ_C) (Bishop et al., 1997).

In addition, in relation to mass transport mechanism inside and outside the biofilm, the velocity profiles and the oxygen gradients in X and Y axis are studied in detail (see Figures 4.10 and 4.11). Figure 4.10A depicts the velocity profiles along the flat plate (X-axis), and in the middle of the liquid phase and the concentration boundary layer. As expected, the predominant velocity component, and equal to the absolute value of velocity, was the one corresponding to X direction, i.e. velocity U_x . Figure 4.10B represents the oxygen gradient profiles in X and Y directions along the flat plate, and in the middle of the liquid phase and the concentration boundary layer. Figure 4.11 shows the oxygen gradients and velocity profiles in other zones of the bioreactor.

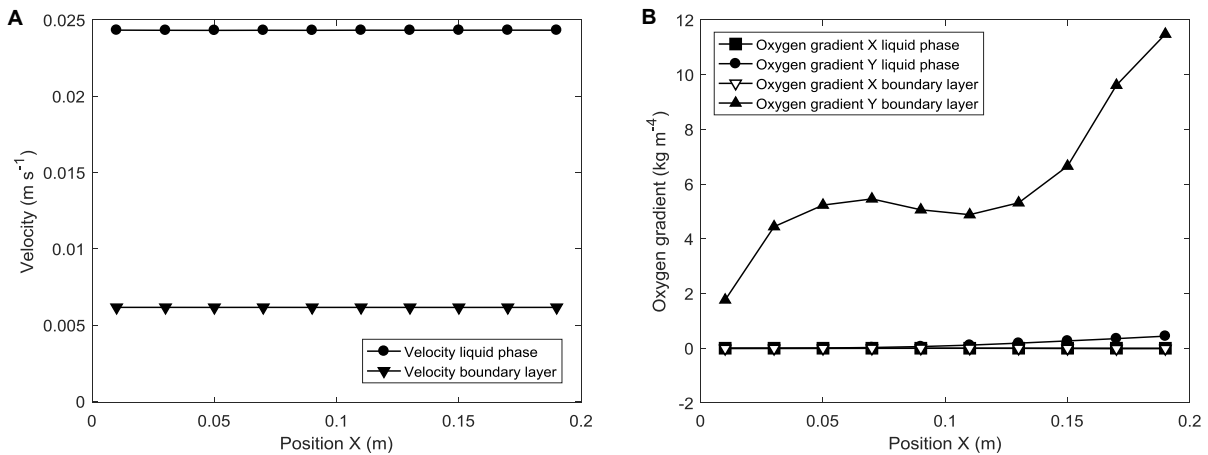


Figure 4.10. Mass transport mechanism characteristics along the bioreactor: (A) Velocity profiles along the flat plate (X-axis) in the liquid phase and in the concentration boundary layer, (B) Oxygen gradient profiles (X and Y axis) along the flat plate (X-axis) in the liquid phase and the boundary layer.

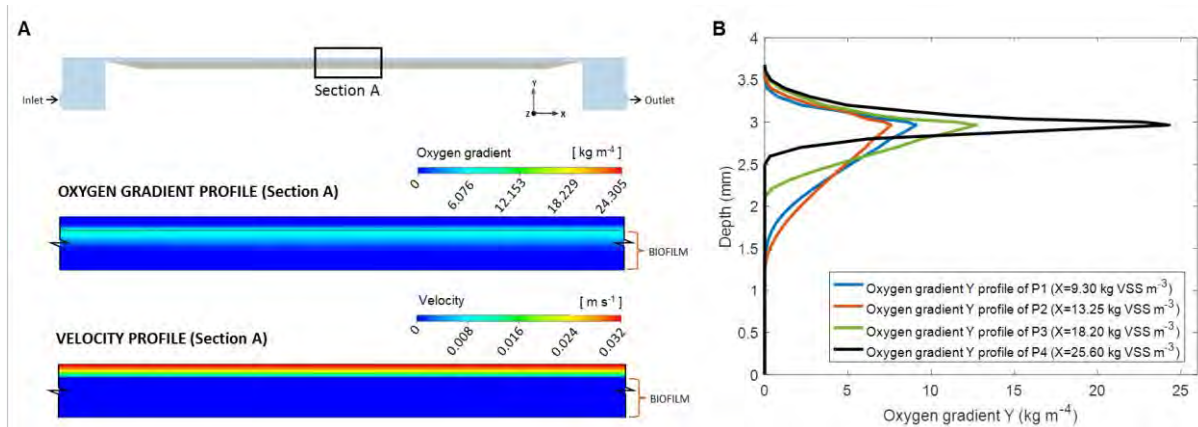


Figure 4.11. Oxygen gradient and velocity profiles in different zones of the bioreactor. (A) Oxygen gradient and velocity profiles in section A, and (B) oxygen gradient profiles along the P1, P2, P3 and P4 profiles (with biomass densities of 9.30, 13.25, 18.20 and 25.60 kg VSS m⁻³ respectively).

As can be seen in Figures 4.10 and 4.11A, it is observed that advection phenomena in the liquid phase were governing over the diffusive mechanics, since the oxygen gradients are negligible in this phase along the bioreactor. In contrast, in the concentration boundary layer,

diffusion was greatly notable in the Y direction (Figure 4.10B) and convection decreases its effect in relation to the liquid phase (Figures 4.10A and 4.11A). As can be seen in Figure 4.11B, the oxygen gradient Y-axis profiles increased along the bioreactor in the liquid phase and the CBL, having P3 and P4 the highest values. Then, the oxygen gradients Y-axis profiles decreased inside the biofilm, being the deepest profiles the ones with low biomass density (P1 and P2) and the more diffusive zones (as defined by Expression 4.1 for the biofilm diffusion coefficients). Finally, the mass transport was purely diffusive within the biofilm as demonstrated in Figure 4.11.

The phenomena above described were also observed analyzing in detail the convection and diffusion along the P1, P2, P3 and P4 simulated profiles in Figure 4.11. The velocity profiles in the X direction had the same shape and values than those above presented in Figure 4.9D, being larger in the liquid phase, reducing their velocities through the concentration boundary layer and reaching zero at biofilm interface. Moreover, the diffusive effect began in the liquid phase, but mainly occurred in the CBL as depicted in Figure 4.11B, where the oxygen gradient in the Y direction is represented, increasing up to the maximum value within the biofilm, and decreasing through the active region of biofilm. Therefore, it can be assumed that a duality of transport mechanisms (convection plus diffusion) was present in the liquid phase and the diffusive effect governed within the biofilm, as it is discussed in Lewandowski and Beyenal (2007) and Guimerà et al. (2016).

Finally, the CFD model allowed us to characterize the behavior of the dissolved oxygen variable along the bioreactor length. As can be seen in a top view of the bioreactor (Figure 4.12A), CFD model reproduces consistently oxygen depletion at the interface level, decreasing its concentration along the flat plate and showing the zone with lower concentration at the end of the flat plate. Moreover, in a frontal view of the bioreactor (Figure 4.12B), CFD model reproduces expected oxygen profile along the biofilm, showing deeper oxygen profiles near the bioreactor inlet, as it was found experimentally, and the anaerobic volume, i.e zone specified in blue color, inside the biofilm region, which was also measured in the experimental set-up.

Therefore, this simulation technique allows us to determine nutrients and substrate limitations anywhere in the bioreactor geometry. This characteristic could be very useful to simulate complex geometries of reactors, e.g. packed beds, where the mass transfer can be affected by the packing material geometry and porosity, creating preferential channels or changing the liquid phase velocity. In order to model rigorously mass transfer, it should be considered a wide range of factors such as the pollutant physical-chemical properties, the medium properties, the internal reactor characteristics, as well as the operating conditions. All these factors can be coupled using CFD codes, defining the different flow regimes, the properties of fluid phases and the reactors geometry, although introducing computational expense. Hence, the use of CFD techniques to model fixed-bed biofilm systems offers a great potential for the detailed analysis of local mass transfer behavior, besides allowing the

optimization of bioreactor operations. The developed 3D CFD model could be useful to predict species behavior under several operating conditions at different phases and bioreactor zones.

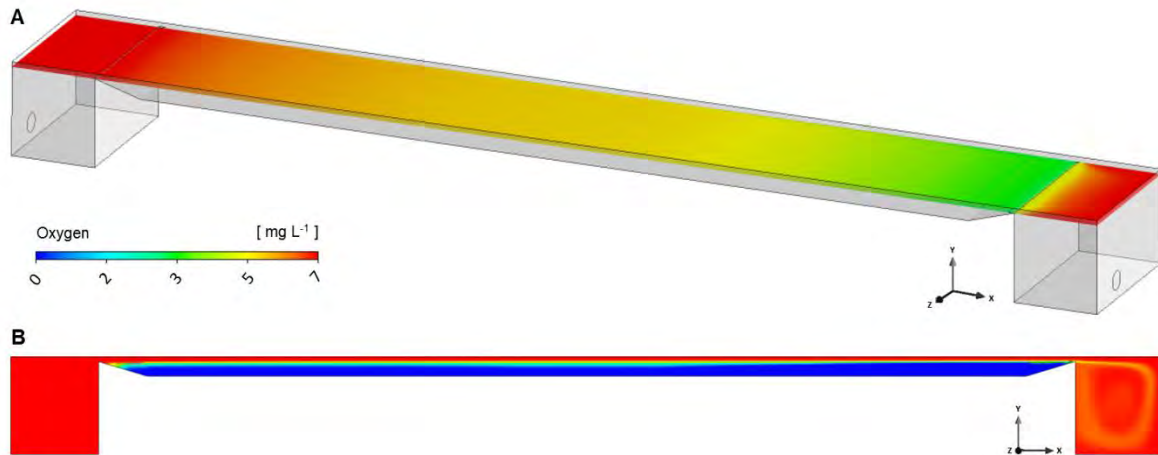


Figure 4.12. The behavior of the dissolved oxygen variable along the bioreactor length. (A) Oxygen degradation profile along the liquid-boundary layer interface, and (B) oxygen concentration profile along the bioreactor.

4.5. CONCLUSIONS

The use of different techniques for bioreactors modeling was evaluated, verified and used to determine in which scenarios would be suitable the use of more accurate modeling such as CFD. Results indicated that the hydrodynamic behavior should be considered in the liquid phase to model precisely the performance of biofilm reactors, since this phase acts as a major medium to transfer oxygen and nutrients to the biofilm.

Another important finding was that CFD techniques were more appropriate to model satisfactorily the performance of biological systems in a wide range of conditions, reproducing accurately measured experimental data along the bioreactor. These findings suggest that the application of CFD techniques for modeling bioreactors can help to develop more rigorous models, especially when mass transfer in the biofilm is limiting, allowing to underline the role of the hydrodynamic in the process.

Still, further research related to associate the physical properties in the biofilm, i.e. growth and detachment phenomena, is required, since it is essential to consider these effects over the fluid dynamics, and to relate the changes in the hydrodynamics which, in turn, affect over the biofilm physical properties too. For this reason, further investigation is needed to clearly find out how to model the biofilm as an independent phase.

Finally, it was concluded that the procedure described in this chapter to develop accurate models of fixed-bed biofilm reactors, coupling hydrodynamics and biological behavior by means of CFD techniques, was successfully stated and applied. The defined

procedure allowed defining 3D bioreactor model and studying in detail fluid flow characteristics, mass transport mechanisms and biodegradation phenomena along the bioreactor in transient states.



DETAILED RHEOLOGICAL CHARACTERIZATION OF FIXED AND SUSPENDED HETEROTROPHIC BIOMASS

The motivation of this chapter was to gain knowledge about the characterization of biofilms as a pseudoplastic fluids and viscoelastic materials by using rheometry analysis. Considering their viscous and viscoelastic properties would allow defining the biofilm as an independent phase in the bioreactor model, hence including its physical behavior, i.e. growth, stretching and detachment. Since there is no fundamental understanding of intrinsic rheological properties of heterotrophic biofilms, analyses under different shear flow conditions were performed, allowing examining both mechanical and structural properties. Complementary analyses of suspended biomass samples were also performed to contrast biofilm rheological properties. This supplementary study helped to obtain an extensive characterization and modeling of the biomass rheological properties in function of its concentration. This fact is interesting to underline since biomass concentration along bioreactors could be significantly different due to the intrinsic heterogeneity of bioreactors.

Abstract

A detailed rheological study program was performed to test and characterize the response of aerobic heterotrophic biofilms cultivated on a fixed-bed biofilm reactor. Suspended biomass was also analyzed to identify the nexus between the rheological responses of both biological samples. Rheological analyses under steady, oscillatory and transient shear flow conditions were performed, determining macroscopic mechanical properties (i.e. yield stress, elastic modulus, etc) and analyzing the interactions and binding mechanisms between the structural components at microscale. Experimental results pointed out that biofilm and suspended biomass samples exhibited gel-like character, showing shear-thinning behavior with yield stress and determining an equivalent rheological response in steady shear measurements. The rheological parameters obtained were strongly dependent on the biomass concentration in both cases, being possible to correlate rheological characteristic parameters within a range of concentrations. In oscillatory and transient measurements, similar tendencies were also found for both biological samples, even if some variations in the structural and viscoelastic properties were detected, which were related to the components of the hydrogel network present in the biofilm. To interpret the behavior as a pseudo-plastic fluid and as a viscoelastic material of both biological samples, the rheological data of steady and transient measurements were successfully modeled adopting Herschel-Bulkley and Burger models, respectively. Therefore, models to describe biofilm behaviors as a pseudo-plastic fluid as well as a viscoelastic material were provided, finding a good self-consistency between experimental data, and fits and predictions. This study makes a further step in the characterization of heterotrophic biofilms dynamic properties, providing models which can be used to couple biofilm mechanical response with fluid dynamics.

A modified version of this chapter has been submitted for publication as:

L. Prades, Y. Bautista, J. Climent, V. Sanz, S. Chiva, A.D. Dorado, X. Gamisans, 2018. **A comprehensive rheological analysis of fixed and suspended heterotrophic biomass linking macroscopic properties to shear-induced microstructure**, *Water Res.*

5.1. INTRODUCTION

Biofilms are considered as complex microbial aggregates encased in a matrix containing mainly microorganisms, nucleic acids, proteins, water and extracellular polymeric substances (EPS) (Wloka et al., 2004; Flemming and Wingender, 2010). The EPS network provides stability and specific mechanical properties (Sheng et al., 2010; Wilking et al., 2011; Peterson et al., 2015). Biofilms typically behave as a viscoelastic structure if shear forces are applied over them (Ohashi and Harada, 1994; Stoodley et al., 1999a; Klapper et al., 2002). When considering biofilm dynamics, this shear stress/rate caused by fluid circulation is a factor of paramount importance which influences the biofilms development, mass transfer and detachment (Rittmann and Laspidou, 2001; Horn and Lackner, 2014) and, hence, affecting the bioreactor operation. A deeper knowledge in the characterization of flow effects on biofilms response, examining their physical properties as well as the associated interactions, could allow establishing rigorous models to predict more accurately the behavior of real bioreactor systems.

Rheological analyses can characterize mechanical properties under various shear flow conditions, providing information on how the material reacts both in regard to time-scale and applied stress. The application of rheometry to study biofilms has been widely performed (Böl et al., 2012; Karimi et al., 2015; Fabbri and Stoodley, 2016), investigating pure and mixed culture biofilms, but mainly for medical applications. Most works have been focused on the study of the rheological dynamics properties of biofilms and EPS to study their internal structure (Vinogradov et al., 2004; Wloka et al., 2004, 2005; Di Stefano et al., 2009; Lieleg et al., 2011), and the transient shear flow in response to short period of loading by studying biofilms deformability to external forces (Towler et al., 2003; Vinogradov et al., 2004; Di Stefano et al., 2009). However, the understanding of viscous response with steady-state flow behavior in a biofilm system is rather limited. No studies have been found in the literature addressed to determine the yield stress with conventional rheometry, which will be useful for the prediction of fixed biofilm detachment (Towler et al., 2003), since biofouling is one of the critical issues in the efficiency of fixed-bed biosystems. In contrast, this type of analysis has been widely performed for different types of sludge from wastewater treatment plants (WWTPs) (Eshtiaghi et al., 2013; Ratkovich et al., 2013; Ma et al., 2014; Wang et al., 2016), demonstrating its suitability to characterize the viscous behavior of the system and providing models which can be implemented in combination with fluid dynamics codes (Ramin et al., 2014). In addition, although critical parameters (e. g. yielding viscosity, intrinsic viscoelasticity) play essential roles in the biofilm response coupling simultaneously solid and fluid behavior, biofilms rheological characterization has barely been reported as a combined study to examine their response in function of various shear flow conditions. A complete experimental program (i.e. steady, oscillatory and transient shear flow analyses) would allow relate physical and structural characteristics. Only Wloka et al. (2005) performed the steady shear analyses to compare the results with oscillatory ones, and discussed the interactions

among the components of the EPS extracted of *Pseudomonas aeruginosa* biofilms, stating that the formation of physical interactions such as entanglements was predominant.

The aim of this chapter was to investigate extensively the viscous and viscoelastic properties of heterotrophic biofilms by means of performing rheological tests, characterization analysis and models development. Data from those analyses would allow defining the biological system as an independent phase when modeling biosystems, hence considering fluid-biofilm interactions and including biofilm physical behavior, i.e. growth, stretching and detachment. Additionally, in order to develop a detailed study, suspended biomass samples were also analyzed, comparing their rheological behavior with that obtained from the biofilms, i.e. fixed biomass, and establishing connections in the response terms of both biological samples under the different shear flow conditions. Steady, oscillatory and transient shear flow measurements were performed to determine macroscopic mechanical properties (i.e. yield stress, elastic modulus, relaxation time). The non-steady shearing analyses results were also used to probe the samples time-dependent nature, and to further investigate the binding mechanisms between samples structural components at microscale.

5.2. MATERIALS AND METHODS

5.2.1. Cultivation and preparation of the samples

Biological samples from cultivated biofilms and suspended biomasses were analyzed in this work. Aerobic heterotrophic biofilms were grown on a flat plate bioreactor (FPB). After sterilizing the FPB, it was seeded with 40 ml of a sludge (4 g of volatile suspended solids (VSS) L⁻¹) obtained from the WWTP of Manresa (Barcelona, Spain). The remaining volume of the FPB was filled with a nutrient solution, and it was operated in batch mode for 24 hours to promote the bacteria immobilization. Then, the FPB was operated continuously for 10 days until well-defined biofilms were cultivated. Oxygen saturation conditions, taking into account salinity and temperature, were achieved aerating solutions with standard air. Glucose, fed in excess to avoid biomass growth limitation, was used as the sole carbon source. During biofilm growth, flow rate and residence time were adjusted to approximately 1 m h⁻¹ and 12 h. Further details about reactor setup and operation can be found in Guimerà et al. (2016). After heterotrophic biofilm growth, the well-fixed samples were carefully removed from the FPB and transferred into the rheometer plate, following the indications of Wloka et al. (2005). Biofilm density was determined using protein analysis, as described in Guimerà et al. (2016). The suspended biomass samples were obtained from the same inoculum of heterotrophic microorganism used for the FPB immobilization. These samples were diluted using distilled water to obtain samples in the usual concentrations of heterotrophic biofilms (from 5 to 45 g VSS L⁻¹ (Guimerà et al., 2016)). Subsequently, they were also transferred to

the rheometer plate. The concentration of the VSS in the suspended biomass samples was measured following standard methods (APHA, 1998).

5.2.2. Rheological characterization

5.2.2.1. Rheological tests

Rheological tests were carried out using a BOHLIN CVO 120 HR rheometer, connected to a controlled water bath which kept the samples at 25 °C during the measurements. As recommended in related works (Wloka et al., 2005), the experiments were performed using a cone-plate geometry, with a diameter of 40 mm and a 4° truncated cone angle, and a solvent trap to avoid evaporation. Moreover, at the beginning of each test series, two samples from the same biological system were tested and their results were compared verifying the repeatability of the measurements.

The experimental essays were carried out in three different shear modes: steady, oscillatory and transient. In the steady shear mode, equilibrium flow curve measurements were conducted with controlled shear stress, raising the shear stress σ (Pa) stepwise and measuring also the shear rate $\dot{\gamma}$ (s^{-1}), obtaining also the corresponding viscosity curves (Mezger, 2006). The sample undergoes constant shear stress at each step for the time required to reach a practically steady state. In the oscillatory shear mode, a shear stress was varied sinusoidally at an angular frequency obtaining also a sinusoidal shear strain response, which allows to determine the storage modulus G' (Pa) and the loss modulus G'' (Pa) after being mathematically decomposed in two functions. G' represents the elastic property and solid behaviors of materials and G'' represents its viscous property and fluid behaviors. The loss factor or the tangent of phase angle δ ($^\circ$) is calculated as the quotient of loss and storage modulus ($\tan \delta = G'' / G'$). Further details on theoretical aspects of oscillatory test parameters (complex shear modulus, complex viscosity, storage modulus, loss modulus and loss factor) and related information can be found elsewhere (Mezger, 2006; Schramm, 1994). In this study, amplitude sweep test was performed to determine the effect of shear stress (from 10 to 200 Pa) on G' and G'' at a frequency of $f = 1$ Hz. The linear viscoelastic regimen (LVR) was determined defining the strain limit value with a tolerance of 10%. The frequency sweep test was conducted to measure the frequency dependence of G' and G'' in the linear viscoelastic regimen (1% strain), characterizing all samples between 0.01 and 10 Hz. In the transient shear mode, shear creep tests were performed by applying a constant shear stress (σ) and measuring shear strain ϵ (-) over time (Findley et al., 1978). Based on similar previous studies (Towler et al., 2003), tests were conducted by applying σ for a 180 seconds retardation period (loading), followed by a 180 seconds recovery period (unloading). In this work, different σ values inside the LVR (3, 12 and 40 Pa) were examined during the tests.

5.2.2.2. Modeling and characterization under steady shear flow behavior

Since no references were found in the literature for biofilm modeling under steady shear flow, the good modeling practice (GMP) suggested for rheological studies of sludge (Ratkovich et al., 2013) were followed to characterize the biological samples as non-Newtonian fluids. To select the adequate model, the concentration grade of the samples and the accuracy in the description of the flow curves were taken into account, being necessary the use of models with a minimum of three parameters (Ratkovich et al., 2013), and which can also describe the behavior of high concentration samples (Eshtiaghi et al., 2013). Among the proposed formulations to model flow behavior with yield stress (Mezger, 2006), the Herschel-Bulkley rheological model was adopted to characterize the behavior of biofilm and suspended biomass samples. The shear stress σ and the viscosity η of the model based on shear rate $\dot{\gamma}$ are described by expressions 5.1 and 5.2 respectively.

$$\sigma = \sigma_y + K \cdot \dot{\gamma}^n \quad (5.1)$$

$$\eta = \sigma / \dot{\gamma} \quad (5.2)$$

Where σ_y is the yield stress (Pa), K is the fluid consistency index (Pa s) and n is the flow behavior index (-). The flow was considered to have yielded once the critical shear rate ($\dot{\gamma}_c = \sigma_y / \eta_y$) is reached, being η_y the yielding viscosity (Pa s).

For the parameters estimation, the yield stress was accurately determined using the tangent crossover method (Mezger, 2006). Subsequently, following the GMP (Ratkovich et al., 2013), this parameter was fixed to obtain small confidence intervals during the estimation of the parameters K and n. Least-squares fitting method solved using MATLAB® Release 2016b was employed to estimate these parameters from the experimentally measured flow curves. Developed model's verification was completed to evaluate their performance against available experimental data.

5.2.2.3. Modeling and characterization under transient shear flow behavior

The four elements Burger approach was selected to model de viscoelastic behavior of biological samples, since previous works demonstrated its suitability (Jones et al., 2011; Towler et al., 2003). The Burger model is made up of a Maxwell liquid (spring G_1 and dashpot η_1) and a Kelvin-Voigt solid (spring G_2 and dashpot η_2) linked in series to each other (Figure 5.1A). The Burger model mathematical evaluation leads to a differential equation which can be solved for the shear strain of creep (Expression 5.3) and recovery (Expression 5.4) phases as follows (Findley et al., 1978):

$$\varepsilon(t) = \sigma \cdot \left[\frac{1}{G_1} + \frac{t}{\eta_1} + \frac{1}{G_2} \cdot \left(1 - e^{-G_2 t / \eta_2} \right) \right] \quad (5.3)$$

$$\varepsilon(t) = \sigma \cdot \left[\frac{t_s}{\eta_1} + \frac{1}{G_2} \cdot \left(e^{-G_2 t_s / \eta_2} - 1 \right) \cdot e^{-G_2 t / \eta_2} \right] \quad (5.4)$$

Where $\varepsilon(t)$ is the shear strain (-), t is time (s), σ is the applied shear stress (Pa), G_1 and η_1 are the elastic (Pa) and viscous (Pa s) moduli of the Maxwell element, G_2 and η_2 are the elastic (Pa) and viscous (Pa s) moduli of the Kelvin-Voigt element and t_s is the time (s) at the end of the creep period.

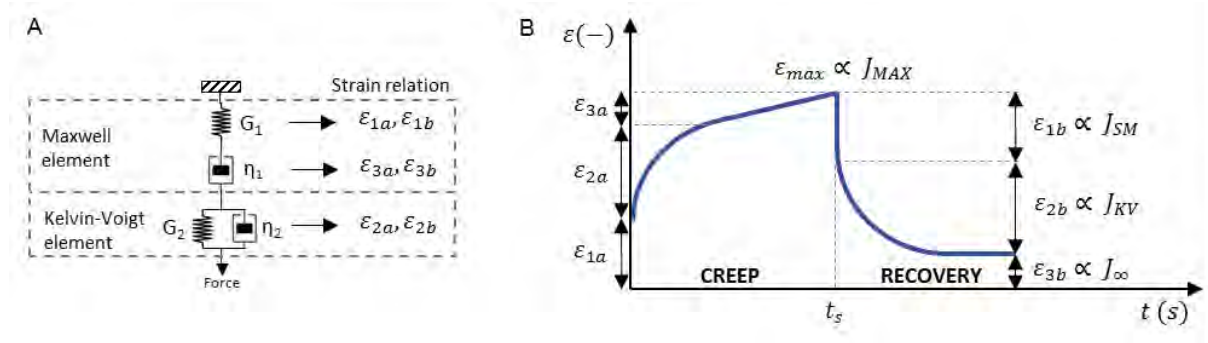


Figure 5.1. The Burger model elements and their relations with creep and recovery strains (A) and theoretical creep and recovery strains dependent on time for viscoelastic materials (B) (adapted from Mezger (2006)).

An iterative procedure was employed to determine the optimized parameters (G_1 , η_1 , G_2 , η_2) in the Burger model for each sample. The algorithm was implemented and solved using MATLAB® Release 2016b. In this algorithm, the strains predicted by the model were compared with the experimentally measured data and the deviations between both were used to obtain updates for elastic and viscous parameters. Parameter values were sought to minimize the objective function given in Expression 4.3 (see Chapter 4, section 4.2.2), which corresponds to the normalized root mean square error (NRMSE). In this case, for the optimization of parameters G_1 , η_1 , G_2 and η_2 , $X_e(t)$ is the strain measured ($\varepsilon_e(t)$), $X_p(t)$ is the predicted strain ($\varepsilon_p(t)$) according to equations 5.3 and 5.4, and $X_{e,max}$ is the maximum experimental strain ($\varepsilon_{e,max}$) and $X_{e,min}$ is the minimum experimental strain ($\varepsilon_{e,min}$).

Additionally, the creep and recovery compliance $J(t, \sigma)$ (-) was calculated using the shear stress and the deformation function obtained in the creep and recovery phases:

$$J(t, \sigma) = \varepsilon(t, \sigma) / \sigma \quad (5.5)$$

Figure 5.1B depicts the strain behavior of the Burger creep and recovery phases. As can be seen, the elements of the Burger model cause three different strain responses in each phase, giving an equal contribution both phases if the sample has been tested under conditions within the linear viscoelastic range (Schramm, 1994). The creep phase shows: the instantaneous strain elastic response (ε_{1a}) as a result of the Maxwell spring G_1 ; the exponential increase of the strain (ε_{2a}) related to the Kelvin-Voigt elements G_2 and η_2 ; and the viscous response of the strain (ε_{3a}) related to the Maxwell dashpot η_1 . In the recovery phase, the following information can be collected: the instantaneous strain elastic recovery (ε_{1b}) after removing σ , which is related to the Maxwell spring and defines the compliance J_{SM} ; the strain (ε_{2b}) decreases exponentially as a result of the Kelvin-Voigt elements, describing

the compliance J_{KV} ; and the permanent and non-recoverable viscous strain (ϵ_{3b}) related to the Maxwell dashpot, which determines the compliance J_{∞} . Note that the compliance J_{MAX} determines the maximum deformation, which corresponds to the compliance values $t=t_s$ in the transient analysis. Additionally, the deformation suffered by the Maxwell spring (J_{SM}) was obtained using Expression 5.6 (Dolz et al., 2008).

$$J_{SM} = J_{MAX} - (J_{\infty} + J_{KV}) \quad (5.6)$$

From the values of the different compliances, the percentage of deformation of each element and the final percentage recovery of the entire system can be calculated. The percentage of deformation of each element of the Burger model, concerning to the maximum deformation to which the system is subjected, was defined by the Expression 5.7.

$$J(\%) = \frac{J_{element}}{J_{MAX}} \cdot 100 \quad (5.7)$$

Where $J_{element}$ is the corresponding compliance: J_{SM} , J_{KV} or J_{∞} . The final percentage recovery of the entire system was calculated by means of the Expression 5.8, as proposed by Dolz et al. (2008):

$$\%R = \frac{J_{MAX} - J_{\infty}}{J_{MAX}} \cdot 100 \quad (5.8)$$

5.3. RESULTS AND DISCUSSION

5.3.1. Steady shear flow test results

Steady shear flow tests were performed to analyze the non-Newtonian character of biological samples, and their viscoelastic behavior, i.e. a fluid behaves like an elastic solid below a certain threshold stress value (yield stress) but the fluid starts to behave as a fluid when the yield stress is exceeded (Fabbri and Stoodley, 2016). Then, the deformation under a shear stressing flow was analyzed, recording the shear rate to obtain the basic flow behavior of the biofilm and suspended biomass samples, while characterizing the effect of their concentration over their viscoplastic properties in detail.

5.3.1.1. Viscous properties of biofilm and suspended biomass samples

The biofilm on a fixed-bed bioreactor develops through the interaction between the inoculum of heterotrophic suspended biomass and the fluid flow; therefore, it was enlightening to compare typical rheological measurements of suspended biomass with those from the resulting from the fixed biofilm. In addition, since both samples had the same biological background, the comparison assisted to verify the assumption that both samples share a wide range of mechanical and viscoplastic properties.

The behavior of biofilm and suspended biomass samples with equivalent VSS concentration was studied. Figure 5.2 shows flow and viscosity curves of biofilm and suspended biomass samples (denominated as BHC and SB respectively) with equivalent

VSS concentration ($34.7 \pm 0.2 \text{ g VSS L}^{-1}$). As can be seen, the behavior of both samples was analogous under steady flow conditions, having similar values of stress and viscosity in the entire interval of shear rate examined. Both samples behaved as non-Newtonian shear-thinning fluids and they showed the presence of yield stress at low shear rates, which is characteristic of gel-like structures (Mezger, 2006). These findings were in accordance with previous rheological studies of biofilms and sludge (Wloka et al., 2005; Ma et al., 2014; Ramin et al., 2014). For shear stress higher than the yield stress, the microorganism aggregates and networks were broken down and the cells and molecules were aligned into the flow direction (Mayer et al., 1999; Klapper et al., 2002), exhibiting both samples a weaker interaction between the structural components and poor flow resistance.

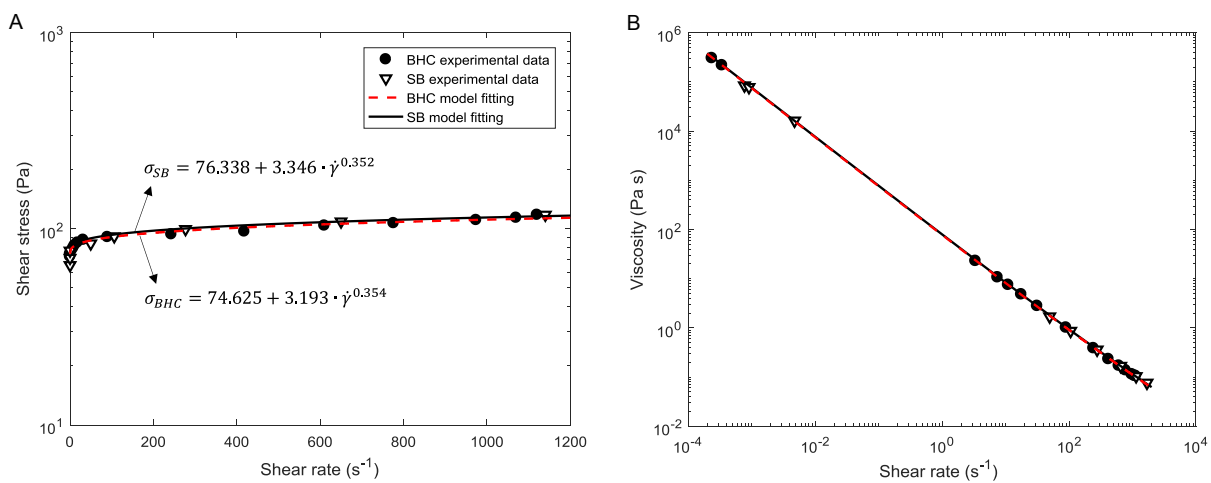


Figure 5.2. Flow (A) and viscosity (B) curves of biofilm BHC and suspended biomass SB samples with equivalent concentration ($34.7 \pm 0.2 \text{ g VSS L}^{-1}$). Symbols are experimental data and solid/stripped lines represent the Herschel-Bulkley model fitting.

In addition, this equivalent behavior was also revealed in the fitting of samples to the Herschel-Bulkley model (Expressions 5.1 and 5.2), characterizing their representative parameters: yield stress (σ_y), the fluid consistency index (K) and the flow behavior index (n). The coefficient of determination (R^2) between experimental data and corresponding models, being 0.9994 and 0.9971 for BHC and SB samples respectively, indicated the accurate reproduction of their non-Newtonian flow behavior. As can be seen in Figure 5.2, SB model parameters ($\sigma_y=76.338 \text{ Pa}$, $K=3.346 \text{ Pa s}$, $n=0.352$) were close to those for biofilm ($\sigma_y=74.625 \text{ Pa}$, $K=3.193 \text{ Pa s}$, $n=0.354$), being slightly higher the yield stress and the consistency index, and insignificantly smaller the flow behavior index. These variations, despite almost insignificant, could be related to the slight difference in samples concentration. This finding ensures the assumption that both biological samples, independently of the aggregation state, share the same viscoplastic properties. In this respect, one should also consider that suspended biomass samples, which are characterized

by practical and low invasive samples extraction, could be used to determine the rheological behavior of biofilms under steady shear flow.

5.3.1.2. Effect of biomass concentration on shear stress and viscosity

To develop a complete characterization in steady shear flow, the analysis of biofilms and suspended biomass in a wide range of concentrations was required, since biofilm density is a crucial parameter in biofilm strength and detachment rate (Rittmann and Laspidou, 2001).

Figure 5.3 depicts the rheograms of suspended biomass and biofilm samples considering a wide range of concentrations, up to a shear rate of 1200 s^{-1} . Both samples were analyzed in the steady shear flow, ranging their concentrations from 8.0 to $43.1 \text{ g VSS L}^{-1}$ and 32.6 to $34.5 \text{ g VSS L}^{-1}$ respectively.

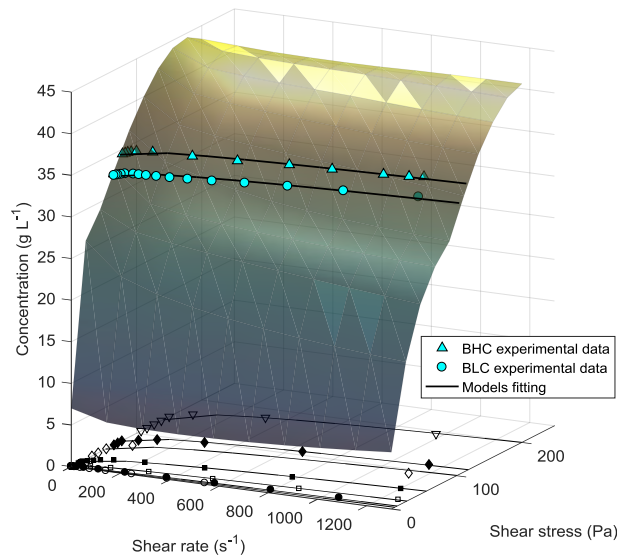


Figure 5.3. Flow curves of suspended biomass (2D plot bottom part) and biofilms (3D plot) samples at different concentrations. Isosurface was generated from 2D plot, incorporating samples concentration. Symbols are experimental data and solid lines represent Herschel-Bulkley model fitting.

As can be seen in Figure 5.3, the suspended biomass experimental data at different concentrations (detailed in Figure 5.4A) are depicted in the bottom, showing the samples with higher concentration the largest shear stress and viscosity. The flow curves of suspended biomass were used to generate the 3D isosurface, representing their rheological behavior dependent on concentration. The biofilm experimental data are depicted taking into account their respective densities, showing the good agreement with the viscoplastic behavior of the suspended biomass samples. Both fixed and suspended biomass samples exhibited the same behavior for the studied conditions, presenting a yield stress at the low range of shear rates. Furthermore, the flow curves were shifted up with an increase in concentration, indicating an increase in yield stress. The yield stress was higher in the more concentrated samples, showing a stiffer behavior. Therefore, the biomass concentration had a noticeable

effect on shear stress and also in the apparent viscosity (Figure 5.4B), obtaining higher apparent viscosities as the concentration was increased. The viscosity of all samples was sharply decreased as an increase in shear rate, demonstrating that these systems exhibited a marked non-Newtonian shear-thinning behavior. Results also revealed a reinforcement of the shear thinning effect with increasing biomass samples concentration.

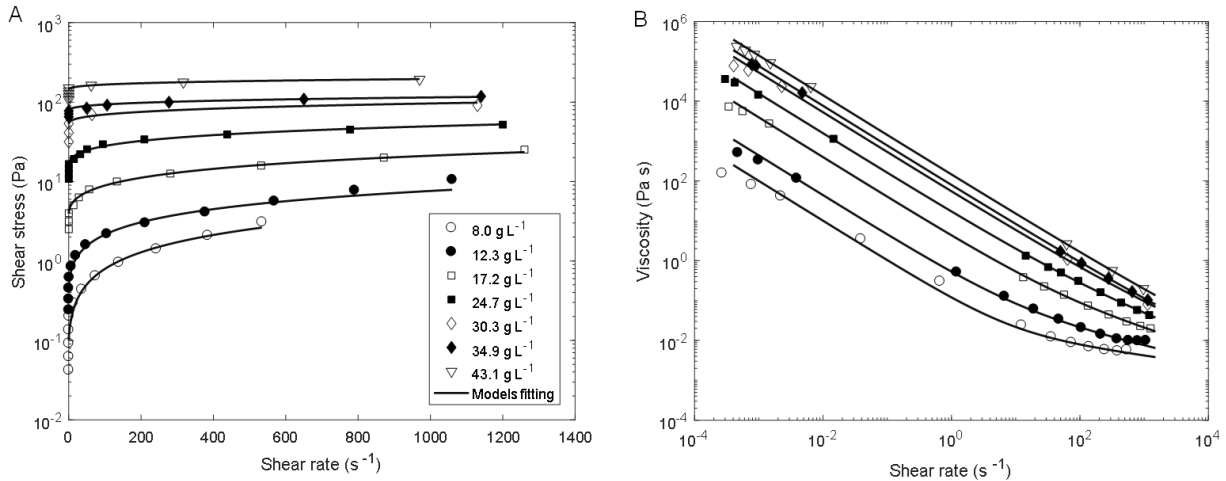


Figure 5.4. Flow (A) and viscosity (B) curves of suspended biomass samples at different concentrations. Symbols are experimental data and solid lines represent Herschel-Bulkley model fitting.

Experimental results were fitted to the Herschel-Bulkley model (Expressions 5.1 and 5.2) to describe the shear-thinning behavior with a yield stress. A detailed study was performed to know the yield limits at low shear rates. In this sense, the accurate estimation of yield stress (σ_y) and, hence, of the limiting shear rate allowed to estimate the yielding viscosity (η_y) from the results of the flow and viscosity curves (Figure 5.4B). The samples concentration, the characteristic parameters of the flow and viscosity curves from the measurements and the goodness of the model fit are summarized in Table 5.1. The effect of the biomass concentration previously observed over the stress and viscosity was also perceived in the characteristic parameters fitted for both samples. σ_y , η_y and n increased and K decreased as concentration raised. In addition, as can be seen in Figures 5.3 and 5.4, the Herschel-Bulkley model described accurately the rheological behavior of the samples in a wide range of concentrations, which is confirmed by the correlation factor ($R^2 > 0.98$).

Particularly, a non-negligible variation in the behavior of biofilm samples (BLC and BHC) was detected, although there is no large variation between biofilm samples density. The yield stress and the fluid consistency index augmented as biofilm concentration increased, while the flow behavior index decreased with the concentration rising (Table 5.1). These patterns indicated the shear-thinning behavior of biofilms, decreasing the slope of the flow curves as concentration was raising. It should be pointed out that the described tendency for the parameters of biofilm samples was analogous to the reported in different studies for sludge

from WWTP (Ramin et al., 2014; Wang et al., 2016), thus revealing the influence of the heterotrophic biofilm density in its rheological behavior.

Table 5.1. Estimated parameters of the Herschel-Bulkley rheological model (σ_y , K and n) and the yielding viscosity (η_y) for biofilm and suspended biomass samples with the indicated concentration (X).

	BLC	BHC	Suspended biomass						
X (g VSS L ⁻¹)	32.6	34.5	8.0	12.3	17.2	24.7	30.3	34.9	43.1
σ_y (Pa)	56.44	74.63	0.09	0.44	3.94	15.57	52.62	76.34	140.37
K (Pa s)	2.87	3.19	0.02	0.10	0.42	1.66	2.63	3.35	5.65
n (-)	0.39	0.35	0.77	0.62	0.54	0.44	0.41	0.35	0.33
η_y (Pa s)	52890	65044	42	233	4613	2174	47258	73267	113730
R ²	0.994	0.999	0.995	0.994	0.997	0.984	0.980	0.986	0.985

Qualitatively, these last findings were in agreement with the pioneering work of Ohashi and Harada (1994), who found that biofilms behaved as Bingham fluids with a yield stress, performing viscosity measurements of biofilm suspensions. Moreover, these authors defined a logarithmic correlation between the Bingham yield stress and the density of the samples. Figure 5.5 depicts the yield stresses calculated for biofilm and suspended biomass samples of this work, together with the experimental data and the correlation reported by Ohashi and Harada (1994).

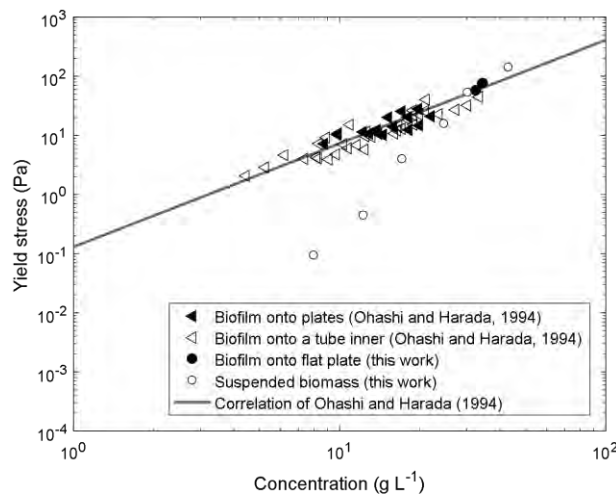


Figure 5.5. Relation between yield stresses and VSS concentration values of the different biofilms and suspended biomass samples. Solid line represents the logarithmic correlation described by Ohashi and Harada (1994), and symbols are the experimental data (triangular symbols are the experimental data determined by Ohashi and Harada (1994) and circle symbols are the experimental data showed in this work).

As can be seen, the yield stress calculated for biofilm and suspended biomass samples of this work at concentration over 15 g VSS L⁻¹ followed the same trend as the described correlation and their experimental data. However, some discrepancies were detected at

lower concentrations, in which smoother transition from solid to liquid regime was observed in this work; this difference may be attributed to: (a) the very different experimental method employed to measure rheological properties (viscosity test using pressure capillary viscometer), and (b) the characterization of the yield stress using the Bingham model by Ohashi and Harada (1994).

Results presented herein showed that the development of a new correlation to establish the yield stress dependent on concentration is supported, since a more accurate characterization of the shear stress limits was performed, considering a low range of shear rates. In addition, the flowing behavior was described with the Herschel–Bulkley model, which takes into account the low to intermediate shear rate (Markis et al., 2014). Although the correlation of the concentration dependency and the parameters of the Herschel–Bulkley model has not been reported in the literature for biofilms, pioneering studies were done in sludges for the power law model parameters (Slatter, 1997), and recently for Herschel–Bulkley model parameters (Markis et al., 2014; Ramin et al., 2014). Thus, the study was extended to analyze the dependency to the concentration of all parameters of the Herschel–Bulkley model, and the yielding viscosity. The yielding viscosity is directly related to yield stress (Expression 5.2), thus its behavior could be also related to samples concentration. In addition, the consistency index parameter (K) is a measure of the consistency of the substance (Chhabra, 2010), giving an idea of the fluid viscosity. Possibly, similar trends depending on samples concentration could be found for yielding viscosity and K . Lastly, the flow behavior index (n) parameter is an indicator of the shear-thinning or shear-thickening nature of the analyzed fluids, i.e. $n < 1$ for shear-thinning, $n > 1$ for shear thickening, and $n = 1$ for Bingham plastic behavior. Then, when smaller is the value of n more shear-thinning or pseudoplastic character has the material (Chhabra, 2010), which could be also associated with samples concentration.

5.3.1.3. New correlations for steady shear flow rheological parameters dependent on concentration

Suspended biomass experimental data assessed under a wide range of concentrations were used to propose new correlations for the steady shear flow rheological parameters as a function of concentration. The estimated parameters values of the Herschel–Bulkley model (summarized in Table 5.1) are represented in Figure 5.6, showing the remarkable dependency between σ_y , K , n and η_y with the concentration. Taking into account the previously determined correlations for Herschel–Bulkley model parameters in sludge rheological studies (Slatter, 1997; Markis et al., 2014; Ramin et al., 2014), a new set of relations for were established to describe accurately the behavior in a wide range of concentrations representative of fixed biofilms. As suggested by Ramin et al. (2014), the new correlations were based on the assumption that the apparent viscosity (Expression 5.2) of the suspended biomass correctly converges to water viscosity (η_w) at very low

concentrations, i.e. if $X \rightarrow 0$ then $\sigma_y \rightarrow 0$, $K \rightarrow \eta_w$, $n \rightarrow 1$ and $\eta_y \rightarrow \eta_w$. Expressions 5.9-5.12 were determined for correlating the yield stress (σ_y), the fluid consistency index (K), the flow behavior index (n) and the yielding viscosity (η_y) with samples VSS concentration (X) respectively.

$$\sigma_y = a \cdot X^b \quad (5.9)$$

$$K = \eta_w \cdot (1 + c \cdot X^d) \quad (5.10)$$

$$n = f^X + g \cdot X^h \quad (5.11)$$

$$\eta_L = \eta_w \cdot (1 + j \cdot X^k) \quad (5.12)$$

With $a=0.00093$ ($\text{kg}^{1-b} \text{m}^{3 \cdot b-1} \text{s}^{-2}$), $b=3.17$ (-), $c=0.73$ ($\text{m}^{3 \cdot d} \text{kg}^{-d}$), $d=2.38$ (-), $f=0.94$ (-), $g=0.09$ ($\text{m}^{3 \cdot h} \text{kg}^{-h}$), $h=0.28$ (-), $j=4512$ ($\text{m}^{3 \cdot k} \text{kg}^{-k}$) and $k=2.7$ (-). All the correlations showed a high precision in the estimations ($R^2 > 0.99$).

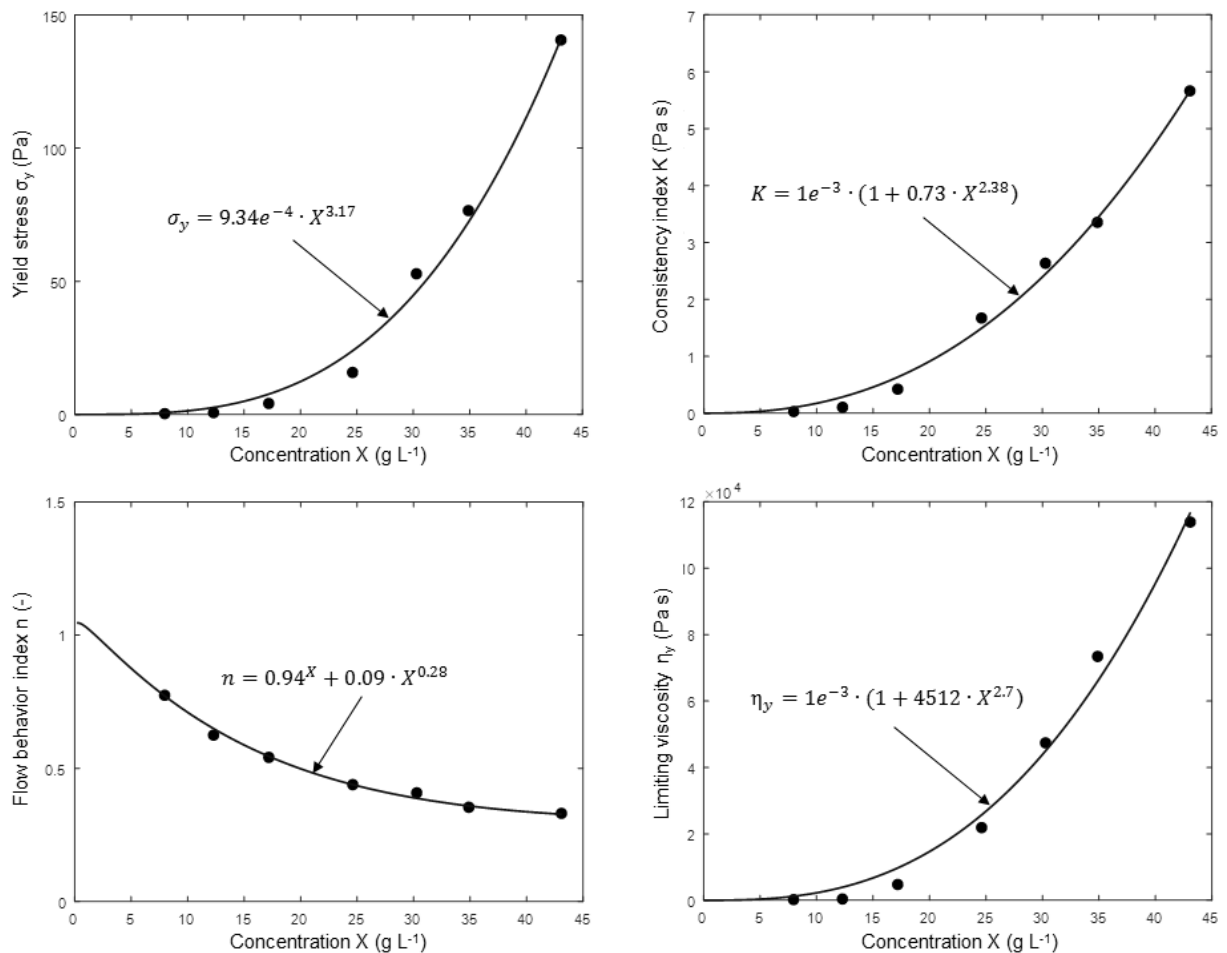


Figure 5.6. Estimated and fitted data of the yield stress (σ_y), the fluid consistency index (K), the flow behavior index (n) and the yielding viscosity (η_y) at different concentration (X). Symbols are estimated experimental data and solid lines represent the correlations fitting.

To verify the defined correlations, a prediction of the rheological parameters for biofilm samples with different densities was performed. The biofilms experimental data aforementioned (BLC and BHC) together with data from Ohashi and Harada (1994) (BOH) were used. Biofilms density, estimated parameters from Expressions 5.9-5.11 and determination coefficient of the predictions are summarized in Table 5.2.

Table 5.2. Estimated parameters in the predictions of flow behavior for biofilms BOH, BLC and BHC.

	BOH prediction	BLC prediction	BHC prediction
X (g VSS L ⁻¹)	13.5	32.6	34.5
σ_y (Pa)	3.562	58.262	69.722
K (Pa s)	0.359	2.917	3.338
n (-)	0.620	0.372	0.360
R ²	0.973	0.992	0.999

Figure 5.7 depicts the comparison of the experimental data with the predicted flow curves. As can be seen, the predictions exhibited an excellent agreement for all the analyzed biofilms at various densities. Low deviations ($R^2 > 0.97$) were obtained for the developed correlations in the behavior predictions, which successfully matched the pseudo-plastic response under steady shear flow. Specifically, the predictions for the biofilms samples examined in this work were very close to those calculated from the direct fit (Table 5.1).

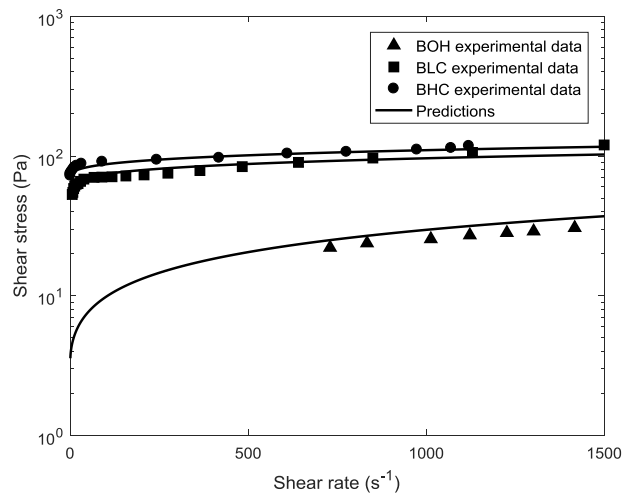


Figure 5.7. Predictions of flow behavior for biofilm samples using the developed correlations and the comparison with the experimental data at various densities (BOH, BLC and BHC). Symbols are experimental data and solid lines represent predictions data.

The good self-consistency between experimental and predicted flow parameters proves the practical applicability of the novel correlations proposed for modeling biofilms as a shear thinning fluids, allowing to change the viscous properties in function of the concentration,

thus considering the spatial variation of mechanical properties in heterogeneous biofilms. The proposed correlations are a new tool to couple biofilm mechanics with flow, e.g. by means of fluid dynamics codes, which opens new doors for optimizing bioreactors design and strategies to control biofilms.

5.3.2. Oscillatory shear flow tests results

In addition to the non-Newtonian behavior, biofilms are also viscoelastic, i.e. materials which behave either as an elastic solid or a viscous fluid depending how fast they are deformed (Fabbri and Stoodley, 2016). Dynamic oscillatory analyses are generally used to examine for testing the short-time viscoelastic response behavior. In this study, dynamic strain-sweep measurements were performed for biofilm and suspended biomass samples, to determine the linear viscoelastic regimen (LVR) and to examine the viscoelastic behavior in large amplitude oscillatory shear (LAOS), interpreting the samples microstructure (Hyun et al., 2002). Dynamic frequency-sweep measurements were conducted to judge the viscoelastic character in the LVR. Finally, the exploration of the microscopic structure was completed through the comparison of the dynamic and steady shear viscosities.

5.3.2.1. Viscoelastic properties of biofilm and suspended biomass samples

Figure 5.8 depicts the strain dependence of G' , G'' and phase angle (δ) of the analyzed biofilms samples at different densities (Figure 5.8A) and biofilm and suspended biomass samples with equivalent VSS concentration (Figure 5.8B). Both biofilm samples (BLC and BHC) exhibited very similar behavior for the studied conditions. Strains of 2% and 3% were determined as the limit of the LVR, being the smallest for the less concentrated biofilm. Considering the changes in δ for both samples from 10° to 75° , BLC was supposed to transform before from solid-like to liquid-like than BHC. In addition, at low strain amplitude values, i.e. within the LVR, the storage and loss moduli were only function of the angular frequency, being characterized by constant rheological properties. The elastic behavior dominated the viscous one ($G' > G''$), showing the gel character of the samples. Relevant works (Mayer et al., 1999; Flemming and Wingender, 2010; Wilking et al., 2011), related to research and describe the complex structures of biofilms and their polymeric compounds, have suggested that biofilms might represent gel-like structures. These authors stated that biofilms consist of microorganisms embedded in a cross-linked polymer hydrogel retaining a huge quantity of water. Also, they claim that the self-produced extracellular polymeric substances (EPS) are responsible for the cohesion of the biofilm through entanglements, hydrogen bonds, dispersion forces and electrostatic interactions. For small deformations, i.e. low strain, these internal forces and interactions would be acting as permanent junction points enhancing elastic character (Klapper et al., 2002), thus biofilm samples were effectively resisting high, short-time disturbances. At strain amplitudes higher than the LVR, the storage modulus and loss modulus were very similar in the LVR for both biofilm samples, while the crossover point $G' = G''$, and the LVR limit occurred at smaller strain amplitude for

BLC sample than for more concentrated sample BHC. In addition, G' decreased drastically, while G'' passed through a peak before decreasing rapidly for both samples. This non-linear viscoelastic behavior is referred as the *Payne effect* (Payne, 1962), which has been observed in filled and cross-linked polymers. More specifically and providing insights into the biofilms microscopic structure, the presence of G'' -peak, i.e. *Payne effect*, presupposes that the samples an internal network structure at rest (Wang, 1999; Mezger, 2006), being in accordance with the hydrogel network description assumed by the authors aforementioned. Thus, the hydrogel network of the biofilms resisted against deformation up to certain critical strain, where G'' increased and the large deformation over the critical deformed the samples irreversibly, occurring the final breakdown and beginning to flow in the crossover point $G' = G''$.

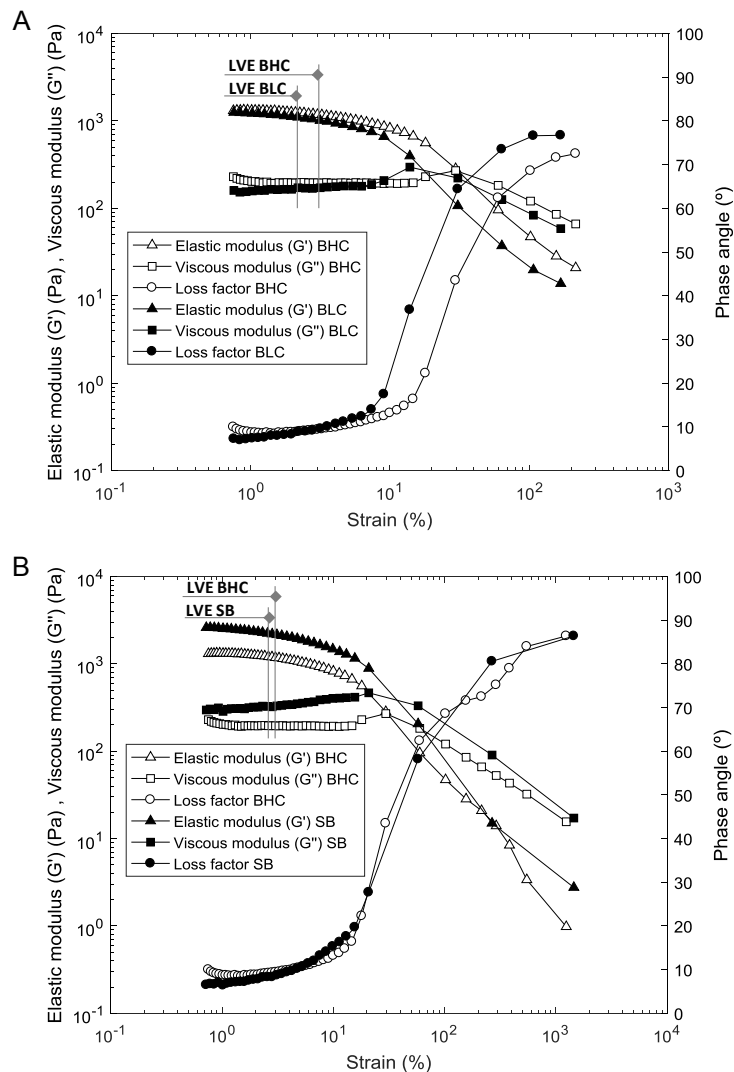


Figure 5.8. Dynamic properties of the storage modulus G' , the loss modulus G'' and the phase angle δ as a function of the applied strain γ for (A) biofilms at various concentrations (BLC and BHC) and (B) biofilm (BHC) and suspended biomass (SB) with equivalent concentration.

Figure 5.8B shows the comparison of the strain dependence of G' and G'' for biofilm BHC and SB samples with equivalent concentration ($34.7 \pm 0.2 \text{ g VSS L}^{-1}$). These samples exhibited quite similar rheological behavior. Both samples showed a gel character ($G' > G''$) in the LVR, very close LVR limit values, and maximums of G'' -curves and crossover points $G' = G''$ at similar strain values. The phase angle changes were produced at practically the same strains, being the transformation from solid-like to liquid-like equal for both samples. However, it was observed that the G' and G'' values were greater for SB than biofilm sample, which indicated the stronger interaction among the SB structure components. For strain values higher than the LVR, another interesting observation is that SB sample showed a progressive increase of viscous modulus G'' , instead of the sudden maximum, i.e. *Payne effect*, observed for biofilms. Both biological samples show the same generic LAOS type III behavior described by Hyun and coworkers (Hyun et al., 2002, 2011). The local maxima are related to the balance between the formation and the destruction of interactions, i.e. network junctions, with the strain amplitude. Nevertheless, the progressive maximum is generated by the higher rate of formation than destruction for lower strain amplitude, resulting in a higher density of network junctions, which indicates a stiffer gel character (Grillet et al., 2012). These differences could be associated to biological alterations, i.e. biofilm maturation, since the stability of the hydrogel network existing in biofilm samples is dominated by weak physicochemical interactions between the EPS components (Flemming and Wingender, 2010). The repulsive forces form a highly extended structure, where the molecules may align and associate due to hydrogen bonding and charges, forming a weakly structured gel-like material similarly to xanthan gum polymer (Ross-Murphy, 1995; Hyun et al., 2011).

Based on results from Figure 5.8, fixed strains of 1% were chosen to perform frequency sweep analysis inside de LVR. Figure 5.9 depicts the frequency dependence of G' , G'' and loss factor ($\tan\delta$) of biofilms with different concentration (BLC and BHC) and suspended biomass (SB) samples. As can be seen in Figure 5.9, The samples exhibited analogous behavior for the studied conditions. Their viscoelastic behavior was patent, being described by both G' and G'' modulus that indicate the solid-like (elastic) and the fluid-like (viscous) character respectively. G' was approximately 10 times larger than G'' , showing a gel-like regime across the analyzed frequency range. Since the loss factor was greater than 0.1, these samples present a structure between a true gel and a concentrated biopolymer (Ross-Murphy, 1995), so they can be characterized as weak gels (Ikeda and Nishinari, 2001). The storage and loss moduli were independent of the frequency in the studied conditions. The storage moduli were approximately 1290 Pa and 2970 Pa whereas the loss moduli were 143 Pa and 287 Pa for biofilms and SB samples respectively. These characteristic plateau values were similar to the results reported for biofilms of *Pseudomonas aeruginosa* (Lieleg et al., 2011), *Pseudomonas aeruginosa FRD1* (Wloka et al., 2005) and *Streptococcus mutans* (Vinogradov et al., 2004). The plateau presence at low frequencies reflects only the chemical

crosslinks in the gel, since the lifetime of physical entanglements is much shorter than the oscillation period (Grillet et al., 2012).

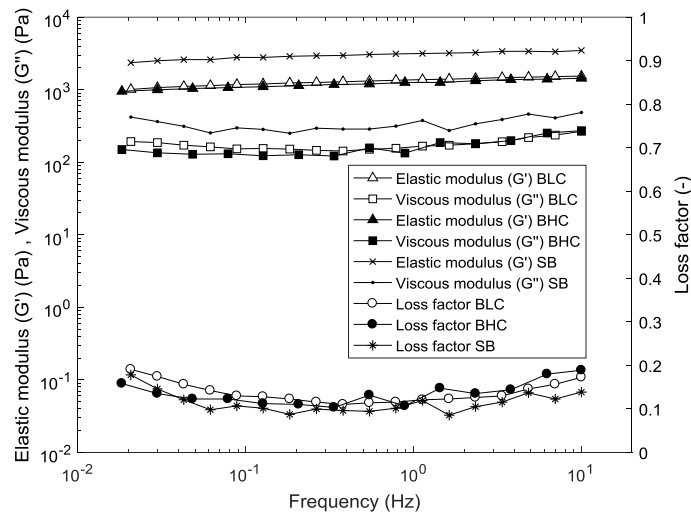


Figure 5.9. Dynamic properties of the storage modulus G' , the loss modulus G'' and the loss factor as a function of the frequency for biofilms (BLC and BHC) and suspended biomass (SB).

Results from oscillatory shear flow tests, together with those previously made under steady shear flow conditions, could prove valuable for using constitutive models to represent the elastoviscoplastic behavior of this biological samples, considering thixotropic character, thus describing the time evolution of stress/viscosity as a function of the shear rate. In this case, the one-dimensional extended version of Herschel-Bulkley model described by Saramito (2009) could be used. The model parameters are the same as those for the Herschel-Bulkley model (Expressions 5.1 and 5.2), with one additional parameter for the elastic modulus (Stickel et al., 2013), which is equal to the storage modulus due to the conditions of the oscillatory analysis performed.

5.3.2.2. Comparison between steady shear and complex viscosity

In the oscillatory shearing mode, the macroscopic mechanical properties determined for both immobilized and suspended biomass samples were consistent between them. However, oscillatory characterization showed inequalities for both samples in the microscopic structure and their viscoelastic properties, observing weaker interactions for the fixed biofilm samples. A comparison between steady and oscillatory shear flow mechanical properties can also provide insights into the microscopic structure. The empirical Cox-Merz rule (Cox and Merz, 1958) states that values of the dynamic or complex viscosity (η^*) and the steady shear viscosity (η) should be identical at a comparable time scale of observation. Figure 5.10 depicts the test of Cox-Merz rule, comparing the results of viscosity curves for steady and dynamic analysis for biofilm and suspended biomass samples, BHC and SB respectively. As can be seen, under the steady shear flow, equivalent shear thinning behavior was observed

along the shear rate applied for both biological samples. Nevertheless, for the results under oscillatory shear flow at a comparable frequency, the η^* values were larger than those of the η , being the greatest the η^* of SB sample. The discrepancy in Cox-Merz rule has been reported in gels and polysaccharides (Ross-Murphy, 1995; Ikeda and Nishinari, 2001). Samples with gel character have another kind of physical interactions and/or chemical interactions (Mezger, 2006). Thus, the large deviations between η and η^* are associated with the presence of binding mechanisms additional to entanglements, such as Coulomb forces, complex formations or hydrogen bonds (Kulicke and Porter, 1980). These junction points are subjected to rupture processes under a steady state flow, but they remain intact in the LVR of the oscillatory analysis (Mayer et al., 1999; Klapper et al., 2002; Wloka et al., 2004), determining the interaction level among the structural components. In the studied conditions, the predominant binding type (chemical or physical) among the biological structure components at higher frequencies could not be estimated since the oscillatory results were not dependent on the timescale (Grillet et al., 2012).

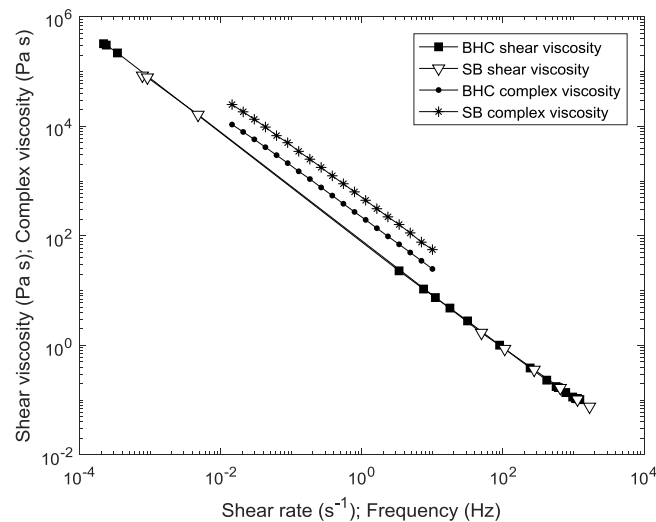


Figure 5.10. Cox–Merz rule test: Comparison of the steady-state shear viscosity $\eta(\dot{\gamma})$ and the magnitude of the complex viscosity $\eta^*(f)$ at equal values of the frequency and shear rate for biofilm and suspended biomass samples (BHC and SB, respectively).

5.3.3. Transient shear flow test results

Transient shear flow measurements, i.e. creep and recovery test, are used for studying material viscoelastic response over long-time scales. Thus, transient tests were performed to prove the time-dependent nature of biofilm BHC and suspended biomass SB samples with equivalent concentration ($34.7 \pm 0.2 \text{ g VSS L}^{-1}$), and to discriminate between the elastic and viscous responses in the LVR. In this case, these measurements were mainly performed to analyze the microscopic structure of both samples. From the results of the oscillatory analysis, three different values of shear stress were selected inside the LVR (3, 12 and 40 Pa) to thoroughly describe the strain response of biological samples.

5.3.3.1. Creep and recovery characteristics

Figure 5.11 shows the creep and recovery curves for both tested samples at the various shear stress (σ), describing the time-dependent deformation behavior during the load (from $t=0$ to $t=180$ seconds) and the relaxation (from $t=181$ to $t=360$ seconds) phases. This time-dependent strain response undoubtedly pointed out that the BHC and SB samples presented viscoelastic fluid behavior, showing a reversible elastic strain and an irreversible viscous portion. This supports the findings of previous works over different types of biofilms, using rheometry (Towler et al., 2003; Vinogradov et al., 2004; Jones et al., 2011) and other experiments made through non-conventional testing (Stoodley et al., 1999a).

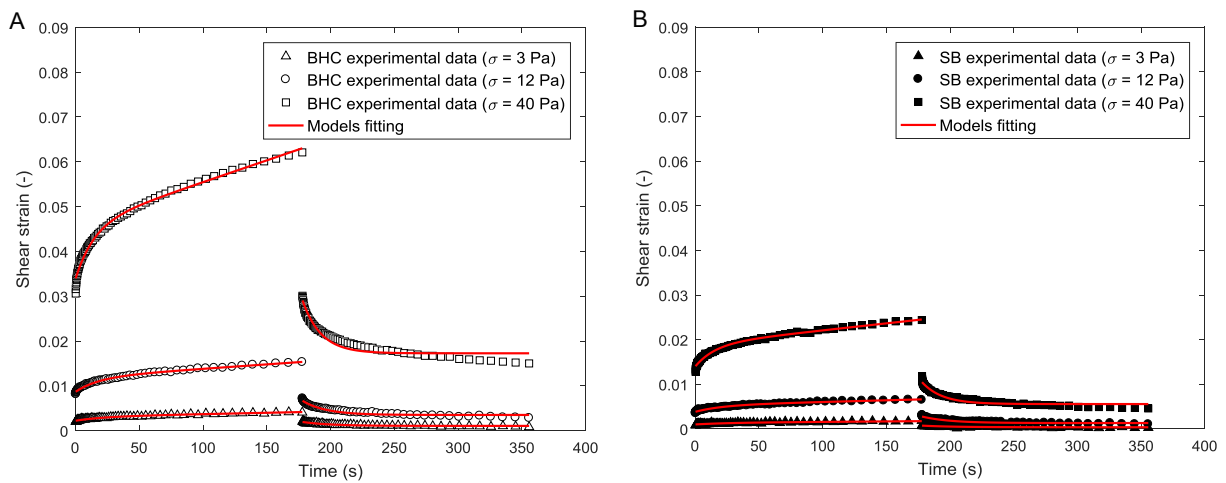


Figure 5.11. Creep and recovery of BHC and SB samples (A and B respectively) at different shear stress (3, 12 and 40 Pa) applied for 180 seconds and then removed. Symbols are experimental data and solid lines represent Burger model fitting.

The creep and recovery curves were modeled with the four element Burger model (Expressions 5.3 and 5.4). The curves modeled by the Burger model correlated well to the experimental data, as can be seen in Figure 5.11. The values of the fitted parameters (G_1 , η_1 , G_2 and η_2), the relaxation times and the NRMSEs are summarized in Table 5.3.

Table 5.3. Optimized parameters for the elastic (G) and viscous (η) elements in the Burger model and relaxation times for biofilm and suspended biomass samples tested at different shear stress (3, 12 and 40 Pa).

Sample	σ	G_1 (Pa)	η_1 (Pa s)	G_2 (Pa)	η_2 (Pa s)	λ (s)	NRMSE
BHC	3	1360.10	503616.23	3383.05	74370.01	370.28	0.0607
	12	1387.89	609170.81	3763.10	69068.35	438.92	0.0357
	40	1383.23	411997.35	3345.76	48695.71	297.85	0.0357
	Mean	1377.07	508261.46	3497.30	64044.69	369.02	0.0440
SB	3	2984	1414602.52	8267.43	213129.09	474.06	0.0975
	12	3132.02	1613364.10	8173.77	174480.47	515.12	0.0484
	40	2859.99	1275834.60	8058.16	127039.45	446.10	0.0369
	Mean	2992	1434600.41	8166.45	171549.67	478.43	0.0609

As can be seen in Figure 5.11, BHC and SB samples behavior for the same shear stress showed remarkable dissimilarities during the creep and recovery test. Biofilm sample exhibited higher strain than SB sample for all tested shear stress, presenting the softest gel character (Grillet et al., 2012). This behavior is also observed in the G_1 , η_1 , G_2 and η_2 parameters (Table 5.3). For the biofilm sample at $\sigma = 40$ Pa, the parameters of Burger model were the lowest of all values, explaining why its deformation was much greater than in the rest of tests samples (Dolz et al., 2008). Moreover, the parameters values of SB sample for the same shear stress exceed the values of biofilm sample, determining that the suspended biomass had the greatest opposition to deformation. These results indicated that the internal structure and the mechanical properties of biofilm are controlled by the hydrogel network components (Wilking et al., 2011), which contributed to rearrangement of biofilm to mitigate the external shear stress by means of deformation, highlighting the elastic response of the network (Flemming and Wingender, 2010). In addition, comparing these results with those from the dynamic analysis (section 5.3.2.1) as proposed by Dolz et al. (2008) and Giboreau et al. (1994), the elastic elements of Maxwell model (G_1) were in accordance with the elastic moduli determined during the oscillatory analysis ($G' = 1290$ Pa and $G' = 2970$ Pa for BHC and SB respectively), being also G_1 higher for the SB sample.

Regarding the characterization of the recovery behavior, three compliance values (J_∞ : Maxwell dashpot, J_{SM} : Maxwell spring, J_{KV} : Kelvin-Voigt element) were determined from data results of Figure 5.11, and by using Expressions 5.5 and 5.6. Then, the contribution of each element in the total deformation of the system and the percentage recovery of the entire system were calculated with respect to J_{MAX} , using expressions 5.7 and 5.8 respectively. Values of these parameters and recovery percentage are summarized in Table 5.4. The contributions to deformation of the J_{SM} and the J_{KV} were similar in biofilm and SB samples, whereas the percentage contributions of J_∞ were reduced in the suspended biomass, with fewer differences among them. This reflected more homogeneous structure in SB than biofilm samples, being in a good agreement with the biofilm heterogeneity described by others authors (Towler et al., 2003; Wilking et al., 2011). Higher contribution of the Maxwell dashpot (J_∞) in biofilm sample coincides with the presence of hydrogel network. Possibly, as the bonding is weak, the biofilm deforms more irreversibly on the time scale, depending also on the lower bonding density (Klapper et al., 2002). In addition, the more homogeneous structures of SB than biofilm sample was confirmed by the similar recovery percentages values obtained from the three tests.

Table 5.4. Maximum compliance value (J_{MAX}), percentage participation of each compliance element (J_{∞} , J_{SM} , J_{KV}) of the Burger model in the maximum compliance, and recovery percentage (%R) for biofilm BHC and suspended biomass SB samples at different shear stresses.

σ	BHC					SB				
	J_{MAX} (Pa^{-1})	J_{∞} (%)	J_{SM} (%)	J_{KV} (%)	%R	J_{MAX} (Pa^{-1})	J_{∞} (%)	J_{SM} (%)	J_{KV} (%)	%R
3	0.00135	23.26	40.00	36.74	76.74	0.000568	14.17	46.30	39.52	85.83
12	0.00128	18.36	45.55	36.09	81.64	0.000543	16.21	47.15	36.65	83.79
40	0.00155	24.19	44.58	31.23	75.81	0.00061	18.85	46.72	34.43	81.15

5.3.3.2. Relaxation times

Related to the relaxation time ($\lambda = \eta_1/G_1$), it was found that the fitted parameters G_1 and η_1 for both samples followed the tendency of the correlation described by Shaw et al. (2004). These authors compared the experimental creep data of a wide variety of biofilms and reported a range of relaxation time values for all the studied biofilms. The mean relaxation times calculated for biofilm and SB samples (Table 5.3) were within the reported range and, specifically, were in a good agreement with the experimental data of the biofilms grown from pond water inoculum (Towler et al., 2003). This viscoelastic property can be related to the structure and composition of the samples, associating the rearrangement of the sample upon an induced deformation. A polymer gel with more junctions will relax more slowly because of the higher presence of constrained at the crosslinks (Grillet et al., 2012). In addition, Peterson et al. (2014) observed the reestablishment of bacterial and EPS, showing the EPS samples faster relaxation processes. The stated above is in accordance with the relaxation time for BHC and SB samples, where the biofilm sample had lower relaxation time than SB samples. Therefore, the binding points existing prior to the deformation in both samples, were more quickly re-established along the hydrogel network, which EPS components can help to the ready rearrangement (Peterson et al., 2015).

Thence, the characterization under transient shear flow also showed differences between the behavior of biofilm and SB, suggesting the significant role of the hydrogel network formed during biofilm maturation, when they are subjected to higher shear stress inside LVR (2 to 50 Pa). In such conditions, a direct characterization of the biofilm sample should be performed in order to describe correctly its behavior.

5.4. CONCLUSIONS

Biofilm and suspended biomass were extensively characterized in rheological terms under steady shear, oscillatory and transient shear flow conditions, which has not been previously reported in other studies. A significant amount of rheological measurements are available from biofilms developed on fixed substrates, providing information about their mechanical

properties. However, no studies have been reported on comprehensive rheological measurements on heterotrophic biofilms providing knowledge about the effect of diverse shear flow properties on the same biological system, allowing to know its response under a wide range of shear stresses, i.e. from repose, passing by stretching and finally detachment. The study of the biological samples under different shear flows allowed the examination of macroscopic mechanical properties as well as providing insights into the microscopic structure, which was necessary to properly understand the behavior of the biological samples when an external stress is applied over them.

The reported rheological measurements confirmed the non-Newtonian and gel-like character of fixed and suspended biomass samples. The macroscopic mechanical properties (i.e. yield stress, elastic modulus, relaxation time, etc.) of both samples were stated, clarifying the interaction of the biological system with the flow field. Equivalent rheological properties were found for both samples under steady flows, whereas dissimilarities in the properties and structural characteristics were observed under oscillatory and transient flows, identifying the weaker network junctions in the biofilm structure. During samples deformation under non-steady flows, the important role of the hydrogel network present in biofilms on the internal binding mechanisms was also detected. These findings imply that the suspended biomass just can be used for the characterization of the biofilms viscosity and flow curves, due to its practicality for the samples extraction with low invasion.

Pseudo-plastic and viscoelastic responses under steady-state and transient shear flows were satisfactorily described through Herschel-Bulkley and Burger models respectively for both biological samples. The characterization as a pseudo-plastic fluid was also evaluated in a wide range of concentrations, quantifying the strong dependency of the rheological parameters to the biomass concentration. This work demonstrated that the defined correlations for the rheological parameters of the Herschel-Bulkley model can predict biofilms behavior rigorously.

The proposed models can be used to develop fluid-structure interaction models of biosystems. Specifically, the non-Newtonian models can be readily implemented into fluid dynamics codes for a more realistic description of bioreactors performance, aiding to include biofilm physical characteristics. Then, growth, deformation and detachment of biofilms dependent on the operating conditions can be predicted, which plays an important role in terms of mass transfer and transport, and over the bioreactors operation.

Results obtained in this chapter also provide complementary information to the research related to viscous and viscoelastic properties characterization of fixed and suspended biomasses, establishing relations between the responses of both biological samples. This work could also help in the development of measurement protocols for the rheological analysis in biofilms.



MULTIPHASE CFD MODELING OF FIXED-BED BIOFILMS BIOCHEMICAL PHENOMENA AND MECHANICAL BEHAVIOR UNDER LAMINAR FLOW CONDITIONS

In this chapter, the methodology developed in Chapter 4 was applied and extended for the implementation of multiphase bioreactors models using CFD codes. In addition, the experimental data which characterize the biological system as a non-Newtonian fluid in Chapter 5 were used to define the biofilm into the CFD code. In this case, the study was mainly focused in the implementation of multiple phenomena (transport and transfer of dissolved oxygen, and biofilm growth, deformation, and detachment) in two-phase CFD models, besides examining the performance of this novel model for reproducing biosystems behavior. Models performance was verified for transport mechanisms of dissolved oxygen under laminar conditions. Similarly, model capabilities to mimic biosystems performance were tested under different scenarios where hydrodynamic could have an effect on biofilm (e.g. considering growth kinetic and external shear stresses which could deform or detach the biofilm).

Abstract

Mechanical properties consideration in biofilm modeling is a new research path which might help in the design of new strategies for biofilms control. In this chapter, a novel approach for biosystems modeling using CFD codes was described, defining the biofilm as a non-Newtonian fluid with experimentally measured rheological data. The aim of this chapter was to investigate the capabilities and limitations of this new approach for reproducing the biofilm growth, and the biofilm-flow interaction in various laminar flow conditions and biosystems geometries where the biofilm was attached to flat and curved walls. Multiphase models (liquid-biofilm) were developed and solved using the volume of fluid (VOF) method, tracking accurately the interfacial area, and coupling hydrodynamics with transfer mechanisms, biofilm growth, deformation or detachment. The model was verified under different operating conditions considering fluid dynamics and mass transport and transfer. The model predicted growth patterns consistent with heterogeneous distributions of substrate. In addition, shear-induced deformation and detachment in biofilms were reproduced, being in qualitative agreement with experimental observations. The effectiveness of biofilm backwash was also studied using the CFD model. Stretching, recoil and ultimate detachment phenomena in biofilms were demonstrated in diverse simulations.

A modified version of this chapter is being prepared for publication as:

L. Prades, R. Arnau, A.D. Dorado, S. Chiva, X. Gamisans, 2018. **Multiphase CFD modeling of biochemical phenomena and biofilm mechanical behavior in fixed-bed reactors.**

6.1. INTRODUCTION

Considering biofilm mechanics properties instead of modeling rigid biofilm structures is an emerging research field, which has opened new doors describing biological systems that can grow, produce, deform and/or even detach (Horn and Lackner, 2014). Several experimental analyses have been performed to study biofilm mechanical properties, explaining the way in which the biofilm matrix behaves as the shear stress increases and it brings closer to yield stress (Böl et al., 2012; Fabbri and Stoodley, 2016). These characterizations can be classified in two categories based on biofilm matrix representation (Rittman and Laspidou, 2003): 1) viewing the biofilm matrix as a viscoelastic structure; 2) or as a non-Newtonian fluid. For the first approach, experimental analysis has been widely performed for characterizing parameters (e.g. Young's modulus, shear modulus) and models have been implemented using fluid-structure interactions approaches (Towler et al., 2007; Böl et al., 2009; Taherzadeh et al., 2010), focusing mainly in the simulation of biofilm deformation or motion induced by the liquid flow (Mattei et al., 2017). However, little attention has been paid to the second approach, finding few works in the literature related to the characterization of biofilms as non-Newtonian fluids. The main reference is the pioneering analysis performed by Ohashi and Harada (1994), where the biofilm was described as a Bingham fluid. Recently, rheological studies (Chapter 5) in heterotrophic biofilms have shown the important role of the biofilms hydrogel matrix to mitigate external shear stress, exhibiting biofilms shear-thinning character with yield stress. This non-Newtonian behavior is strongly dependent on the biomass density, allowing to define correlations for describing it. Therefore, contemplating the biofilm as a non-Newtonian fluid coupled with fluid dynamics is a novel approach to model bioreactors performance, which permit to combine the biochemical aspects (substrate transport/consumption and biomass growth/distribution) with mechanical characteristics and biofilm behavior (deformation and detachment).

Several biofilm constitutive models have been developed using discrete and continuum approaches over the last decades. For comprehensive reviews, see Horn and Lackner (2014), Fabbri and Stoodley (2016), and Mattei et al. (2017), and references therein. In biosystems modeling, the consideration of the biofilm as a non-Newtonian fluid is classified inside the continuum approach (Böl et al., 2012; Storck et al., 2014). Focusing on that continuum models, some researchers have used the phase-field approach to understand the combined motion of the laminar flow and the biofilm (Zhang et al., 2008; Tierra et al., 2015). With this approach it has been possible to simulate deformations, detachment and rippling phenomena in a mesoscale biofilm system, considering constant viscosity values for the biofilm matrix components. An approach for modeling this biofilm performance on a larger scale can be the use of CFD techniques. CFD has been increasingly used in the wastewater treatment (WWT) field for modeling bioreactors performance at pilot and full scales (Samstag et al., 2016). This approach is capable of incorporating non-Newtonian fluids, multiphase systems and biokinetics (Le Moullec et al., 2010; Craig et al., 2013; Ramin et al., 2014;

Prades et al., 2017; Climent et al., 2018), being the bioreaction behavior generally associated to the liquid phase dynamics. Nevertheless, the hydrodynamic effect of the liquid phase over biofilm dynamics (i.e. mass transfer, bioreaction) and mechanics (i.e. deformation, detachment) have not been described using this type of techniques for fixed biofilm reactors. Thus, the potential of CFD techniques as an alternative approach to incorporate a realistic representation of biofilm mechanical properties as a non-Newtonian fluid and its coupling with fluid dynamics should be explored.

Taking into account the stated above, the aim of this chapter is to use CFD techniques to model fixed-bed biosystems behavior, considering biofilm and liquid phase as independent phases, i.e. defining an interface between them, and considering several phenomena simultaneously. For this purpose, multiphase models (liquid-biofilm) were developed using the volume of fluid (VOF) method, tracking accurately the interfacial area. For the implementation of the biochemical part (substrate transport/consumption and biomass growth/distribution), the experimental data of biokinetics and mass transfer of the species were required, helping also to validate the simulated results for the biosystem performance. For the implementation of the mechanical properties (i.e. biofilm as a non-Newtonian fluid), the correlations described for the rheological parameters in Chapter 5 were used. The developed 3D CFD model was used to study the influence of hydrodynamics over mass transport, studying the effect of liquid velocity fields on the transport rate of substrate. In addition, the biosystem performance was predicted including the biofilm growth, and studying how the changes in transfer and transport phenomena and fluid dynamics affect over the biofilm growth. Finally, this novel approach was tested on a non-flat biofilm (i.e. a curved channel) to examine the model potential to reproduce stretching, recoil and detachment phenomena in biofilms.

6.2. MATERIALS AND METHODS

A detailed characterization of the experimental set-up used in this chapter was developed in previous works of our research group (Guimerà et al., 2015, 2016; Guimerà, 2016; Chapter 4 (Prades et al., 2017); and Chapter 5).

6.2.1. Bioreactor operation and dissolved oxygen (DO) microprofiles recording

Microprofiles measurements were conducted through an aerobic heterotrophic biofilm grown on a flat plate bioreactor (FPB). Further details about the bioreactor operation and the procedure for dissolved oxygen profiles recording with Clark-type microsensor can be found in Chapter 4 (Prades et al., 2017) and Guimerà (2016). In this case, the effect of external velocity fields on the transport rate of substrates to the liquid-biofilm interface was studied by measuring dissolved oxygen DO profiles in changing flow conditions. The flow rate was adjusted before each experiment using a calibrated peristaltic pump. Experimental data were recorded in less than one hour, in order to avoid the biofilm dynamic effect on the profile. The

DO profiles were recorded at the same position along the FPB, i.e. 5.5 cm from the bioreactor inlet, under different liquid phase velocities (from 5 to 20 m h⁻¹, i.e. typical operating conditions in biofilters and biotrickling filters), and during substrate consumption conditions.

The biofilm density in the region where the profiles were recorded was quantified measuring the volatile suspended solids (VSS) concentration following standard methods (APHA, 1998).

6.2.2. Biofilm modeling: biological kinetics and rheological parameters

In order to correctly reproduce biofilm behavior inside the biosystem, the characterization of bacterial growth and consumption rates was performed. In this case, for simplification, the biofilm system under consideration was a mono-species biofilm with one limiting dissolved component, i.e. dissolved oxygen (DO). The biological reaction rate for the DO was given by Expressions 4.7 in Chapter 4. DO was related to microbial growth as described in Expression 6.1.

$$\frac{dX}{dt} = \mu_{\max} \cdot \frac{C_{BDO}}{K_{S,DO} + C_{BDO}} \cdot X + k_d \cdot X \quad (6.1)$$

Where X is the biomass concentration (kg m⁻³); t is the time (s); μ_{\max} is the maximum specific growth rate (s⁻¹); C_{BDO} is the DO concentration in the biofilm phase (kg m⁻³); $K_{S,DO}$ is the Monod half-saturation coefficient for DO (kg m⁻³); and k_d is the maintenance factor (s⁻¹).

Regarding the kinetics parameters characterization from experimental DO profiles, see details in section 4.4.1.1 (Chapter 4) about the evaluation of the profiles and the estimation of the biological kinetics parameters. The estimated parameters are summarized in Table 6.1.

Finally, the rheological characterization performed in Chapter 5 was used to describe the heterotrophic biofilm as a non-Newtonian fluid. The rheological parameters of the Herschel-Bulkley model (Expressions 5.1 and 5.2, Chapter 5) were predicted by means of the proposed correlations dependent on biofilm density (Expressions 5.9-5.12, Chapter 5). The values of these parameters, i.e. yield stress (σ_y), the fluid consistency index (K), the flow behavior index (n), and the yielding viscosity (η_y) are showed in Table 6.1.

Table 6.1. Parameters for the CFD model of two-phase biosystem (liquid-biofilm).

Parameter	Symbol	Value	Units	Source
Hydrodynamics parameters				
Water density (20 °C)	ρ_w	998.2	kg m ⁻³	Perry and Green (1997)
Water dynamic viscosity (20 °C)	η_w	10 ⁻³	Pa s ⁻¹	Perry and Green, (1997)
Water inlet velocity (flat plate)	v_{in}	0.0014, 0.0028, 0.0042, 0.0056, 0.0069	m s ⁻¹	Operating conditions
Water inlet velocity (non-flate plate)	$v_{in,2}$	0.005, 0.1, 0.2	m s ⁻¹	Chosen
Biofilm density	ρ_B	ρ_w	kg m ⁻³	Equal to water (Zhang et al., 2008; Tierra et al., 2015)
Rheological parameters for biofilm phase implementation				
Shear stress	σ_y	18.65	Pa	Experimentally determined (Chapter 5)
Fluid consistency index	K	1.24	Pa s	Experimentally determined (Chapter 5)
Flow behavior index	n	0.46	-	Experimentally determined (Chapter 5)
Yielding viscosity	η_y	20881.62	Pa s	Experimentally determined (Chapter 5)
Dissolved components and mass transfer				
Inlet DO concentration value	C_{LDO}	6.1-6.8·10 ⁻³	kg m ⁻³	Experimentally determined (this work)
Diffusion for DO in liquid phase	D_{LDO}	1.88·10 ⁻⁹	m ² s ⁻¹	Perry and Green (1997)
Diffusion for DO in biofilm phase	D_{BDO}	Expression 4.1	m ² s ⁻¹	Guimerà et al. (2016)
Mass transfer coefficient	k_L	Expression 6.5	m s ⁻¹	Guimerà et al. (2016)
Microbial growth and substrate consumption rate				
Maximum specific growth rate	μ_{max}	1.39·10 ⁻⁶	kg DO kg VSS ⁻¹ s ⁻¹	Experimentally determined (this work)
Monod half-saturation coefficient for DO	K_S	5.29·10 ⁻⁴	kg DO m ⁻³	Experimentally determined (this work)
Maintenance factor for DO	k_d	2.29·10 ⁻⁸	kg DO kg VSS ⁻¹ s ⁻¹	Experimentally determined (this work)
Maximum biomass concentration in biofilm	$X_{b,max}$	22.78	kg VSS m ⁻³	Experimentally determined (this work)

6.2.3. Mass transfer model (liquid-biofilm)

In hydrodynamics the mass transfer coefficient can be determined by the Sherwood number (Sh) as a function of the Reynolds number (Re) and the Schmidt number (Sc) (Expressions 6.2-6.4) (Horn and Lackner, 2014):

$$Sh = \frac{k_L \cdot L}{D} \quad (.) \quad ; \quad Sh = f(Re, Sc) \quad \text{ith} \quad Re = \frac{U \cdot L \cdot \rho}{\eta} \quad (.3) \quad \text{and} \quad Sc = \frac{\eta}{\rho \cdot D} \quad (.)$$

Where k_L is the mass transfer coefficient (m s^{-1}), D is the diffusion coefficient ($\text{m}^2 \text{s}^{-1}$), L is the characteristic length (m), U is the flow velocity (m s^{-1}), η and ρ are the dynamic viscosity (Pa s) the density (kg m^{-3}) of the fluid, i.e. water in this case, respectively.

Numerous works have defined the Sherwood number in several biofilm systems and under different conditions (Horn and Lackner, 2014). However, only a few of these authors focused their studies on flat plate biofilm reactors (Zhang and Bishop, 1994; Picioreanu et al., 2000a; Guimerà et al., 2016) and biofilm tube reactors (Horn and Hempel, 1995; Wäsche et al., 2002). When describing the correlations, some of these authors contemplated the biofilm surface structure (Picioreanu et al., 2000a; Wäsche et al., 2002), or the external mass transfer was characterized dynamically including all mass transfer mechanisms (Guimerà et al., 2016).

To properly reproduce mass transfer between the phases, Expression 6.5 (Guimerà et al., 2016) was implemented into the CFD code in order to characterize mass transfer of oxygen between liquid and biofilm phases, since the operating conditions selected in that study were equivalent to which set up in this work.

$$Sh = 0.239 \cdot Re^{0.8} \cdot Sc^{0.33} \quad (6.5)$$

It should be noted that in this study the characteristic length (L) for hydrodynamics was the average height of the flow channel. Thus, the length used in both Sh and in Re numbers is the average of the measured thickness for the liquid layer ($L \approx 1000 \mu\text{m}$). The physical properties of the fluid (water) used in these dimensionless numbers are detailed in Table 6.1.

6.3. MODELS DEVELOPMENT

6.3.1. Two-phase CFD models

CFD models were implemented and simulated using ANSYS® Academic Research, Release 17.2 software. Initially, both ANSYS CFD codes, i.e. CFX and Fluent, were tested in parallel to know which was the most suitable to reproduce the two-phase cases modeled in this chapter. Due to some limitations in mass transfer description presented by CFX code, the possibility to implement volume of fluid (VOF) models in Fluent, and the better convergences found in Fluent for cases with low velocities, this software was chosen as the adequate CFD code to model the two-phase cases.

Multiphase models were used to describe the biological system performance. Specifically, the biosystem was defined by a single multifluid domain, including two different liquids inside it: the liquid phase and the biofilm phase. The biofilm was characterized as a Herschel-Bulkley fluid (see section 6.3.2), a non-Newtonian class of fluid which only exhibit viscous flow when strained beyond its elastic limit. This assumption was based on the experimental results of Chapter 5. The liquid phase was circulating from the inlet to the outlet of the domain, passing over the biofilm phase. The liquid phase was composed of water, which transports dissolved oxygen (DO) when mass transfer mechanisms were considered.

6.3.1.1. Volume of fluid (VOF) approach

The VOF approach (Hirt and Nichols, 1981) can model two or more immiscible phases by solving a single set of momentum equations and tracking the volume fraction (α) of each phase throughout the computational domain. The VOF approach is based on the fact that two or more fluids (or phases) are not interpenetrating. For each additional phase considered in the model, a new variable is introduced, i.e. the α of the phase in the computational cell. The α of each of the fluids in each control volume (or computational cell) is computed throughout the domain. In each control volume, the volume fractions of all phases sum to unity. Considering a two-phase model (p_1 and p_2), being the primary and the secondary phases respectively, if the fluid's volume fraction in the cell is denoted as α_{pi} , being i the index referring to phases, then the following three conditions are possible (see Figure 6.1):

- $\alpha_{pi} = 0$: the cell is empty of the i fluid
- $\alpha_{pi} = 1$: the cell is full of the i fluid
- $0 < \alpha_{pi} < 1$: the cell contains the interface between the p_1 and p_2 fluids.

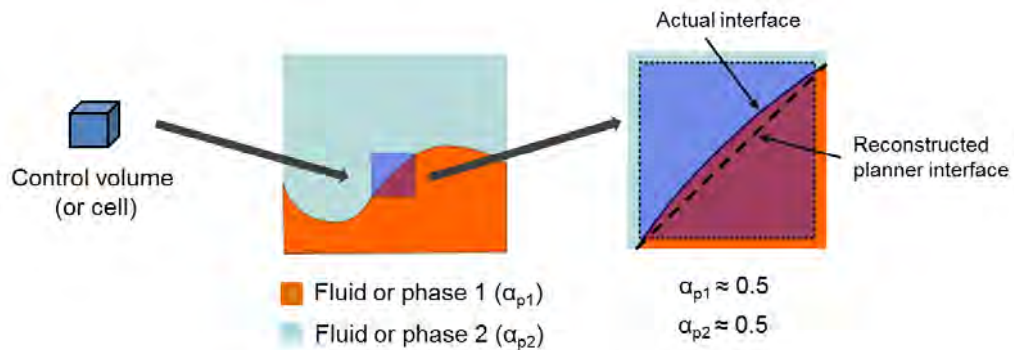


Figure 6.1. Interface tracking based on VOF approach (adapted from ANSYS Inc, (2016)).

The fields for all variables and properties are shared by the phases and represent volume-averaged values, as long as the volume fraction of each of the phases is known at each location. As can be seen in Figure 6.1, the VOF model also approximate and reconstruct the interface based on the local value of alpha. Thus the variables and properties in any given

cell can be representative of one of the phases, or representative of a mixture of the phases, depending upon the volume fraction values (ANSYS Inc, 2016).

Various techniques have been proposed to properly interpolate the data near the interface, being classified in two categories: donor-acceptor formulation and line techniques (geometrical reconstruction). Briefly, the donor-acceptor formulation uses the information about the volume fraction downstream as well as the upstream of a cell in order to establish a crude interface shape, whereas in the line techniques the interface is represented using a piecewise-linear approach aligned with the grid. Further details about these techniques can be found elsewhere (Yeoh and Tu, 2010).

In ANSYS Fluent the geometrical reconstruction scheme is the most accurate, being applicable for general unstructured meshes. This scheme uses the piecewise linear interface construction (PLIC) method proposed by Youngs (1982) to reconstruct the interface, assuming that the interface between the two fluids has a linear slope within each cell, and using such linear shape to calculate the fluid advection through the cell faces (see Figure 6.1). Thus, three steps are required in this method to achieve the geometrical reconstruction: 1) the position of the linear interface relative to the center of each partially-filled cell is calculated based on information about the volume fraction in the cell; 2) the transported amount of fluid through each face is computed, using the computed linear interface representation and the normal and tangential velocity distribution on the face; and 3) the volume fraction in each cell is calculated using the balance of fluxes of the previous step (ANSYS Inc, 2016).

1. Governing equations

The governing equations of mass continuity and momentum are used to describe fluid patterns in the biosystems considered in this chapter.

The solution of the continuity equation for the volume fraction of one (or more) of the phases is used for tracking of the interface(s) between the phases. For the secondary phase (p_2), this equation can be defined as Expression 6.6.

$$\frac{1}{\rho_{p_2}} \left[\frac{\partial}{\partial t} (\alpha_{p_2} \rho_{p_2}) + \nabla \cdot (\alpha_{p_2} \rho_p \overline{U_{p_2}}) \right] = S_{\alpha_{p_2}} \quad (6.6)$$

Where ρ_{p_2} is the density of the phase p_2 , t is the time, U_{p_2} is the velocity in the phase p_2 , and $S_{\alpha_{p_2}}$ is the mass source term for the phase p_2 .

Expression 6.6 is not solved for the primary phase; the primary-phase volume fraction is computed based on the following constraint (Expression 6.7):

$$\sum_{p_1=1}^n \alpha_{p_1} = 1 \quad (6.7)$$

In this case the volume fraction expression is solved through explicit time formulation. Further details can be found in ANSYS Fluent theory guide (ANSYS Inc, 2016).

The properties appearing in the transport equations are determined by the presence of the component phases in each control volume. For instance, in a two-phase system, a mixture of the phases exists when the cell is not fully occupied by the primary phase (p_1) or the secondary phase (p_2). Thus, the density of the mixture is given as the volume-fraction-averaged density and it takes the form of Expression 6.8:

$$\rho = \alpha_{p_2} \rho_{p_2} + (1 - \alpha_{p_2}) \rho_{p_1} \quad (6.8)$$

All other properties are computed in this manner. Thus the dynamic viscosity of the mixture is given by Expression 6.9.

$$\eta = \alpha_{p_2} \eta_{p_2} + (1 - \alpha_{p_2}) \eta_{p_1} \quad (6.9)$$

Regarding the momentum equation, defined by Expression 6.10, it is dependent on the volume fractions of all phases through the properties ρ and η (Expression 6.8 and 6.9 respectively). A single momentum equation is solved throughout the computational domain, and the resulting velocity field is shared among the phases.

$$\frac{\partial}{\partial t}(\rho \vec{U}) + \nabla \cdot (\rho \vec{U} \vec{U}) = -\nabla P + \nabla \cdot [\eta(\nabla \vec{U} + \nabla \vec{U}^T)] + \rho \vec{g} + \vec{F}_{ST} \quad (6.10)$$

Where P is the pressure, g is the acceleration of gravity and F_{ST} is the surface tension force. The F_{ST} is included to consider the effect of surface tension along the interface between the two phases and it is described by the continuum surface force (CSF) model (ANSYS Inc, 2016).

More details about the VOF model in ANSYS Fluent can be found in ANSYS Inc (2016).

6.3.1.2. Assumptions

The general assumptions of the models, based on similar biological systems models reported in the literature (Eberl et al., 2004; Prades et al., 2017), are the following:

1. Liquid and biofilm are defined as two separate phases, which are connected by an interface.
2. The liquid phase is defined by the absence of biomass.
3. The biofilm is implemented as a non-Newtonian fluid (see Chapter 5), in which density is equal to water.
4. The biomass concentration is assumed to be constant throughout the biofilm.
5. In the liquid region, the dissolved substrate (DO) is transported by advection and diffusion. In the biofilm, only diffusive transport is taken into account.
6. Degradation within the biofilm is described by a Monod-type kinetics expression (see Chapter 4).

7. The concentration of dissolved oxygen in the liquid phase at bioreactor inlet is kept constant at saturation conditions (see Table 6.1 for details in concentration values).
8. Flow fields are computed in the liquid phase, i.e. advective transport is considered.

6.3.1.3. Parameters of the computational models

Three different computational domains were used in this chapter. First, the same 3D domain as described in Chapter 4 (Figure 4.1A) for the flat plate was used. Adopting this domain, named D0 domain, mass transport and transfer of dissolved substrate in a two-phase model were simulated. After validating the model, new domains were developed to test the full capabilities of the implemented two-phase model. Secondly, due to the model complexity and in order to save computational resources, a smaller 3D domain for the flat plate (Figure 6.2A) was defined (named D1 domain), to implement biofilm growth kinetics and reproduce the biosystem behavior with another two-phase model. The D1 domain became inspired by the one used in the benchmark problem 2 as described by the IWA biofilm modeling group (Eberl et al., 2004). Thirdly, as depicted in Figure 6.2B, a 2D domain for a curved channel was defined (D2 domain), mimicking carriers or a packed bed, in order to reproduce biofilm deformation and detachment using a new two-phase model.

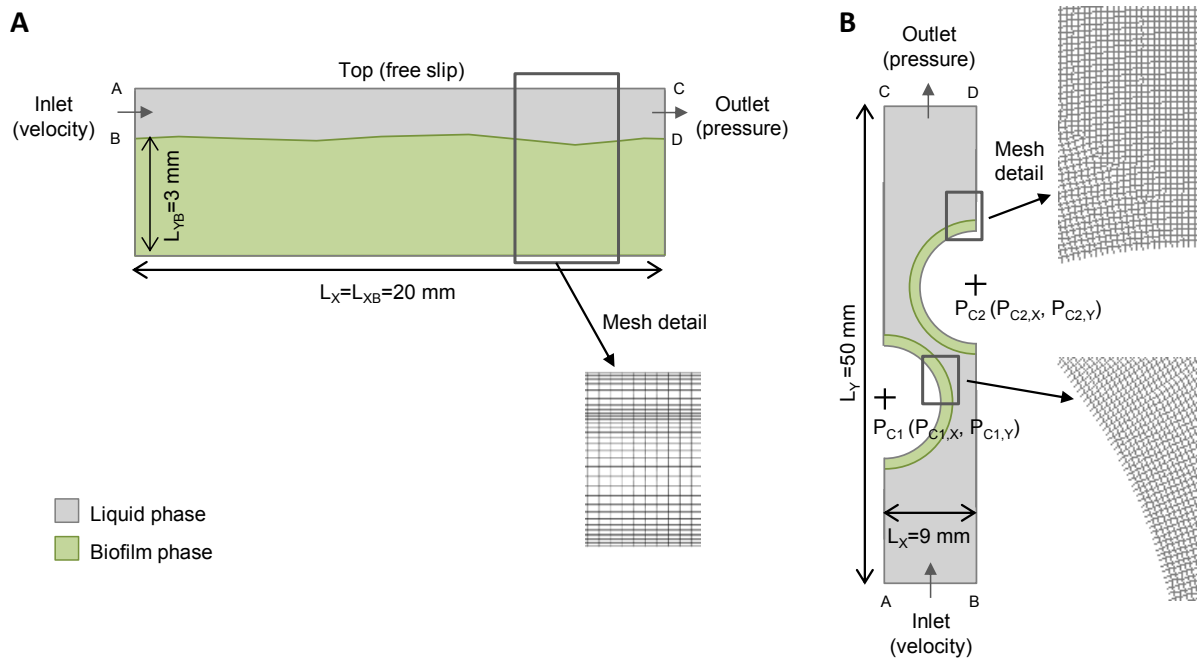


Figure 6.2. Description of model domains: D1 domain (A) and D2 domain (B).

Regarding the boundary conditions, as can be seen in Figures 6.2, three types were used to describe the flow fields within the computational domains: velocity inlet (line A-B), pressure outlet (line C-D) and walls (rest of surface with no indications). Particularly, in line A-C a free slip wall was defined for the top in the D1 domain (Figure 6.2A). The velocity inlet boundary

condition considered a uniform velocity profile. In the pressure outlet boundary, the value for the relative static (gauge) pressure was set to zero, i.e. atmospheric pressure was assumed. The wall boundary condition establishes a non-slip condition on the walls, and the free slip wall set zero shear stress. As explained in Chapter 4, the same boundary conditions as in D1 domain were used in the D0 domain.

During the meshing process, an adaptive mesh refinement was considered, besides testing meshes dependence and discretization schemes. A sensitivity analysis of the mesh was performed and the results were independent, based on the suggestions described in Chapter 4. Regular meshes had to be defined in order to obtain high quality meshes. Thus, uniform meshes by a prism scheme were defined in all the domains, using refined grids in the regions near the interfaces liquid-biofilm. Meshes quality was checked with the orthogonal quality parameter, which had average values of 1 in all domains, confirming the good quality of the defined meshes. Table 6.2 summarizes the sizes and the grid cells number defined for each of the domains previously described, being L_x , L_y and L_z the corresponding dimensions of the length, height, and width of the computational domain respectively. Particularly, length (L_x) and height (L_y) distances, for D1 and D2 domains respectively, were chosen as a compromise between the computational demands and the required length to prevent entrance and exit effects. Initial testing indicated that the 5 mm of entrance and exit length was sufficient to prevent any of these effects. In addition, the height (L_y) in D1 domain is higher than in D0 domain, because of the height of the zone where the liquid phase remains was duplicated for non-compromising the biofilm behavior (i.e. biofilm growth) with possible numerical problems.

Table 6.2. Computational domains characteristics.

Domain name	Domain description	Size (mm)	Grid cells number
D0	3D flat plate	$L_x = 180, L_y = 4, L_z = 35$	≈ 350.000
D1	Reduced 3D flat plate	$L_x = 20, L_y = 5, L_z = 2$	≈ 100.000
D2	2D curved channel	$L_x = 9, L_y = 50$	≈ 150.000

In the initialization step, all parameters were set to default values except for the volume fraction. The volume fraction of the biofilm phase was initialized inside the domains, patching the regions defined in green color (Figure 6.2) and setting the biofilm volume fraction equal to 1 in that region. In the D1 domain case, the biofilm region was defined in all the bottom of the domain, having a length equal to the D1 domain ($L_{xB}=20$ mm), and a height (or thickness) of $L_{yB}=3$ mm (bioreactor design requirement, Guimerà (2016)). In the same way, D0 domain was patched having larger length for the biofilm region ($L_{xB}=180$ mm). In the D2 domain case, the biofilm region was patched using two circles (radius=6 mm), defining the center position in the P_{C1} point ($P_{C1,x}=0$ mm and $P_{C1,y}=0$ mm) for the bottom circle, and in the P_{C2}

point ($P_{C_2,X}=9$ mm and $P_{C_2,Y}=9$ mm) for the top circle (see Figure 6.2B). In this last case, the thickness of the initialized biofilms was 1 mm.

6.3.1.4. Numerical simulations

The governing equations were discretized using the second-order upwind scheme. The interpolation of the pressure values at the cell faces, by means of the momentum equation, was carried out using the PRESTO (PREssure STaggering Option) scheme. The PISO (Pressure-Implicit with Splitting of Operators) algorithm was used to obtain the pressure-velocity coupling. Choosing the previous schemes and a segregated solver helped to save computational time and also improved convergence and computation stability. In the implemented VOF method, the momentum equations were solved throughout the domain, and the resulting velocity field was shared among the phases. To track the free surface deformation, the geo-reconstructed scheme was also applied. Transient simulations were run with the first order implicit formulation.

Processes considered in the model (substrate transport, biofilm growth and decay, and biofilm deformation and detachment produced by external shear stress) occur at very different time scale (ts). As proposed by Picioreanu et al. (2000b), three different observation windows were considered: Processes in momentum balance (ts order of seconds), processes in substrate mass balance (ts order of minutes), processes in the biomass balance (ts order of hours or days). Therefore, biomass balance was considered frozen in time for modeling substrate transport whereas a pseudo-steady approximation was considered for velocity and substrate profiles when biomass growth was modeled. Moreover, both substrate transport and biomass growth were frozen to describe deformation and detachment on biofilm structure (IWA Task Group on Biofilm Modeling, 2006). After a sensitivity study, maximum and optimum time steps giving stable transient solutions were found for each of the simulated cases with the two-phase models. For the computation with the D0 domain, simulating the mass transport and transfer of DO, the time step was found to be 10^{-2} s. When using the D1 domain, time steps of 1 s were found suitable for modeling biofilm growth. And for the simulations with the D2 domain, the recommended time step to reproduce biofilm deformation and detachment was found to be 10^{-5} s. The defined time step fulfilled the condition of the Courant number. In the cases computed with large time steps, a sequence for time step adaptation was performed, starting the simulation with a time step smaller (about three orders of magnitude) and increasing it in one magnitude order after approximately 200 iterations. Convergence was assumed when the maximum residual each equation (continuity, velocity components, and additional variables) reached a value of less than $1 \cdot 10^{-7}$, and mass balances were accomplished in the system.

6.3.2. Implementation of the rheological model into CFD codes

In ANSYS Fluent Release 17.2, the Herschel–Bulkley model (Expressions 5.1 and 5.2, Chapter 5) is modified at low shear rates to avoid infinite apparent viscosities, due to the discontinuity of Expression 5.2 when the shear rate is equal to zero. For the model adjustment, the critical shear rate parameter ($\dot{\gamma}_c = \sigma_y/\eta_y$) is introduced, indicating when the flow is considered to have yielded, being σ_y and η_y the yield stress (Pa) and yielding viscosity (Pa s) respectively. In ANSYS Fluent, the model is implemented via a switch between the linear stress-strain region (Expression 6.11) and the shear-thinning region (Expression 5.2). Note that Expression 6.11 reduces to Expression 5.2 at $\dot{\gamma} = \dot{\gamma}_c$.

$$\eta = \frac{\sigma_y \left(2 - \frac{\dot{\gamma}}{\dot{\gamma}_c}\right)}{\dot{\gamma}_c} + K(\dot{\gamma}_c)^{n-1} \left[(2 - n) + (n - 1) \frac{\dot{\gamma}}{\dot{\gamma}_c} \right] \quad (6.11)$$

Instead of the linear relationship shown in Expression 6.11, some works (Bakker et al., 2009; Ramin et al., 2014) have assumed a constant value for the apparent viscosity below the critical shear rate. However, this is not a characteristic of materials which exhibit yield stress, i.e. form-stability at rest. In the current study, the critical shear rate was estimated by means of defined correlations for yield stress (σ_y) and yielding viscosity (η_y) (for further details see Chapter 5). Values of these parameters and the other rheological parameters (i.e. K and n) are summarized in Table 6.1.

6.3.3. Customizing CFD code: implementation of expressions and correlations

In order to customize ANSYS Fluent code and to enhance its standard features, user-defined functions (UDFs) can be implemented as C or C++ functions and dynamically loaded with the ANSYS Fluent solver. UDFs can be used to implement ‘tailored’ user-defined specifications such as boundary conditions, material property, source terms in transport equations, and diffusivity functions, among others. UDFs are defined using DEFINE macros provided by ANSYS Fluent. They are coded using additional macros and functions that access ANSYS Fluent solver data and perform other tasks.

Since ANSYS Fluent solver data is defined in terms of mesh components, it is required to understand the mesh terminology before implementing a UDF. A mesh is divided into control volumes, i.e. cells. Each cell is defined by a set of nodes, a cell center, and the faces that bound the cell. ANSYS Fluent uses internal data structures to define the domain(s) of the mesh; to assign an order to cells, cell faces, and nodes in a mesh; and to establish connectivity between adjacent cells. A domain is a data structure in ANSYS Fluent that is used to store information about a collection of nodes, face threads, and cell threads in a mesh. Finally, a thread is a data structure that is used to store information about a boundary or cell zone, e.g. cell threads are groupings of cells and face threads are groupings of faces. When a UDF is used in ANSYS Fluent, it can access solution variables at individual cells or

cell faces in the fluid and boundary zones. UDFs need to be passed appropriate arguments such as a thread reference and the cell or face identifiers in order to enable individual cells or faces to be accessed (ANSYS Inc, 2017).

In addition to the data types above presented, there are special thread and domain data structures that are specific to multiphase UDFs, i.e. UDFs used in multiphase models (Mixture, VOF, or Eulerian). The data types are used to store properties and variables for the mixture of all of the phases, as well as for each individual phase. In multiphase modeling, the concept of a mixture is used to represent the sum over all the phases, while in single-phase represents the sum over all the species (components). Therefore, the data structures that are passed to a UDF depend on the multiphase model that is enabled, the property or term that is being modified, the DEFINE macro that is used, and the domain that is to be affected (mixture or phase) (ANSYS Inc, 2017).

Finally, the variable defined in the UDF is denominated user-defined scalar (UDS) in ANSYS Fluent. In the same way, due to the data structure hierarchy defined in ANSYS Fluent, the UDSs can be associated and transported by mixture or phase domain, depending on the multiphase model which is required to implement. Using the VOF or Mixture model, only one velocity field is resolved for the mixture of all the phases, being recommended to transport the UDS by the mixture in this case. Whereas, the velocity field is resolved by phase using a Eulerian multiphase model, being suggested to associated and transport a different UDS in each of the phases defined in this second case.

For more details in the implementation of UDF in ANSYS Fluent, see ANSYS Inc (2017).

6.3.3.1. Defining biokinetics expressions

The implementation of biological reactions in ANSYS Fluent was performed using the methodology described in Chapter 4 (or Prades et al., 2017), defining an extra transport equation (Expression 4.14) for each variable or UDS used in the model. All terms in Expression 4.14 (temporal, convective, diffusive and source terms) were considered for defined variables.

In ANSYS Fluent, the UDSs are dimensionless defined as the conserved quantity (ϕ) of n variable per unit mass of fluid ($\phi=C_n/\rho$), where C_n is the concentration of the n variable (kg m^{-3}) and ρ is the fluid density (kg m^{-3}). Since the biosystem models were implemented as a multiphase VOF model, it was needed to define variables pairs, i.e. a UDS for each variable in each of the phases (transferring the value between them at the interface, see subsection 6.3.3.2 for further details), and being them associated and transported by the mixture. Moreover, the kinematic diffusivity coefficient was defined for the UDSs present in liquid and biofilm phases, using the macro DEFINE_DIFFUSIVITY (ANSYS Inc, 2017). Note that the UDSs were transported by the mixture in the model, then the diffusion coefficient has to be equal to 0.0 if the volume fraction of the phase that transport the scalar is equal to 0.0. In this

case, for modeling approach illustration, only one limiting compound or variable was considered, i.e. DO. Thus, two variables or UDS were defined (UDS_i): UDS_1 for the DO in the liquid phase and UDS_2 for the DO in the biofilm phase; forming UDS_1 and UDS_2 a UDS pair for the specific compound DO. Diffusion coefficients defined for UDS_1 and UDS_2 in liquid and biofilm phases respectively are summarized in Table 6.1.

In addition, the expression for the biodegradation kinetic for DO (i.e. Expressions 4.7) was included as source term, using the DEFINE macro DEFINE_SOURCE, which have five arguments: *name*, *cell*, *thread*, *dS*, and *eqn*. The *name* of the UDF should be supplied by the user, and *cell*, *thread*, *dS*, and *eqn* are variables that are passed by the ANSYS Fluent solver to the UDF. The units on all source terms are of the form generation-rate/volume, e.g. $\text{kg/m}^3 \text{s}^{-1}$. ANSYS Fluent is calling the DEFINE_SOURCE from within a loop on cell threads. The solver passes to the DEFINE_SOURCE term UDF everything which is needed, since source terms are solved on a cell basis. Then, the UDF will need to compute the real source term only for a single cell and return the value to the solver, but the way of performing that computation will be chosen by means of *dS* value, i.e. source term derivatives. If the *dS* is set equal to 0.0, the source linearization is not estimated, whereas if a source derivative is indicated, the source linearization is forced. Further details of DEFINE_SOURCE macro can be found in (ANSYS Inc, 2017).

Taking advance of *dS* property, in this model the source linearization was forced in order to enhance the stability of the solver and to avoid negative values in the defined UDSs. To linearize the source term, the *Always-positive variables method* proposed by Patankar (1980) was implemented. The source *S* dependency on variable or scalar UDS is expressed in linear form by Expression 6.12:

$$\bar{S} = S_1 + S_2 \cdot \overline{UDS} \quad (6.12)$$

Where S_1 is the constant part of the linearized source S (\bar{S}), and S_2 is the coefficient of the scalar or variable UDS (\overline{UDS}). Thus, S_1 was defined equal to the source term S and S_2 was designated as S divided by the current value of the scalar UDS_i .

6.3.3.2. Defining mass transfer correlations

Related to mass transfer phenomenon description, the defined variables pair for dissolved oxygen UDS was used to implement mass transfer between the phases model compound, i.e. DO transfer from liquid to biofilm phase. The mass flux from the boundary layer to the biofilm, i.e. mass transfer source term, was computed by means of Expression 6.13:

$$\frac{dC_{BDO}}{dt} = k_L \cdot a \cdot (C_{LDO} - C_{BDO}) \quad (6.13)$$

Where C_{BDO} is the concentration of DO compound in the biofilm phase (kg m^{-3}) or UDS_1 , t is time (s), k_L is the mass transfer coefficient (m s^{-1}), a is the specific mass transfer area of the cell or interfacial area ($\text{m}^2 \text{m}^{-3}$) and C_{LDO} is the concentration of DO compound in the

liquid phase (kg m^{-3}) or UDS_2 . The mass transfer coefficient value was obtained from Expression 6.5.

The transfer between the UDS s pairs at the interface should be implemented using `DEFINE_SOURCE` macro. In this case, two different sources were defined, one for adding to the UDS_1 the mass transfer source computed by Expression 6.13, and the second one for subtracting to the UDS_2 its equivalent. These mass transfer sources terms were defined in the mixture thread for the UDS s pairs of each compound, and they were linearized indicating the term dS to enhance solver stability.

6.3.3.3. Implementation of biofilm growth model

As proposed by Picioreanu et al. (2009), an adaption of the discrete cellular automata (CA) biofilm model was performed to couple the effect of fluid dynamics over biofilm development. In the CA approach (Picioreanu et al., 1998a, 2001), the biomass balance includes terms for accumulation, transport, growth and decay, attachment and detachment. The computational domain is divided by a cubic elements mesh, where the cubes contain biomass with a concentration greater than zero in the biofilm region, and the cubes in the liquid region have biomass concentration equal to zero.

The CA approach has similarities with the CFD model presented in this chapter, since the model was computed with a hexahedron domain, and liquid/biofilm regions were limited by the volume fraction of the phases. In addition, the possibility to use fluid mass sources implemented in the CFD code (see Expression 6.6) could facilitate the implementation of the growth model. The generation rate of fluid mass sources is in $\text{kg}\cdot\text{m}^{-3}\cdot\text{s}^{-1}$, the same units used for the microbial growth kinetic (Expression 6.1).

Therefore, an adapted CA biofilm model was implemented into CFD code, considering growth, decay, accumulation and transport in the biofilm. Attachment and detachment were neglected, although due to the non-Newtonian character of the biofilm phase, detachment could be considered depending on the hydrodynamic conditions settings (see subsection 6.4.2.2). The terms included in the biofilm model took place in a different way that in the CA approach, since here it was considered the volume fraction of the biofilm phase.

In each cell, biomass concentration (X) was computed proportionally to the volume fraction of the biofilm phase (α_{p2}), i.e. $X = X_{b,\text{max}} \cdot \alpha_{p2}$, being $X_{b,\text{max}}$ the maximum value of concentration reached in the biofilm. This assumption was based on biofilm growth models implemented using phase-field approach (Zhang et al., 2008), in which the volume fraction of the polymer network in the production rate is considered. Therefore, biofilm growth and decay occurred if the volume fraction of the biofilm phase was greater than 0 but lower than 1, i.e. the biofilm mass source $S_{\alpha_{p2}}$ (Expression 6.14) acted at the interface liquid-biofilm.

$$S_{\alpha_{p2}} = \frac{dX}{dt} \cdot \alpha_{p2} \quad (6.14)$$

Where the accumulation rate (dX/dt) is equal to Expression 6.1, in which X is equal to $X_{b,max}$.

The biofilm transport was produced itself with the biofilm growth and decay, since the biofilm accumulation, i.e. growth, in a particular cell was displacing the liquid-biofilm interface to the neighboring cells as the biofilm volume fraction in the cell increased. Then, in the new cell where some of the biofilm volume fraction arrived, the growth was starting there with the biofilm concentration proportional to the biofilm volume fraction of the cell.

For the implementation of the fluid mass source was also required the use of DEFINE macro DEFINE_SOURCE (see previous sections). In addition, for accomplishing continuity criteria, the same mass that is introduced in the biofilm phase needs to be subtracted from the liquid phase.

6.4. RESULTS AND DISCUSSION

Various sets of simulations were carried out with the three different developed two-phase models. In the first series of simulations (D0 domain), the two-phase model of the flat plate bioreactor was verified using experimental data, analyzing mass transport and transfer of DO for different hydrodynamic conditions. Second and third series were performed to test the capabilities of the model for reproducing biofilm characteristics such as growth, deformation, and detachment. In the second series of simulations (D1 domain), the growth kinetic was implemented on the model, examining if a fluid mass source could simulate the biofilm growth, and analyzing the influence of the external shear stress on the growth. In the third series of simulations (D2 domain), the effects of the flow velocity on biofilm structure were evaluated, computing cases with weak and strong shear rates to establish the limits in deformation and detachment.

6.4.1. Model verification: comparison of simulated results with experimental data

As a first stage, the simulation results reproducing substrate transport and transfer in the D0 domain were shown.

Regarding the implementation of biological kinetic expressions, a methodology was validated in Chapter 4 for the ANSYS CFX code. CFD simulated results and experimental data were compared, showing satisfactory agreement for different biofilm densities along the bioreactor. In order to show the adequacy of the methodology proposed, the case presented in Chapter 4, i.e. one phase CFD model, was simulated using Fluent. For computational time saving, in this case, only the flat plate was included in the domain definition (D0 domain), since the same hydrodynamic conditions were kept in that zone. As can be seen in Figure 6.3, the recorded DO profiles (through liquid and biofilm phases' depths) were reproduced with the same accuracy in Fluent than in CFX (ANSYS Release 17.2) at various positions from the bioreactor inlet with different density values. Therefore, both ANSYS solvers can

reproduce adequately biosystems behavior using one-phase models. However, in this chapter it was needed to take advantage of the greater capacity that Fluent offered to model the required two-phase cases.

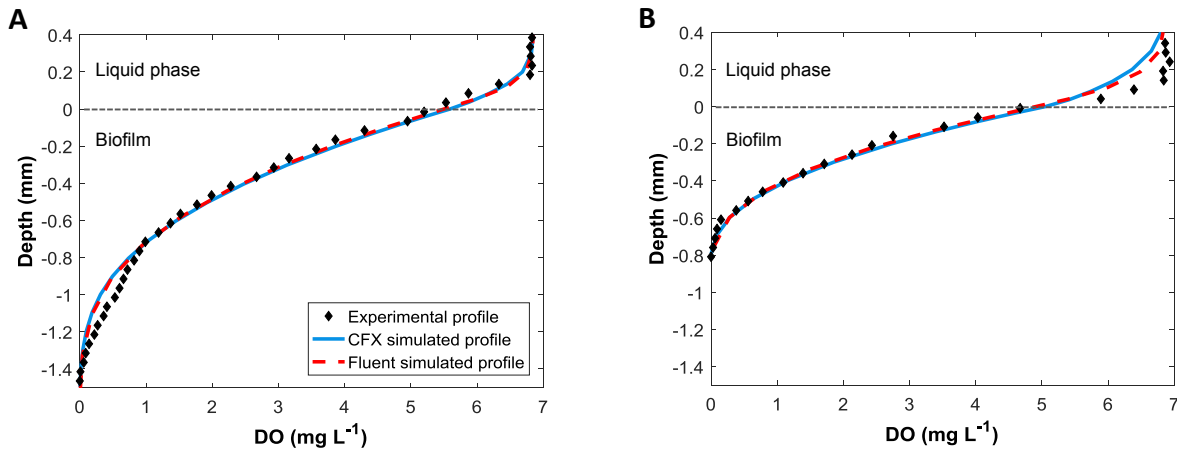


Figure 6.3. DO profiles at different densities and positions from the bioreactor inlet (P1 and P3): (A) Measured at P1 (6 cm from the beginning of the flat plate) and $9.3 \text{ kg VSS m}^{-3}$; (B) Measured at P3 (15 cm from the beginning of the flat plate) and $18.2 \text{ kg VSS m}^{-3}$. Symbols are experimental data and lines are the simulated results in CFX (solid) and Fluent (striped) ANSYS software.

After verifying the correct reproduction of the biosystem performance using ANSYS Fluent code, new sets of CFD simulations were carried out to test the model under different hydrodynamic conditions. Two-phase models were implemented for the flat plate, i.e. water-biofilm interaction, considering the biofilm as non-Newtonian fluid, while DO transport and transfer to the biofilm were evaluated under different liquid velocities. Thus, the defined model coupled hydrodynamics with substrate transport mechanisms.

Experimentally, duplicated DO profiles were recorded at the same position of the bioreactor (Guimerà, 2016), and at different liquid phase velocities (from 5 to 20 m h^{-1}), reproducing the real operating conditions of liquid phase biosystems such as biofilters or biotrickling filters. As can be seen in Figure 6.4, the concentration boundary layer (CBL) thickness (δ_c) was reduced with the velocity, and thus increased mass transfer coefficient at the interface liquid/biofilm. Moreover, the slope of DO profiles increased with the flow rate, so oxygen flux was intensified to higher flow conditions. These trends were in agreement with previous works which studied external mass transfer resistance (Zhang and Bishop, 1994; Horn and Hempel, 1995; Guimerà et al., 2016).

In addition, the performance of the two-phase developed model is verified in Figure 6.4, comparing these experimental results with the simulated ones. Simulated CFD profiles showed a good agreement with recorded profiles. The same DO profiles behavior, noticed experimentally at different liquid velocities, was reproduced correctly using the two-phase CFD model described in this chapter. Experimental and CFD simulated profiles presented

the same trend throughout liquid phase, CBL and biofilm, reaching a zero DO concentration in the biofilm at identical depths for all the studied flow conditions. The normalized root mean square errors (NRMSE) between the experimental and simulated DO profiles for the $10 \text{ m}\cdot\text{h}^{-1}$ and $20 \text{ m}\cdot\text{h}^{-1}$ fluid velocities were 3.77% and 2.34% respectively. It should be pointed out that the measurements with larger deviations between experimental and simulated data were mainly in the concentration boundary layer (CBL) and in the liquid phase, being these zones the most difficult to reproduce accurately. Possibly, the transport mechanisms were driven by the heterogeneous biofilm structure in the analyzed experimental conditions (Guimerà et al., 2016). The voids could facilitate convective mass transport, which became increasingly significant at higher flow velocities (De Beer et al., 1996), producing slightly variability in DO transport. Even so, the trends in the DO concentration profiles were correctly reproduced for the liquid phase and the CBL in all the studied conditions.

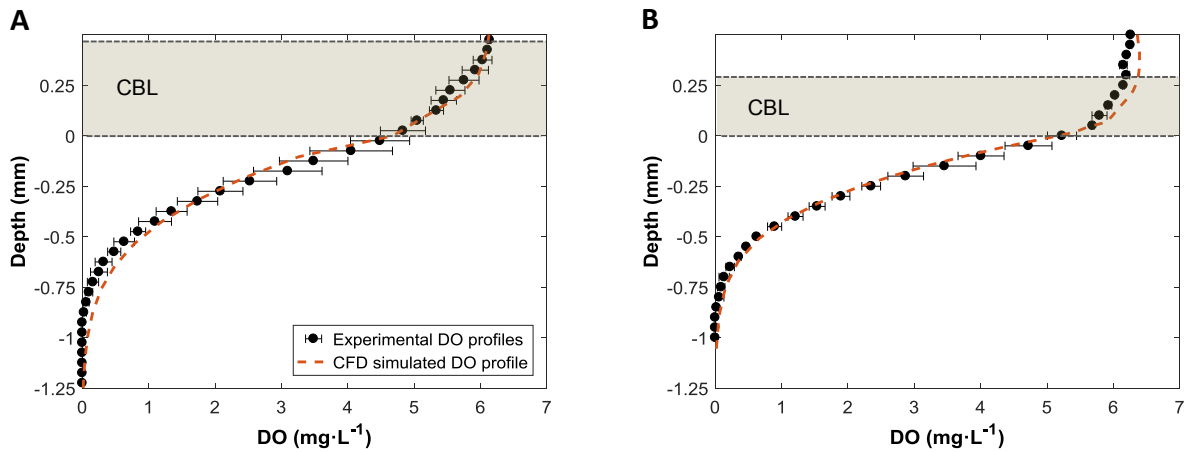


Figure 6.4. Illustration of experimental and simulated DO profiles at two different liquid phase velocities: (A) $10 \text{ m}\cdot\text{h}^{-1}$ and (B) $20 \text{ m}\cdot\text{h}^{-1}$. The DO profiles were recorded at the same position along the FPB, i.e. 5.5 cm from the bioreactor inlet, where the biomass density was $22.78 \text{ kg VSS m}^{-3}$.

6.4.1.1. Mass transfer analysis

Mass transfer at the concentration boundary layer (CBL) is decisive to supply all types of substrates to the active biomass. The CBL thickness (δ_c) is a parameter with an important role in the external mass transfer resistance, being essential in the implementation of one-dimensional biofilm models (Boltz et al., 2010). In film theory, the mass transport within this layer is assumed to be diffusive, and the mass transfer coefficient (k_L) can be estimated dividing the diffusion coefficient (D) by the CBL thickness (Horn and Lackner, 2014), as reported in Expression 6.15.

$$k_L = \frac{D}{\delta_c} \quad (6.15)$$

However, as discussed in Chapter 4 and in other works (Wäsche et al., 2002; Lewandowski and Beyenal, 2007; Guimerà et al., 2016), both diffusive and advective

processes drive the transport within the CBL. Therefore, the film theory approach for the k_L is unconnected to reality (Wäsche et al., 2002; Horn and Lackner, 2014; Guimerà et al., 2016), and more elaborated correlations for mass transfer are used such as previously discussed (section 6.2.3). These correlations include the relation of advection and diffusive processes in mass transfer by means of Re and Sc numbers, i.e. $Sh = f(Re, Sc)$, but the real role of δ_c over mass transfer is not elucidated. The aforementioned CFD results, in which DO microprofiles were modeled including an accurate description of hydrodynamic effects, could help to link advection and diffusion mechanisms and CBL characteristics to mass transfer properties.

Microsensors measurements performed by Wäsche et al. (2002) suggested that advective process and substrate conditions during biofilm cultivation had a direct influence on the CBL thickness. In addition, the CBL thickness is directly correlated to the hydrodynamic boundary layer (HBL), which results from the flow pattern over the biofilm surface (Bishop et al., 1997; Picioreanu et al., 2000b). Theoretically, the CBL and HBL thicknesses in a plate are related through the Schmidt number (Sc), as described by Expression 6.16 (Clussler, 1984).

$$\frac{\delta_c}{\delta_H} = Sc^{-1/3} \quad (6.16)$$

$$\delta_H = 4.91 \cdot x_L \cdot Re^{-1/2} \quad (6.17)$$

Being the HBL thickness (δ_H) calculated by Expression 6.17, where x_L is the distance from the leading edge of the plate (Clussler, 1984). In the present case, x_L is the distance from the beginning of the flat plate to the point where the microprofiles were recorded.

From the previous expressions, arise that the dimensionless form of δ_c , i.e. δ_c/x_L , should be function of Re and Sc numbers. In this work, all the DO microprofiles were recorded at the same distance from the edge. In order to describe in a more general way the dimensionless form of δ_c , being independent of plate longitude, the δ_c dimensionless form can be defined by means of the Péclet number (Pe). Pe is a dimensionless number used to correlate the ratio of advection and diffusion in transport phenomena, which can be written as Expression 6.18 for the CBL thickness.

$$Pe = \frac{\delta_c \cdot U}{D} \quad (6.18)$$

Therefore, a correlation for δ_c could be established using Pe, Re and Sc numbers. From the simulated DO profiles at different velocities (5, 10, 15, 20 and 25 m h⁻¹), the δ_c was estimated for the diverse profiles, following the methodology described in Chapter 4. Pe number was calculated for the CBL from operational conditions previously mentioned, and the DO diffusivity in the liquid phase (Table 6.1). In the same way, Re and Sc numbers were computed, considering the liquid phase properties described in section 6.2. Then, with these estimated data, Expression 6.19 was found for the Pe number depended on Re and Sc, by means of the least-squares fitting method solved using MATLAB® Release 2016b.

$$Pe = c \cdot Re^{7/10} \cdot Sc^{-1/3} \quad (6.19)$$

Where $c = 3134$ is a constant value. As can be seen in Figure 6.5A, estimated and calculated data was in good agreement, describing the Expression 6.19 the estimated data tendency for the Pe number.

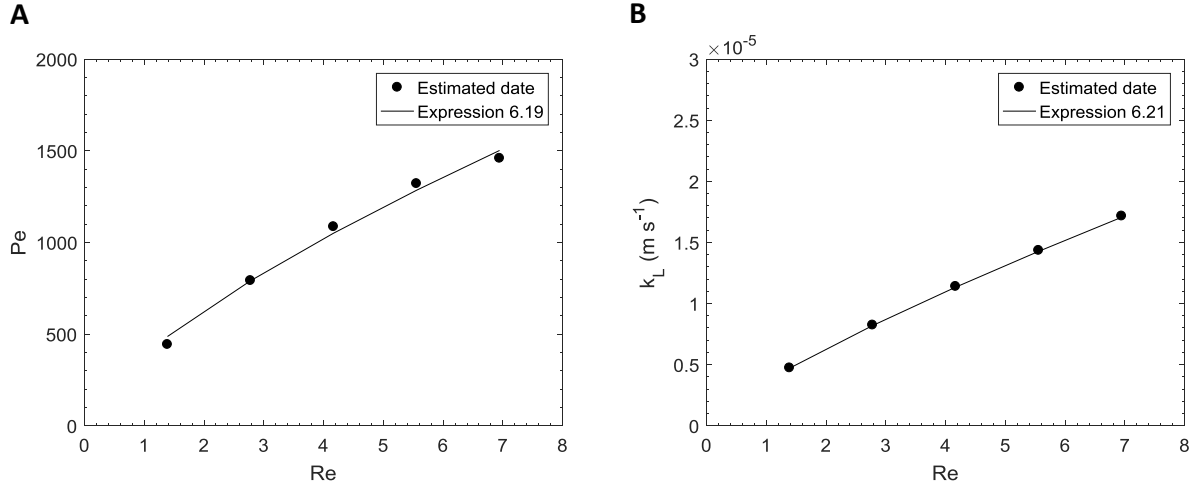


Figure 6.5. Estimated data and calculated from Expressions 6.19 and 6.21 for Péclet number (A) and mass transfer coefficient (B) respectively as a function of the Reynolds number.

From the previous expressions (Expressions 6.19 and 6.20), the δ_c can be calculated as described in Expression 6.20, being function of flow velocity, diffusion coefficient, and Re and Sc numbers in the liquid phase.

$$\delta_c = \frac{D}{U} \cdot Pe = \frac{D}{U} \cdot c \cdot Re^{7/10} \cdot Sc^{-1/3} \quad (6.20)$$

By analogy of Expressions 6.5 and 6.20, a correlation for mass transfer coefficient in function of CBL thickness should follow the rule $k_L = f(D, \delta_c^{-1})$. The characteristic k_L in each of the operational conditions abovementioned was given by Expression 6.5. Finally, the data estimated herein was also used to propose a k_L correlation by means of the least-squares fitting method, as described in Expression 6.21.

$$k_L = c' \cdot D \cdot \frac{1}{\delta_c} \cdot Re^{1/2} \quad (6.21)$$

Where $c' = 1$ is a constant value. It should be noted that combining Expressions 6.20 and 6.21, Expression 6.22 was found for k_L in function of Re and Sc numbers, which was consistent with the k_L found from Expression 6.5.

$$k_L = c'' \cdot \frac{\eta}{L \cdot \rho} \cdot Re^{0.8} \cdot Sc^{1/3} \quad (6.22)$$

Where the constant c'' equal to $c'' = c'/c$.

Figure 6.5B depicts the estimated data for k_L and calculated k_L from Expression 6.21, which provided a reliable, overall, mass transfer description. Thus, Expression 6.21

accurately reproduced the mass transfer coefficient value for the studied conditions in plates ($Re < 8$), showing the elementary dependency of k_L with the Re number and δ_c when both diffusion and advection process are considered in the CBL.

Ideally, the evolution of a compound concentration (e.g. DO) transferred across the liquid-biofilm interface (Expression 6.13) can be represented in discrete form by the Expression 6.23, showing the local dependency of all the parameters with the volume in which mass transfer is taking place, e.g. a full scale WWTP or a microscale study volume.

$$\left. \frac{dC_{B_i}}{dt} \right|_{\forall_i} = \int_{\forall_i} k_{L_i} a_i (C_{L_i} - C_{B_i}) d\forall_i \quad (6.23)$$

Where \forall_i is a defined volume i , C_{B_i} is the compound concentration in the biofilm phase in \forall_i , t is the time, k_{L_i} is the mass transfer coefficient in \forall_i , a_i is the interfacial area in \forall_i , and C_{L_i} is the compound concentration in the liquid phase in \forall_i .

Considering the closest approach to reality, mass transfer coefficient cannot be treated constant in a real and dynamic environment, such as a living biofilm. Several phenomena could happen in a real control volume located in the biofilm interface: the biofilm structure and micro-structure would influence the liquid phase behavior (turbulence and shear stress) near to the interface, thus, influencing the mass rate transfer phenomena; the mass transfer ratio is the key factor to determine the biofilm growing rate, thus considering it a microscale level, a growing biofilm might vary or substantially change its shape and the available area (a_i) for transfer phenomena, leading again to changes into the liquid phase behavior.

Therefore, the parameters in Expression 6.23 could not be constant values to study in detail the process, and the calculus of compound evolution across the interface should be an iterative procedure, since fluid dynamics play an important role modifying all parameters. As previously discussed, the mass transfer coefficient is clearly influenced by fluid conditions and properties. The biofilm-fluid interfacial area is another parameter which has an identical key role than the mass transfer coefficient in the evaluation of fixed-bed biofilm reactors. As described by Piciorenu et al. (1998b), biofilm surface enlargement and irregularities should be considered for biofilm modeling to reproduce the complex biofilm shapes observed in natural systems.

VOF models are characterized by tracking the volume fraction across the domain, allowing to reconstruct accurately the interface between fluids (Kelly, 2008). This particular characteristic opens new doors to explore the capacity of VOF approach to model biosystems performance. In the CFD results showed above, the global performance of bioreactor was reproduced correctly considering a flat biofilm, since perceptible surface variations were not noticed during experimental data recording. However, in cases where the interfacial area could have notorious changes, it would be required to contemplate the real

shape of biofilm surface, considering also an accurate hydrodynamics modeling and linking both aspects.

In the next sets of simulations to test VOF model capabilities, biofilm growth was considered and external shear stresses were applied. In both cases, the biofilm response was analyzed, discussing also the requirement of considering real biofilm shape when modeling mass transfer mechanisms.

6.4.2. Model capabilities testing

6.4.2.1. Implementation of the bacterial growth model

In this new set of simulations, the D1 domain was used to simulate biosystem performance including the growth kinetics in the biofilm. In this case, the defined domain was a reduced part of the flat plate used in the previous simulations, being duplicated the height of the zone where remains the liquid phase for not to compromise the growth to possible numerical problems. This setup mimicked a flat fixed biofilm being feed off with nutrients through the liquid phase. This phase was flowing over the biofilm driven by an inlet velocity of 10 m h^{-1} (i.e. 0.0028 m s^{-1} , and $Re=5.5$), reproducing the real operating conditions of liquid phase flow in biosystems such as biofilters or biotrickling filters. The growth kinetic was implemented by means of a fluid mass source in the biofilm phase, exploring a new way to consider this phenomenon into CFD codes. Therefore, the defined model considered hydrodynamics, transport mechanisms, and growth in a whole.

Since the biofilm growth depends on the dissolved oxygen availability at the liquid-biofilm interface (Expression 6.14), two scenarios could be considered to reproduce either a homogenous biofilm growth, or a heterogeneous growth. Specifically, the two scenarios considered were the following: (1) homogenous growth conditions from a uniform distribution of biofilm and substrate; and (2) heterogeneous growth conditions from a uniform distribution of biofilm but with a heterogeneous distribution of substrate. In this set of simulations, the two different scenarios were considered in the same domain in order to capture the growth phenomenon within a reasonable computational time frame, since the required time step for both scenarios separated, could expend considerable amount of computing time with the available computing power. The first scenario was implemented on the left side of the domain, i.e. from the domain start to the middle part, whereas the second scenario was defined on the right side of the domain, i.e. from the middle of the domain to its end. It should be pointed out that the zones to prevent entrance and exit effects were not show in the results.

Figure 6.6 shows the 3D view of the biofilm surface structure and the contours of biofilm volume fraction, dissolved oxygen and velocity for simulated times from 0 to 48 hours. The line depicted in the center of contours and 3D view indicated the limit between the scenarios 1 and 2. At $t=0 \text{ h}$, the initial conditions of the simulations can be observed. In the biofilm

volume fraction profile, the red color indicates the zones full of biofilm, i.e. volume fraction equal to one, initially well uniform distributed in both scenarios with a height of 3 mm. The blue color refers to the zone where the liquid phase remained. In the dissolved oxygen profiles, it can be observed at initial conditions that higher concentrations were present in the liquid phase, decreasing in the CBL and inside the biofilm. In the left-hand part of the domain (scenario 1), a homogenous distribution of dissolved oxygen was considered (as the profile depicted in Figure 6.3A), whereas in the right-hand part (scenario 2), a heterogeneous distribution was contemplated, with smaller values in mean near the liquid-biofilm interface.

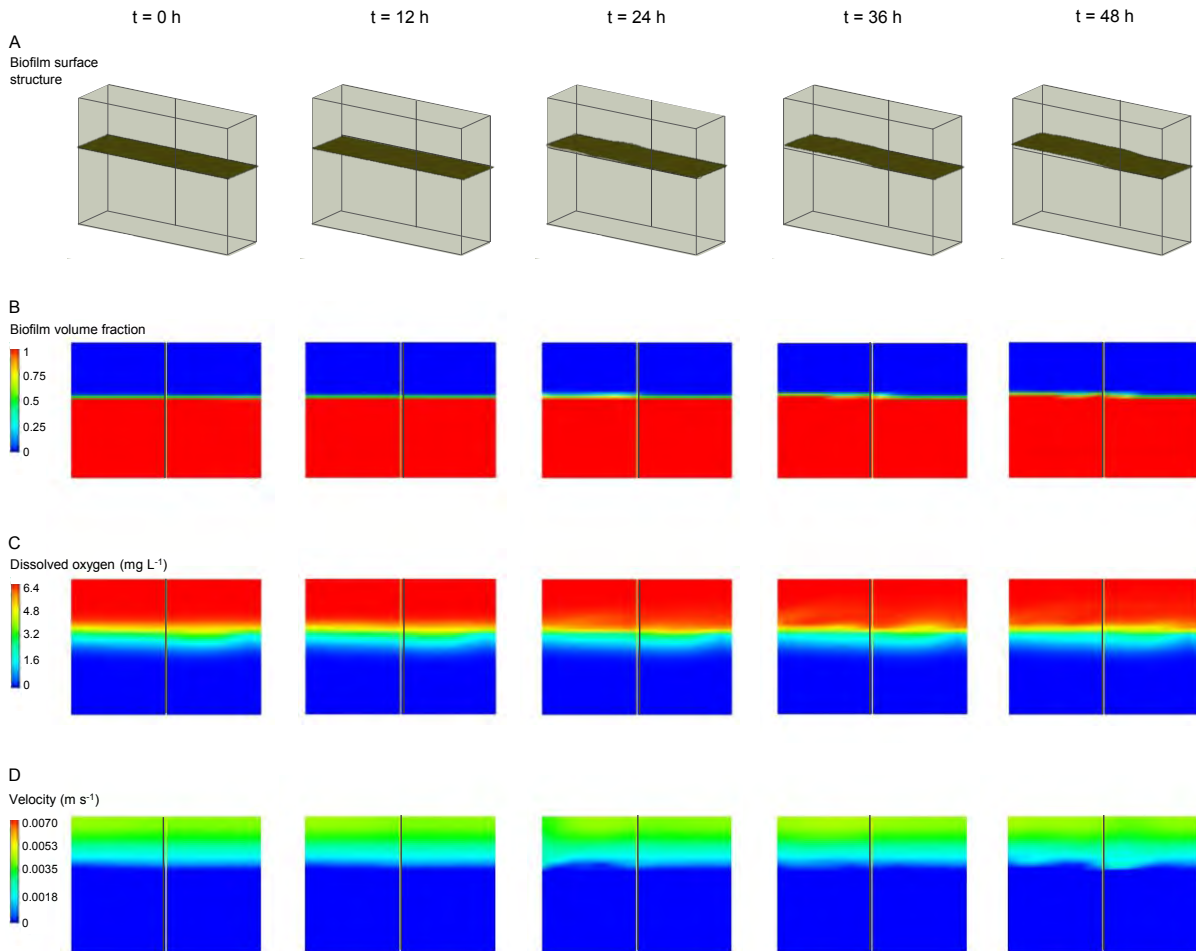


Figure 6.6. Simulated results for a 3D view of the biofilm surface structure (A) and biofilm volume fraction (B), dissolved oxygen (C) and velocity (D) contours for simulated times equal to 0, 12, 24, 36 and 48 hours.

Moreover, the velocity profile (Figure 6.6D) was the representative one for 10 m h^{-1} considering laminar flow regime, and the biofilm surface structure was completely flat initially. The initial situation was still remaining untouched for $t=12 \text{ h}$, without appreciating the presence of biofilm growth. After 1 day, changes in all of the profiles could be observed. At $t=24 \text{ h}$, in scenario 1, biofilm started to growth due to the higher accessibility to DO at the interface. The velocity profile also showed variations in this first part of the domain. For $t=36$ and $t=48 \text{ h}$, the biofilm continued to grow in scenario 1, and it started the growth in scenario

2, possibly by its higher accessibility to DO, coming also from its lateral region. Variations of the velocity profile in both scenarios were noticed for times over 36 hours, thus the biofilm growth could have an effect over the fluid flow velocity. Observing the 3D view of the biofilm surface structure in scenario 1, the growth occurred nearly uniformly for a time from 24 to 48 hours, without generating surface irregularities or area enlargement.

Figure 6.7 shows the 3D view of the biofilm surface structure and the contours of biofilm volume fraction, dissolved oxygen and velocity for simulated times from 60 to 108 hours. In the time range from 60 to 108 hours, it can be observed in Figure 6.7 that the dissolved oxygen profiles were not homogeneously distributed in scenario 1, which led to heterogeneous growth. In $t=60$ and $t=72$ h, the higher accessibility to DO in the initial part of scenario 1 produced biofilm development in that zone. For times from 84 to 108 hours, it can be seen that the liquid-biofilm interface became inhomogeneous as the biofilm grows in scenario 1. Even so, the biofilm surface structure (3D view) depicted that the growth in scenario 1 was more homogenous than in scenario 2. The heterogeneity present in scenario 2 produced some irregularities in the biofilm surface at $t=108$ h.

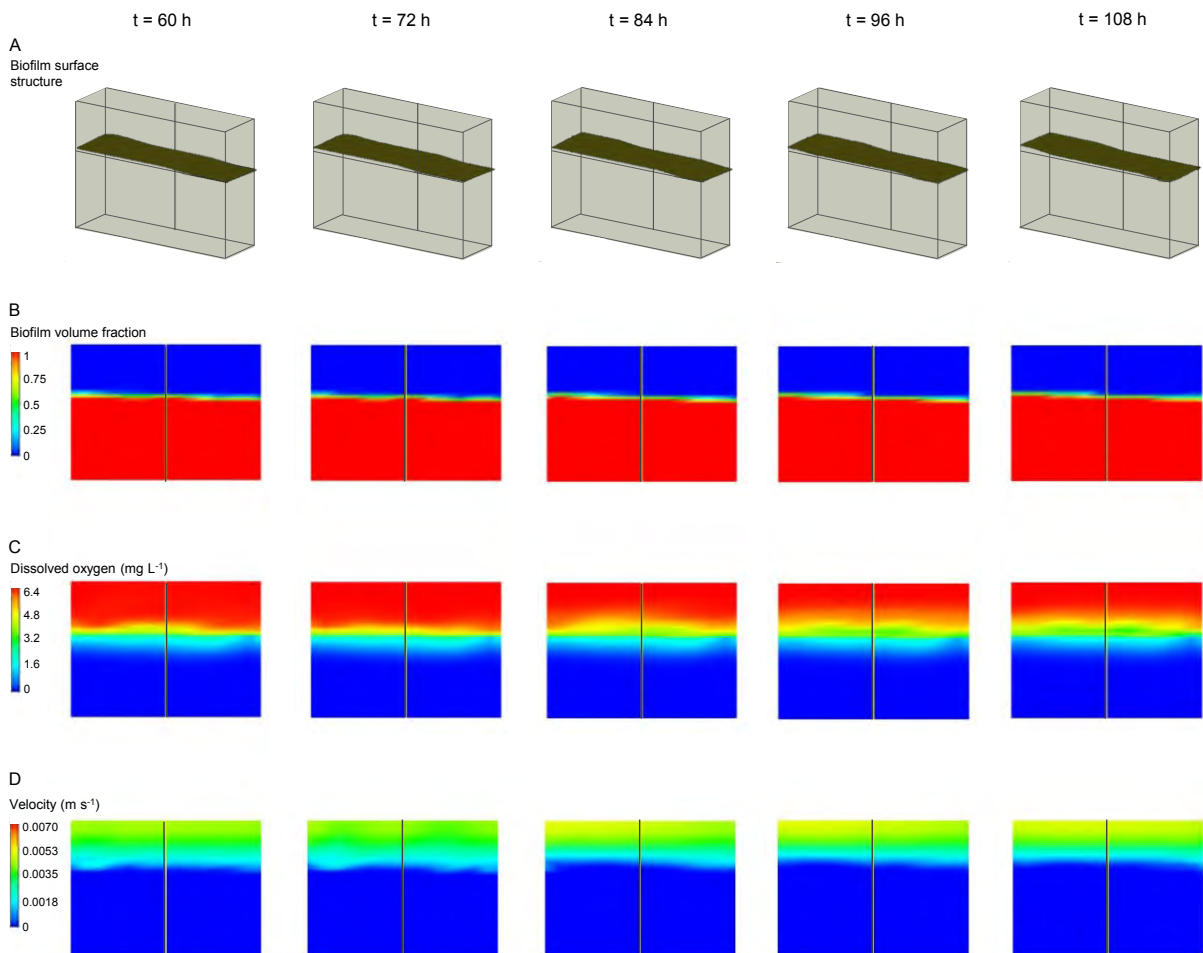


Figure 6.7. Simulated results for a 3D view of the biofilm surface structure (A) and biofilm volume fraction (B), dissolved oxygen (C) and velocity (D) contours for simulated times equal to 60, 72, 84, 96 and 108 hours.

In the range of time analyzed in Figure 6.7, it was clearly noticed that the biofilm growth produced changes in the velocity profiles near the interface, which affected on the transport mechanisms, modifying dissolved oxygen profiles too.

Figure 6.8 shows the 3D view of the biofilm surface structure and the contours of biofilm volume fraction, dissolved oxygen and velocity for a simulated time from 120 to 156 hours. Similar patterns than in Figure 6.7 were found in this range time, being heterogeneous the growing in scenarios 1 and 2. The heterogeneity in DO profiles noticed in the scenario 2 had a direct effect over the biofilm surface structure, having higher DO concentration near the interface the last part of the scenario 2 and, thus, larger production rate and growing faster in that zone. In scenario 1, the DO profiles were more constant than in scenario 2, but still the growth was produced in the zones which higher DO concentration available. The 3D view show, in general, the more homogenous biofilm surface structure generated for scenario 1 than for scenario 2, presenting more irregularities in the second scenario. Thus, the biofilm surface area enlargement in non-homogenous growth cases should be considered.

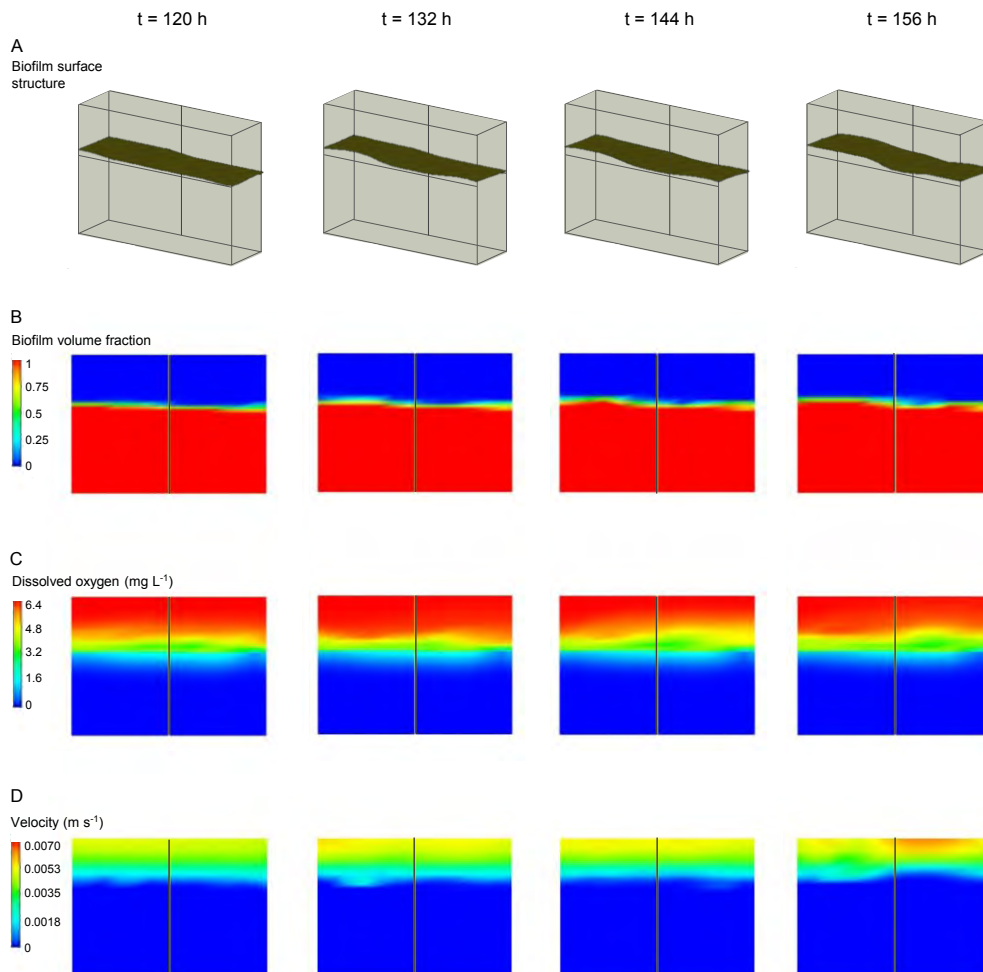


Figure 6.8. Simulated results for a 3D view of the biofilm surface structure (A) and biofilm volume fraction (B), dissolved oxygen (C) and velocity (D) contours for simulated times equal to 120, 132, 144 and 156 hours.

The effect of biofilm growth over hydrodynamics was also observed in Figure 6.8, being the velocity profiles higher than in the previous times, due to the narrowing of the fluid flow section. Specifically, the highest velocity gradients were noticed in the last simulation of this set ($t=156$ h). High gradients of velocity could come from numerical instabilities. During the computation of this case, the stabilization of the models was complex, requiring the use of second-order algorithms and small time steps (10^{-5} s) for the initial calculations. The time steps were changed to higher ones after stabilizing the case convergence, but it was required large computational time to gradually increase the time step to one which allowed us to model biofilm growth in an acceptable time. Possible solutions to improve the case convergence, such as a mesh refinement or consider smaller time steps could result in computational times too large. Additionally, experimental data for model verification could not be measured in the available experimental set-up. Therefore, although promising results coupling biofilm growth, fluid dynamics and transport mechanisms had been shown in this section, further research is required in order to clarify if biofilm growth can be modeled using fluid mass sources into CFD codes.

Other sets of simulations were performed considering higher inlet velocity in the domain, e.g. 0.01 m s^{-1} ($Re=20$) and 0.05 m s^{-1} ($Re=100$), being greater than the typical operating conditions. In particular, the results for 156 hours of simulated time and considering an inlet velocity of 0.05 m s^{-1} are shown in Figure 6.9. The biofilm growth was not observed in the volume fraction profile (Figure 6.9A), due to the shear rate produced on the biofilm phase (approximately 8 times higher than in normal operating conditions). In addition, it should be pointed out that the velocity gradients (Figure 6.9C) were not produced for this velocity.

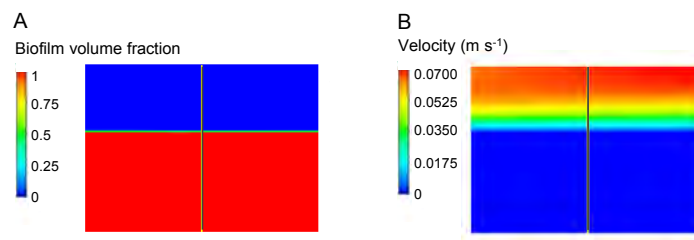


Figure 6.9. Simulated results for biofilm volume fraction (A), and velocity (B) contours for a simulated time equal to 156 hours and $v_{in}=0.05 \text{ m s}^{-1}$.

6.4.2.2. Effect of flow stress in curved channels: biofilm deformation and detachment

The last run of simulations was performed using curved channel geometry, i.e. D2 domain, to study the flow stress effect over a curved layer of biofilm (1 mm of thickness), mimicking the shape of carriers or a packed bed bioreactor. Biofilm mechanical responses were analyzed by imposing different flow velocities under laminar flow conditions. These velocities applied wear or strong shear stress over the fixed biofilm, producing biofilm deformation and/or detachment. Moreover, the modification in the biofilm structure could

influence the flow velocity field. Thus these numerical simulations could provide insights into the liquid-biofilm interaction, when hydrodynamics and complex biofilm structures present in a biosystem are considered. Particularly, Figure 6.10 shows the effect of weak shear flow conditions over fixed curved biofilms, with an inlet flow velocities of 0.005 m s^{-1} ($Re=45$).

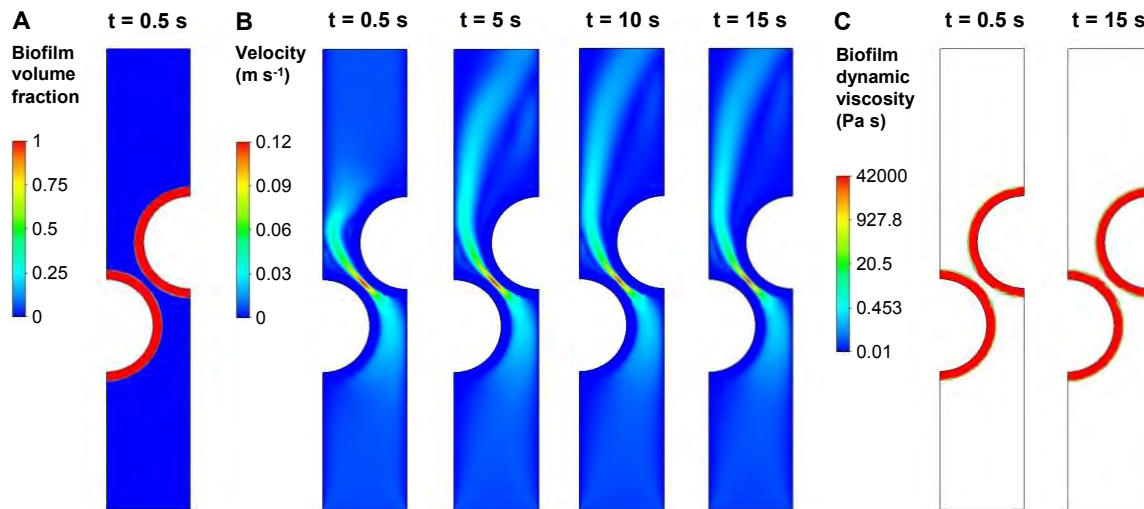


Figure 6.10. Simulated results of biofilm volume fraction (A), velocity (B) and viscosity (C) contours at the inlet flow velocity $v_{in2}=0.005 \text{ m s}^{-1}$ at different times.

In Figure 6.10, only one biofilm volume fraction profile is depicted, since the volume fraction of biofilm remained steady for all the computing time, i.e. constant shape, whereas velocity and biofilm viscosity contours are shown at different times. In all the profiles and contours, the red color indicates the highest values, e.g. for biofilm volume fraction profile the red zones are the ones where the biofilm volume fraction was equal to 1 (region full of biofilm). As can be seen in Figure 6.10, the biofilm structure shapes remained steady due to the shear stresses produced were low, remaining the viscosity value from 20 to 1000 Pa s in the flow pass zone, and above 10000 Pa s in the interior zones. The velocity profile was as the characteristic one between curved-solid regions, with higher velocity in the narrowing between the curves.

It should be pointed out that the abovementioned patterns were found in various simulations where inlet velocities were set above 0.005 m s^{-1} ($Re=45$) and below 0.01 m s^{-1} ($Re=90$), remaining always steady the biofilm structure shape, without deformation or surface enlargement as shown in Figure 6.10A. Due to the non-Newtonian character considered in the biofilm properties, slight differences were found in the values of the viscosity and velocity contours compared with the ones showed in Figure 6.10. The velocity profiles had the same profile, obtaining higher velocities in the contours as the inlet velocity was increased in the different simulations, i.e. from 0.005 m s^{-1} to 0.009 m s^{-1} . The increase in the velocity profiles produced changes in the shear rate profiles, which affected to the viscosity values. Lower

biofilm viscosities were obtained in the patterns when the cases with higher inlet velocities were computed. For inlet velocities over 0.01 m s^{-1} , small deformations in the biofilm shape started to appear near the zone with the narrowing between the curves. The phenomena simulated here correlate qualitatively with what Tierra and coauthors (Tierra et al., 2015) observed in experiments and simulations. In that work, defining the value of viscosity parameter similar to experimental measurements (1000 Pa s), the simulated biofilm protrusions showed negligible deformation for a maximum velocity of 0.008 m s^{-1} .

Figure 6.11 shows the deformation produced on biofilm structure and the velocity profiles at different instants for an inlet velocity of 0.1 m s^{-1} (corresponding to $\text{Re}=900$). The contours of biofilm volume fraction, velocity and biofilm viscosity are depicted. Initially, i.e. $t=0$ seconds, the profile of the volume fraction was equal to the one which is shown in Figure 6.10.

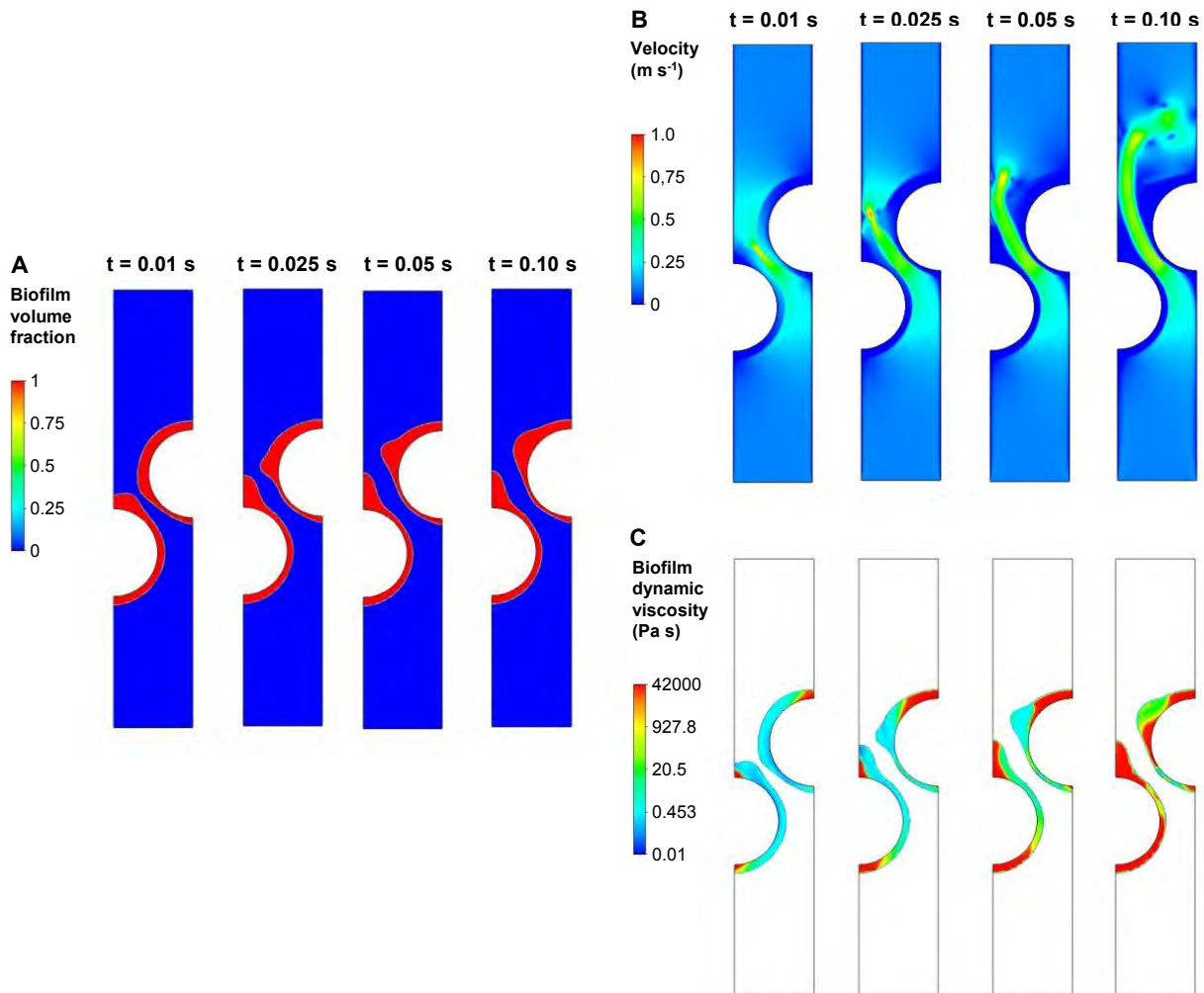


Figure 6.11. Simulated results of biofilm volume fraction (A), velocity (B) and viscosity (C) contours at the inlet flow velocity $v_{in2}=0.1 \text{ m s}^{-1}$ for times equal to 0.01, 0.025, 0.05 and 0.10 seconds.

As can be seen in the contours of volume fraction and velocity of Figure 6.11, the biofilm deformation started in the narrowing between the curves, where the velocity was initially the highest. In this zone, both biofilms were pushed by the flow, being the top curved biofilm the most exposed to the higher velocity field. Moreover, the velocity profile evolved and formed a jet passing between the two biofilms, for finally forming an eddy over the top curved biofilm ($t=0.1$ s). At that time, the viscosity in most of the biofilm was over 10000 Pa s, being from 10 to 1000 Pa s in the flow pass zone. It should be noted that Stewart (2012) detailed the formation of complex hydrodynamic behaviors, such as recirculating eddies, both on the upstream and downstream of biofilm protuberances under laminar flow conditions. Similar flow patterns and biofilm deformation were also noticed in simulations with inlet velocities over 0.1 and below of 0.19 m s^{-1} , but the shear rate reached was still not enough for detaching the biofilm. Even so, an observable biofilm surface area enlargement was generated in all the cases, which should be considered in mass transfer mechanisms.

Quantitatively, for the case depicted in Figure 6.11, after 0.04 seconds the biofilm structure of the bottom curve achieved a stable state in the deformation, the structure of the top curve reached it after 0.02 seconds more, and the fluid flow was steady between the curved regions, starting to form an eddy over that region. When biofilm structures reached the constant shape ($t>0.06$ s), the 24% of the initial volume fraction present in the bottom curved zone had been displaced, whereas in the top curved zone, the 27.3% of initial volume fraction had been moved.

Figure 6.12 depicts the deformation and detachment produced on biofilm structure at different instants for an inlet velocity of 0.2 m s^{-1} (corresponding to $Re=1800$). The contours of biofilm volume fraction, velocity and biofilm viscosity are shown. Initially, i.e. $t=0$ s, the profile of the volume fraction was equal to the one which is shown in Figure 6.10. As can be seen in Figure 6.12, after 20 milliseconds, the biofilms over curved zones were displaced in the flow direction, forming accumulations in both upper parts of each curved region. After 30 milliseconds more, the accumulated biofilm over the bottom curved zone was stretched, and a streamer was formed in the biofilm accumulation over the top curved region. The streamer was stretched until detached ($t>0.05$ seconds), and the loose part of biofilm was moving by the domain top part, propelled by the flow patterns ($t=0.1$ and $t=0.15$ s). At $t=0.155$ s, the biofilm loose part started to leave the domain, and another different streamer was formed in the biofilm accumulated over the top curved region. For $t>0.2$ s, the biofilm structure shape reached a steady-state, having significant values of viscosity (from 5 to 42000 Pa s) most of the structure.

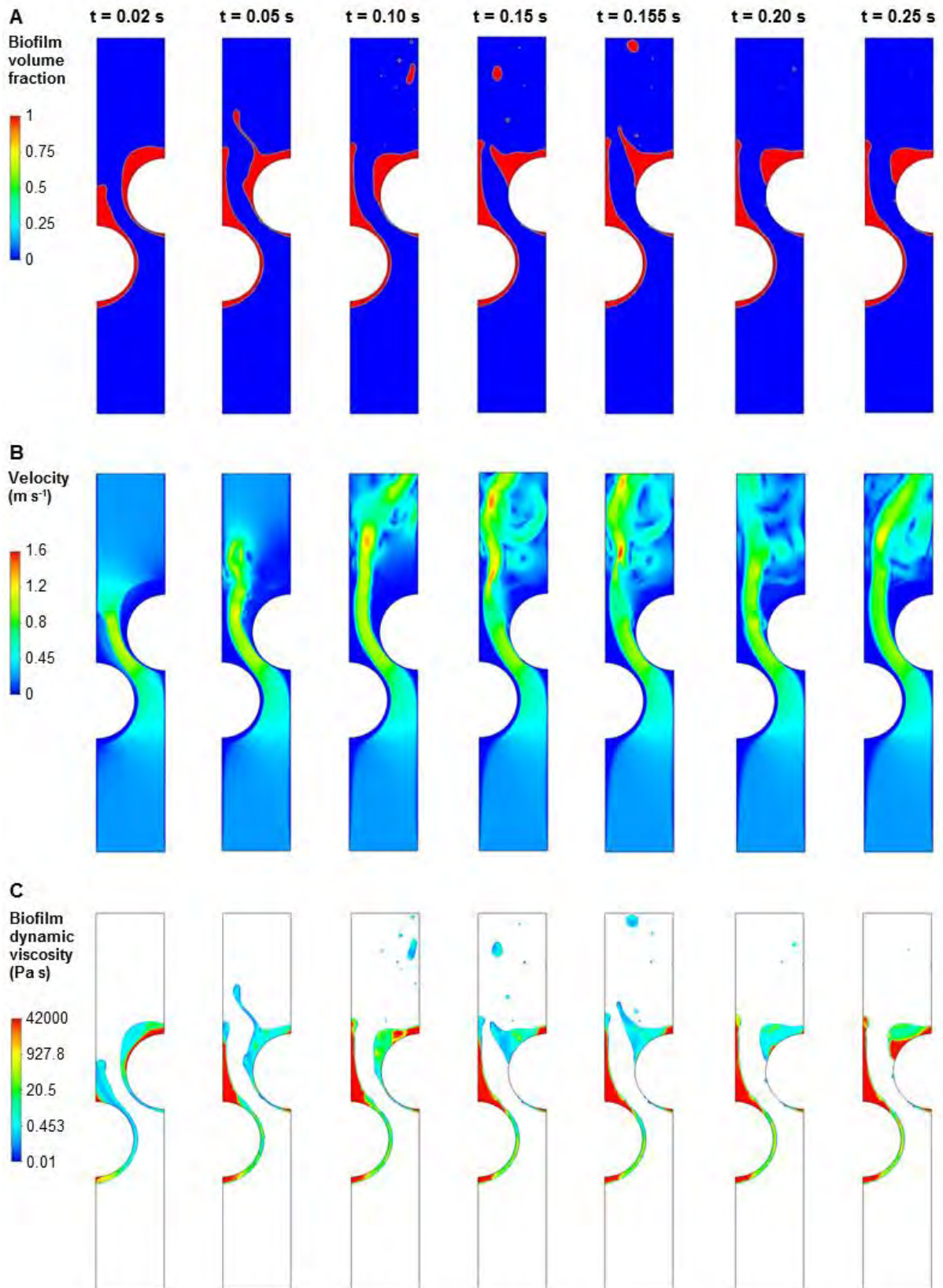


Figure 6.12. Simulated results sequence of biofilm volume fraction (A), velocity (B) and viscosity (C) contours at the inlet flow velocity $v_{in2}=0.2 \text{ m s}^{-1}$ and for times equal to 0.02, 0.05, 0.10, 0.15 s, 0.0155, 0.20 and 0.25 seconds.

The results reported in Figure 6.12 could be in qualitative agreement with the experimental observations reported by Stoodley et al. (1999a), who described biofilm deformation, streamers formation and streamers detachment for velocities of 1 m s^{-1} . Later, same conditions were reproduced in a fluid-structure interaction model (Towler et al., 2007), considering the biofilm as a viscoelastic material using the Burger model, which parameters were chosen such that the biofilm strain response was approximately equal to the strain observed experimentally by Stoodley et al. (1999a). The Burger parameters listed on Towler et al. (2007) were greater (almost always one order of magnitude) than the Burger parameters reported for the biofilms considered in this work (see Chapter 5). As explained in Chapter 5, larger parameters indicate high opposition to deformation, presenting a stiffer character the biofilm examined by Stoodley and coworkers (Stoodley et al., 1999a) than the biofilm analyzed in this chapter. Therefore, it was consistent with the flow regime required in our case to deform and detach the biofilm, since our heterotrophic biofilm was softer.

The irregularities and the area enlargement generated over biofilm surface were patent for the considered flow conditions, including the mass loss. The local interfacial area had much greater variability than in the previous cases. In a quantitative analysis, the 42% of the initial volume fraction present in the bottom curved zone had been displaced (from its initial position) after 0.2 seconds; in the top curved zone, the 56% of initial volume fraction had been moved or detached, the second one due to the streamer formed in that zone. This streamer finally detached, representing the quantity of biofilm which left the computational domain only the 5.5% of initial biofilm volume.

In general, the instabilities presented by the velocity pattern, i.e. formation of jets and eddies, produced the deformation and detachment in the biofilms zones where viscosity had lower values due to the higher shear rates applied over that regions. After to biofilm deformation and previous to its detachment, biofilm accumulations formed were stretched out forming streamers, which finally detached from the whole of biofilm. Recently, the vortical motion has been pointed as a hydrodynamic mechanism responsible for the formation of the streamers (Rusconi et al., 2010). Additionally, the formation of a Kármán vortex street behind the biofilm streamer has been computationally confirmed to create eddies that influenced the streamers growing downstream (Taherzadeh et al., 2010).

Finally, the results above presented implied that biofilm mechanics required for resistance to deformation, stretching and detachment can be largely attributed to biofilm viscosity and its non-Newtonian character. These findings were in agreement with previous experimental and numerical works (Stoodley et al., 1999a; Rusconi et al., 2010; Tierra et al., 2015).

6.4.2.3. Model application example: Simulation of biofilm control strategies

In biofilm-based technologies for waste abatement, mechanical strategies such as backwashing are used to remove the accumulation of unwanted biofilms on the surfaces (Mendoza et al., 2004; Safari et al., 2015). In treatment plants which employ these

technologies as a major unit process, backwashing is the key operational step to control biofilm growth, removal, and renewal (Liu et al., 2016). In this section, the CFD model effectiveness to reproduce biofilm backwash was analyzed.

In the previous set of simulations, biofilm detachment was observed for an inlet velocity of 0.2 m s^{-1} (Figure 6.12). This velocity was used in the simulations of backwashing control strategies, but in these new simulations the flow direction of the liquid phase was in the opposite direction, i.e. from top to bottom. Two different strategies were simulated: (1) a continuous backwashing with a fluid flow velocity of 0.2 m s^{-1} ; and (2) a sequence of ON-OFF pulses (time of pulse equal to 0.05 s) being the velocity equal to 0.2 m s^{-1} in ON periods. Both strategies were computed for a total time of 0.30 s.

Figure 6.13 depicts the deformation and detachment produced on biofilm structure at different instants for a continuum backwash velocity of 0.2 m s^{-1} (strategy 1). The contours of biofilm volume fraction, velocity and biofilm viscosity are shown. The patterns found were not symmetric with respect to the results presented in Figure 6.12 (reverse flow), having a larger destructive effect the backwash simulation. Detachment of small biofilm pieces was produced earlier than $t=0.05 \text{ s}$ and in the curved zone close to the fluid entrance, which was not been noticed in the previous simulations. Comparing equal frame times (Figure 6.12 versus 6.13), it is observed that a larger amount of biofilm fraction was displaced and/or detached from its initial position with the backwashing strategy. In addition, the biofilm structure shape still had not reached a steady-state after 0.2 seconds. For $t=0.3 \text{ s}$, the biofilm in the curved zone near the fluid entrance was reaching a constant shape, having significant values of viscosity (from 5 to 42000 Pa s) most of the structure. In the other curved zone, still some detachment could be produced on biofilm structure in the regions where the flow patterns were affecting, with lower biofilm viscosity. Probably all these differences can be attributed to the formation of small eddies near the biofilm surfaces, producing additional forces to pinch and elongate or detach the biofilm. The formation of small eddies near the biofilm surface was rarely observed in the previous simulations when the flow went up from the inlet to the outlet.

Figure 6.14 depicts the deformation and detachment produced on biofilm structure at different instants for a non-continuous backwash (strategy 2), showing the contours of biofilm volume fraction, velocity and biofilm viscosity. The strategy 2 alternated pulses of 50 milliseconds with velocities of 0.2 m s^{-1} in the ON period, and 0 m s^{-1} in the OFF period, i.e. the simulation started with an ON period, being the ON periods the ones from $t>0$ to $t=0.05 \text{ s}$, $t>0.1$ to $t=0.15 \text{ s}$, and $t>0.2$ to $t=0.25 \text{ s}$. The results for times equal to $t=0.02$ and $t=0.05 \text{ s}$ were the same that were shown in Figure 6.13.

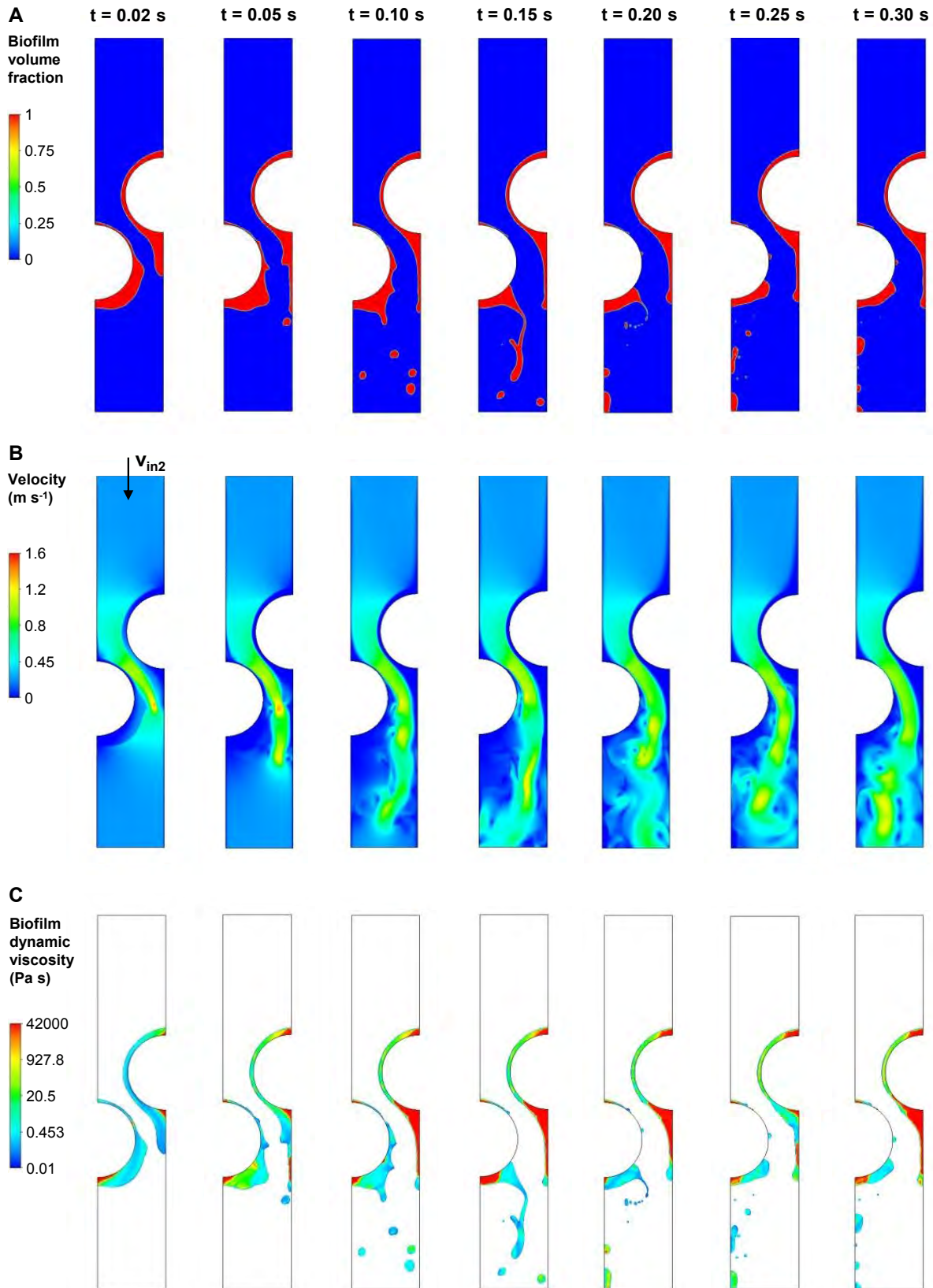


Figure 6.13. Simulated results sequence of biofilm volume fraction (A), velocity (B) and viscosity (C) contours at continuous backwash flow velocity $v_{in2}=0.2 \text{ m s}^{-1}$ (frame time (t) equal to 0.02, 0.05, 0.10, 0.15 s, 0.20, 0.25 and 0.30 seconds).

As can be seen in backwashing strategy 2 (Figure 6.14), after $t=0.05$ s, the first ON period was generated until $t=0.1$ s. Comparing the results for time $t=0.10$ s (Figure 6.13 versus 6.14) some differences can be observed. The most remarkable dissimilarities were in the thickness and the shape of the biofilm in the areas most affected by fluid patterns. It can be observed a thicker biofilm and less deformed surface after the OFF period (Figure 6.14), instead of a thin biofilm and more deformed structure after 10 milliseconds of continuous backwashing (Figure 6.13). In Figure 6.14, some frames of a backwashing OFF period (from 0.05 to 0.10 s) for times equal to 0.055, 0.065 and 0.075 s can be observed. Analyzing in detail the sequence for the volume fraction profiles, it was noticed a viscoelastic behavior showing biofilm time-dependent recoil (or recovery) and residual strain when the shear-stress caused by the flow was removed. The biofilm recoil was produced for 40 milliseconds approximately, being the biofilm back to a close position to the original one. In the velocity profiles, it can be observed the residual velocity patterns, which were reducing their intensity and forming eddies along the OFF period. The vortexes remained formed until the end on OFF period, possibly playing a role in biofilm recovery. After that time, the biofilm viscosity was near to reach steady values, being the larger ones in the curved zone proximate to the fluid entrance. In the downstream curved zone, biofilm viscosity was lower, since the residual velocity patterns still had an effect. These results were in agreement with previous studies, which have reported that biofilms exhibit both elastic recoil and residual strain caused by viscous flow (Klapper et al., 2002; Towler et al., 2003; Fabbri et al., 2016b). In addition, other biofilm models, such as the one presented by Alpkvist and Klapper (2007b) to simulate deformation and detachment of biofilms based on the immersed boundary method, can reproduce the recovery behavior. After $t=0.10$ s, another ON period started in which the biofilms in both curved zones where stretched again in the direction of the flow, forming a streamer in the curved zone near the outlet. The second OFF period began at $t=0.15$ s, in which the biofilm recoil was generated in both zones, being more noticeable in the downstream curved zone. During the biofilm recovery, the residual velocities produced the detachment of the formed streamer and other biofilm pieces. In the third ON period ($t > 0.20$ and $t > 0.25$ s), the biofilms deformation was again generated in the flow direction.

In a quantitative analysis, in the backwashing strategy 1, the 67% of the initial volume fraction present in the bottom curved zone (which now is near the inlet fluid) had been displaced (from its initial position) after 0.2 seconds, and in the top curved zone, the 56% of the initial volume fraction had been moved or detached. In backwashing strategy 2, the 35% of the initial volume fraction present in the bottom curved zone had been displaced after 0.2 seconds, and the 38% of initial volume fraction had been moved or detached in the top curved zone, having a strong effect in the biofilm conservation the different OFF periods present in this second strategy.

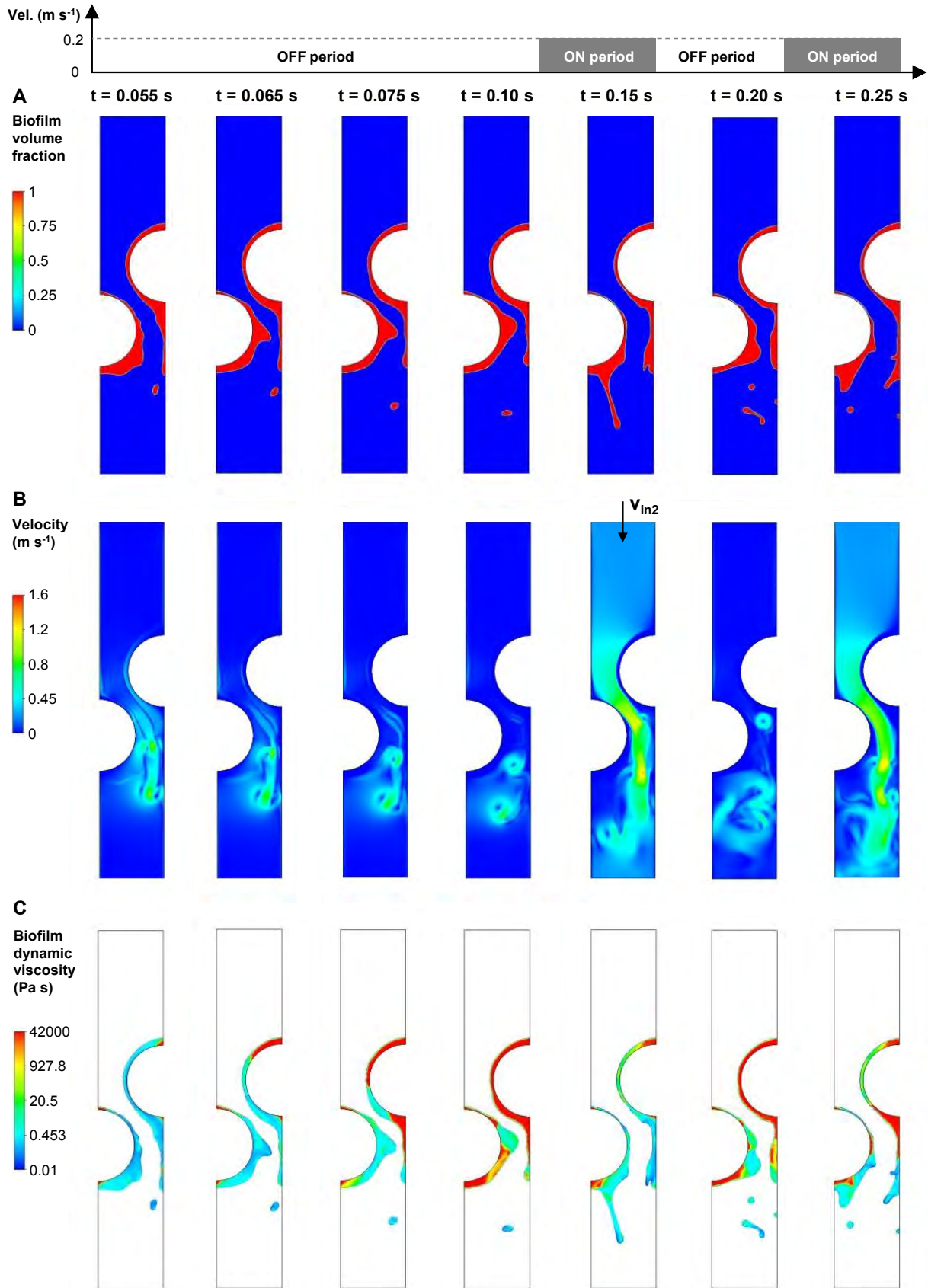


Figure 6.14. Simulated results sequence of biofilm volume fraction (A), velocity (B) and viscosity (C) contours at non-continuous backwash flow velocity of $v_{in2}=0.2 \text{ m s}^{-1}$ (frame time (t) equal to 0.055, 0.065, 0.075, 0.10, 0.15 s, 0.20 and 0.25 seconds).

From previous results arise that variations in the backwashing strategies are required to help to maintain the biofilm fixed on the support in some biosystem parts. The OFF periods present in strategy 2 produced a backwashing less destructive than in strategy 1. Even so, both strategies seem to be quite aggressive in some biosystem regions, where high shear rates were generated, thus reducing considerably biofilm viscosity and facilitating its detachment. Possibly, a pulse strategy with different velocities in the ON periods, where second and third ON pulse have velocities below 0.2 m s^{-1} , e.g. 0.1 m s^{-1} , could produce lower shear rates. Another variation on the strategies could be the redirection of incoming fluid, e.g. propelling with an angle of 45° , in order to soften the flow pattern that directly hits on biofilm curved zones.

6.5. CONCLUSIONS

In this chapter, CFD two-phase models which couple fluid dynamics over viscoplastic fixed-bed biofilms were developed to evaluate the capabilities of this novel approach to model biosystems performance. Therefore, the biofilm-flow interaction in various laminar flows and geometries were simulated, showing important findings. Mass transfer and transport mechanisms in a flat biofilm were properly verified, analyzing transfer process to the biofilm. The role of the concentration boundary layer thickness under laminar flow was observed and described numerically by correlating inversely Re number and mass transfer coefficient. The two-phase model predicted growth patterns consistent with heterogeneous substrate distributions. Moreover, stretching, recoil and ultimate detachment phenomena in biofilms were reproduced in the simulations. These findings suggest that the new biosystems modeling approach achieved qualitatively good simulation results.

The present study confirms previous findings and promotes additional evidence suggesting that biofilm mechanics required for resistance to deformation, stretching and detachment can be largely attributed to biofilm viscosity and its non-Newtonian character. In addition, the obtained results provided very significant insight about the influence of liquid fluid dynamics on biofilms structure. In this way, it would be interesting to assess the effects of turbulent and/or gas flow patterns over fixed biofilms, which are present in biofiltration systems. As a future work, the development of much more computationally intensive three-dimensional models contemplating different scale times could be used to study biofilm control strategies in complex biosystems.

Finally, although promising results coupling biochemical phenomena with mechanical behavior of biosystems have been found, further research is required to improve the growth model using a fluid mass source. Additionally, experimental data are required to validate the model capabilities when growth, deformation or detachment are reproduced.



MULTIPHASE CFD MODELING OF TURBULENT FLOWS OVER FIXED-BED BIOFILMS

After the promising results for modeling the effect of shear flow over fixed biofilms showed in Chapter 6, the motivation of this chapter was to test more capabilities of the developed two-phase CFD models, in order to reproduce all hydrodynamics conditions to which biosystems can be exposed. Particularly, CFD multiphase models were developed to characterize turbulent gas flows behavior over biofilms attached to walls, and verifying simulated results to confer identity to CFD approach. Thus, this chapter is surely the most ambitious of this thesis since extreme flow conditions, i.e. very high strain rates, were reproduced, additionally to consider the interaction air-biofilm, which is rarely modeled. To this aim, the CFD multiphase model developed in the previous chapter was completed including turbulence and near-wall treatment models. After verifying the performance of the developed model, the model allowed to estimate the predominant parameters influencing the biofilm disruption and removal under air-jet impingements.

Abstract

Experimental evidence exists showing that high-speed micro-sprays can be used effectively to remove biofilms from the surface where they grow, producing instabilities such as biofilm displacement, ripples formation, biofilm elongation to finally breaking off, droplets formation, and fluidization. The aim of this chapter was to extend the use of fluid-structure interaction approach developed in Chapter 6 to model turbulent flows over fixed-bed biofilms, being this the first numerical interpretation of the mechanisms behind the impact of turbulent flows ($Re_{inlet} > 2500$) on the biofilm structure. 2D multiphase models were developed, thus mimicking scenarios where air jet impacts perpendicularly on a thin biofilm layer ($\approx 55 \mu\text{m}$) with velocities over 40 m s^{-1} , and verifying the results with experimental data recorded with high-speed camera. In this study, it was examined whether the impingement at a high shear rate, together with the properties of the fluid jet and biofilm, were both enhancing ripples formation, biofilm disruption and removal by liquefaction. Hereby, it was clearly shown that high-speed jets favor the mixing process between the fluid jet and the biofilm, causing a quick fluidization of the biofilm. Additionally, it was shown that the biofilm viscosity and thickness, and the surface tension (between biofilm and jet fluid), play relevant roles in biofilm disruption and removal.

A modified version of this chapter is being prepared for publication as:

L. Prades, S. Fabbri, A.D. Dorado, X. Gamisans, P. Stoodley, C. Picioreanu, 2018. **Computational investigation of biofilm disruption induced by gas jets impingement.**

7.1. INTRODUCTION

During the last years, closer attention has been paid to the behavior of biofilms under turbulent flows, since it can be directly related to biofilm control. Different patterns have been described during the exposure to turbulent flows, such as the formation of migratory ripples and surface instabilities (Stoodley et al., 1999c; Fabbri, 2016), fluid-like behavior, and stretching to finally breaking off of the biofilm (Fabbri, 2016; Fabbri et al., 2016b). In addition, experimental studies have reported the viscoelastic character of biofilms when they were exposed to turbulent flows (Klapper et al., 2002), hypothesizing that both generated instabilities and biofilm viscoelastic properties can enhance mass transfer (Fabbri et al., 2016a).

Several biofilm constitutive models have been developed considering viscoelastic properties and interaction biofilm-fluid (Horn and Lackner, 2014; Fabbri and Stoodley, 2016). Biofilms elongation and detachment under laminar flow conditions have been modeled using the phase field approach (Zhang et al., 2008; Tierra et al., 2015) and the immersed boundary method (Alpkvist and Klapper, 2007b). Fluid-structure interaction models have been used to describe the movement of biofilms streamers (Taherzadeh et al., 2010) and the deformation of biofilm with shape of half-circle under high-speed flow (Towler et al., 2007). In addition, the interfacial instabilities generated by jet impingements have been modeled as Kelvin-Helmholtz instabilities (Fabbri et al., 2017). However, the real interaction between biofilm and turbulent flow and how turbulent impact disrupts biofilm properties and structure have not been yet reproduced.

The turbulent character of air/water jet impingements over biofilms and their efficiency as a removal techniques have been experimentally demonstrated and analyzed in detail, (Fabbri, 2016; Fabbri et al., 2016b, 2017). Therefore, their numerical investigation can help to clarify the mechanics behind the biofilm disruption generated by those turbulent flows. Computational fluid dynamics (CFD) models have been developed to describe air jet impingements into water vessels (Forrester and Evans, 1997; Nguyen and Evans, 2006; Solórzano-López et al., 2011), using the volume of fluid (VOF) method to track accurately the interface position between fluids. VOF method has also been used to predict the wall shear stress produced by turbulent flows over biofilms (Rmaile et al., 2015) and to characterize the removal of biofilm by impinging water droplets (Cense et al., 2006). Nevertheless, the turbulence effect on the walls and the biofilm as an extra phase have not been considered in these last models.

Taking into account the stated above, the aim of this chapter was to extend the multiphase model developed in Chapter 6, in order to test new model capabilities, trying to reproduce all hydrodynamic conditions to which biosystems can be exposed. In particular, the turbulent character of air jet perpendicular impingements over fixed-bed biofilms experimentally analyzed by Fabbri (2016) was reproduced. Thus, 2D CFD models were

developed to simulate the described behavior of air impingements biofilms, including turbulent models to compute fluid dynamics and considering near-wall treatment. The non-Newtonian character of the biofilm was tested under high shear rates, analyzing the biofilm response to know what mechanisms were driving its disruption under perpendicular air jet impacts. The verification of the simulated results was performed with part of the experimental data published in the work of Fabbri (2016). The developed model was used to study the parameters influence, such as biofilm viscosity and thickness, nozzle-jet velocity, and surface tension (between biofilm and jet fluid), over biofilm deformation and removal.

7.2. MATERIALS AND METHODS

7.2.1. Inoculum and culture media for biofilm growth

Streptococcus mutans (*S. mutans*) biofilms UA159 (ATCC 700610) were grown for 72 hours on microscope glass slides. After the growth period, the biofilm covered-slides were gently rinsed in 1 % (wt/vol) phosphate-buffered saline solution (Sigma-Aldrich) and placed in petri plates. Further information can be found in Fabbri (2016).

7.2.2. Experimental set-up

Biofilm samples were exposed to an air jet generated from a piston compressor (ClassicAir 255, Metabo) at a 90° angle. The internal diameter of the piston compressor tip was 2 mm, which was held at a distance of 5 mm from the biofilm. The shooting was recorded at 2000 frames per seconds with a high-speed camera MotionPro X3 (IDT). The high-speed camera was placed in order to record the back view of the biofilm covered microscope slide. Experiments were performed in triplicates. A rotameter was used to estimate the average air jet velocity outside the nozzle ($v=41.7 \pm 1.5 \text{ m s}^{-1}$). Considering the viscosity and density of air at 20°C and 1 atm, the relative Reynolds number of the jet ($Re_{jet}=5516 \pm 203$) was also determined. Further details about the experiments can be found in Fabbri (2016).

With the previous data, a coarse estimation of Re numbers (Expression 6.3) for air and biofilm in the set-up was performed. For the air, an average velocity of 10 m s^{-1} and length characteristic (L) equal to the distance between the tip and the biofilm ($L = 5 \text{ mm}$) were considered, obtaining $Re_{air} = 3300$. For the biofilm, the characteristic length was defined equal to biofilm thickness ($L \approx 55 \mu\text{m}$), the density was considered equal to the water density, and to consider the worst-case scenario, i.e. the largest number of Reynolds, velocity and viscosity values of 0.2 m s^{-1} and 0.001 Pa s , respectively, were used, computing a $Re_{bio} = 11$.

7.2.3. Biofilm thickness measurement

Biofilm samples, i.e. the control samples and those exposed to shootings, were fixed with 4 % (wt/vol) paraformaldehyde and subsequently stained with Syto 63. Samples were imaged by confocal laser scanner microscope (CLSM, Leica TCS SP5). To determine the

biofilm thickness prior to the experiments, three random confocal images were taken on each of three independent replicate control biofilm slides. The thickness of the control biofilms was measured by COMSTAT software from the confocal images (Heydorn et al., 2000). Further information about these procedures can be found in (Fabbri, 2016).

7.2.4. Data post-processing

Fast Fourier transform (FFT) was used to determine the dominant period (T) and frequency (f) of transient ripples formed during the *S. mutans* biofilm exposure to the air jet. Frames from experimental videos and data exported from the simulated results were post-processed in a MATLAB® Release 2016b function implemented to calculate the FFT.

The ripples wavelength (λ_R), defined as the distance between two peaks, was measured using the protocol described in (Fabbri, 2016) for the experimental and the simulated data.

The ripples velocity (v_R), i.e. the distance the wave travels in a given time, was calculated using the Expression 7.1 for both experimental and simulated data.

$$v_R = \frac{\lambda_R}{T} = \lambda_R \cdot f \quad (7.1)$$

7.3. MATHEMATICAL MODEL

7.3.1. Assumptions

The main assumptions considered in the mathematical model are the following:

- The gas and liquid phases are assumed to be incompressible. In the particular case of gas phase, a Mach number below 0.3 was computed thus neglecting compressibility effects (Potter et al., 2012).
- A uniform velocity profile with a constant value is considered to leave the compressor nozzle.
- The flow is considered to be symmetric with respect to the vertical plane.
- The gas jets are in turbulent regime (see section 7.2.2).
- The biofilm is considered as a thin layer with a constant thickness.
- The biofilm is characterized as a non-Newtonian fluid with density equal to water.

7.3.2. Governing equations

7.3.2.1. Coupled Level-Set and Volume of fluid (VOF) model

Level-set and VOF model are methods which consider an accurate tracking of the interface for computing two-phase flows with topologically complex interfaces. In the level-set method (Osher and Sethian, 1988), the interface is captured and tracked by the level-set function, defined as a signed distance from the interface. The spatial gradients can be

rigorously calculated, since the level-set function is smooth and continuous, producing accurate estimates of interface curvature and surface tension force caused by the curvature. However, the level-set method is found to have a deficiency in preserving volume conservation (ANSYS Inc, 2016). On the other hand, in the VOF method (Hirt and Nichols, 1981), the volume fraction of a particular phase is computed and tracked in each cell rather than the interface itself, being naturally a volume-conserved method. The VOF function, i.e. the volume fraction of a particular phase, is discontinuous across the interface which difficulty the accurate calculation of its spatial derivatives. ANSYS Fluent provides a coupled level-set and VOF approach, offering a robust interface-tracking solution, which is governed by the following equations (ANSYS Inc, 2016).

The level-set function, φ_{LS} , is defined as a signed distance to the interface, ϑ :

$$\varphi_{LS}(x, t) = \begin{cases} +|d| & \text{if } x \in \text{the primary phase} \\ 0 & \text{if } x \in \vartheta \\ -|d| & \text{if } x \in \text{the secondary phase} \end{cases} \quad (7.2)$$

Where x is the position in the grid, t is the time, and d is the distance from the interface.

The evolution of the level-set function is given in a similar fashion as to the VOF model:

$$\frac{\partial \varphi_{LS}}{\partial t} + \nabla \cdot (\vec{U} \varphi_{LS}) = 0 \quad (7.3)$$

Where \vec{U} is the underlying velocity field.

Finally, the momentum equation is defined as the VOF model momentum equation (further details of the VOF model can be found in Chapter 6, section 6.3):

$$\frac{\partial(\rho \vec{U})}{\partial t} + \nabla \cdot (\rho \vec{U} \vec{U}) = -\nabla P + \nabla \cdot [\eta(\nabla \vec{U} + \nabla \vec{U}^T)] + \rho \vec{g} + \vec{F}_{ST} \quad (7.4)$$

Where ρ is the density, η is the viscosity, g is the gravitational constant and F_{ST} is the force arising from surface tension effects.

More details about the implementation of the couple level-set and VOF model in ANSYS Fluent can be found in ANSYS Inc (2016).

7.3.2.2. Turbulence model

The standard k - ε model (Launder and Spalding, 1972) has been used to describe gas jet impingements onto liquid free surfaces (Nguyen and Evans, 2006; Solórzano-López et al., 2011). However, examinations of Reynolds-averaged Navier–Stokes (RANS) numerical modeling techniques showed that these models give large errors compared to experimental data sets, recommending the shear-stress transport (SST) k - ω model which produce better predictions of fluid properties in impinging jet flows (Zuckerman and Lior, 2006). In addition, SST k - ω model was employed, instead of large eddy simulation (LES) approach, since it has

the best compromise between solution speed and results accuracy for modeling of jet impingements (Zuckerman and Lior, 2006).

The SST k - ω model was developed by Menter (1994) using the standard k - ω model (Wilcox, 1998) and a transformed k - ϵ model. The main difference respects other turbulence models is the way in which the SST k - ω model calculates the turbulent viscosity, taking into account the transport of the principal turbulent shear stress. The SST k - ω model also incorporates a cross-diffusion term in the ω equation and a blending function to properly calculate the near and far-wall regions. The blending function triggers the standard k - ω model in near-wall regions and changes to the k - ϵ model in regions away from the wall.

I. Transport equations for the Shear-Stress Transport (SST) k - ω model

The turbulence kinetic energy, k , and the specific dissipation rate, ω , are obtained from the following transport equations, respectively:

$$\frac{\partial}{\partial t}(\rho k) + \frac{\partial}{\partial x_i}(\rho k U_i) = \frac{\partial}{\partial x_j} \left(\Gamma_k \frac{\partial k}{\partial x_j} \right) + G_k - Y_k + S_k \quad (7.5)$$

$$\frac{\partial}{\partial t}(\rho \omega) + \frac{\partial}{\partial x_j}(\rho \omega U_j) = \frac{\partial}{\partial x_j} \left(\Gamma_\omega \frac{\partial \omega}{\partial x_j} \right) + G_\omega - Y_\omega + D_\omega + S_\omega \quad (7.6)$$

Where U is the velocity field of the fluid. G_k represents the production of turbulence kinetic energy. G_ω represents the generation of ω . Γ_k and Γ_ω represent the effective diffusivity of k and ω , respectively. Y_k and Y_ω represent the dissipation of k and ω due to turbulence. D_ω represents the cross-diffusion term. S_k and S_ω are user-defined source terms for k and ω , respectively. More details about this model and definition of the individual terms can be found in ANSYS Inc (2016).

II. Wall boundary conditions for SST k - ω model

The no-slip condition, which has to be satisfied at the wall, has an effect in the mean velocity field, thus turbulent flows are significantly affected by the presence of walls. Nevertheless, the way in which the presence of the wall changes the turbulence is non-trivial. Very nearby to the wall, the tangential velocity fluctuations are reduced by the viscous damping, and the normal fluctuations are decreased by the kinematic blocking. In the outer part of the near-wall region, the large gradients in mean velocity produce turbulence kinetic energy and the turbulence is quickly augmented (ANSYS Inc, 2016).

In the near-wall region, the solution variables have large gradients, and transport of momentum and other scalar occur most vigorously. Therefore, the successful numerical solutions of wall-bounded turbulent flows are determined by a precise representation of the flow in the near-wall region.

The region near the wall is subdivided into three layers (see Figure 7.1). The innermost layer is called the *viscous sublayer*, in which the flow almost laminar, and the molecular

viscosity presents a predominant role in momentum and transfer. The outer layer is denominated the *fully-turbulent layer*, and turbulence has the dominant role. And the intermediate region between the *viscous sublayer* and the *fully turbulent layer* is called *log-layer* or *buffer layer*, where the molecular viscosity and turbulence effects are equally relevant.

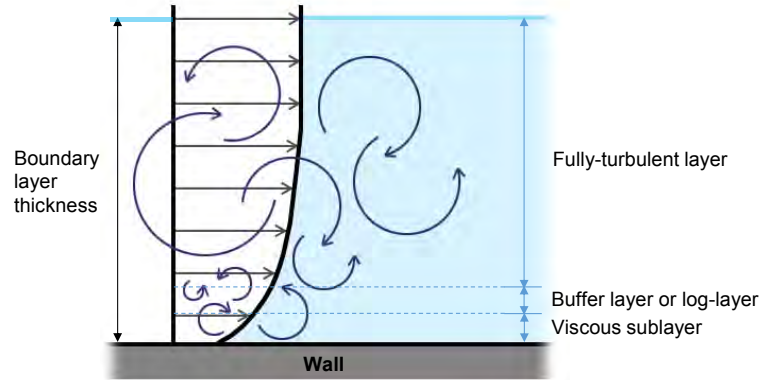


Figure 7.1. Development of the boundary layer over a flat plate under turbulent conditions (adapted from ANSYS Inc (2016)).

Two approaches can be used to model the near-wall region. In the first one, the regions in which the molecular viscosity plays a role, i.e., *viscous sublayer* and *buffer layer*, are not resolved. Instead, semi-empirical formulas, which are known as *wall functions*, are used to connect the viscosity-influenced region between the wall and the fully turbulent layer. The *wall functions* use obviates the need to modify the turbulence models to consider walls presence. On the other hand, in the second approach, the turbulence models are modified to enable the viscosity-influenced region will be resolved all the way to the wall, including the *buffer layer* and *viscous sublayer*, terming it as the *near-wall modeling* approach (ANSYS Inc, 2016).

The wall boundary conditions for the k equation in the $k-\omega$ models are treated in the same way as the k equation is treated when enhanced wall treatments are used with the $k-\epsilon$ models. This means that all boundary conditions for a relatively coarse mesh in the near-wall region will correspond to the wall function approach, while for the fine near-wall meshes, the appropriate low-Reynolds number boundary conditions, i.e. near-wall modeling approach, will be applied. In ANSYS Fluent, the *y^+ -insensitive wall treatment* is the default formulation for all ω equation-based models. Based on the dimensionless wall distance of the first grid cell (y^+), the *y^+ -insensitive wall treatment* is achieved by blending the linear (laminar) and logarithmic (turbulent) law-of-the-wall formulations, being y^+ defined as:

$$y^+ \equiv \rho \cdot U_\tau \cdot y / \eta \quad (7.7)$$

Where U_τ is the friction velocity computed as $U_\tau = (\tau_w / \rho)^{1/2}$ and y is the distance to the next wall, being τ_w the wall shear stress.

Moreover, ANSYS Fluent computes the value of ω at the wall as:

$$\omega_w = \frac{\rho \cdot (U^*)^2}{\eta} \cdot \omega^+ \quad (7.8)$$

Where U^* is the non-dimensional friction velocity and ω^+ is computed with the following analytical solutions for both the laminar sublayer and the logarithmic region, respectively:

$$\omega^+ = \frac{6}{\beta_i \cdot (y^+)^2} \quad (7.9)$$

$$\omega^+ = \frac{1}{\sqrt{\beta_\infty^*}} \cdot \frac{du_{\text{turb}}^+}{dy^+} \quad (7.10)$$

With parameters $\beta_i = 0.072$ and $\beta_\infty^* = 0.09$, and being $\frac{du_{\text{turb}}^+}{dy^+}$ the turbulent law-of-the-wall and inversely proportional to y^+ (for further details see ANSYS Inc (2016)).

It should be noted that Expression 7.9 goes to zero far enough away from the wall because of the $1/y^2$ dependency. Therefore, the wall treatment is defined for the ω -equation, which switches from the viscous sublayer to the log-layer formulations by means of blending function F1 as detailed in Menter (1994). To resolve the viscous sublayer, the first grid cell needs to be at about $y^+ \approx 1$. Instead, to locate the first cell in the log-layer, i.e. using wall functions, the y^+ value should have values in the range $30 < y^+ < 300$ (ANSYS Inc, 2016).

In the two-phase case computed in this chapter, one of the fluids (biofilm phase) has to be initialized as a thin layer with constant thickness over the entire wall. This fluid is characterized by being several magnitude orders more viscous than the air, i.e. the second phase present in the model. Therefore, the air is the only phase with turbulent behavior in the system (see Re numbers in section 7.2.2.), requiring to resolve the viscous sublayer from the interface air-biofilm, instead of from the wall as usually is done. In this work, due to the viscous character of biofilm phase, the viscous sublayer is resolved from the wall to the air-biofilm interface in equivalent conditions, since the viscosity is inversely proportional to y^+ (Expression 7.7) and low y^+ values are computed for high viscosities.

III. Turbulence modeling in the interface

When a multiphase system is considered, the physical properties of the phases present in the model should be taken into account, since an enormous contrast among them can be detected across the interface. This difference is manifested as a high-velocity gradient at the interface between two fluids, resulting in high turbulence generation in both phases. In this case, certain damping of turbulence is required for the accurate modeling of the interfacial area and the fluids flow behavior.

Various works (Egorov et al., 2004; Vallée et al., 2008; Höhne and Mehlhoop, 2014) have validated the use of the turbulence damping correction model. In ANSYS Fluent, the turbulence damping is available for the k - ω models. As described by Egorov et al., (2004),

the turbulence damping adds the following term S_i as a source S_ω to the ω -equation (Expression 7.6):

$$S_i = a_{pi} \cdot \Delta_n \cdot \beta \cdot \rho_{pi} \cdot \left(\frac{B \cdot \eta_{pi}}{\beta \cdot \rho_{pi} \cdot \Delta_n^2} \right)^2 \quad (7.11)$$

Where a_{pi} is the interfacial area density for the phase i , Δ_n is the cell height normal to the interface, β is the k - ω model closure coefficient ($\beta=0.075$), ρ_{pi} is the viscosity of phase i , B is the damping factor ($B= 0-100$) and η_{pi} is the viscosity of phase i . The factor a_{pi} activates the source term S_ω only at the free surface, where it cancels the standard ω destruction term of the ω -equation (Y_ω) and enforces the required high value of ω , and thus the turbulence damping.

In ANSYS Fluent, the Δ_n is calculated internally using grid information, and the default values for B is 10, since bigger values do not change the result for a solid wall (Egorov et al., 2004). In addition, the interfacial area density is computed as a function of the volume fraction:

$$a_{pi} = 2.0 \cdot \alpha_{pi} \cdot |\nabla \alpha_{pi}| \quad (7.12)$$

Where α_{pi} is the volume fraction of phase i and $|\nabla \alpha_{pi}|$ is the gradient magnitude of volume fraction.

Finally, the turbulence damping model near a free surface requires a grid which resolves the viscous sublayer near a free surface, i.e. the grid should have $y^+ \approx 1$ near the interface (Egorov et al., 2004).

7.3.3. Computational model parameters

7.3.3.1. Geometry and mesh

The schema of full experimental set-up, and the detailed description of the computational domain used to model the air jet impingements over biofilm thin layer are both shown in Figures 7.2A and 7.2B, respectively. A 2D axisymmetric computational domain was considered to represent the elevation view of the jet impact over biofilm, representing a slice of the actual experimental set-up. The domain length and height measured $L_x=15\text{mm}$ and $L_y=5\text{ mm}$, respectively. A uniform mesh by a prism scheme was defined in the entire domain. A refined grid was used in the region defined among points A-C-G-I to keep the aforementioned y^+ requirements ($y^+ \approx 1$) near walls and in the free surface, capturing accurately the deformation of the air-biofilm interface. In this 2D model, a prism layer mesh with growth rate no higher than ≈ 1.2 should be used (ANSYS Inc, 2016). The computational mesh used was composed of 450000 cells. A detail of the mesh in the more refined regions is shown in Figure 7.2C. Mesh quality was checked with the orthogonal quality parameter,

which had average values of 1 in all domain, confirming the good quality of the defined regular mesh.

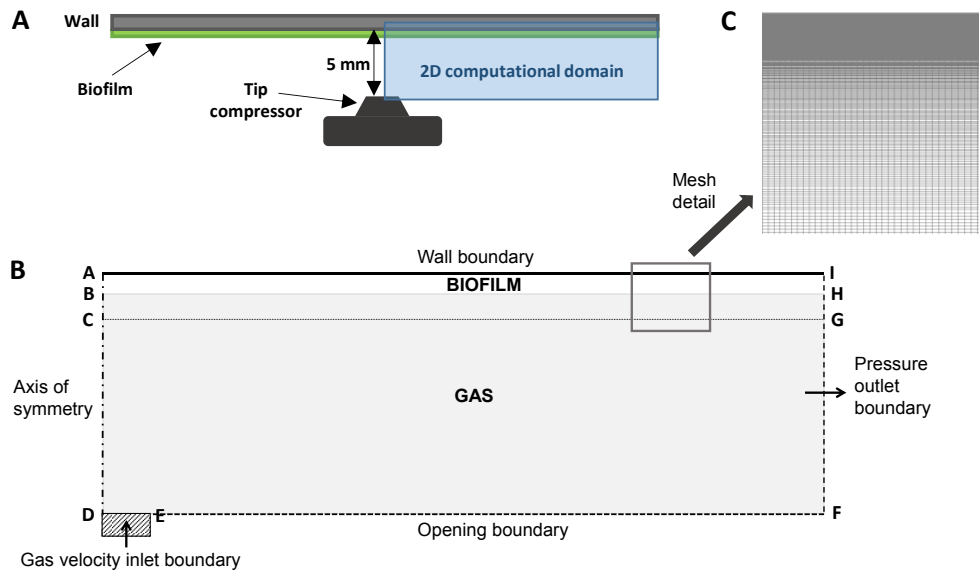


Figure 7.2. Full experimental set-up schema (A) and two-dimensional model description (B).

7.3.3.2. Boundary conditions

According to Figure 7.2, five types of boundary conditions were used to describe the flow field within the computational domain.

I. Axis of symmetry

The symmetry axis boundary was used along the line defined between the points A-D. The radial velocity component and the dependent variables gradients were equal to zero.

II. Walls

The wall boundary condition was imposed in the line between the points A-I, where the non-slip condition and zero turbulence were established. The near-wall modeling formulation was used to model the wall-bounded turbulent flow (for further details see the previous section).

III. Opening

The opening boundary was located in the line E-F. This part was opened to the atmosphere, being possible for the flow to enter and leave. Besides, the mass entering or leaving the domain depends on the mass balance.

IV. Pressure outlet

The pressure outlet boundary was located in the line defined by F-I points. The value for the relative static (gauge) pressure was set to zero, i.e. atmospheric pressure was assumed.

V. Velocity inlet

The inlet condition was established in the line D-E. Due to the symmetry condition, the length of the inlet is the half of the nozzle diameter, i.e., 1 mm. The velocity inlet boundary condition considered a uniform velocity profile and evaluated the turbulence as follows.

The turbulent energy, k , was computed as:

$$k = \frac{3}{2} \cdot (U \cdot I)^2 \quad (7.13)$$

Where U is the mean flow velocity and I is the turbulence intensity defined as (Solórzano-López et al., 2011):

$$I = 0.16 \cdot \text{Re}^{-1/8} \quad (7.14)$$

Where Re is the Reynolds number.

The specific turbulent dissipation rate, ω , was computed as:

$$\omega = C_{\mu}^{-1/4} \cdot \frac{\sqrt{k}}{l} \quad (7.15)$$

Where C_{μ} is an empirical constant with equal to 0.09 and l is the turbulent length scale, which is assumed to be 7% of the nozzle diameter.

7.3.3.3. Initial conditions

In the parameters initialization step, the gauge pressure, the velocity components and the set function level were set to zero in the entire domain. On the other hand, the values for the turbulent energy and the specific turbulent dissipation rate were computed using equations 7.13-7.15. Since the turbulent parameters were computed for the entire domain, an average velocity value calculated in the domain was used for determining U while the characteristic length was defined as $L_y=5$ mm. Finally, the volume fraction of the biofilm phase was initialized inside the domain, patching the region defined by the points A-B-H-I and setting the biofilm volume fraction equal to 1 in this region. In the default case, the length and height of the biofilm region were defined as $L_{xb}=15\text{mm}$ and $L_{yb}=0.055$ mm, respectively.

7.3.4. Numerical simulations

The mathematical model was implemented into the commercial fluid dynamics code ANSYS® Academic Research, Release 17.2. In particular, the finite-volume ANSYS Fluent solver was used to solve the equations of continuity and momentum. The governing equations were discretized using the second-order upwind scheme. The interpolation of the pressure values at the cell faces was performed by the momentum equation, and using the PRESTO (PREssure STaggering Option) scheme. The PISO (Pressure-Implicit with Splitting of Operators) algorithm was used to characterize the pressure-velocity coupling. Choosing the previous schemes and a segregated solver helped to save computational time and also improved convergence and computation stability. In the implemented VOF method, the

momentum equations were solved throughout the domain, and the resulting velocity field was shared among the phases. To track the free surface deformation, VOF model was coupled with level-set and the geo-reconstructed scheme was also applied. Transient simulations were run with the first order implicit formulation. After a sensitivity study, the maximum and optimum time step giving stable transient solutions was found to be 10^{-7} s. A total time of 20 ms of real-time was reached in each computation to guarantee stability in the solution, since the simulations reached a steady condition after 10 ms.

Two sets of simulations were carried out with the two-phase model. In the first series of simulations (from run 1 to 7), using experimental parameters measured for jet velocity (v) and biofilm thickness (th), the biofilm response (velocity, pressure, volume fraction, etc) with different non-Newtonian viscosities (η), i.e. estimated viscosity curves (EVC), and two surface tension values (γ) were recorded to fit the viscous properties according to the experimental data. The shear rate at which viscosities curves reached water viscosity values (i.e. fluidization) ranged from $10^4 - 3 \cdot 10^6 \text{ s}^{-1}$ (see section 7.4.1 for further details about the estimated viscosity curves (EVC₁, EVC₂, EVC₃, and EVC₄)). In the second series of simulations (from run 8 to 13), the effects of the inlet jet velocity and the biofilm thickness on biofilm response were determined by means of a parametric study, computing simulations with values for such parameters different from the experimentally used. Table 7.1 shows an overview of the numerical experiments.

Table 7.1. Overview of numerical simulations of jet impingements at velocity v on biofilm layer with thickness th , surface tension γ , and viscosity η .

Run	1	2	3	4	5	6	7	8	9	10	11	12	13
η (Pa s)	EVC ₁	EVC ₁	EVC ₂	EVC ₂	EVC ₃	EVC ₃	EVC ₄	EVC ₃					
γ (mN m ⁻¹)	36	72	36	72	36	72	36	36	72	36	72	36	36
th (μm)	55	55	55	55	55	55	55	55	55	55	55	27.5	110
v (m s ⁻¹)	40.1	40.1	40.1	40.1	40.1	40.1	40.1	20	20	60	60	40.1	40.1

7.4. RESULTS AND DISCUSSION

7.4.1. Biofilm characterization

Biofilm thickness and viscosity values of biofilms exposed to gas-jet impingement were required for model implementation.

The biofilm thickness was experimentally measured before the jet impingements, being $51.8 \pm 4.9 \mu\text{m}$ the thickness of the biofilm control samples (Fabbri, 2016). Therefore, the reference value of the biofilm thickness (th) was fixed in $55 \mu\text{m}$.

Regarding the viscous properties of *S. mutans*, it was necessary to know the dynamic viscosity at higher shear rates ($10^4 - 10^6 \text{ s}^{-1}$). Viscosity measurements at such high strain

rates are usually not possible, since a large diameter system is needed. In addition, no data has been found in the literature related to the characterization of the rheological behavior as a non-Newtonian fluid of *S. mutans* based biofilms. The only reference which can provide experimental data is Vinogradov et al. (2004), in which performing oscillatory analysis, they measured the complex viscosity besides demonstrating the shear-thinning character of *S. mutans* biofilms.

The complex viscosity can be related to the dynamic viscosity (Kulicke and Porter, 1980). As mentioned in Chapter 5, the empirical Cox-Merz rule states that values of the complex viscosity and the dynamic shear viscosity should be identical at a comparable time scale of observation (angular frequency and shear rate, respectively). Wloka et al. (2004) performed steady and oscillatory shear flow rheological analysis on extracellular polymeric substances (EPS) solution extracted from *Pseudomonas aeruginosa*. They applied the Cox-Merz rule to compare the dynamic and complex viscosities, obtaining an equivalent trend between both parameters. However, some discrepancies in the Cox-Merz rule has been reported in gels and polysaccharides (Ross-Murphy, 1995; Ikeda and Nishinari, 2001), obtaining larger values for the complex viscosity. Biofilms have been frequently characterized as biopolymer gels (Mayer et al., 1999; Wilking et al., 2011; Chapter 5), which was also noticed by Vinogradov et al. (2004) when performing oscillatory analysis in *S. mutans*. Samples with gel character have another kind of physical interactions, in addition to mechanical and/or chemical ones, leading to deviations between dynamic and complex viscosities values (Mezger, 2006).

In this work, the dynamic viscosity of the biofilms tested and modeled was estimated using the complex viscosity reported by Vinogradov et al. (2004) and the dynamic viscosity presented in Chapter 5 for heterotrophic biofilms as references. The shear-thinning behavior described by Vinogradov et al. (2004) showed the non-Newtonian character of the *S. mutans* biofilms. To reproduce this non-Newtonian character, the Herschel-Bulkley model (Expressions 5.1 and 5.2) was used, as in the heterotrophic biofilms characterization described in Chapter 5. Therefore, assuming that the dynamic viscosity should be lower than the complex one (i.e. considering deviations in the Cox-Merz rule), four different dynamic viscosity curves were defined by means of the Herschel-Bulkley model, in order to fit the value for the *S. mutans* biofilms examined in this chapter.

These estimated viscosity curves (EVC_1 , EVC_2 , EVC_3 , and EVC_4) and the experimental reference values (biofilm complex viscosity and the dynamic viscosity of heterotrophic biofilms) are represented in Figure 7.3. The inset graph in Figure 7.3 depicts the pertinent flow curves of the estimated viscosities. It should be pointed out that the estimated values for the dynamic viscosity, were reaching the values of water viscosity at higher shear rates to reproduce the fluidization behavior reported in the air/water jets impingements experiments (Fabbri et al., 2016b, 2017). As can be seen, EVC_1 corresponds to the model with the

highest dynamic viscosity and shear stress, while EVC₄ is the curve with the lowest dynamic viscosity and shear stress.

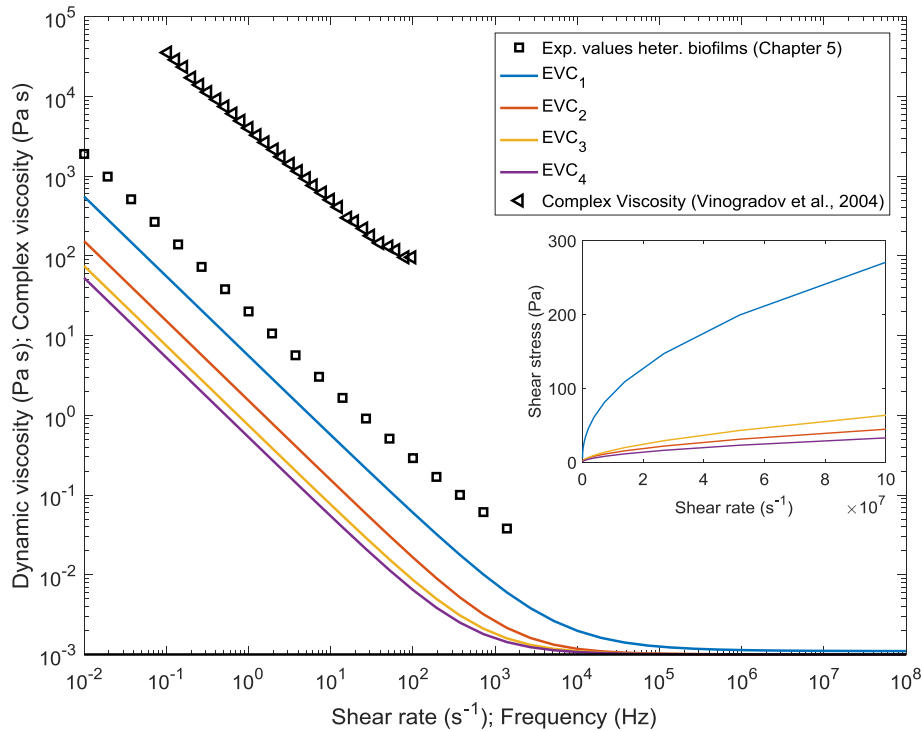


Figure 7.3. Dynamic and complex viscosity curves of *S. mutans* and heterotrophic biofilms. Symbols are experimental data and solid lines represent estimated values. The *Inset* graph shows the flow curves (shear stress versus shear rate) of the estimated data.

In Table 7.2 the main characteristic of the estimated viscosities are summarized. The values of the shear rates at which viscosity reached water viscosity, and the values of rheological parameters of Herschel-Bulkley model, i.e. yield stress (σ_y), the fluid consistency index (K), the flow behavior index (n), are detailed for the four estimated viscosity curves (EVC₁, EVC₂, EVC₃, and EVC₄).

Table 7.2. Rheological parameters of Herschel-Bulkley model (yield stress (σ_y), fluid consistency index (K) and flow behavior index (n)), and shear rates at which viscosity reached water viscosity for biofilm viscosity models (EVC₁, EVC₂, EVC₃, and EVC₄).

Estimated viscosity curve (EVC) denomination	σ_y (Pa)	K (Pa s)	n (-)	Shear rate (s^{-1}) value when reaching water viscosity
EVC ₁	5.529	0.0407	0.477	$>10^8$
EVC ₂	1.529	0.0012	0.568	10^8
EVC ₃	0.745	0.0010	0.600	$2 \cdot 10^6$
EVC ₄	0.529	0.0013	0.550	$2 \cdot 10^5$

7.4.2. Model verification: Simulated and experimental data comparison

The biofilm disruption by perpendicular air-jets impingement can be described by various states: cavity generation and expansion over biofilm surface by jet-impact, formation of the biofilm surface instabilities inside and outside impact region, and propagation of instabilities along the interface (Zuckerman and Lior, 2006). The biofilm displacement is the process in which the biofilm is displaced from its original position, due to the states previously described are produced. The biofilm removal is the process in which the cavity is formed until the wall surface is reached, being related to the formation of surface instabilities.

7.4.2.1. Biofilm displacement

Biofilm response to air jet impingements was simulated implementing four different viscosity curves (see Table 7.2 for parameters details) in order to fit the viscosity model which better can reproduce biofilm behavior. In addition, two different values for the surface tension (γ) parameter at air-biofilm interface were considered, i.e. $\gamma=72$ mN/m and $\gamma=36$ mN/m. The first one is the reference value for air-water surface tension at 20 °C. The second surface tension value was defined smaller than the first one, in this case being half of the reference surface tension (i.e. 36 mN/m). Finally, an inlet constant velocity of 41.7 m/s was defined for the air jet as experimentally measured (Fabbri, 2016).

Since the air jet impingement over biofilm drags the biofilm into motion, the biofilm displacement is the variable used to compare the model performance with the experimental data. The biofilm displacement is defined as the maximum length of disruption over the biofilm for a given time. This variable can be characterized in both experimental and simulated data. In the experimental measurements, since the perpendicular impact produces a radial propagation, the displacement was computed as an average of the biofilm displacements in the different directions for each of the given times (see the white striped circles in Figure 7.4), whereas in the simulated results, due to the defined 2D axisymmetric computational domain direction (see the slide for simulated results in Figure 7.4), the biofilm displacement was produced only in one direction, computing a unique value.

After testing the four viscosity curves, EVC_3 was the estimated viscosity curve which better reproduced the biofilm displacement experimentally reported. In order to illustrate aforementioned explanation about the biofilm displacement, Figure 7.4 shows a qualitative comparison of the displacement observed in the experimental and simulated data with such viscosity, and surface tension equal to 36 mN/m. Different frames experimentally recorded with a high-speed camera are contrasted with the results simulated for the same given times ($t=5$, $t=10$, $t=15$ and $t=20$ ms). Specifically, the biofilm displacement in the triangular slice marked in the experimental frame is compared with the simulated results, delimiting the biofilm displacement reached in each simulated and experimental results by means of the stripped white line.

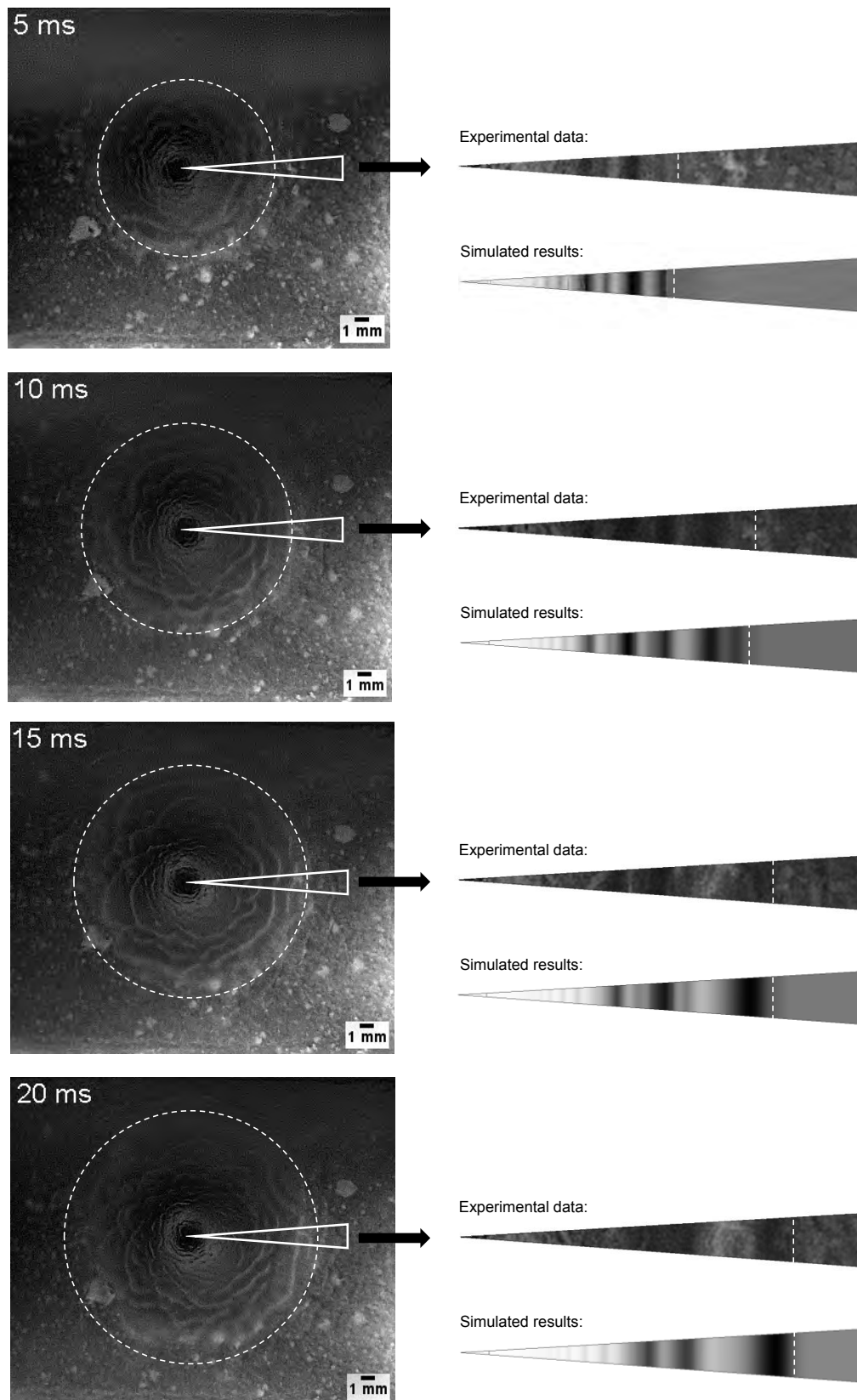


Figure 7.4. Frames ($t=5$, $t=10$, $t=15$ and $t=20$ ms) from a high-speed camera illustrating *S. mutans* biofilm disruption during the exposure to an air jet ($v=41.7 \text{ m s}^{-1}$). Biofilm displacement is indicated by the striped white circle. Qualitative comparison of experimental and simulated results is done in the triangular region.

As it can be noted, the model mimicked correctly the distance reached by the disruption (white striped lines), being more close the simulated results for frames at 15 and 20 ms. In addition, the model reproduces several waves (darkest areas in the simulated results), as can be observed in the experimental results.

A quantitative comparison of the biofilm displacement calculated from the experimental and simulated data is done in Figure 7.5. The biofilm responses computed with EVC_3 and with both surface tension values are showed. As can be seen, the displacements simulated with both surface tensions exhibited the same trend than the observed experimentally, although the displacement observed experimentally was reproduced more rigorously considering $\gamma=36$ mN/m than the higher surface tension. These results are in agreement with findings for *Bacillus subtilis*, *Pseudomonas fluorescens* and *Pseudomonas aeruginosa* biofilms, which surface tensions measurements were inside the range 25-47 mN/m (Koza et al., 2009; Fauvart et al., 2012; Rühls et al., 2013). Various studies (Angelini et al., 2009; Rühls et al., 2013) have associated colonies amphiphilic character and surfactants production as main effects controlling surface tension. Surface tension reductions have been attributed to the presence of surface-active agents such as surfactants (Koza et al., 2009; Rühls et al., 2013). In addition, the amphiphilic nature of the EPS has been related to interface interactions in the biofilm, having a surface-active effect (Flemming et al., 2007).

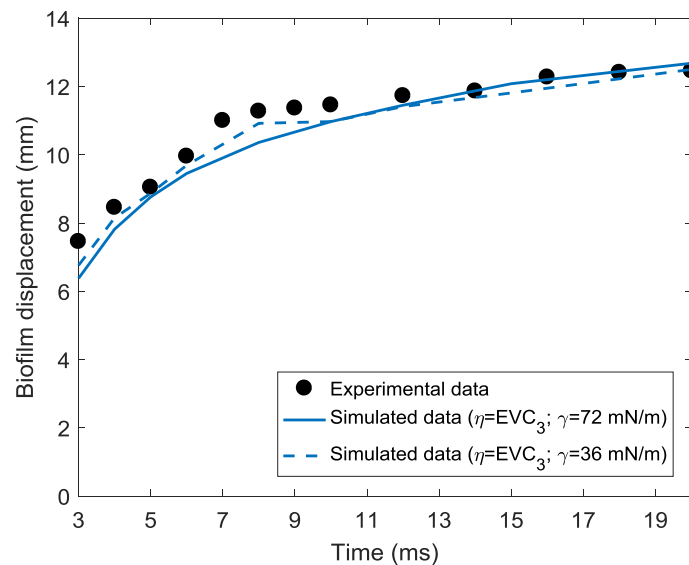


Figure 7.5. Experimental and simulated data of the biofilm displacement (mm) over jet exposure time (ms). Symbols are experimental data and lines represent simulated results ($\gamma=72$ mN/m (solid line) and $\gamma=36$ mN/m (striped line)).

The agreement between the modeling and the experimental measurements implies non-Newtonian fluid behavior of *S. mutans* based biofilms when high shear stresses are applied. Biofilm fluidization was confirmed to be the mechanisms behind the impact of turbulent flows, reproducing the extremely quick and transient mechanical behavior of *S. mutans* during high-

velocity (Fabbri, 2016; Fabbri et al., 2016b). Regarding the viscous properties, the Herschel-Bulkley parameters of EVC₃ estimated viscosity curve (Table 7.2) described the required shear-thinning behavior of the biofilm. Specifically, the yield stress ($\sigma_y = 0.745$ Pa) is in accordance with the observations performed by Vinogradov et al. (2004) for *S. mutans*, where creep analysis showed that the biofilms exceeded the viscoelastic linearity limit for shear stress over 3.5 Pa.

7.4.2.2. Ripples formation and biofilm removal

After the perpendicular impact of air jet over *S. mutans* biofilm, a ripple-like structure is developed at the air-biofilm interface (Fabbri, 2016). Ripples propagate radially outwards from the impact point (see Figure 7.4), changing their morphology as they migrated outwards (Fabbri, 2016). In Figure 7.6, a simulated sequence ($t=5$, $t=10$, $t=15$ and $t=20$ ms) of the air-jet impingement over the biofilm layer in the lateral view is shown. As can be seen, the behavior previously explained was reproduced with the developed model.

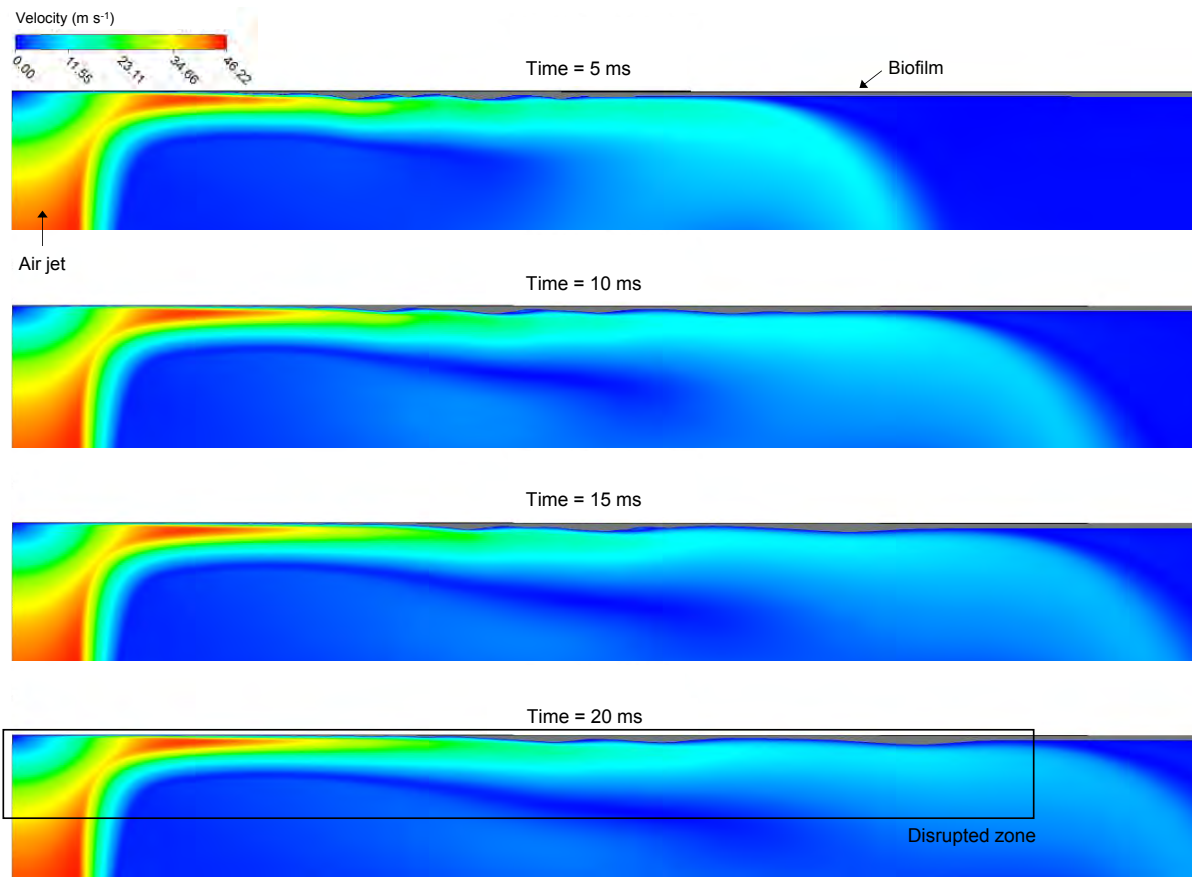


Figure 7.6. Simulated sequence ($t=5$, $t=10$, $t=15$ and $t=20$ ms) of the air-jet impingement over the biofilm layer (represented in color grey). Velocity profiles of air-jet are represented by the color scale. Simulated results were computed with η =EVC₃ and γ =36 mN/m.

In Figure 7.6, the velocity profiles of air-jet impingement for the different frames are showing how initially higher velocities were dragging faster the biofilm (forming ripples on its

surface) until practically steady-state was reached, producing slow displacements. Thus, after 20 ms of air-jet exposure, a disrupted zone with approximately 13 mm of length was generated. Interestingly, biofilm displacement is reaching the steady-state as the jet velocity profile is also reaching it, suggesting that a short-impacts series could be more efficient as biofilm removal strategy (which has also been observed in Chapter 6).

In order to characterize the ripples formed in the biofilm during the air-jet disruption, the characteristic frequency, the wavelength and the velocity of the ripples were determined for both experimental and simulated data ($\eta = \text{EVC}_3$ and two surface tensions: $\gamma = 72 \text{ mN/m}$ and $\gamma = 36 \text{ mN/m}$). The frequency was calculated for experimental and simulated data by means of FFT. The wavelength of the experimental data was estimated in a previous work (Fabbri, 2016) while the ripples velocity was determined using Expression 7.1. The values are summarized in Table 7.3.

Table 7.3. Ripples characterization: frequency (f), wavelength (λ_R) and ripples velocity (v_R).

Data	f (Hz)	λ_R (mm)	v_R (m/s)
Experimental	366.65	0.9 ± 0.3	0.33
Simulated ($\gamma = 72 \text{ mN/m}$)	310.94	1.012 ± 0.13	0.31
Simulated ($\gamma = 36 \text{ mN/m}$)	382.81	1.047 ± 0.14	0.40

The experimental values (frequency, wavelength and ripples velocity) fell between the values computed from the simulations results. The wavelength and ripples velocity values were in the same order of magnitude than the ones measured in *S. mutans* biofilm after air-jet parallel impact (Fabbri et al., 2017). Specifically, the values were very close to results for the air-jet velocity of 44.9 m/s. From the simulated results, a non-negligible effect of the surface tension over the ripples was noticed.

It is known that these ripples are generated because of pressure variations in the gas or by shear stress variations in phase with the wave (Cohen and Hanratty, 1965). The influence of stress is usually of secondary importance since the pressure for air flows is much bigger than the shear stress. Nevertheless, for very thin fluid films, the fluctuations in the fluid have much larger components in the tangential direction than in the normal direction, consequently, the shear stress can be the dominant mechanism (Hanratty, 1983). In order to examine this effect for the case modeled in this work, the shear rate, biofilm dynamic viscosity, and pressure profiles (Figure 7.7), and the profiles of velocity components U_x and U_y (velocities in X and Y directions, respectively) (Figure 7.8) are depicted for the disrupted zone previously defined (see Figure 7.6), and at different computed times, i.e. $t = 0.7$, $t = 0.8$, $t = 0.9$, $t = 1$, $t = 2$, $t = 2.5$, $t = 5$, $t = 10$, $t = 15$, and $t = 20$ ms. These results were computed with $\eta = \text{EVC}_3$ and $\gamma = 36 \text{ mN/m}$, and the Y-axis corresponded to the horizontal plane in the domain definition.

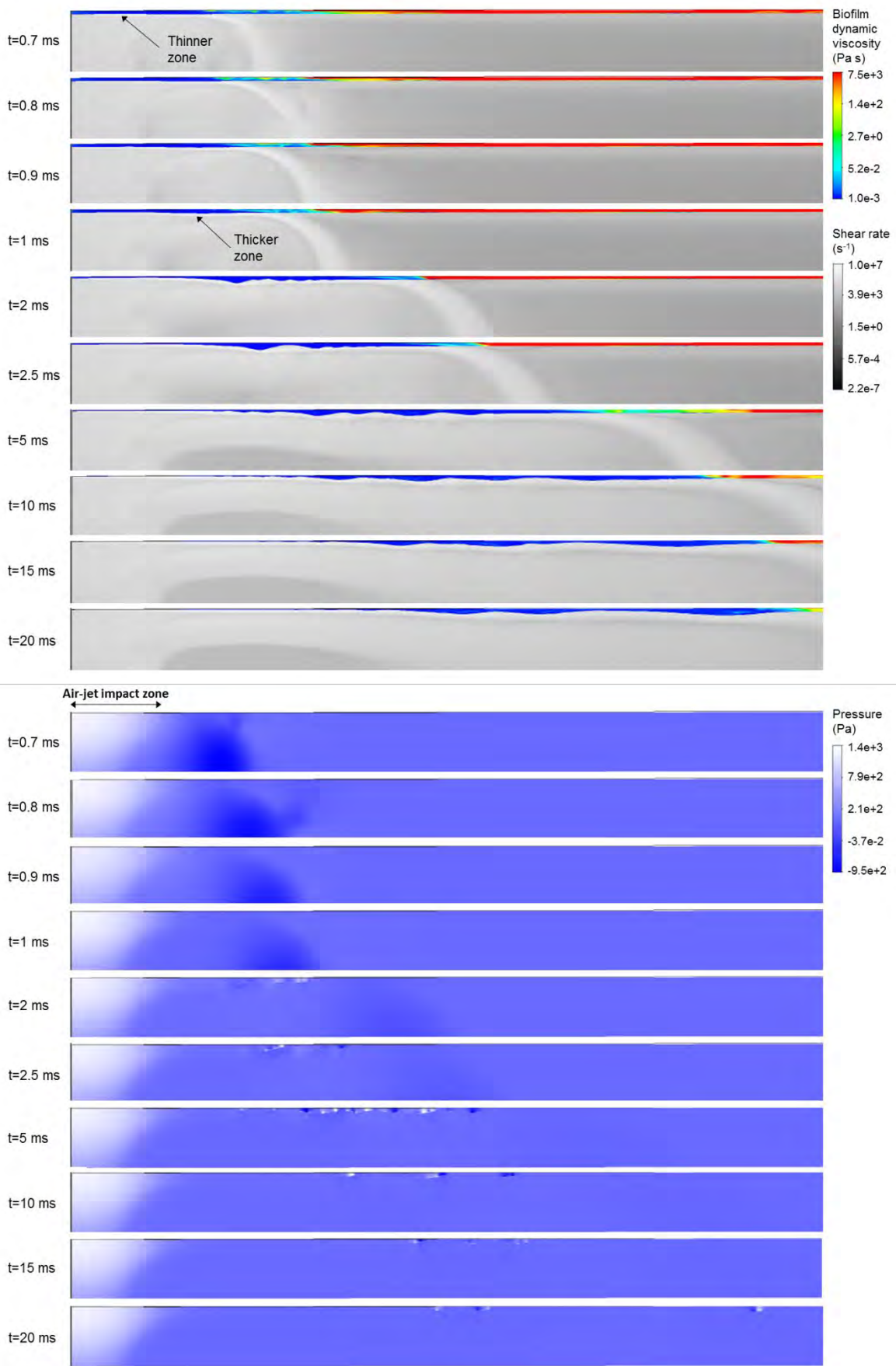


Figure 7.7. Simulated profiles of biofilm dynamic viscosity, shear rate and pressure in the disrupted region for different times. Simulated results were computed with η =EVC₃ and γ =36 mN/m.

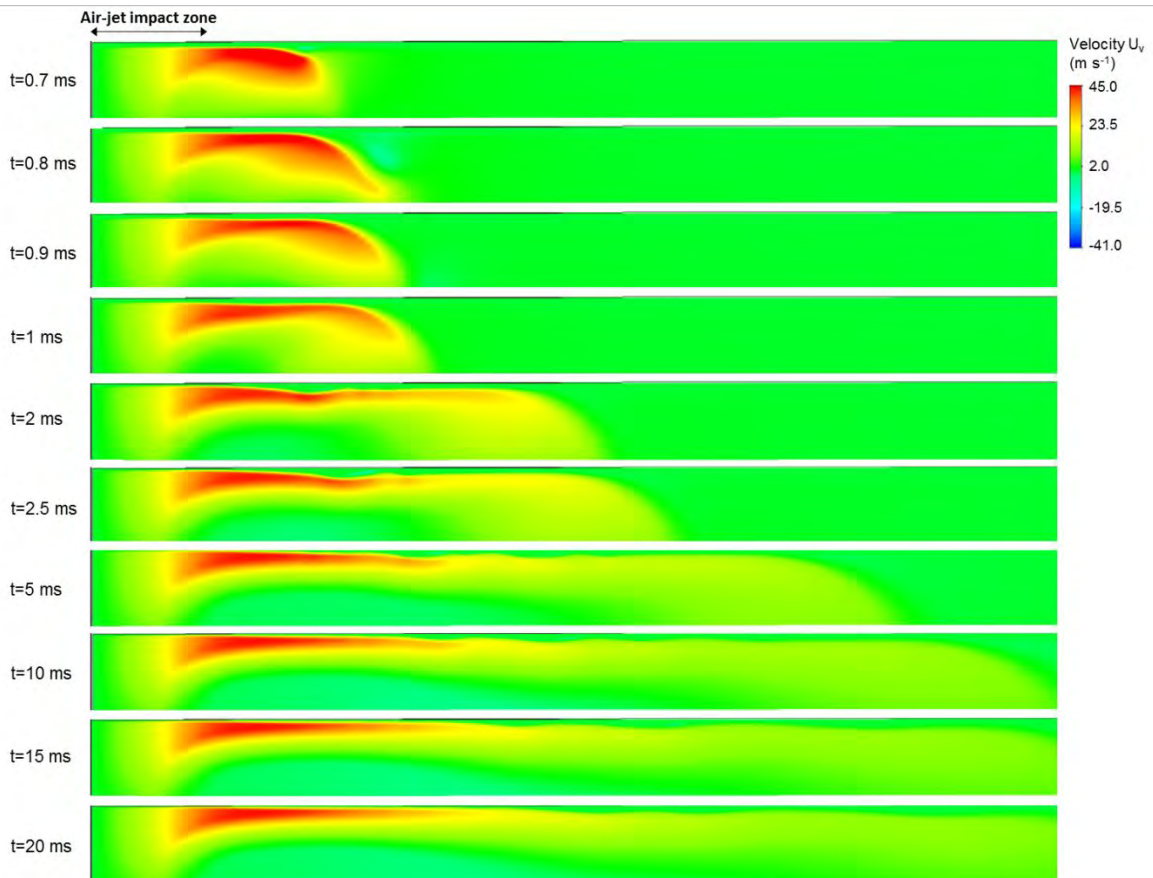
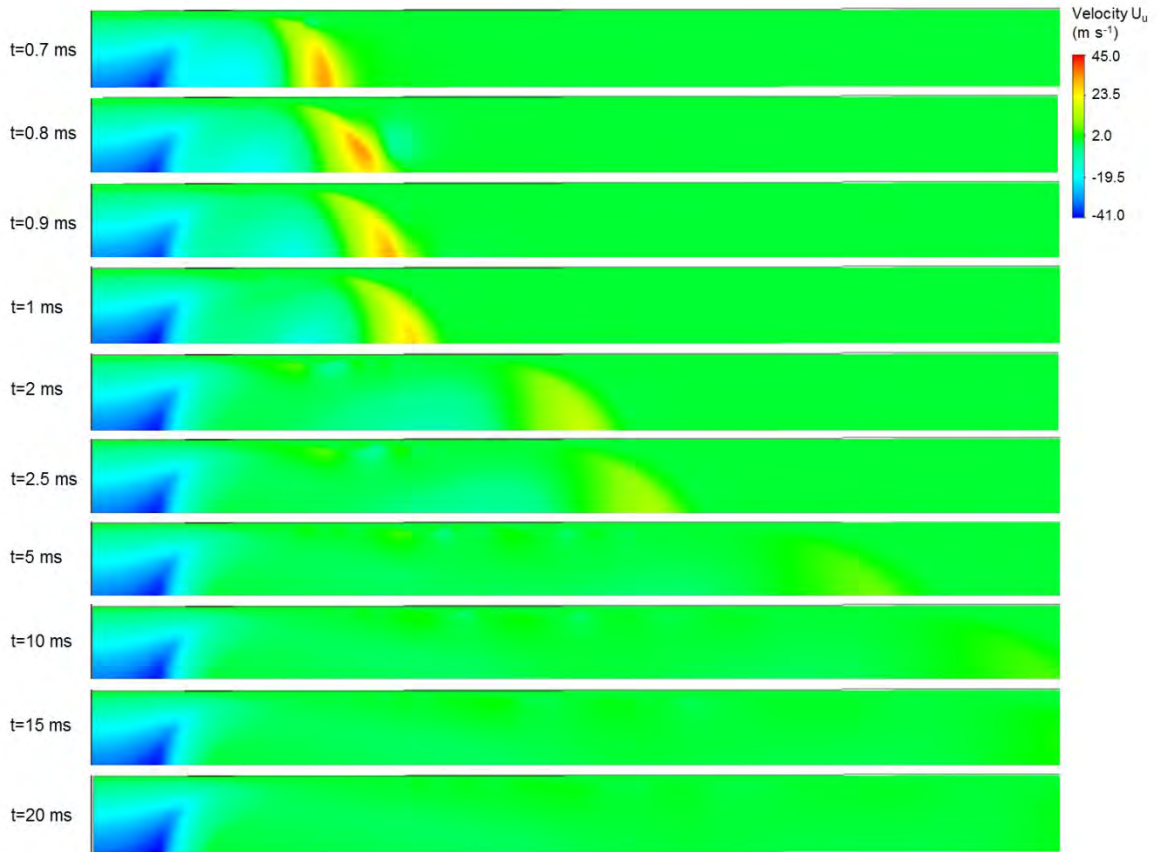


Figure 7.8. Simulated profiles of air-jet velocity in X and Y directions (velocity U and V, respectively) in the disrupted region for different times. Simulated results were computed with $\eta=\text{EVC}_3$ and $\gamma=36 \text{ mN/m}$.

As can be seen in Figure 7.7, the simulated results exhibited high values of shear rates ($>10^6 \text{ s}^{-1}$), which directly produced high shear stresses (in the range of 10^4 Pa), and also high values of pressure (in the range of 1400 Pa) in the air-jet impact zone (1.5 mm of length from the symmetry plane) during all time of air-jet exposure. In addition, it can be observed how the large shear rates generated on the air-biofilm interface changed the dynamic viscosity from the initial value (7500 Pa s) to water viscosity value, confirming again the biofilm fluidization. In this case, the biofilm liquefaction seems to play an important role in its displacement and removal.

The pressure and shear forces produce on the biofilm in the zone of jet-impact produced slightly changes in biofilm thickness from 0.7 to 1 ms. At 1 ms, a biofilm surface with thicker and thinner zones can be observed in the area disrupted by the jet (Figure 7.7). Thus, both pressure and shear stress forces started the biofilm movement. The biofilm displacement can be also confirmed by analyzing the velocity profiles in X and Y directions (velocity U and velocity V, respectively). As can be seen in Figure 7.8, the velocity profile in the tangential direction (velocity V) was predominant for all time of jet exposure, which indicates the drag direction on the biofilm surface. It should be pointed out that between 1 and 2 ms, first ripples in the biofilm surface started to form. The ripples formation coincided with a larger biofilm area being fluidized (approximately 5 mm of biofilm length had been fluidized at 2 ms). Interestingly, the movement of this part of fluidized biofilm produced pressure oscillations, thus generating the ripples. In the pressure profiles (Figure 7.7), the pressure gradients in the biofilm ripples can be observed from 2 ms. Highest gradients can be observed for 5 ms, but decreasing the pressure variations when the ripples were near a steady-state (from 15 ms). Possibly, the wave decay was produced because of the energy transmitted from the air to the biofilm (i.e. pressure and shear stress variations) was less than the viscous dissipation in the biofilm (Cohen and Hanratty, 1965).

Therefore, two mechanisms were present due to the jet impingement over the thin biofilm layer: the friction produced by the forces which drag the biofilm; and the pressure oscillations generating the ripples on the surface. Both mechanisms were governing the disruption along the air-biofilm interface. However, as the case approached a steady state ($t > 15 \text{ ms}$), the shear stress had a more important role at the interface, since pressure gradients in the biofilm were decreased.

The ripple damping can be analyzed in detail representing the contours of biofilm surface over time, from the initial jet impingement until the decay effect was noticed. Figures 7.9 and 7.10 depict the biofilm thickness variations for cases simulated with $\eta = \text{EVC}_3$ and surfaces tension values $\gamma = 72 \text{ mN/m}$ and $\gamma = 36 \text{ mN/m}$, respectively. Once the air-jet impacts on the surface of the biofilm, the disrupted zone can be divided into two regions: the impingement region or cavity in the center of the impact (length of 0 - 3 mm approximately) followed by a region where the waves generated over biofilm surface spread outward.

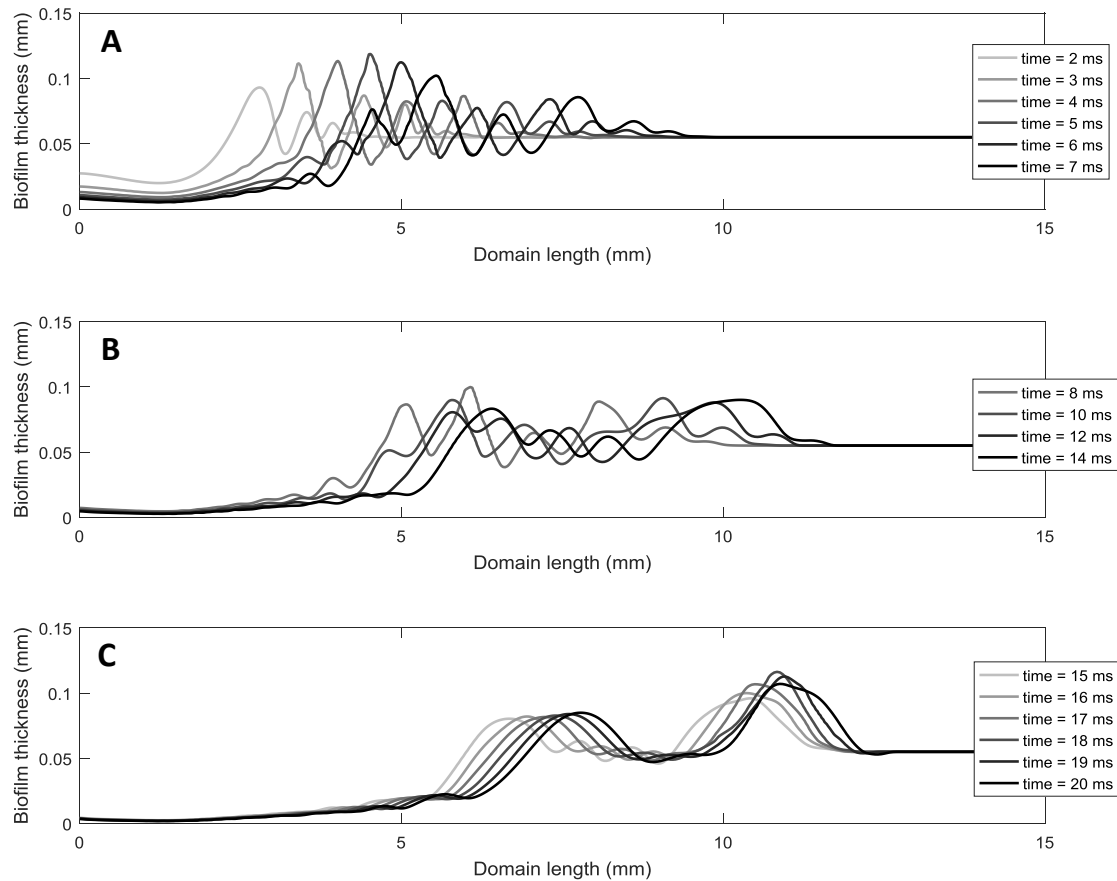


Figure 7.9. Simulated biofilm thickness contours caused by air-jet impingement from: (A) $t=2$ to $t=7$ ms; (B) $t=8$, $t=10$, $t=12$, and $t=14$ ms; (C) $t=15$ to $t=20$ ms. Simulated results were computed with $\eta=\text{EVC}_3$ and $\gamma=72$ mN/m.

As can be seen in both cases, three different phases can be noticed during the biofilm disruption: from 2 to 6 ms, from 7 to 14 ms and from 15 to 20 ms. In the first phase (Figures 7.9A and 7.10A), the ripples generated had constant wavelength and equivalent amplitude for the first wave formed, which was then accompanied by a series of short waves. In the second phase (Figures 7.9B and 7.10B), the ripples had a distorted behavior, reducing the amplitude in the first wave formed and evolving the short waves on the tail, forming bigger waves with the double wavelength than the first wave but with constant amplitude. Finally, at the third state (Figures 7.9C and 7.10C) and the more stable, this showed ripples with constant wavelength, and constant amplitude for the first ripple formed, but varying the amplitude in the last ripple as a sign of damping. As a global indicator, the biofilm deceleration was computed in each of the cases, obtaining -0.0253 m/s² and -0.0264 m/s², respectively. Lower deceleration can be related to higher wavelength and ripples velocity characterizing the case with $\gamma=36$ mN/m.

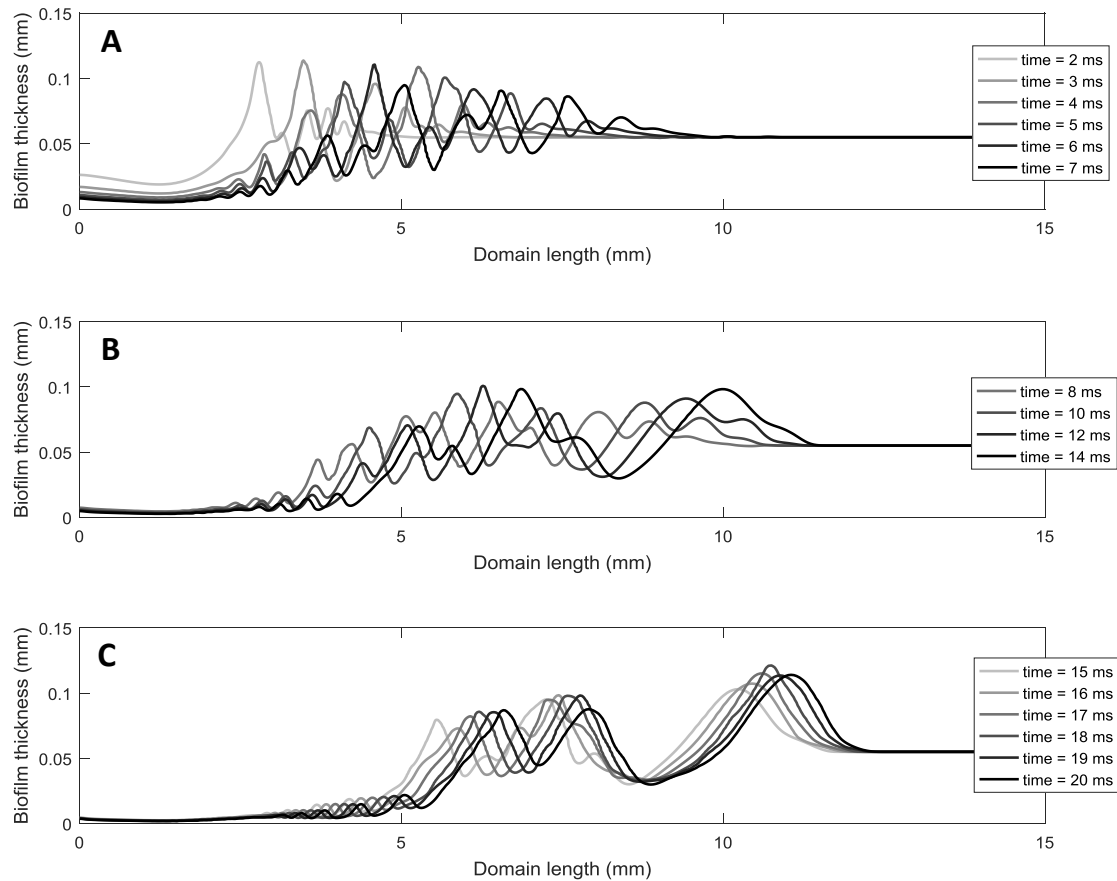


Figure 7.10. Simulated biofilm thickness contours caused by air-jet impingement from: (A) $t=2$ to $t=7$ ms; (B) $t=8$, $t=10$, $t=12$, and $t=14$ ms; (C) $t=15$ to $t=20$ ms. Simulated results were computed with $\eta=\text{EVC}_3$ and $\gamma=36$ mN/m.

These rippling phenomenon produced by turbulent flow over biofilm has been also related to the viscoelastic nature of biofilms (Stoodley et al., 1999c, 2002), establishing that the biofilm structural and mechanical response is dominated by EPS matrix (Klapper et al., 2002). The EPS matrix also provides mechanical stability to the biofilm (Flemming and Wingender, 2010). Therefore, an analogy between the described disruption phases and the EPS matrix response to an external stress could be done. Klapper et al. (2002) explained that the EPS matrix responds to stress by exhibiting: firstly an elastic tension caused by the combination of polymer entanglement and weak hydrogen bonding forces; secondly a viscous damping due to the polymeric friction and hydrogen bond breakage; and thirdly the polymers alignment in the shear direction. The elastic tension can be directly related to the first biofilm disruption phase, where waves with similar pattern are generated in response to initial jet-impingement. The viscous damping can correspond to the second biofilm disruption phase, due to the deformed ripples generation. And finally, the polymers alignment can be associated with the last biofilm disruption phase, where practically the ripples form is changing slightly, being near to reach steady-state.

In addition, another factor related to the ripples formation is the surface tension. Comparing results from Figures 7.9 and 7.10, additional effects that surface tension had over biofilm disruption can be recognized. A significant difference is that lower surface tension (Figure 7.10) intensifies the formation of small-amplitude waves near the impact zone, generating a greater number of waves, which finally increases the length of the biofilm contour, i.e., the higher interfacial area is available. Small waves generate an interfacial enhanced transport, which is related to distortion of diffusion boundary layer by normal disturbance velocity (Roberts and Chang, 2000). Moreover, oscillating interfaces and interfacial waves and fluctuations have been related to mass transfer enhancement (Chen et al., 1997; Vázquez-Uña et al., 2000; Yu et al., 2006). Therefore, the highest number of instabilities, produced by low values of surface tensions, can enhance transport and transfer processes in the disrupted biofilm.

Finally, in Figures 7.9 and 7.10 the cavity generation by jet-impact and its expansion in the biofilm surface over time can also be observed. The cavity size and geometry depend on a force balance at the free surface including: the inertial force of the impinging jet; the gravity force on the fluid that opposes to the cavity formation; and the interfacial tension force at the interface which opposes to the cavity formation (Solórzano-López et al., 2011). In our case, the gravity force was neglected due to experimental system dimensions, and it can be assumed that inertial forces controlled the cavity depth, while the cavity width was governed by inertial and surface tension forces, due to the small-amplitude ripples formation.

A comparison of the cavity geometry and size it is shown in Figure 7.11. The simulated surface biofilm contour obtained for $\gamma=36$ mN/m is qualitatively compared with the recorded experimental frames for $t=4$ ms and $t=20$ ms. The main ripples observed in the experimental data have been highlighted with the black striped lines, comparing their range with respect to the simulated profile in the cut section marked in the figure. Noticeable ripples began to form from 3 mm and 5 mm for $t=4$ ms and $t=20$ ms, respectively. A good agreement in cavity width and in the ripples displacing the biofilm was found. For $t=4$ ms the cavity width was 2.3 mm approximately, and the cavity depth reached 84% of the initial biofilm thickness ($t_h=55$ μm), while for $t=20$ ms the cavity width was 4mm approximately, and the cavity depth was extended practically in the 100% of the initial biofilm thickness, creating a cleared zone with 2 mm of length after 20 ms of air-jet exposure.

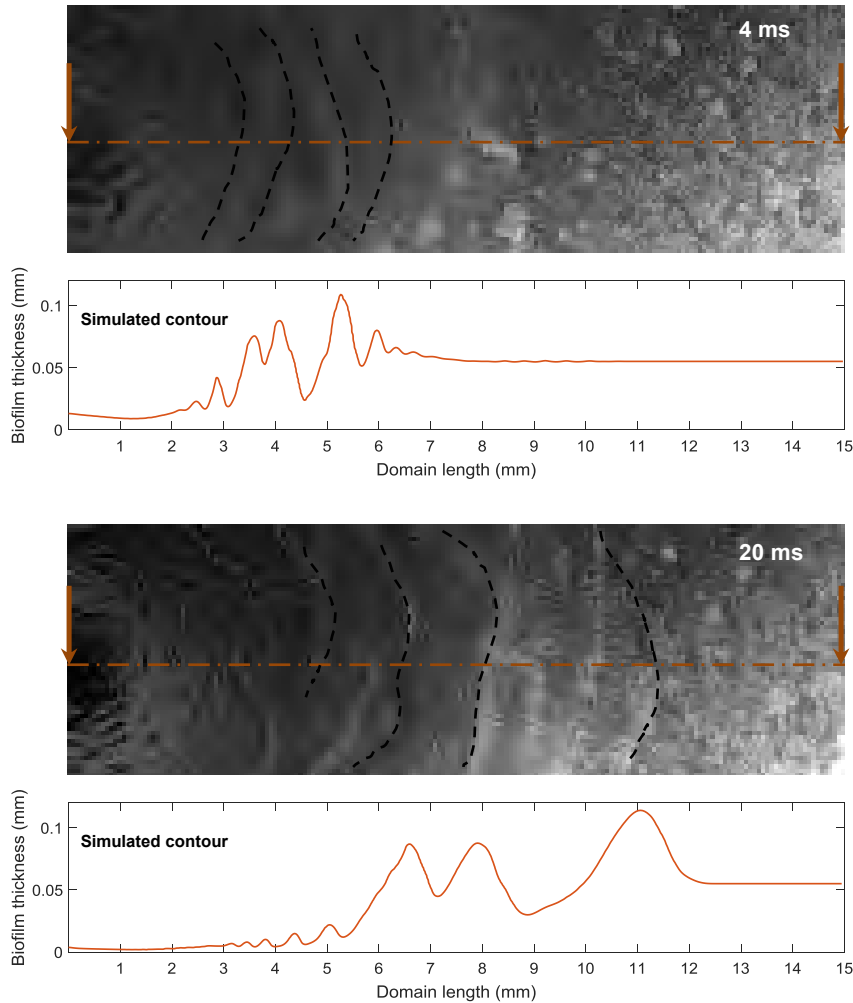


Figure 7.11. Experimental frames qualitatively compared with the simulated profiles of cavity and surface instabilities produced by air-jet impingement for $t=4$ ms to $t=20$ ms. Simulated results were computed with $\eta=EVC_3$ and $\gamma=36$ mN/m.

7.4.3. Parametric study

After the model verification, a parametric study was performed to determine the biofilm response under different conditions. The aim of this study was to show the implications of the different parameters in the biofilm disruption strategies. Therefore, in order to evaluate how biofilm properties and air-jet impact could influence the biofilm displacement, the formation of instabilities in the biofilm surface, and biofilm removal, parametric simulations were performed with changes in parameters, such as air-jet velocity, biofilm thickness and viscosity, and surface tension.

7.4.3.1. Effect of biofilm viscosity and surface tension

Four different viscosities (EVC_1 , EVC_2 , EVC_3 , and EVC_4) were tested (see Figure 7.3 and Table 7.2 for details of the parameters curve which defines these non-Newtonian viscosities).

Moreover, the surface tension effect was also considered, simulating each viscosity with two different values ($\gamma=72$ mN/m and $\gamma=36$ mN/m).

Figure 7.12 depicts the simulated results of the biofilm displacement over jet exposure time for three cases (EVC_1 , EVC_2 , and EVC_3). It should be noted that EVC_4 results were not depicted since the biofilm disrupted along the full length after only a few milliseconds of jet exposure. Similar patterns were found for the rest of simulated results (EVC_1 , EVC_2 , and EVC_3), increasing the biofilm displacement as more time of jet exposure, and reducing displacement velocity after 8 ms in general. As the viscosity increased, the biofilm displacement tended to decrease due to the higher flow resistance, obtaining the lower displacement for the higher viscosity value (EVC_1). Moreover, there is a similar trend between the values computed with lower surface tension ($\gamma=36$ mN/m), which displaced more biofilm initially, i.e. being over the values computed with $\gamma=72$ mN/m, until arriving at a steady-state displacement. This could be explained by the stabilization effect that characterizes surface tension (Barmak et al., 2016). The particular case of EVC_2 should be discussed. Although this viscosity also followed the same tendency, initially it was displacing the biofilm slightly far than EVC_3 . This behavior is because the parameters of EVC_2 represents lightly large viscosity than EVC_3 , while the shear stress of EVC_2 is shorter than EVC_3 (see Figure 7.3), then flowing earlier.

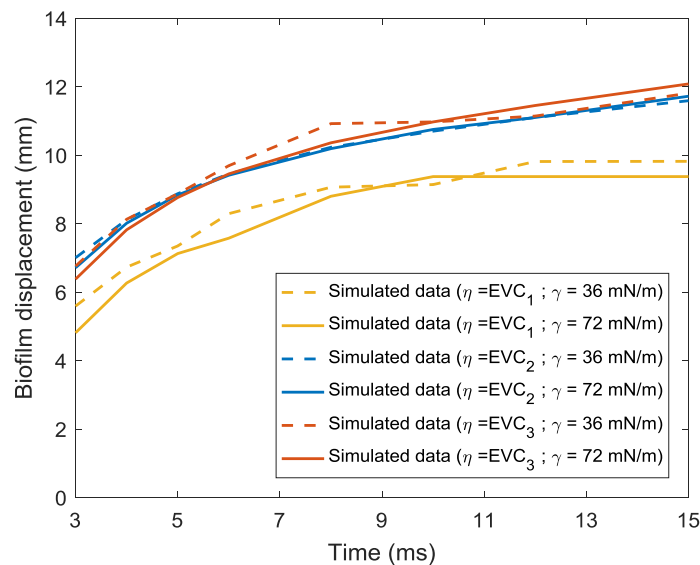


Figure 7.12. Simulated data of the biofilm displacement (mm) over jet exposure time (ms) computed using three different viscosities (EVC_1 , EVC_2 , and EVC_3), and two different surface tension values ($\gamma=72$ mN/m (solid lines) and $\gamma=36$ mN/m (striped lines)).

In Figure 7.13 the cavity geometry, i.e. from 0 to 3 mm in length approximately, and surface instabilities produced by air-jet impingement over biofilm surface with surface tension $\gamma=36$ mN/m and two different viscosity values (EVC_1 and EVC_3) are represented at $t=3$ ms, $t=9$ ms, and $t=15$ ms. As it can be seen, the same nozzle-jet velocity (41.7 m s⁻¹) produced

similar instabilities and ripples in both cases, but the biofilm with the lowest viscosity was disrupted in more length, displacing farther the biofilm. As the jet produced similar instabilities in both biofilms, they had an equivalent available interfacial area. However, the cavity geometry presented dissimilarities in both cases. The cavity of the less viscous biofilm (EVC_3) had a more defined parabolic form, and being more width. Possibly, the presence of more large-amplitude oscillations was perturbing the width definition in EVC_1 cavity. Moreover, for the more viscous biofilm (EVC_1), it was removed with more difficulty in the center of the impingement zone, although an equivalent depth to the low viscous biofilm (EVC_3) was reached in the rest of the cavity.

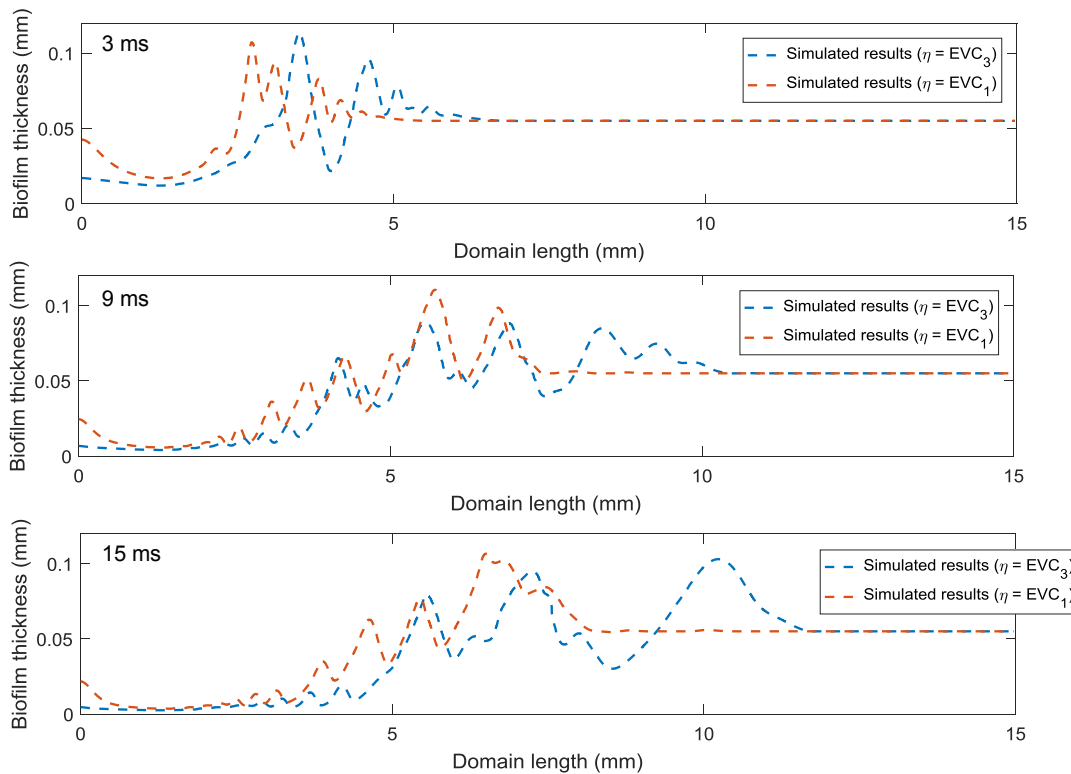


Figure 7.13. Simulated data of cavity geometry and surface instabilities produced by air-jet impingement over biofilms with different viscosities (EVC_1 and EVC_3) for $t=3$, $t=9$, and $t=15$ ms.

It should be noted that cases with lower viscosity than EVC_2 and EVC_3 were computed, e.g. EVC_4 . In that simulations, the biofilm was disrupted practically for all its length (reaching 13 mm) from 2 ms of simulated time (data not shown), while experimentally was found that the displacement is less than 6 mm for 2 ms. Therefore, viscosity values below EVC_3 disrupted the biofilm along the full length after only a few milliseconds of jet exposure. Finally, from the results stated above, the lowest values of biofilm viscosity and surface tension had a major effect on the biofilm displacement and removal.

7.4.3.2. Effect of jet velocity and surface tension

Three different velocities for the air jet-nozzle (20, 40 and 60 m/s) were computed for biofilm viscosity which fitted with the experimental data (i.e. EVC₃). Moreover, the surface tension effect was also considered, simulating each velocity with two different values ($\gamma=72$ mN/m and $\gamma=36$ mN/m).

Simulated results of the biofilm displacement over jet exposure time for the velocities of 20 and 40 m/s are represented in Figure 7.14. It should be noted that the results for the cases with inlet velocity equal to 60 m/s are not depicted, since the full biofilm length was disrupted after just 2 ms of simulated time. For 20 and 40 m/s, similar patterns were found for all the simulated results, increasing the biofilm displacement as more time of jet exposure, reducing displacement velocity after 10 ms. The largest displacements were achieved with high velocity due to the higher shear rates produced. Interestingly, the biofilm displacement computed with the lowest velocity was initially displaced very slowly. This effect can be explained better analyzing the cavity formation and surface instabilities generation during air-jet impingement (Figure 7.15).

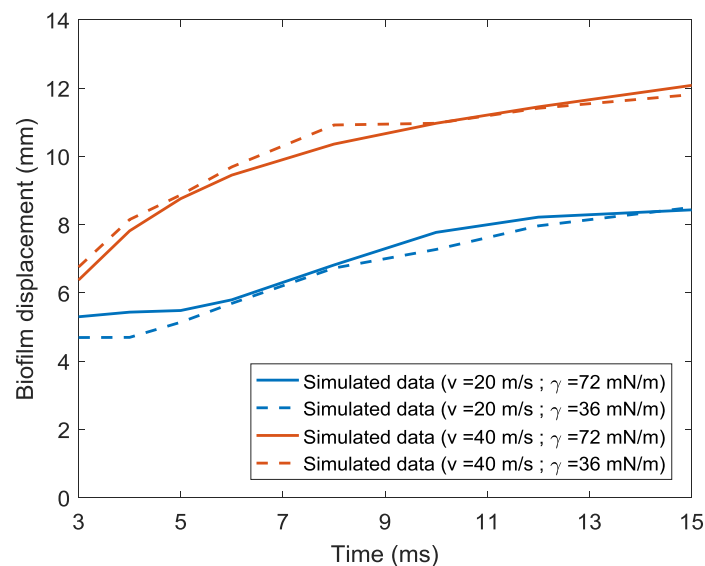


Figure 7.14. Simulated data of the biofilm displacement (mm) over jet exposure time (ms) computed using two different jet-nozzle velocity values (20 and 40 m/s), and two different surface tension values ($\gamma=72$ mN/m (solid lines) and $\gamma=36$ mN/m (striped lines)).

In Figure 7.15 the cavity geometry and surface instabilities produced by air-jet impingement at 20 and 40 m/s over biofilm surface with two different surface tensions are represented at $t=3$, $t=9$, and $t=15$ ms. Higher air velocity produced more instabilities and ripples because of the higher shear force at air-biofilm interface, resulting in higher biofilm flowing and larger available interfacial area, which can also enhance mass transfer. In general, as the gas jet velocity is increased the cavity becomes deeper and wider with the

walls tending to be more vertical, and the outer boundary of the cavity rising above the original biofilm level. Interestingly, for the simulation with low velocity, initially the cavity not describes a parabolic form, which could cause a delay in the biofilm displacement. In addition, the surface tension had a more noticeable effect over surface contour for the simulations computed with higher velocity. A larger number of surface instabilities were generated for the lowest surface tension, with oscillations in the cavity width which produced less extension of the cavity. The larger cavity widths were obtained for the higher surface tension. Even so, the cavity depth was not affected by the surface tension in the range of studied values.

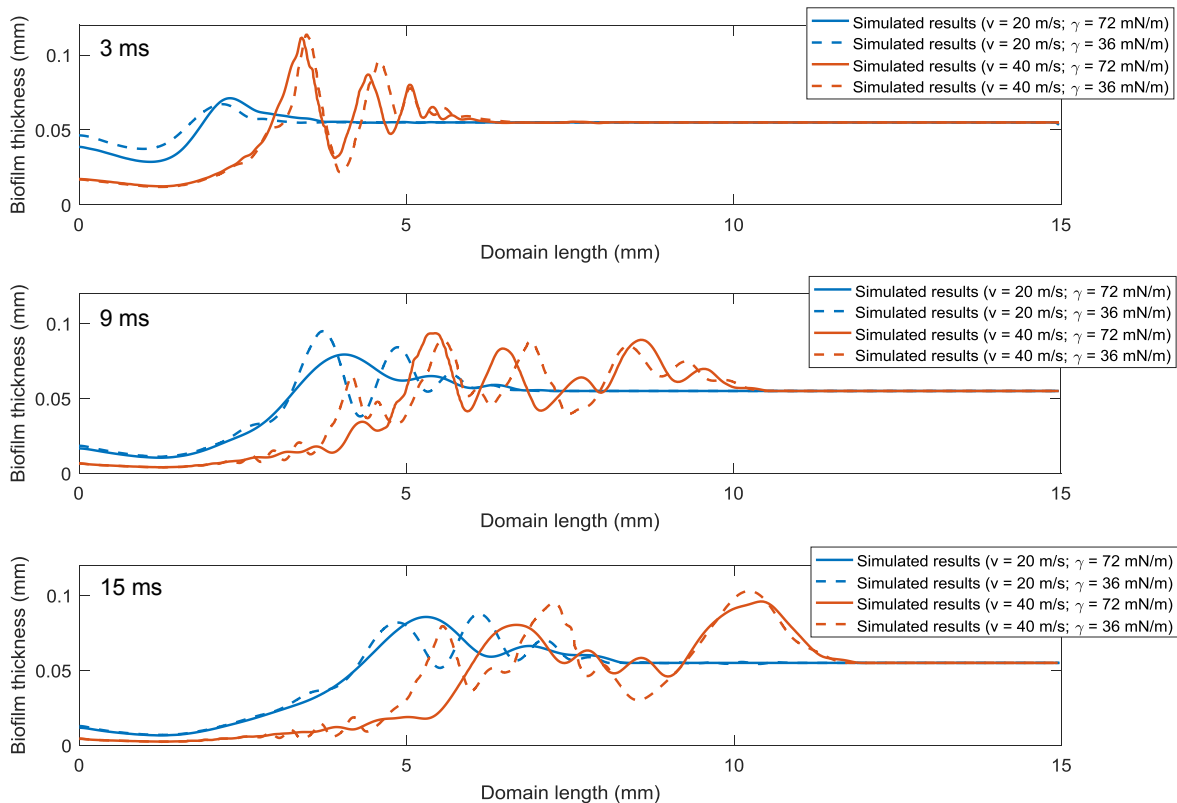


Figure 7.15. Simulated data of cavity geometry and surface instabilities produced by air-jet impingement at different velocities (20 and 40 m/s), and different surface tension values ($\gamma = 72$ mN/m (solid lines) and $\gamma = 36$ mN/m (striped lines)) for $t = 3$, $t = 9$, and $t = 15$ ms.

The results showed in this section showed that the highest air velocity had the major implications on the biofilm displacement and removal, corroborating also that the lowest values of surface tension had major effects on biofilm disruption.

7.4.3.3. Effect of biofilm thickness

Finally, different biofilm thickness (th) (i.e. $th = 27.5$ μm and $th = 55$ μm) were computed for biofilm viscosity EVC_3 , surface tension of 36 mN/m and jet-velocity of 41.7 m/s. Specifically, the biofilm thicknesses considered were the value estimated from the experimental data (i.e. $th = 55$ μm), and the half of such estimated value (i.e. $th = 27.5$ μm).

Figure 7.16 depicts the simulated results of the biofilm displacement over jet exposure time for the two cases. As it can be seen, similar patterns were found for all the simulated results with different thickness, increasing the biofilm displacement as more time of jet exposure was reached. The biofilm with higher thickness ($th=55 \mu\text{m}$) had a more constant velocity in the biofilm displacement, while the thin biofilm ($th=27.5 \mu\text{m}$) increased the displacement velocity to reach the steady-state in less than 10 ms. Even so, the thin biofilm reached a higher displacement than the thicker one.

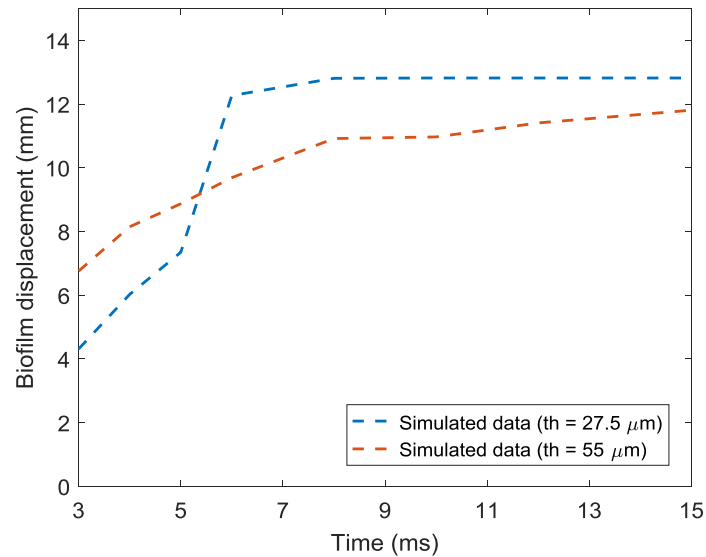


Figure 7.16. Simulated data of the biofilm displacement (mm) over jet exposure time (ms) computed for two different biofilm thickness ($th=27.5$ and $th=55 \mu\text{m}$).

In order to complete the analysis, Figure 7.17 depicts the cavity formation and surface instabilities generation during air-jet impingement over the biofilm surface are represented at $t=3$, $t=9$, and $t=15$ ms. As can be seen in Figure 7.17, the same nozzle-jet velocity produced more instabilities and ripples in the thicker biofilm. Possibly, the fact of having fewer surface instabilities in the thin biofilm favored reaching before the steady-state in the biofilm displacement. Interestingly, the thin biofilm was more disrupted along its length, but with fewer presences of noticeable surface instabilities. Indeed, very small instabilities were noticed in the zones far from the cavity (see in Figure 7.17 the surface profile for the frame of 9 ms and around 10 to 12 mm of domain length, and the surface profile for the frame of 15 ms and around 11 to 13 mm of domain length). Thus available interfacial area was smaller than for the thicker biofilm. In addition, the cavity geometry was very similar for the different cases, being practically independent of the biofilm thickness in the range of studied values.

Therefore, thin biofilms (under 30 microns) seems to be that could be quickly displaced, causing more disruption along its surface. However, the biofilm removal in the region of jet-impingement was very similar to the one found for thicker biofilm. In this case, thinner

biofilms did not imply major effects on the biofilm removal and the generation of significant surface instabilities.

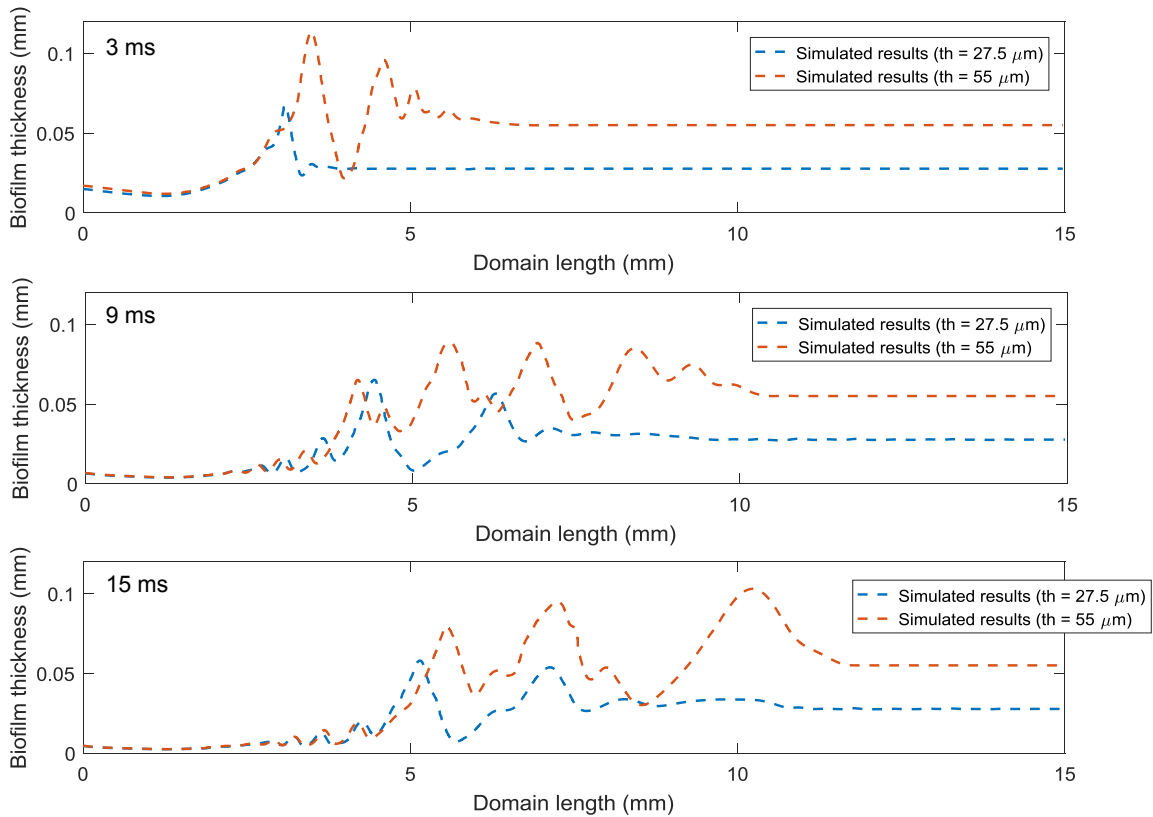


Figure 7.17. Simulated data of cavity geometry and surface instabilities produced by air-jet impingement over biofilms with different thickness ($th=27.5$ and $th=55$ m) for $t=3$, $t=9$, and $t=15$ ms.

7.5. CONCLUSIONS

In this chapter, the new approach of continuum model presented in Chapter 6 was applied to simulate the biofilm disruptions induced by air-jet impingements, thus CFD multiphase models were developed considering turbulent flows and defining the biofilm as a non-Newtonian fluid.

To the best of our knowledge, this is the first numerical study where the mechanisms behind the impact of turbulent flows on the biofilm structure were interpreted. Biofilm-air interactions under different turbulent conditions were simulated and verified, showing important findings which indicated that the new biosystems modeling approach can be also used to reproduce the most aggressive strategies for biofilm removal.

The results of this chapter indicated that inertial, shear and interfacial tension forces are the mechanisms governing the impact of turbulent air-jets over the biofilm structure. Moreover, it was shown that the air-jet exposures presented herein generate high shear rates, which coupled with the shear-thinning properties of the biofilm produced its quick fluidization. These findings demonstrated that the applied forces and the biofilm properties

are both enhancing biofilm disruption, by ripples and surface instabilities generation, and removal by liquefaction.

The present study confirms previous findings and contributes additional evidence that suggests the physics of jet impacts changes biofilm properties and enhances mass transfer phenomenon. The results of this work revealed that high jet-nozzle velocities, low viscosity and surface tension values intensify biofilm disruption, generating interfacial instabilities which result in a greater interfacial area available. These findings might have important implications on new strategies for controlling and preventing biofilms, such as using antimicrobial which could potentiate the change of biofilm properties in that way.

Future work should consider biofilm morphology, i.e. structural and thickness variability, and include the elastic component in the biofilm mechanical properties to provide better insight into the transient nature of the biofilm seen in the experiments. In this respect, numerical tools may help to increase the knowledge on how the biofilm structures behave under turbulent flows, as currently the difficulty of performing measurements of biofilm dynamics and physical properties in those extreme conditions is a challenging issue.



STUDY ON THE APPLICATION OF LOCAL CAPACITANCE NEEDLE-PROBES FOR IN-SITU BIOFILM LAYER CHARACTERIZATION AND INTERFACE DETECTION

In this chapter, the work was focused on the accurate analysis of fluid-biofilm interface, and on the necessity of acquiring local experimental data to verify biosystems models. In previous chapters, the developed multiphase CFD models have shown the importance on the tracking of phases volume fractions across the domain, thus allowing an accurate reconstruction of biofilm structure. This research examined the applicability of local capacitance needle-probes for in-situ biofilm layer and fluids interfaces detection. The probe performance was calibrated and verified in multiphase systems, revealing its practicability for interface detection, depth measuring, and surface reconstruction. Thus, this sensor probe became a potential tool for the experimental characterization of biosystems and models verification at mesoscale.

Abstract

Biofilms are dynamic communities of microorganisms which growth attached to a surface having a beneficial or adverse impact. Biofilm detection and characterization of its geometric properties (i.e. thickness, roughness, etc.) can help to eliminate harmful biofilms, or to maintain and control biofilms that have a favorable effect. Biofilm thickness measurement should be optimally obtained in-situ without influencing the sample. Current non-destructive techniques can have some limitations such as the availability, the affordability, and the applicability to practical situations. In other research fields, capacitance sensors have been used to measure/detect film layers, due to their simple structure, well dynamic response and high-sensitivity. The aim of this study was to investigate the applicability of a novel sensor, based on capacitance needle-probes, to characterize biofilm layer and thickness, and fluids interfaces detection inside biosystems. The needle-probes were positioned at different axial locations of the biosystems (from the gas phase, through the liquid phase to the biofilm), and were placed normal to the biofilm, obtaining at each position a voltage value relative to biofilm thickness. Experimental data demonstrated this sensor can measure minimal change with high precision, obtaining accurate measurements with the presence of a conductive liquid layer upon the biofilm. The developed sensor can be placed virtually anywhere within the medium with minimum invasiveness due to its design, allowing in-situ and real-time measurements of the biofilm and fluids layers.

A modified version of this chapter is being prepared for publication as:

G. Monrós-Andreu, L. Prades, A.D. Dorado, X. Gamisans, S. Chiva, 2018. **A local capacitance needle-probe for in-situ detection of interface and biofilm layer.**

8.1. INTRODUCTION

Biofilms are microbial communities growing attached to a surface, which formation can be desirable in some cases (e.g. wastewater treatment) whereas in other cases it can generate severe problems (e.g. medical infections). Quantitative description of biofilms and fluid phases present on biosystems allows for the better application of biofilm control strategies, since biofilm thickness and the location of fluid interfaces are key role parameters in mass transfer processes in both experimental applications and numerical studies (Bakke and Olsson, 1986). In addition, biofilm thickness is directly related to diffusion phenomenon and biofilm development (Hoehn et al., 1973). In these sense, several works studied mass transport and biodegradation processes inside biofilms using microsensors (Lewandowski et al., 1991; Zhang and Bishop, 1994; Horn and Hempel, 1995; Wasche et al., 2000; Guimerà et al., 2015, 2016), obtaining species (i.e. dissolved oxygen) profiles in both the liquid and biofilm phases. Later, these profiles were used to roughly estimate the position of the concentration boundary layer and the biofilm thickness following different methods (Wäsche et al., 2002; Lewandowski and Beyenal, 2007) which can report inconsistent results. Therefore, to increase accuracy in biofilm systems modeling, more quantitative experimental information about phases' thickness and interfaces location is highly desirable. Nevertheless, measurement of biofilm thickness in biosystems can result in a complex task, which has led researchers to develop a wide range of methods.

Biofilm and liquid phase thickness measurement should be optimally obtained in situ without influencing the sample. Non-destructive methods based on optical and laser technologies have been used to measure biofilm thickness in biofilm fixed-bed systems, using light microscopy (Bakke and Olsson, 1986; Bakke et al., 2001), confocal laser scanning microscopy (CLSM) (Stoodley et al., 1999b; Heydorn et al., 2000), a laser triangulation sensor (Okkerse et al., 2000), or a scanner with an image acquisition system (Milferstedt et al., 2006). During the last decade, a fast and non-invasive imaging technique such as optical coherence tomography (OCT) has emerged to investigate the mesoscale biofilm structure (Wagner et al., 2010). In addition, a mechanical method based on uniaxial compression (Paramonova et al., 2007) and magnetic resonance imaging (Manz et al., 2003) are other non-destructive techniques which have been also proposed for adequately measuring biofilm thickness. The mentioned non-destructive techniques can have some limitations such as the availability, the affordability, and the applicability to practical situations, i.e. medium opacity, complex instrumentation, etc. (Denkhaus et al., 2007). Even so, all described methods have filled the existing gap in the experimental verification of heterogeneous biofilms models (Beyenal and Lewandowski, 2005). However, to facilitate the use of such systems and extend their application are required techniques more feasible, and more easy to incorporate in the bioreactor or biosystems which are already operating, ensuring in-situ and real-time monitoring. More affordable techniques, such as capacitance and impedance sensors, have been used in other fields to detect film layers and to measure

local parameters, such as void fraction and interfacial area concentration (Boyer et al., 2002), due to their simple structure, well dynamic response and high-sensitivity. Zenit et al. (2001) proposed a dual sensor probe based on local impedance measurement to measure the gas fraction in bubble columns. Da Silva et al. (2007) also proposed a dual sensor probe, but by combining conductance and permittivity measurements, showing the applicability of needle probes measurement systems in three-phase flows. In addition, Monrós-Andreu et al. (2016) extended the works previously mentioned by designing a multi-needle capacitance probe for characterizing non-conductive two-phase flows. This type of sensors has also been proved their potential in biofilm systems characterization. The pioneering work for biofilm thickness measurement with stainless-steel probes (Characklis et al., 1982) was an ex-situ method based on the detection of non-conductive and conductive media (i.e. air and biofilm, respectively), being applicable only when the difference in the relative electrical permeability (E_r) between the media is significant. Recently, Ferreira et al. (2005) examined the use of a commercial capacitance sensor for on-line monitoring biomass concentration. This sensor showed the capability to discriminate between biomass and the liquid medium in which it was suspended due to the annular design of the probe, i.e. larger measurement area. Sensors with a high measurement area are used to discriminate very low E_r differences compared to air-water, such in the water-biofilm case where the E_r differences are lower than 0.05, i.e. capacity measurements are in the order of pF. In this way, Maurício et al. (2006) presented a large capacitance sensor (surface area of 85 cm²) to measure the biofilm thickness in rotating biological contactors. Even so, no references have been found in the literature on impedance or capacitance systems allowing a local discrimination of the phases present in the biosystem at mesoscale, and providing the possibility to reconstruct the fluid-biofilm interface layer, thus determining key parameters, such as interfacial area, in biosystems modeling.

From the stated above, the application of local sensor probe for in-situ biofilm layer characterization and interfaces detection in biosystems was examined in this chapter. A needle-probe sensor based on local capacitance measurements was developed to measure the thickness of a heterotrophic biofilm, and fluid phases inside a biosystem. Measurements in different dimensions were performed to analyze and verify the capacity of the developed system to deeply characterize interfaces and phases' thickness in multiphase systems (i.e. gas-liquid-biofilm, and liquid-biofilm). In addition, the post-processing of the data recorded in 2D and 3D to examine the fluid-biofilm interface allowed the reconstruction of the biofilm surface, verifying the feasibility of the proposed system with the experimental data, thus characterizing accurately essential parameters in mass transport and transfer such as available interfacial area and fluids thickness.

8.2. MATERIALS AND METHODS

8.2.1. Experimental set-up

In the present study, the experimental set-up consisted of four parts: the biosystem, the measurement system, the motion system, and the control program. In Figure 8.1, a schematic diagram showing all the components is presented. The biosystem is the bioreactor or the measuring chamber where the heterotrophic biofilm and the fluid phase/phases were located. The measurement system was made of the physical sensor itself; the signal function generator; the dedicated electronics capable to convert the information of phase fraction into representative voltage signals; and the data acquisition (DAQ) system, which collects, compute and store the data gathered from the needle-probe sensors. The motion system was formed by the three actuators, which allowed the three-dimensional positioning of the sensor, and the micro-step controller to drive the stepper motors in the actuators. All this group of components was used to accurately position the sensors at any location in the biosystem. The control program was developed using NI LabVIEW® 2011 to synchronize the functionalities of the DAQ system and the motion system during the experimental measurements performance.

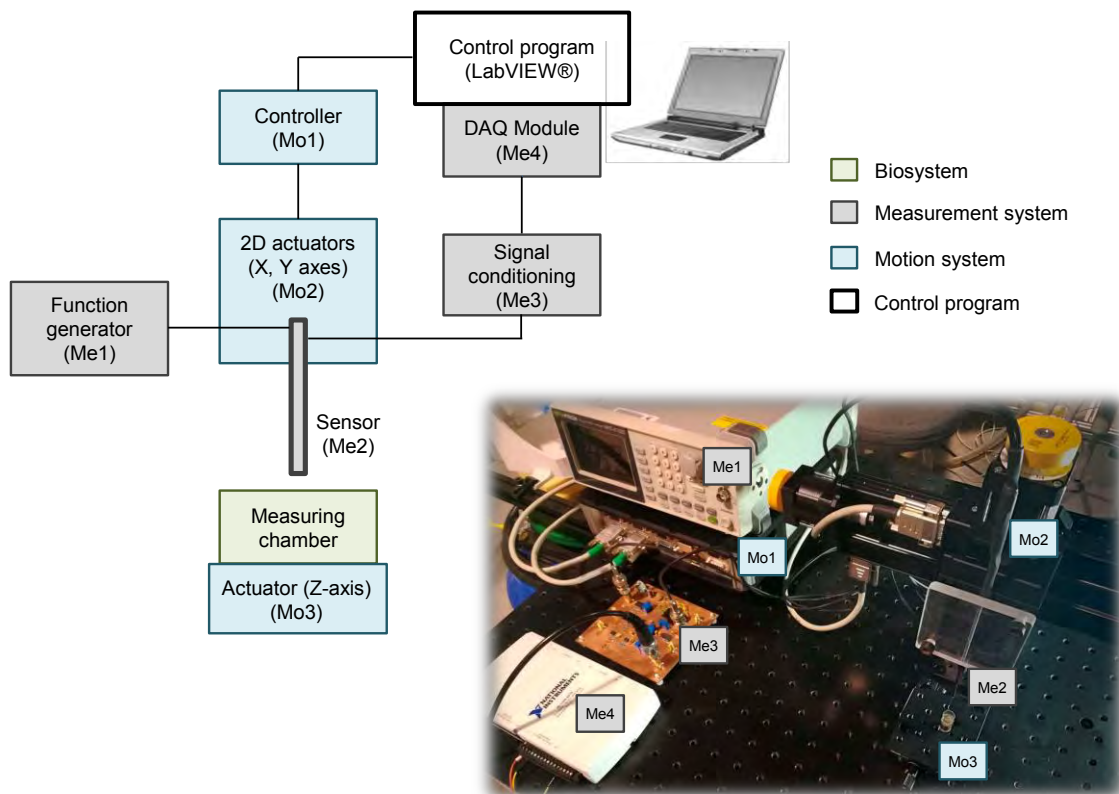


Figure 8.1. Experimental set-up components, classified in four parts: the biosystem or measuring chamber (green box); the measurement system including function generator, the sensor, the signal conditioning and the DAQ module (grey boxes); the motion system including controller and actuators (blue boxes); and the control program (white box).

Therefore, for making the experimental measurements, the needle-probe sensors were mounted on an automatized 2D stage micromanipulator, and the measuring chamber was placed on a manual actuator. Then, in a section of the measuring chamber, the sensor was positioned at different axial locations of the phases (from the gas phase to support), and in several positions in the length of the chamber, being driven by the motion system and the orders of the control program. In each position, the control program also recorded a voltage value relative to the measured phase, and finally obtaining a complete spatial matrix of measurements in the X-Y plane. Further details of the mentioned systems are explained in the following sections.

8.2.2. Biofilm growth and samples preparation

Aerobic heterotrophic biofilms were grown on a flat plate bioreactor (FPB). After sterilizing the FPB, it was seeded with 40 ml of a sludge (4 g of volatile suspended solids (VSS) L⁻¹) obtained from the WWTP of Manresa (Barcelona, Spain). The remaining volume of the FPB was filled with a nutrient solution containing glucose (13 g L⁻¹) as the sole carbon and energy source, and it was operated in batch mode for 24 hours to promote the bacteria immobilization. Then, the FPB was operated continuously for 10 days until well-defined biofilms were cultivated (flow rate and residence time were adjusted to approximately 1 m h⁻¹ and 12 h). Further details about biofilm growth can be found in Chapters 4 and 5.

Before the experiment, the biofilm samples were prepared immediately for analysis. Pieces of the biofilm (measuring approximately 35x35 mm) were placed on the measuring chambers to prepare the different scenarios to analyze, i.e. biosystems. Then, the measuring chambers were filled with the fluid phase over the biofilm (i.e. mineral medium or water).

8.2.3. Sensor development and set-up overview

The developed system consists of a two-needle probe and a dedicated electronics to measure and to process the sine wave signal from a signal generator affected by the medium between electrodes (Figure 8.2).

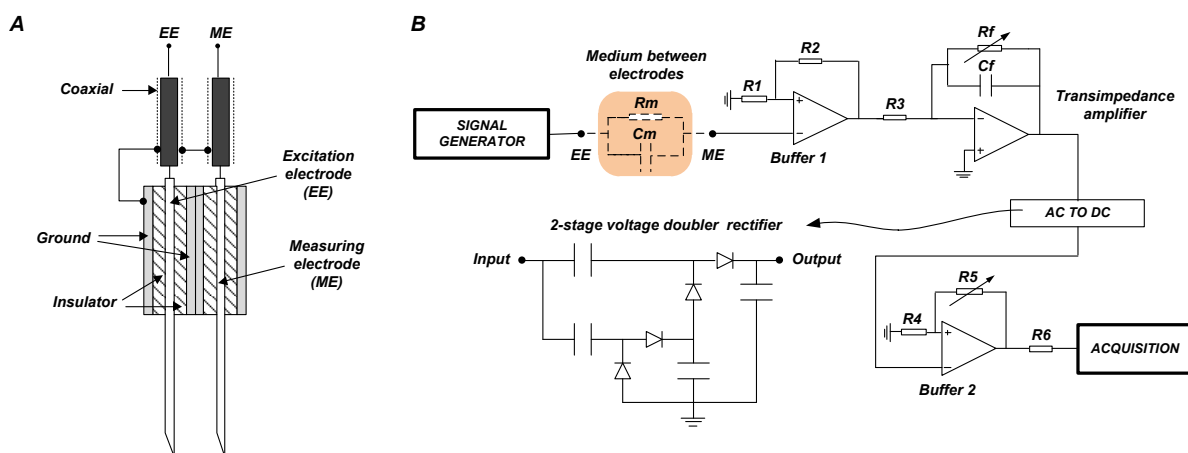


Figure 8.2. A) Needle-probe and B) electronics schemas.

In this work, the goal was to observe the variation in the signal amplitude (i.e. direct current (DC) value) due to changes in the medium, which was modeled as a parallel capacitor and resistance (C_m and R_m , respectively). As depicted in Figure 8.2A, the probe itself is built in a double coaxial geometry. Two $\varnothing 0.1$ mm electrodes (excitation and measuring electrodes, EE and ME respectively) were completely insulated except of their tip, and then the zone between the tips was the active measuring region.

The principle of operation is as follows (Figure 8.2B):

- A sinusoidal voltage was injected by means of a signal generator, passing through the medium (air phase, liquid phase, biofilm-layer or biofilm) from the EE to ME, and controlling its frequency and amplitude. The excitation signal was generated by a commercial signal generator (AFG-21225, ISO-Tech Kunststoff GmbH, Ahaus, Germany). The signal obtained in ME was passed through a non-inverting amplifier for two main reasons: providing a preliminary buffering of the sensor probe signal, and the impedance isolation between the signal generator and the measurement circuit, as detailed in the next steps. In the current set-up, R1 and R2 were 100 k Ω resistors to double the input voltage signal (buffer gain equals to two), and R3 was 50 k Ω resistor.

- The impedance value in the region located between the excitation electrode and a measuring electrode was determined by the volume fraction of the phases in this region, and the total sensing area of both electrodes. For the impedance measurement, a trans-impedance amplifier configuration (also known as auto-balancing bridge or current-voltage converter) was chosen as capacitance to voltage converter. This circuit presents a high signal-to-noise ratio and stray-capacitance immunity, being able to measure small inter-electrode impedances (Da Silva et al., 2007), which is required for this application. The operational amplifier (Op-Amp) employed was the TLE2086 (Texas Instruments), which has a JFET input and gain-bandwidth product of 10 MHz, hence being suitable for high-impedance and noisy measurements.

- In order to obtain a manageable signal, it was necessary to demodulate the sinusoidal output of the trans-impedance amplifier and, therefore, to obtain a DC value which was representative of the actual media between electrodes. We use a passive rectifier used widely in wireless applications, a two-stage voltage-doubler rectifier (Wang et al., 2012), shown in Figure 8.2B. Essentially, the circuit is a charge-pump structure. The left-sided capacitors and diodes make up a DC-level shifter, and the right-sided capacitors and diodes form a peak detector. It presents a very low ripple at the output for selected frequency operating conditions.

- The obtained signal from the rectification stage was also buffered by means of a non-inverting amplifier in order to provide a high impedance output and low impedance input. In the current study, R4 and R5 were 100 k Ω and 0-1 M Ω resistor and potentiometer,

respectively. One defining characteristic of an ideal Op-Amp is that it has effectively zero output impedance. The non-inverting amplifier exactly reproduces the amplified input voltage signal, which can have large impedance associated with it, with nearly zero output impedance. Therefore, instead of directly measuring the voltage signal with the DAQ board from the high impedance capacitance probe, the same signal could be measured from the output of the non-inverting amplifier with a low impedance. This reduced the impedance of the probe sensor signal as it was seen by the DAQ board, which eliminated problems due to impedance matching (i. e. signal measurement attenuation), and further problems if more signals had to be measured by the same DAQ board, such as signal ghosting (Worosz et al., 2016). Potentiometer R5 allowed adjusting the output DC signal level amplitude. An additional resistor R6, that is within the suggested input impedance range for the DAQ (about 320 kΩ), was included between the output of the voltage follower and the DAQ board, in order to ensure the stability of the Op-Amp. The corresponding DC output signals from this stage output were acquired by means of a NI-USB-6210 (National Instruments, TX, USA) at 10 kHz sampling frequency, and a custom acquisition software designed with LabVIEW (see section 8.2.4 for further details).

The frequency response of the circuit should be analyzed in order to a better understanding of the proposed methodology. An extended explanation of this type of circuit configuration can be found in Da Silva (2008). Considering the transfer function module of the trans-impedance circuit, and by assuming that the Op-Amp is ideal, the output voltage V_o is determined by Expression 8.1.

$$\frac{V_o}{V_i} = - \left(\frac{1/R_m + j\omega_f C_m}{1/R_f + j\omega_f C_f} \right) \quad (8.1)$$

Where $\omega_f = 2\pi f$ and f is the frequency of the excitation signal V_i , C_f and R_f are the capacitor and resistor at the feedback of the Op-Amp, and C_m and R_m are the capacitor and resistor which represents the electrical behavior of the media between electrodes.

In many practical situations only one parameter, i.e. C_m or R_m , is of interest or present as a physical quantity. In this way, the circuit may then be dimensioned as capacitance or resistance dominant, respectively, by selecting the proper excitation frequency. Since the resistance R_m is directly proportional to the conductivity of the material, and the capacitance C_m is directly proportional to the electric permittivity of the material, the measurement of the resistance and capacitance parameters are an indication of the electrical conductivity and permittivity of the measured substance being measured.

From Expression 8.1, it can be found that, ideally, the resistive measurement (R_m) is dominant at low excitation frequencies meanwhile, capacitance measurement prevails at high excitation frequency (Expression 8.2 and 8.3, respectively).

$$\left| \frac{V_o}{V_i} \right|_{f \rightarrow 0} \approx \frac{R_f}{R_m} \quad (8.2)$$

$$\left| \frac{V_o}{V_i} \right|_{f \rightarrow \infty} \approx \frac{C_m}{C_f} \quad (8.3)$$

It is important to keep in mind that the presented analysis considers an ideal operational amplifier with infinite frequency response. However, existing operational amplifiers have a bounded frequency response, that is, depending on their characteristics they have a limited gain-bandwidth product. Therefore, measurement amplification is limited at high excitation frequencies.

In this study, the target parameter was the capacitance C_m because the liquid media is expected to change its conductivity in most of the practical scenarios, whereas C_m is only dependent on the characteristic electric permittivity of the media (Da Silva et al., 2007). For instance, electrical conductivity change between deionized water and seawater is about 500%, in contrast, the electrical permittivity remains constant. Therefore, relatively high excitation frequency should be used to locate the measurement in the capacitance dominant plateau, as shown in Figure 8.3.

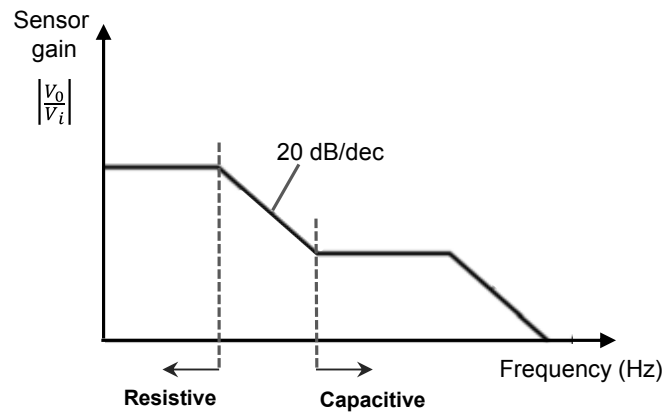


Figure 8.3. Trans-impedance circuit frequency response.

In this work, two similar experimental conditions were tested. Although measurements in both conditions share the same sensor electronics, the measurement sensitivity achieved differs greatly, as well as, its measurement capability: a) Three-phase measurement: air-water interface and water-biofilm interface discrimination; b) Two-phase measurement: water-biofilm interface discrimination.

In case (a) the sensor has to be capable of discriminating between two media with very different conductivity and permittivity, air and water. This is a simple condition if the system was able to change the feedback resistor and capacitor, however, the similar conductivity and permittivity between water and biofilm is a limiting factor for sensitivity adjustment. Input frequency and amplitude have to be tuned in a narrow band in order to avoid the output signal saturation, in this case, higher frequencies and low amplitude. In addition,

discrimination of biofilm surface into water requires lower frequencies and high amplitude to make output signal sensitive to this interface. Therefore, the input frequency and amplitude selected is a compromise between detection capability and phase sensitivity. The best results were obtained with $f=300$ kHz, in combination with $C_f=1$ pF and $R_f=1$ M Ω . Air-water presented a step response without DC output saturation and water-biofilm location could be inferred, although the output signal change was quite smooth.

In case (b), although a tiny change of relative permittivity was expected (i.e. changes in the pF order in the capacitance measurement), a single input parameter (excitation frequency) as chosen to maximize the signal response.

8.2.4. Motion system and control program

The motion system consisted of three actuators that allowed the three-dimensional positioning of the microsensor, and the controller to drive the automatized actuators. Two actuators were part of a two-dimensional stage for horizontal and vertical control of the sensor (X and Y axes respectively) and one actuator was part of a manual micromanipulator for horizontal control of the biosystem (Z-axis). The two-dimensional stage consisted of two fixed one-dimensional stages with stepper motors (VT-80 50-2SM and VT-80 200-2SM, Physik Instrumente (PI) GmbH & Co, Karlsruhe, Germany) that allow the linear movement of two bases. The stepper motors have the capability of moving the bases in two horizontal axes (X and Y) in a range of up to 200 and 50 mm respectively, using micro-stepping technology and producing movements in the micrometers order with a resolution of 0.2 μm , and a uni-directional repeatability of ± 0.4 μm . The manual actuator (DTS50/M, Thorlabs Inc., Newton, New Jersey, USA) was a micromanipulator with a micrometer, which can achieve horizontal movements in a 50 mm range with a maximum resolution of up to 0.2 μm .

The stepper motors of the two-dimensional stage need to be driven by the control program. The two-dimensional stage is connected to a two-axes micro step controller (SMC Corvus-eco, Physik Instrumente (PI) GmbH & Co, Karlsruhe, Germany), which is also plugged into the computer, thus establishing the commutation between the actuators and the control program. The computer program sends movement commands in the form of digital signal to the controller, which interprets that signal and sends an analog signal to the stepper motors, so they finally move.

The control program goal was to synchronize the functionalities of the measurement system and the motion system. The control program needed to have the capability to control the sensor movements in two-dimensions and the data acquisition tasks every time that the sensor was positioned in the desired place, allowing to program the sequences of measurements. The commercial software of the Corvus micro-manipulator controller does not provide the option of a trigger signal for acquisition mixed with movement sequences, so the commercial software package was adapted to fully automate the measuring procedure.

A new graphical user interface with this capability was developed using LabVIEW, employing the low-level functions provided in the Corvus package.

The LabVIEW programs development consist of two main parts: the front panel or user interface, and the block diagram (code side). The front panel comprises all the controls and indicators needed in the system to be controlled, and the block diagram contains the source code of the program. In this work, the front panel composition was aimed to provide the user with a logical and easy way to preset and program different sensor movement and data acquisition tasks (see Figure 8.4). In this sense, controls to indicate the length of displacement in X and Y axes, and to designate the acquisition time and frequency were defined; or for implementing the name of the data files and the folder path to save the data files. Buttons control for starting the execution of measurement sequence, or moving the indicated length of displacement in X and Y axes were also implemented. Moreover, indicators with the actual position (X and Y axis) of the sensor were displayed, among others. In another way, the block diagram contains functions of the DAQ system for recording the experimental data, and the low-level functions of the Corvus controller for driving the movement of the 2D stage, synchronizing both tasks with the developed code. In this sense, an extra effort was made to adapt the provided low-level functions from Corvus, i.e. the micromanipulator controller, to obtain a standalone measurement system capable of combine positioning and measuring steps for time-demanding experiments (large positioning-acquisition steps number).

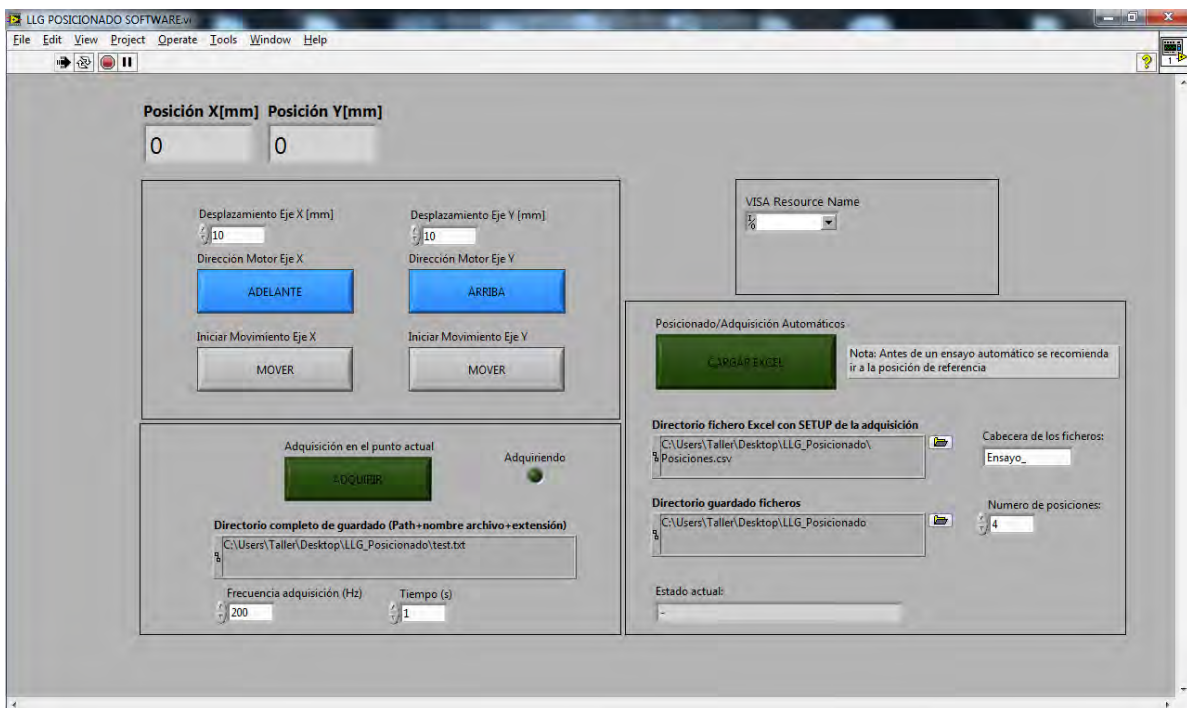


Figure 8.4. The front panel of the control program implemented in LabVIEW.

Finally, the data acquired needed to be processed to accurately reconstruct the detected interfaces. This procedure was developed with a script in MATLAB Release 2016b®, where all the individual files (i.e. each vertical profile generate one individual file) were processed to generate a 2D matrix with data in X and Y dimensions. Then, if it was required a 3D case, the 3D reconstruction was done by linear interpolation by knowing the value of Z-axis for each of the generated 2D planes.

8.3. PRELIMINARY RESULTS AND MEASUREMENT PRINCIPLE

Although the characterization of the media between sensor electrodes is possible (interface location, characteristic electrical magnitude, density, relative depth...), the present work is mainly focused on the sensor probe used to analyses the obtained voltage signal, allowing the interfaces detection in multiphase systems.

As an example, Figure 8.5 depicts a full sequence of measurements in a two-phase system (liquid-biofilm).

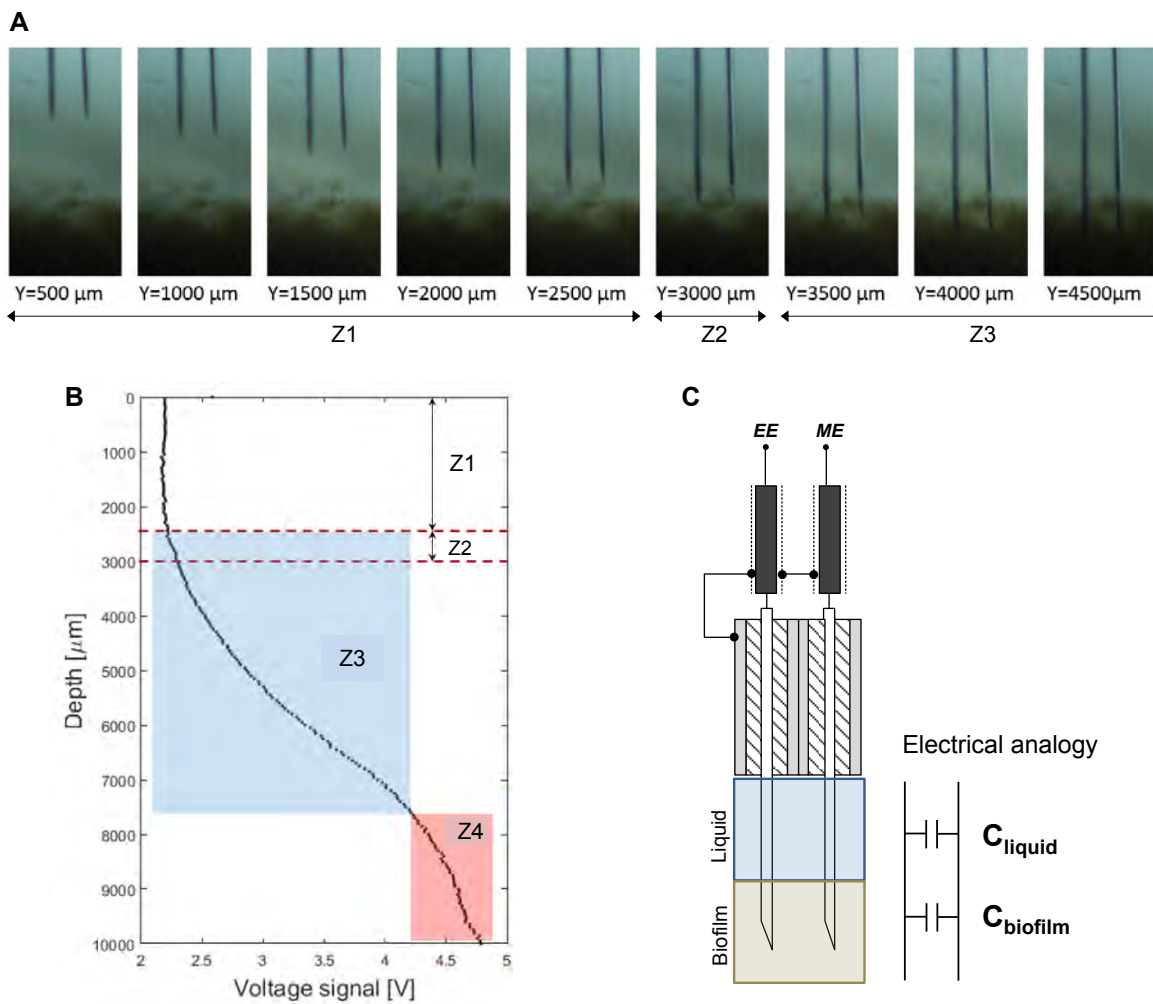


Figure 8.5. A) The sequence of measurements with the needle probe at different depths (Y points) in the experimental set-up for the two-phase system (liquid-biofilm). B) Voltage signal recorded in the experiment at different depths. C) Capacitance measurements analogy in the studied two-phase system.

A set of image frames recorded during a procedure of profiling is shown in Figure 8.5A. In these images, the position of the needle-probes relative to the biofilm phase can be observed. First, the probe was in the liquid phase, after advancing 2000 μm was closer to the biofilm, and by 3500 μm went into the biofilm. It should be pointed out that images from 4500 μm are not depicted, since changes in the images are not noticeable when the sensor probe was into the biofilm.

Figure 8.5B shows the corresponding signal voltage of the probe sensor during the profiling: voltage signal increases exponentially when the probe touches the interface, meanwhile a nearly linear increase can be found as the probe goes into the biofilm. Analyzing the signal acquired in a profile in the XY plane (Figure 8.5B), the recorded profile can be described as follows. As long as the sensor probe was on the water (zone Z1), the signal remained constant until the tip of the sensor reaches the surface of the biofilm. There is an uncertainty region (zone Z2) where the biofilm exists but was well mixed with the water. However, the output voltage increment in this region seems to be sufficient to establish the medium change. In this particular case, it can be observed that the sensor was capable of detecting even a small protuberance in the surface of the biofilm. When a significant part of the needle-probe was submerged into the biofilm substrate (zone Z3), which was more homogeneous than diluted biofilm in zone Z2, the signal voltage increments were almost proportional to the biofilm depth. Finally, it should be pointed out that the attenuation of the voltage signal (zone Z4) was caused by signal saturation. Improvements to limit this effect could also cause negative changes in the measurements sensitivity in zone Z2. As previously explained, it depends on the measurement objective priority, interface detection or biofilm depth: increasing excitation frequency would delay the saturation zone.

Figure 8.5.C aims to describe the principle of operation of the sensor. Ideally, as the sensor goes deep in the biofilm and perpendicular to its surface, the equivalent medium circuit is two-parallel capacitor system. Therefore, the voltage output response measured in the media (C_m) should be proportional to capacitances C_{liquid} and C_{biofilm} . This corresponds (ideally) to Z3 in Figure 8.5B. There are various and non-exclusive probable causes for explaining the non-linear response in Z2: (1) Biofilm is well diluted in this zone, therefore there is a small change between C_{liquid} and C_{biofilm} ; (2) as the detection length of probe sensor is large (needle tips about 11 mm length), the influence of C_{biofilm} is limited; (3) the needle ends are sharp, thus the available sensing area of ME is smaller; and (4) the needle-electrodes could not be perfectly parallel aligned.

In addition, Figure 8.6 shows a three-phase system with gas phase (air), over a liquid phase (water), which in turn is over a heterotrophic biofilm layer, thus, having present different phases in the vertical plane. In the graph, the subsequent voltage profile (voltage versus vertical position) recorded when placing the sensor probe from the gas phase, through the liquid phase, finally being in the biofilm phase is depicted. In this graph, the origin

position on the X-axis was located in the gas-liquid interface, where there was a significant step in the voltage signal (non-conductive to conductive phases). Then, when the sensor was inside the liquid phase, a linear region in the voltage profile with slight slope was detected. Finally, another linear region of the voltage with a larger slope is observed in the profile, assuming to be inside the biofilm. As stated previously, input signal frequency had to be carefully selected in order to not saturate the output signal caused by the large capacitance difference between air-water phases. At the same time, input signal frequency should be large enough to capture the small capacitance difference at water-biofilm interface.

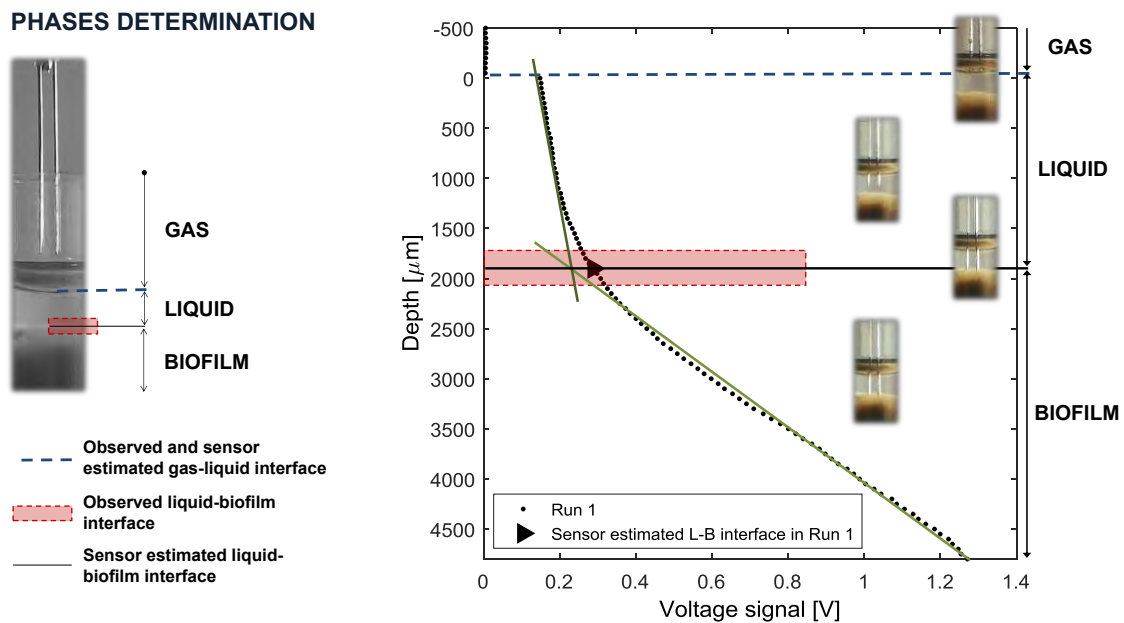


Figure 8.6. Explanation of phase (gas-liquid-biofilm) discrimination based on the voltage signal.

The interface or boundary layer between the liquid and biofilm phases was defined as the distance of the profile between both linear parts recorded. Thus, the estimated liquid-biofilm (L-B) interface was the intersection point between the two regions, which is indicated using a triangular geometry (►). This intersection point, i.e. ►, was obtained post-processing the recorded data in MATLAB, doing two linear interpolations, i.e. one for each of the linear parts recorded in the voltage profile, and using the data which share similar voltage gradient for each of the parts. From the results presented in Figure 8.6, it can be stated that the proposed methods allowed to accurately differentiate the thickness of gas, liquid and biofilm phases from the experimental data.

8.4. RESULTS AND DISCUSSION

The present section was devoted to present several experimental conditions and geometrical configurations to test the sensor probe capabilities. Firstly, measurements for a two-phase system (water-biofilm) were presented. This scenario allowed to evaluate the complete system capacity: positioning system, sensor capability detecting the biofilm interface and the data processing to obtain a 3D representation of a sample interface. Secondly, the sensor was evaluated in different scenarios which involve a three-phase system (air-water-biofilm) with variable liquid phase conductivity and different biofilm depths.

8.4.1. Experimental results of two-phase biosystems

Figure 8.7 will be used to show the agreement between the sensor measurements and the procedure to determine the interface in a two-phase (liquid-biofilm) biosystem. Figure 8.7A shows an image of the real experimental set-up with the liquid phase and heterotrophic biofilm and also depicts the biofilm surface to be measured with the sensor probe. The biofilm was placed in the measuring chamber and covered with water. Measurements were performed with the sensor probe fully covered by water. Therefore, the voltage value associated with the liquid phase was initially known.

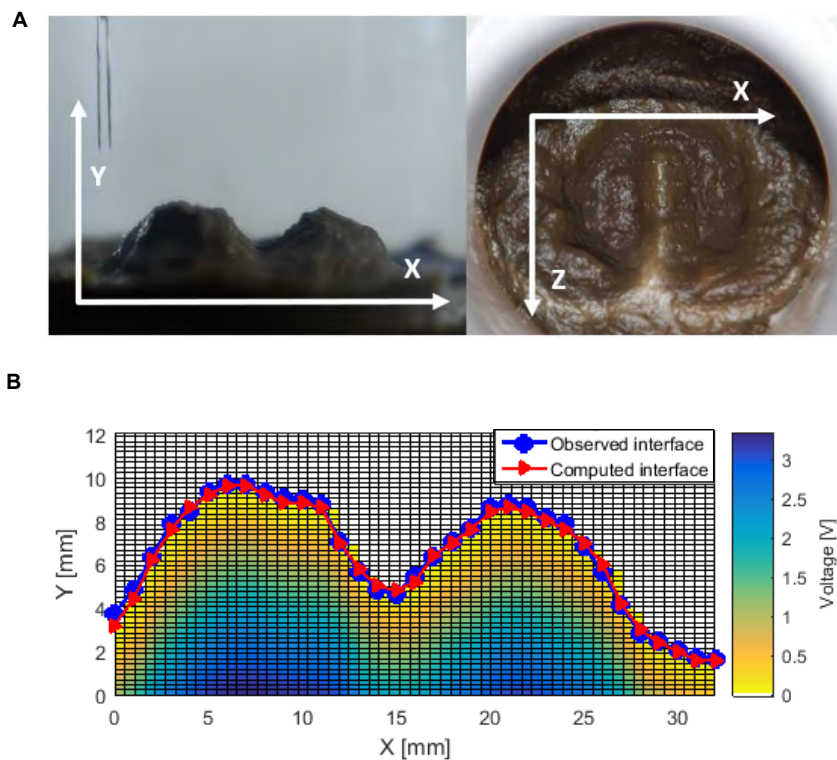


Figure 8.7. A) Real experimental set-up with liquid and biofilm phases. B) Comparison between observed interface location (circle symbols) and the computed interface location (triangular symbols) in a complete signal processing interface reconstruction (2D color map).

The needle-probe was positioned in the origin position, to take measurements every 10 μ m in the vertical direction, and every 1 mm in the horizontal direction. In addition, in Figure 8.7B is depicted the 2D color map obtained after processing data from the sensor, where the voltage measured in each acquisition of the sensor was related to the vertical position of the same. The estimated or computed liquid-biofilm interface is indicated over the color map by the triangular markers. For the visual detection, the micromanipulator was manually moved and visually observing the tip of the needle, the interface was located in the first Y position where the very end of the sensor needle touches the biofilm. The measurements were repeated 3 times in each local point, and using the macro lens of the camera to enlarge the observed contact zone. The observed liquid-biofilm interface is indicated over the color map by circle markers.

As previously stated, to obtain a complete sequence of measurements in X, Y and Z dimensions, the commercial software package from Corvus (micro-manipulator software) was adapted in order to fully automate the measuring procedure. The commercial software does not provide the option of a trigger signal for acquisition combined with movement sequences. A new graphical user interface using LabVIEW had to be developed, using the low-level functions provided in the Corvus package. The developed program inputs were a matrix with sequential XY positions, sampling rate and desired frequency acquisition. Thus the automatic procedure implemented for recording the data across the biosystem is as follows:

1. Giving an excel file with mentioned input parameters, the sensor was positioned in the desired X position and acquired the signal voltage during the requested time (5 seconds for presented experiments), and changing to the following Y position.
2. The same procedure was repeated as the last X position was achieved, thus completing a 2D spatial matrix of measurements (XY plane).
3. By means of a manual micrometer, the measuring chamber was displaced in the Z-axis, which allowed performing the next plane measurements, recording different planes in the Z dimension. The voltage signal was stored in a text file which name includes the absolute XYZ position.
4. With a script developed in MATLAB the 3D surface reconstruction was feasible based on the mean voltage value from each file. The mean voltage at each position was transformed into its equivalent depth value. Using a threshold value to identify the interface points, 2D and 3D surface shapes were obtained using linear interpolation.

Figure 8.7B shows an example of an XY plane measurement, obtained from a 120x300 positioning matrix, where the measured voltage is represented by the 2D color map obtained after processing data. The signal voltage (V) measured in each acquired position is averaged and voltage level corresponding to water subtracted. Therefore, the biofilm interface is defined by means of a voltage threshold ($V_{\text{threshold}}$):

- If $V(x, y, z) < V_{\text{threshold}} \rightarrow$ liquid phase
- If $V(x, y, z) \geq V_{\text{threshold}} \rightarrow$ biofilm phase

Where the voltage threshold used in this experiments was $V_{\text{threshold}} = 0.001$ V, proving its suitability for all conditions tested. It should be pointed out that although different gradient-based methods were tested, a single threshold value provided better results since it was less affected by the small irregularities from the surface of the biofilm.

As a measurement verification procedure, the comparison between the visual detection of biofilm surface against the value obtained from the sensor was performed. For the visual validation, the first Y position where the very end of the sensor needle touches the biofilm was considered. 340 visual detections of the interface were obtained in different XY locations of the test sample. An example is shown in Figure 8.7B, where the computed interface is compared to the observed interface. As can be seen, the results represent a strong agreement between the different interfaces detection methods, thus implying a proper functioning of the proposed capacitance probes. There were significant deviations (by 5%) only for some of the experiments. Thus, Figure 8.7B shows the agreement between the sensor measurements and the procedure to determine the interface. It is important to note that, as illustrated in Figure 8.7B, the voltage measured in each acquisition is related to the vertical position of the same. Thus, clear dependence on the biofilm thickness with the voltage recorded with the needle-probe can be stated.

Figure 8.8A shows the voltage-depth relation for all collected data points during the calibration procedure. Note that the starting point represents the initial detection of the biofilm and measured voltage offset is zero, because the reference voltage corresponds to water. In order to perform a measurements repeatability analysis and acquisition dispersion error, all them (mean voltage value obtained from each XYZ position) were represented together in Figure 8.8A. This relation was necessary to determine the voltage values for biofilm-liquid interface reconstruction, and to delimit real biofilm depth. The highest deviation estimated among all recorded data were less than 2%, which allowed to correctly calibrate the needle-probes by using the mean value of the collected data during the calibration procedure. It should be pointed out that, according to the ideal case depicted in Figure 8.5C, the voltage-depth relation would be expected to be linear. However, the deviations in the measurement were reported, especially in the first millimeter depth, which could be related to the geometric arrangement of electrodes, since slightly changes between electrodes distance can change voltage measurement. The radial distance between measuring electrodes and excitation

electrode must be kept constant, so that the detection volume and the influence of the electric field between excitation and measurement electrodes are as similar as possible in all cases during the measurement. In addition, it should be pointed that the deviations could be also related to not significant voltage measurements for the biofilm at the interface, since the biofilm could be well diluted in such zone, and the transition from liquid to biofilm could be characterized by a small change between C_{liquid} and C_{biofilm} .

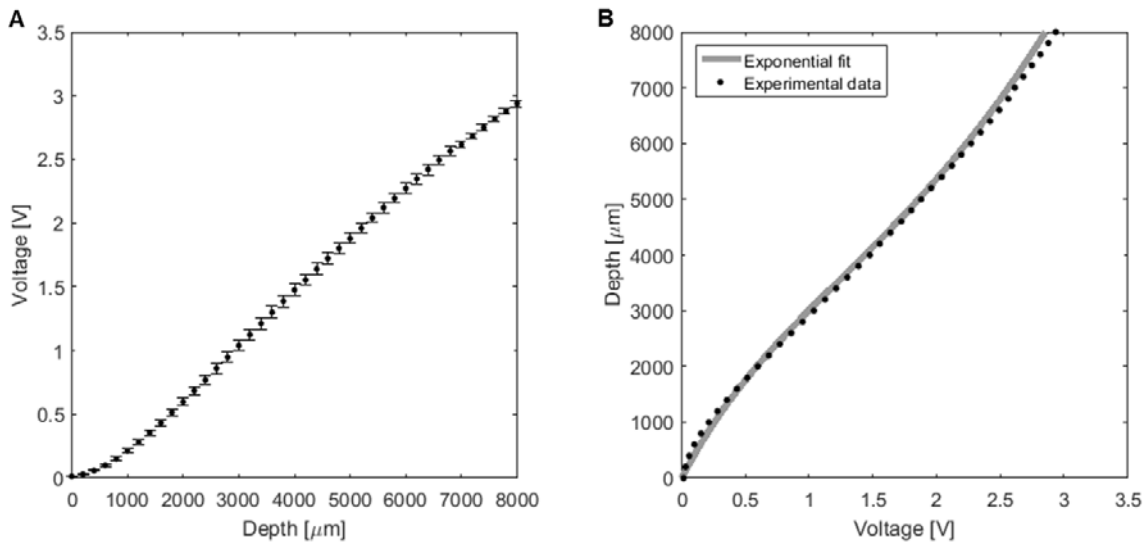


Figure 8.8. A) Voltage-depth relation for the collected data points during the calibration procedure, i.e. showing the mean voltage value obtained from each XYZ position and its dispersion error. B) Depth-voltage relation for the mean of the data collected at each XYZ position, and their fitting by means of Expression 8.4.

Figure 8.8B shows the depth and measurement voltage relationship. Providing an expression to this relation allows the direct conversion of measured voltage into a distance magnitude. For the present experiments, it was found an exponential relationship (Expression 8.4), which fits the experimental data with lower deviations ($R^2=0.99$ and $RMSE=0.023$).

$$\text{Depth(mm)} = 2.22 \cdot (e^{0.45V} - e^{-1.55V}) \quad (8.4)$$

Figure 8.9 illustrates the 3D representation of the complete biofilm surface after the post-processing using MATLAB. Figure 8.9A depicts several XY slice planes obtained and the voltage depth representation. Considering water voltage as the reference value ($V=0$), Figure 8.9A shows the voltage measured increasing with depth and starts to illustrate the final biofilm surface. By means of threshold method aforementioned, the corresponding position in X, Y and Z coordinates for the interface was detected. Once the voltage associated to interface in each position in X, Y and Z coordinates were determined (using Expression 8.4), the maximum local thickness was represented by the maximum voltage measured in the Y direction for each case. These maximum voltages matrix is depicted in Figure 8.9B and Figure 8.9C, representing the final reconstructed biofilm surface depth.

Although the procedure shown in this section to reconstruct the surface biofilm relies on a 3D positioning system, it also can be useful to demonstrate further capabilities and arrangements for the sensor in a real system. For example, if considering flush-mounted sensor applications, the sensor would virtually provide the instantaneous biofilm depth or growth rate. Therefore, from the point of view of biological processes control monitoring, it can be used to detect the biofilm attachment or used to define biofilm-removal times in biological systems.

In addition, this system would provide a feasible and easy implementation method to spatially define the biofilm surface which is of the utmost importance. The biofilm surface is equivalent to the available interfacial area (fluid-biofilm), which is a key parameter to model biofilm behavior and transfer processes as previously discussed in Chapter 6. In the particular case of biofiltration system modeling, although different sensitivity analysis of model parameters revealed that this specific interfacial area was one of the most sensitive parameters, having a direct effect on the system removal efficiency (Dorado et al., 2008; López et al., 2016); this parameter is usually estimated from the packing material characteristics provided by the manufacturer (Kim and Deshusses, 2003; San-Valero et al., 2018), because of the difficulties found to measure it. Nevertheless, it is well known the biofilm surface shape can be very complex and very different from the geometry of the packing material (Piciorenu et al., 1998b). For instance, in the scenario presented in Figure 8.7, the real length of the detected interface is 41.142 mm, whereas the length is 32 mm if a flat geometry is assumed. Thus, the length of the estimated interfacial area would be the 77.78% of the real length in the case of assuming a flat geometry, and then the value of the available interfacial area would be reduced by more than 20%. Therefore, the presented method can make a further step in the reliable estimation of the parameters related to the biofilm surface, and the development of more rigorous models for this type of biosystems.

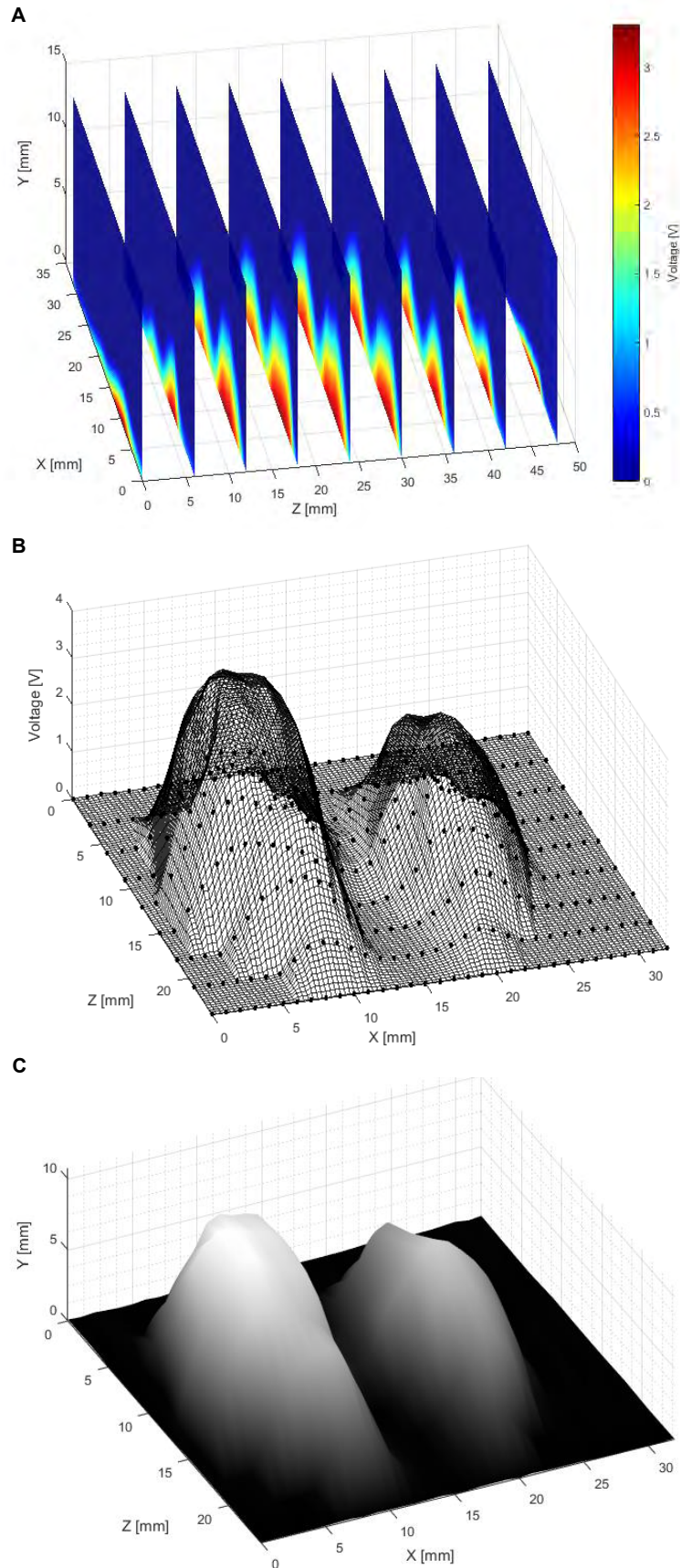


Figure 8.9. A) 2D data acquired during the sequence profiling. B) Reconstruction performed by interpolation (voltage). C) Reconstruction performed by interpolation (depth).

8.4.2. Experimental results of three-phase biosystem

In the developed system, the processing relied on voltage-depth conversion to correctly determine the interface location for each of the phases present in the biosystem. The performance achieved by the system for two phases has been illustrated in the previous section. However, simultaneous measurement of three-phase segregation presents some extra difficulties in terms of sensitivity. The gas-liquid interface is well defined due to the change for conductive to non-conductive media, that means that a large change in capacitance. However, determining the location of the liquid-biofilm interface is arduous due to the conductive and low capacitive character of both phases, thus, a small change in capacitance.

In this section, as illustrated previously in Figure 8.6, several vertical measurement profiles (Y-axis) were evaluated in the presence of three phases: gas, liquid and biofilm. The change between gas-liquid media produces a large output response. The trans-impedance feedback resistor and capacitor are fixed, therefore the voltage gain at the air-water interface could even saturate the sensor if the input frequency and buffering stages are not carefully selected. In contrast, selected frequency and buffering stages should provide enough voltage gain at liquid-biofilm interface. As mentioned in the previous section, an input frequency of 300 kHz and 2:1 amplification of ME signal were found suitable for both interface detection (i.e. air-water and water-biofilm).

As previously illustrated in Figure 8.6, the recorded experimental data profiles were compared with observed interface location by images of the experimental set-up for the verification of the experimental measurements. The local validation can be observed in Figure 8.6 for gas-liquid and liquid-biofilm interfaces. In the case of the gas-liquid interface, the observed interface location was indicated in the image of the multiphase system by a striped line. Additionally, it can be seen at $X=0$ mm the detected interface by the sensor signal, with a marked jump in the voltage signal. In the case of liquid-biofilm interface, exist a boundary layer between the phases, thus the observed liquid-biofilm interface was not clearly defined, and it was indicated as a region by means of a dashed box. This region was then compared with the estimated sensor interface (triangular geometry and solid line), being this point inside the observed liquid-biofilm interface region (dashed box). Thus, the local gas-liquid and liquid-biofilm interfaces detection were stated and verified.

All figures presented in this section share the same characteristics:

- The profiles were measured in the vertical plane for gas, liquid and biofilm phases, i.e. one-dimensional measurements at a fixed point in the horizontal direction.
- Voltage data was referenced to 0mm depth (gas-liquid interface), where a steep change in voltage can be observed.

- Beyond gas-liquid surface voltage signal increased as the sensor probe went deep into the biofilm. The liquid-biofilm interface detection was associated with a change of slope calculating it by linear interpolations, as detailed previously.

8.4.2.1. Measurements repeatability analysis and acquisition dispersion error

It is essential to analyze the accuracy of the measurements performed with the designed electronics. Thus, the possible dispersion that can be computed between the measurements performed in each local point, and the repeatability of the profiles recorded in the vertical plane was examined.

Figure 8.10A shows a profile in the vertical plane for gas, liquid and biofilm phases. Each XY point represents the averaged signal voltage measured during 5 seconds at 10 kHz sampling rate. The error bars in each local measured point indicated the error dispersion (i.e. the standard deviation of the acquired signal) in the acquisition of experimental data points in run 2. As can be observed, very low deviations (less than 0.5%) were recorded.

In order to show the possible discrepancies between experiments, Figure 8.10B shows the analysis of the measurements sensor repeatability. A profile at the same location in the measuring chamber was recorded three times, maintaining the same conditions in all biosystem phases. As can be seen, the different recorded profiles (run 3, run 4 and run 5) followed the same trend for each of the phases characterized. In addition, the estimated interface was located at the same position in the different repetitions, i.e. 1850 μm , with an almost insignificant deviation under 1% in the liquid phase. In this case, voltage data is normalized by means of air-water step voltage (voltage change at 0 mm depth) to clearly observe the relative voltage changes.

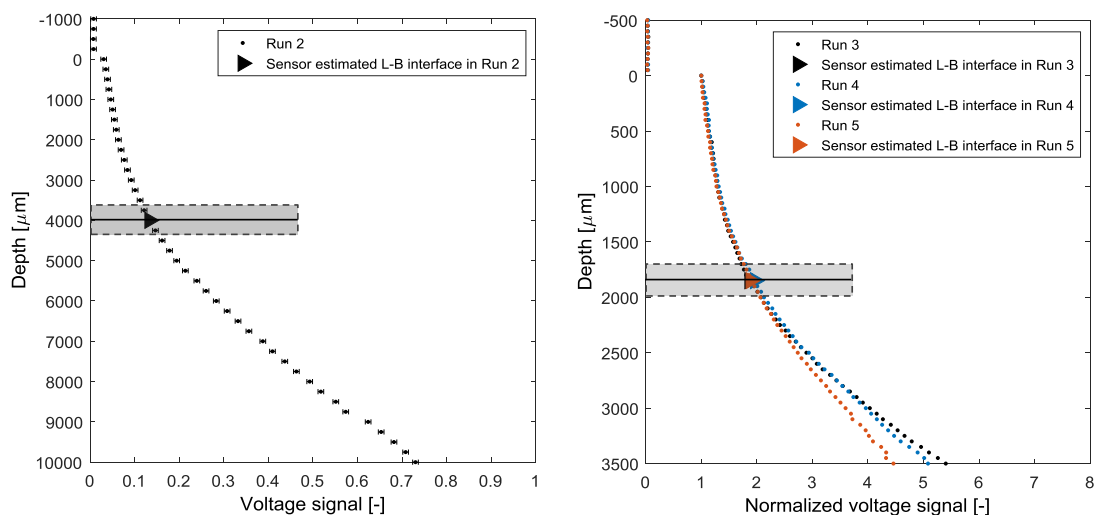


Figure 8.10. A) Error dispersion during the acquisition of the different points in a voltage profile (run 2). B) Sensor repeatability analysis by recording and comparing three different profiles at the same location (from run 3 to run 5).

8.4.2.2. Influence of the mineral medium in the microsensor response

In order to determine the working range of the sensors, their response in media of different composition was also studied. Since the most important variables in the study of biological systems are the nature of the medium, the effects of mineral medium composition conductivity on the capacitance sensor were studied.

Figure 8.11 depicts the measurements performed on two biosystems with different conductivity in the liquid phase. The liquid phase in Run 6 (mineral medium with a conductivity of $6550 \mu\text{S cm}^{-1}$) had approximately 6 times higher conductivity than the liquid phase in Run 7 (tap water and distilled water mixture medium with a conductivity of $1090 \mu\text{S cm}^{-1}$). As can be seen, all the recorded profiles followed the same trend as in the previous cases. Both cases showed very similar behavior and the L-B interface was detected at the same point. However, Run 6 (with higher conductivity) showed slight differences in terms of voltage increase despite normalization, possibly due to sensor polarization after the repetition of the measurement (Davey et al., 1995). Even so, the detected L-B interface obtained by the proposed method was inside the observed region with minimum difference.

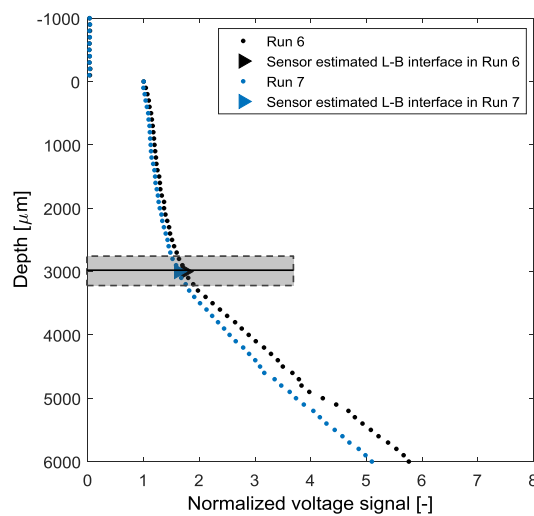


Figure 8.11. Voltage profiles measured with high and low conductive media in the liquid phase (run 6 and run 7, respectively).

8.4.2.3. Liquid layer thickness profiling

In this section, it was analyzed the capability of the capacitance needles to well characterize the thickness of the liquid layer over the biofilm in three phase systems. Depending on the target system, the liquid film could present very small thickness (i.e. few millimeters), as in the case of the flat plate bioreactor modeled in previous chapters. Figure 8.12 depicts four experiments in which the thickness of the liquid layer was different for each of them, which the approximate values determined by the visual inspection were 750, 1700, 1850 and 2500 microns (run 8 to run 11, respectively). As it can be seen, the sensor

detected the liquid-biofilm (L-B) interfaces inside the observed L-B interfaces for all the experiments, in agreement with the corresponding location of the interface from real biosystem image. The L-B interfaces detected by the sensor were at 800, 1800, 1900 and 2400 μm for run 8 to run 11, respectively, so those were the real liquid phase thicknesses for each of the run. In addition, all recorded measurements followed the same tendency after the interface detection.

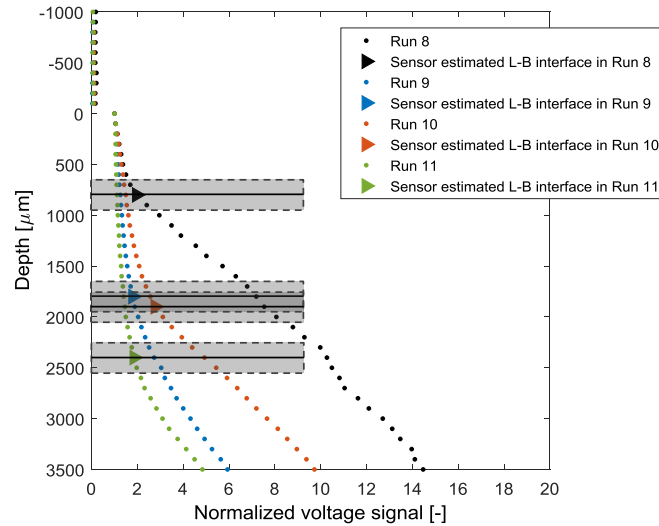


Figure 8.12. Profiles with different liquid phase thickness over the biofilm in three-phase systems (run 8 to run 11).

8.5. CONCLUSIONS

In this chapter, a local capacitance needle probe was presented. This sensor was described and tested in different conditions to prove its suitability to characterize the spatial distribution of multiphase biosystems. The main contributions of the presented sensor were the capability to locate the interfaces (gas-liquid and liquid-biofilm) with high spatial resolution, and providing a direct measurement related to biofilm thickness. In addition, as a requirement for accurate and automated measurements, a complete positioning system was implemented, extending and combining the capabilities of the commercial positioning system (Corvus) through its communication with an acquisition and control software (LabVIEW).

The developed system was proven its applicability to provide robust and consistent measurements for biofilm layer detection in a multiphase system. Experimental data demonstrated this sensor can measure a minimal change of capacitance with high precision, obtaining accurate measurements with the presence of a gas and liquid layers upon the biofilm. In addition, the provided results confirm the system capability to accurately reconstruct the 3D surface of the biofilm. Defining the biofilm surface geometry is equivalent to the determination of available interfacial area, which is a key parameter to model biofilm behavior and transfer processes.

The developed sensor, additionally to act as an interface detector, has also the capability to provide a level voltage related to biofilm depth. The availability of this direct thickness measurement would have practical application in real (industrial) systems: sensor could be mounted in-situ and flush-mounted and, therefore, to be used for monitor biofilm depth or register biofilm growth, without the need of a positioning system. Moreover, it can be used to detect the biofilm attachment or used to define biofilm-removal times in biological processes. Thus, the presented sensor probe becomes a potential tool for the experimental characterization of biosystems and models verification at mesoscale, allowing to acquire local experimental data related to the phases volume fraction (i.e. gas, liquid and biofilm) by means of capacitance measurements.

Finally, the proposed measuring system allows high-frequency measurements for interface/thickness characterization, although it is not a necessary requirement for the presented experiments herein. Nevertheless, this feature shows the potential applicability of the developed sensor in other cases presented along this thesis, such as instantaneous biofilm ripples during biofilm removal using a high-velocity jet or instantaneous and local thickness of the biofilm in packed bed systems.



GENERAL CONCLUSIONS AND FUTURE WORK

9.1. GENERAL CONCLUSIONS

This thesis was focused on to investigate the numerical modeling of fixed-bed biofilm systems through computational fluid dynamics (CFD) techniques and experimental validations. In order to achieve this objective, the characterization of physical, biochemical and mechanical properties of biofilms was conducted, and the procedures implementation of biochemical processes coupled with fluid dynamics into CFD codes were evaluated, and verified with experimental data. As a result, several computational models were developed, including phenomena such as transport and consumption of dissolved components, microbial biomass growth, biofilm deformation and detachment, thus allowing to describe fixed-bed biofilm systems performance under both laminar and turbulent conditions.

In general, this thesis brings the research on biofilms continuum modeling forward, by the representation of biofilms as a liquid (or liquefiable) non-Newtonian fluid, and implementing it into CFD codes. This combination helped to address key aspects of the biofilm modeling such as its deformation and detachment, opening several research lines (i.e. non-Newtonian biofilms in multiphase CFD models; new rheological models for biofilms; biofilm disruption, removal and control strategies using laminar and/or turbulent flows).

More specifically, the conclusions derived from this thesis could be grouped in four main topics: rheological properties characterization of fixed and suspended biomass, CFD models developed to study biosystems performance under laminar flow conditions, CFD models developed to study biosystems performance under turbulent flow conditions, and application of needle-probes to characterize fluid interfaces in biosystems.

9.1.1. Rheological properties characterization of fixed and suspended biomass

The conclusions related to the rheological properties characterization of fixed and suspended biomass arising from Chapter 5 are:

- Biofilm and suspended biomass samples were extensively characterized using rheological test under different shear flow conditions, allowing to provide macroscopic mechanical properties and insights into the microscopic structure. Nexuses between the rheological responses of both samples were also detected in the data analyses.
- Steady, oscillatory and transient shear flow test allowed to quantify relevant mechanical properties (i.e. yield stress, elastic modulus, relaxation time respectively) of both samples, as well as to determine their behavior under various external shear stress. Both samples were found to exhibit shear-thinning with yielding pseudo-plasticity and gel-like characters.
- Equivalent flow characteristics were found for both samples. However, during the samples deformation, i.e. under non-steady flows, the important role of the hydrogel network present in biofilms was also detected, observing dissimilarities in the

structural characteristics. These findings imply that the suspended biomass can be used for the characterization of the biofilms viscosity and flow curves, due to its practicality for the samples extraction, with low invasion.

- Herschel-Bulkley and Burger models were satisfactorily applied to describe the pseudo-plastic and viscoelastic responses under steady-state and transient shear flows respectively, providing new parameters to implement fluid-structure interaction models for both samples.
- In both samples, the pseudo-plastic fluid properties were influenced by the samples concentrations. The strong dependency of the Herschel-Bulkley rheological parameters to the biomass concentration was properly quantified through new correlations.
- The shear-thinning character of biofilms was successfully predicted with the defined correlations for the rheological parameters of Herschel-Bulkley.

9.1.2. CFD models developed to study biosystems performance under laminar flow conditions

The conclusions related to the CFD models developed to study biosystems performance under laminar flow conditions arising from Chapters 4 and 6 are:

- A procedure to describe accurate models of fixed-bed biofilm reactors, coupling hydrodynamic and biological behavior using CFD techniques, was successfully stated and applied. The methodology allowed implementing Euler-Euler models to study biosystems performance by means of 2D and 3D domains, and one-phase and multiphase models (liquid-biofilm).
- The operation of a fixed-bed bioreactor was properly described using the CFD models developed, and verified with experimental data measured in liquid and biofilm phases under different operating conditions.
- The developed CFD models have shown to be highly adequate to study in detail hydrodynamic variables involved in biosystems processes, simulating adequately the DO concentration trend throughout the concentration boundary layer, and liquid and biofilm phases.
- Evaluation of mass transport during the bioreactor operation allowed to determine a duality of transport mechanisms (convection plus diffusion) in the liquid phase, as well as to describe numerically the contribution of the concentration boundary layer thickness to the mechanisms.
- In the multiphase models, the biofilm was successfully implemented as a non-Newtonian fluid with experimental data from the rheological analyses. Thus, a novel approach of biosystems continuum modeling was described, which allowed

considering the physical behavior or motion of the biofilm although increasing the computational time.

- The CFD multiphase models were properly developed and solved using the volume of fluid (VOF) method, tracking accurately the interfacial area, and coupling hydrodynamic with biofilm mechanical properties, biochemical phenomena and/or biofilm behavior.
- A fluid mass source was included in the biofilm phase describing microbial growth kinetics for the two-phase model. The predicted growth patterns were consistent with heterogeneous substrate distributions, despite model stabilization difficulties were found probably because of the low inlet velocities required been computed.
- Stretching, recoil, and detachment phenomena in fixed-bed biofilms, were properly described using two-phase CFD models. Backwash strategies were also studied using the developed models. These findings represent a considerable advance in fluid-biofilm interaction modeling (to the author knowledge). The shear-induced deformation and detachment of the biofilm were reproduced at different hydrodynamic laminar conditions, starting the biofilm to deform for $Re > 900$ and to detach for $Re > 1700$, being this consistent with the reported experimental evidence in different biosystems.
- Biofilm mechanics required for resistance to deformation, stretching, and detachment were found to be largely attributed to biofilm viscosity and its non-Newtonian character.

9.1.3. CFD models developed to study biosystems performance under turbulent flow conditions

The conclusions related to the CFD models developed to study biosystems performance under turbulent flow conditions arising from Chapter 7 are:

- The new approach of the continuum model was applied to simulate the biofilm disruptions induced by air-jet impingements. Therefore, CFD multiphase models were developed considering gaseous, turbulent flows, defining the biofilm as a non-Newtonian fluid and being fixed to a wall.
- The CFD multiphase models (air-biofilm) were properly developed and solved using a coupled method of VOF and level set and SST $k-\omega$ turbulence models, and experimentally verified, besides establishing the use of the new continuum modeling approach for describing biofilm behavior under turbulent conditions.
- The interfacial instabilities on the fixed-bed biofilm, such as a cavity generation (on the impact zone), waves formation, and biofilm displacement and removal from its original position, were correctly described with the developed CFD models.

- Biofilm fluidization was confirmed to be the mechanisms behind the impact of turbulent flows, reproducing the extremely quick and transient mechanical behavior of biofilms during high-velocity exposures.
- The fluid applied forces (i.e. inertial, shear and interfacial tension) and the biofilm mechanical properties are both enhancing biofilm disruption, by ripples and surface instabilities generation, and removal by liquefaction. This is the first numerical study where the mechanisms behind the impact of turbulent flows on the biofilm structure were interpreted, as far as the author knows.
- High jet-nozzle velocities, and low surface tension and viscosity values were confirmed to intensify biofilm disruption, generating interfacial instabilities which result in a larger available interfacial area. These findings could have important implications for new strategies for controlling and preventing undesirable biofilms.

9.1.4. Application of needle-probes to characterize fluid interfaces in biosystems

The conclusions related to the application of needle-probes to characterize fluid interfaces in biosystems arising from Chapter 8 are:

- The proposed capacitance sensor was proven its suitability to locate the interfaces (gas-liquid and liquid-biofilm) with high spatial resolution, measuring minimal changes of voltage, and obtaining accurate in-situ and real-time measurements of the interfaces and the phases' thickness (fluids and biofilm).
- The probe performance was calibrated in multiphase systems (liquid-biofilm and gas-liquid-biofilm), stating the relationship voltage-biofilm depth. Then, the probe performance was verified in these multiphase systems at mesoscale, allowing to reconstruct the 3D biofilm surface, thus determining the available interfacial area in the biofilm.
- The sensor probe design allowed to place the sensor anywhere within the biosystem. In practical, the sensor could be mounted in-situ and flush-mounted in the bioreactor walls, without a positioning system, in order to continuously monitor biofilm growth, and/or to detect biofilm attachment or removal in the biosystem.

9.2. FUTURE WORK

In this thesis, an extensive knowledge of fixed-bed biofilms systems modeling using CFD techniques has been acquired. Furthermore, this is intended to serve as a basis for future CFD codes development. However, further investigation is required in order to improve the developed models and to characterize the biosystems. The following tasks could continue this work in short and long-term.

Regarding the analysis of rheological properties of fixed and suspended heterotrophic biomass, future work focused on the extensive analyses of the macroscopic properties linked to the microstructure of biosystems must be done, in order to deeply study the different biofilm behaviors (i.e. from viscoelastic solids to viscous liquids) and to develop more complete biofilm models:

- Further analyses to characterize the large amplitude oscillatory shear (LAOS) behavior, such as to examine the shear stress waveforms, should be performed to deeply investigate their shear-induced microstructures, and helping to understand the type of network junctions and/or interactions present in the EPS matrix.
- To estimate the dependence of the non-steady shear conditions in a wide range of biofilm densities, to determine the possible variation of rheological parameters (i.e. elastic modulus and relaxation times) related to biofilm properties.
- To evaluate the use of constitutive models to represent the elastoviscoplastic behavior of biofilms, which describe the time evolution of stress/viscosity as a function of the shear rate, and consider thixotropic character. These models couple both elastic and viscous behaviors, which have been commonly reported for several biofilms.

With respect to the CFD models, future work has to be focused on the progression of the developed models, which in some cases can need the implementation of much more computationally intensive models to include three-dimensional domains, additional fluid phases or more accurate numerical methods:

- To analyze the use of the coupled method VOF-level set to improve the biofilm growth model by means of fluid mass sources. Additionally, the isosurface that defines the real interfacial area, i.e. isosurface calculated from volume fractions gradients, needs to be included in the iterative calculation process of the model, in order to contemplate the exchange area in processes where mass transfer is involved.
- To investigate the implementation of elastoviscoplastic models into CFD codes, in order to consider the elastic component in the biofilm properties.
- To implement 2D and/or 3D CFD models to study the fluid-biofilm interaction with more heterogeneous biofilm geometries presenting thickness variations. In addition, with an accurate rheological characterization, future work could also consider biofilm morphology by mechanical properties variability, thus defining it in the CFD models.
- To examine the use of VOF models for simulating a part of a packed bed from a bioreactor, i.e. biofilter or biotrickling filter, comparing the results with detailed experiments characterizing biofilm properties and fluid dynamics. These models

would be very helpful to study biofilm control strategies and to optimize the performance of this type of bioreactors.

- To extend the investigation of turbulent flows over fixed-bed biofilms to model 3D scenarios and/or to implement three-phase models (water-liquid-biofilm), allowing to study the effect of liquid impact over biofilms.
- To use the three-phase models to study the implications of biofilm deformation on mass transport (e.g. enhancing penetration of antimicrobials) and strategies for biofilm control (such as detachment or surfactants effect).
- To examine the use of Large Eddy Simulation (LES) turbulence model, in order to capture more accurately the possible eddies produced in the simulations of turbulent and transitional flows over biofilms.

Related to CFD codes usage, a more long-term task would be the use of open source codes, such as OpenFOAM®, which allows developing CFD solutions literally tailored to a specific case. Additionally, hybrid models could be defined with OpenFOAM®, possibly using the VOF model and the immersed boundary method implemented on the open code.

Finally, regarding the models verification, modifications on the set-ups would be performed by new elements incorporation, and new experimental set-ups must be created, in order to improve the data monitoring during biosystems operation.

- Mounting the capacitance sensor in the experimental set-up (e.g. the flat plate bioreactor) for recording experimental data related to biofilm structure, will help to verify models with biofilm growth, deformation or detachment under laminar conditions. In addition, a flush-mounted capacitance system could be developed, being assembled to bioreactor walls for monitoring readily the biosystem.
- Additionally, the use of capacitance sensors would provide the possibility to couple the measurements of the species present in the biosystem with the detected biofilm layer and interfaces.
- To apply the needles-probe system to perform high-frequency measurements in order to study biofilm behavior under turbulent conditions, being able to characterize instantaneous biofilm ripples during its removal using a high-velocity jet or instantaneous and local thickness of the fixed-bed biofilm.
- Related to create new experimental set-ups, designing an experimental system similar to the curved channel presented in Chapter 6, in order to study its hydrodynamics and verify the complex patterns formed (e.g. eddies). Also, the use of complementary tools such as particle image velocimetry (PIV) must be considered.

NOMENCLATURE

List of abbreviations:

ADV	Acoustic Doppler velocimeter
AFM	Atomic force microscopy
BM2	Benchmark problem 2
BTF	Biotrickling filter
CA	Cellular automata
CBL	Concentration boundary layer
CFD	Computational fluid dynamics
CLSM	Confocal laser scanning microscopy
CSF	Continuum surface force
CSTR	Continuously stirred tank reactor
DAQ	Data acquisition
DC	Direct current
DNS	Direct numerical simulation
DO	Dissolved oxygen
EE	Excitation electrode
EVC	Estimated viscosity curves
EPS	Extracellular polymeric substances
FEM	Finite element method
FFT	Fast Fourier transform
FPB	Flat plate bioreactor
GMP	Good modeling practice
HBL	Hydrodynamic boundary layer
IbM	Individual-based models
IB	Immersed boundary
LAOS	Large amplitude oscillatory shear
LDA	Laser Doppler anemometry
LES	Large eddy simulation
LVR	Linear viscoelastic regimen
ME	Measuring electrode
MRM	Magnetic resonance microscopy
NDFs	Numerical differentiation formulas
NMR	Nuclear magnetic resonance
NRMSE	Normalized root mean square errors

OCT	Optical coherence tomography
Op-Amp	Operational amplifier
PFR	Plug flow reactor
PISO	Pressure-implicit with splitting of operators
PIV	Particle image velocimetry
PLIC	Piecewise linear interface construction
PRESTO	Pressure staggering option
PTM	Particle-tracking microrheology
RANS	Reynolds-averaged Navier–Stokes
RMSE	Root mean square error
RSM	Reynolds stress model
RTD	Residence time distribution
SST	Shear stress transport
TIS	Tank-in-series
UDF	User-defined function
UDS	User-defined scalar
VOF	Volume of fluid
VSS	Volatile suspended solids
WWTP	Wastewater treatment plant
2D	Two-dimensional
3D	Three-dimensional

List of symbols:

α	Volume fraction (-)
α_{pi}	Volume fraction of the phase i, i.e. primary (i=1) or secondary (i=2) (-)
β	Closure coefficient in the SST k- ω model (-)
γ	Surface tension (N m ⁻¹)
$\dot{\gamma}$	Shear rate (s ⁻¹)
$\dot{\gamma}_c$	Critical shear rate (s ⁻¹)
Γ_k	Effective diffusivity term of k in transport equation for the SST k- ω model
Γ_ω	Effective diffusivity term of ω in transport equation for the SST k- ω model
δ	Phase angle (°)
δ_c	Concentration boundary layer thickness (m)
δ_H	Hydrodynamic boundary layer thickness (m)
Δ_n	Cell height normal to the interface (m)
ε	Shear strain (-)
η	Dynamic viscosity (Pa s)

η_{pi}	Dynamic viscosity of the phase i, i.e. primary (i=1) or secondary (i=2) (Pa s)
η_y	Yielding viscosity (Pa s)
η_w	Water dynamic viscosity (Pa s)
η_1	Viscous moduli of the Maxwell element (Pa s)
η_2	Viscous moduli of the Kelvin-Voigt element (Pa s)
θ	Radial angle in 2D axisymmetric geometry
λ	Relaxation time (s)
λ_R	Ripples wavelength (m)
μ	Specific growth rate (s ⁻¹)
μ_{max}	Maximum specific growth rate of biomass (s ⁻¹)
ν	Kinematic viscosity (m ² s ⁻¹)
ρ	Fluid density (kg m ⁻³)
ρ_B	Biofilm density (kg m ⁻³)
ρ_w	Water density (kg m ⁻³)
ρ_{pi}	Density of the phase i, i.e. primary (i=1) or secondary (i=2) (kg m ⁻³)
σ	Shear stress (Pa)
σ_y	Yield stress (Pa)
τ	Hydraulic retention time (s)
τ_w	Wall shear stress (kg m ⁻¹ s ⁻²)
φ	Conserved quantity of n variable per unit mass of fluid (-)
φ_{LS}	Level-set function
ω	Specific dissipation rate (s ⁻¹)
ω_f	Angular frequency (rad s ⁻¹)
ω_w	Specific dissipation rate value on the wall (s ⁻¹)
ϑ	Signed distance to the interface in the level-set function (m)
\forall_i	Defined volume i (m ³)
a	Specific mass transfer area of the cell or interfacial area (m ² m ⁻³)
a_i	Available interfacial area in the defined volume \forall_i (m ² m ⁻³)
a_{pi}	Available interfacial area for the phase i, i.e. primary (i=1) or secondary (i=2) (m ² m ⁻³)
A_l	Available surface area between phases (m ²)
B	Damping factor (-)
C	Concentration (kg m ⁻³)
$C(t)$	Concentration-time function (kg m ⁻³ s)
C_{Bi}	N-compound concentration in the biofilm phase in the defined volume \forall_i (kg m ⁻³)
C_{BDO}	Concentration of oxygen in the biofilm phase (kg DO m ⁻³)
C_{Bn}	Concentration of n-compound in the biofilm phase (kg m ⁻³)

$C_{Bn(i,1)}$	Concentration of n-compound in the first layer of biofilm (kg m^{-3})
C_{Li}	N-compound concentration in the liquid phase in the defined volume \forall_i (kg m^{-3})
C_{LDO}	Concentration of oxygen in the inlet of liquid phase (kg DO m^{-3})
C_{Ln}	Concentration of n compound in the liquid phase (kg m^{-3})
C_{Ln0}	Concentration of n compound in the inlet liquid phase (kg m^{-3})
C_n	Concentration of the n variable (kg m^{-3})
C_f	Capacitor at the feedback of the operational amplifier (F)
C_m	Capacitor which represents part of the electrical behavior of the media measured between electrodes (F)
C_{biofilm}	Proportional part of the capacitor measured in the media (C_m) corresponding to the biofilm phase (F)
C_{liquid}	Proportional part of the capacitor measured in the media (C_m) corresponding to the liquid phase (F)
d	Distance from the interface in the level-set function (m)
dS	Source term derivatives (units dependent on the function in the UDF)
D	Kinematic diffusivity ($\text{m}^2 \text{s}^{-1}$)
D_ω	Cross-diffusion term in transport equation for the SST k- ω model
D_r	Relative diffusivity (-)
D_{Bn}	Diffusion coefficient of n-compound in biofilm phase ($\text{m}^2 \text{s}^{-1}$)
D_{Ln}	Diffusion coefficient of n-compound in liquid phase ($\text{m}^2 \text{s}^{-1}$)
D_N	Dispersion number (-)
$E(t)$	Residence time distribution function of the tracer (-)
E_r	Relative electrical permeability (-)
f	Frequency (Hz)
F_{ST}	Surface tension force (N)
g	Gravitational acceleration constant (m s^{-2})
G_k	Production term of k in transport equation for the SST k- ω model
G_ω	Production term of ω in transport equation for the SST k- ω model
G'	Elastic or storage modulus (Pa)
G''	Viscous or loss modulus (Pa)
G_1	Elastic moduli of the Maxwell element (Pa)
G_2	Elastic moduli of the Kelvin-Voigt element (Pa)
I	Turbulence intensity (-)
J	Creep and recovery compliance (Pa^{-1})
J_{KV}	Recovery compliance related to Kelvin-Voigt element (Pa^{-1})
J_{MAX}	Recovery compliance related to maximum deformation (corresponding to the compliance values $t=t_s$) (Pa^{-1})
J_{SM}	Recovery compliance related to Maxwell spring (Pa^{-1})

J_{∞}	Recovery compliance related to Maxwell dashpot (Pa^{-1})
k	Turbulence kinetic energy ($\text{m}^2 \text{s}^{-2}$)
k_d	Maintenance factor for the compound (s^{-1})
k_L	Mass transfer coefficient (m s^{-1})
k_{Li}	Mass transfer coefficient in the defined volume V_i (m s^{-1})
K	Fluid consistency index (Pa s)
$K_{S,DO}$	Monod half-saturation coefficient for oxygen (kg DO m^{-3})
$K_{S,M}$	Monod half-saturation constant for the compound (kg m^{-3})
l	Turbulent length scale (m)
L	Characteristic length of the flow field (m)
L_x, L_y, L_z	Corresponding dimensions of the length, height, and width in the computational domains (m)
M	Tracer mass (kg)
n	Flow behavior index (-)
n_B	Number of discretizations in the biofilm phase (-)
n_L	Number of discretizations in the liquid phase (-)
N	Number of data points obtained in an experiment (-)
N_R	Number of reactor in series (-)
p_i	Phase i , i.e. primary ($i=1$) or secondary ($i=2$), in a two-phase model (-)
p_1	Primary phase in a two-phase model (-)
p_2	Secondary phase in a two-phase model (-)
P	Pressure (Pa)
Pe	Péclet number (-)
q	Volumetric flow rate of the tracer ($\text{m}^3 \text{s}^{-1}$)
Q	Volumetric flow rate in the inlet bioreactor ($\text{m}^3 \text{s}^{-1}$)
$q_{\max,DO}$	Maximum specific growth rate ($\text{kg DO kg VSS}^{-1} \text{s}^{-1}$)
r	Radii (m)
R	Final percentage recovery of the entire system (-)
R_{Bn}	Biological reaction rate of n -compound ($\text{kg m}^{-3} \text{s}^{-1}$)
R_m	Resistor which represents part of the electrical behavior of the media measured between electrodes (Ω)
R_f	Resistor at the feedback of the operational amplifier (Ω)
Re	Reynolds number
Re_{crit}	Critical Reynolds number
\bar{S}	Linearized source S ($\text{kg m}^{-3} \text{s}^{-1}$)
S_{φ}	Volumetric source term ($\text{kg m}^{-3} \text{s}^{-1}$)
$S_{\alpha p_i}$	Volumetric source term for the volume fraction of the phase i , i.e. primary ($i=1$) or secondary ($i=2$) ($\text{kg m}^{-3} \text{s}^{-1}$)

S_k	User-defined source term of k in transport equation for the SST k - ω model
S_ω	User-defined source term of ω in transport equation for the SST k - ω model
S_1	Constant part of the linearized source S (\bar{S}) ($\text{kg m}^{-3} \text{s}^{-1}$)
S_2	Coefficient of the scalar or variable UDS (\overline{UDS}) (units dependent on the UDS variable)
Sc	Schmidt number (-)
Sh	Sherwood number (-)
t	Time (s)
t_m	Mean residence time (s)
t_s	Time at the end of the creep period (s)
th	Biofilm thickness (m)
T	Period (s)
U	Fluid velocity (m s^{-1})
U^*	Non-dimensional friction velocity (-)
U_τ	Friction velocity (m s^{-1})
U_{pi}	Fluid velocity of the phase p_i of the phase i , i.e. primary ($i=1$) or secondary ($i=2$) (m s^{-1})
U_u, U_v, U_w	Fluid velocity components in the spatial coordinates (m s^{-1})
UDS_i	Defined UDS of the n variable corresponding to the phase i , i.e. primary ($i=1$) or secondary ($i=2$) (units dependent on the UDS variable)
v	Jet velocity (m s^{-1})
v_{in}	Water inlet velocity (flat plate) (m s^{-1})
v_{in_2}	Water inlet velocity (curved channel) (m s^{-1})
v_R	Ripples velocity (m s^{-1})
V	Signal voltage (V)
V_0	Output signal voltage (V)
V_i	Excitation signal voltage (V)
$V_{threshold}$	Voltage threshold (V)
V_L	Liquid phase volume (m^3)
x, y, z	Spatial coordinates (m)
x_L	Distance from the leading edge of a plate (m)
X	Biomass density (kg VSS m^{-3})
$X_{b,max}$	Maximum biomass density in biofilm (kg VSS m^{-3})
$X_e(t)$	Measured value in an experimental analysis (units dependent on the measured variable)
$X_p(t)$	Predicted value according to the model developed to fit the experimental data (units dependent on the measured variable)
$X_{e,max}$	Maximum measured value for the experimental data recorded (units dependent on the measured variable)

$X_{e,min}$	Minimum measured value for the experimental data recorded (units dependent on the measured variable)
y^+	Dimensionless wall distance of the first grid cell in the domain mesh (-)
Y_k	Dissipation term of k in transport equation for the SST k - ω model
Y_ω	Dissipation term of ω in transport equation for the SST k - ω model
$Y_{DO/S}$	Oxygen-glucose yield (kg DO kg S^{-1})
$Y_{X/S}$	Biomass-substrate yield (kg X kg S^{-1})

REFERENCES

A

- Ahmed, W., Shareefdeen, Z.M., Jabbar, N.A., 2013. Dynamic modeling and analysis of biotrickling filters in continuous operation for H₂S removal. *Clean Technol. Environ. Policy* 16, 1757–1765.
- Alpkvist, E., Klapper, I., 2007a. A multidimensional multispecies continuum model for heterogeneous biofilm development. *Bull. Math. Biol.* 69, 765–789. doi:10.1007/s11538-006-9168-7
- Alpkvist, E., Klapper, I., 2007b. Description of mechanical response including detachment using a novel particle model of biofilm/flow interaction. *Water Sci. Technol.* 55, 265–273. doi:10.2166/wst.2007.267
- Alpkvist, E., Picioreanu, C., van Loosdrecht, M.C.M., Heyden, A., 2006. Three-dimensional biofilm model with individual cells and continuum EPS matrix. *Biotechnol. Bioeng.* 94, 961–979. doi:10.1002/bit.20917
- Álvarez-Hornos, F.J., Gabaldón, C., Martínez-Soria, V., Marzal, P., Penya-roja, J.-M., 2009. Mathematical modeling of the biofiltration of ethyl acetate and toluene and their mixture. *Biochem. Eng. J.* 43, 169–177.
- Angelini, T.E., Roper, M., Kolter, R., Weitz, D.A., Brenner, M.P., 2009. *Bacillus subtilis* spreads by surfing on waves of surfactant. *Proc. Natl. Acad. Sci.* 106, 18109–18113. doi:10.1073/pnas.0905890106
- ANSYS Inc, 2015. ANSYS® Academic Research, Release 16.2, Help System, ANSYS CFX Reference Guide.
- ANSYS Inc, 2016. ANSYS® Academic Research, Release 17.2, Help System, ANSYS Fluent Theory Guide.
- ANSYS Inc, 2017. ANSYS® Academic Research, Release 17.2, Help System, ANSYS Fluent Customization Manual.
- APHA, 1998. Standard methods for the examination of water and wastewater. Edition 20.

B

- Bakke, R., Olsson, P.Q., 1986. Biofilm thickness measurements by light microscopy. *J. Microbiol. Methods* 5, 93–98.
- Bakke, R., Kommedal, R., Kalvenes, S., 2001. Quantification of biofilm accumulation by an optical approach. *J. Microbiol. Methods* 44, 13–26.
- Bakker, C.W., Meyer, C.J., Deglon, D.A., 2009. Numerical modelling of non-Newtonian slurry in a mechanical flotation cell. *Miner. Eng.* 22, 944–950. doi:10.1016/j.mineng.2009.03.016
- Baquerizo, G., Gamisans, X., Gabriel, D., Lafuente, J., 2007. A dynamic model for ammonia abatement by gas-phase biofiltration including pH and leachate modelling. *Biosyst. Eng.* 97, 431–440.
- Barmak, I., Gelfgat, A., Vitoshkin, H., Ullmann, A., Brauner, N., 2016. Stability of stratified

- two-phase flows in horizontal channels. *Phys. Fluids* 28. doi:10.1063/1.4944588
- Beyenal, H., Lewandowski, Z., 2005. Modeling mass transport and microbial activity in stratified biofilms. *Chem. Eng. Sci.* 60, 4337–4348. doi:10.1016/j.ces.2005.02.063
- Billings, N., Birjiniuk, A., Samad, T.S., Doyle, P.S., Ribbeck, K., 2015. Material properties of biofilms—a review of methods for understanding permeability and mechanics. *Reports Prog. Phys.* 78, 036601. doi:10.1088/0034-4885/78/3/036601
- Bishop, P.L., Gibbs, J.T., Cunningham, B.E., 1997. Relationship between concentration and hydrodynamic boundary layers over biofilms. *Environ. Technol. (United Kingdom)* 18, 375–385. doi:10.1080/09593331808616551
- Blauert, F., Horn, H., Wagner, M., 2015. Time-resolved biofilm deformation measurements using optical coherence tomography. *Biotechnol. Bioeng.* 112, 1893–1905. doi:10.1002/bit.25590
- Böl, M., Ehret, A.E., Bolea Albero, A., Hellriegel, J., Krull, R., 2012. Recent advances in mechanical characterisation of biofilm and their significance for material modelling. *Crit. Rev. Biotechnol.* 33, 1–27. doi:10.3109/07388551.2012.679250
- Böl, M., Möhle, R.B., Haesner, M., Neu, T.R., Horn, H., Krull, R., 2009. 3D finite element model of biofilm detachment using real biofilm structures from CLSM data. *Biotechnol. Bioeng.* 103, 177–186. doi:10.1002/bit.22235
- Boltz, J.P., Morgenroth, E., Sen, D., 2010. Mathematical modelling of biofilms and biofilm reactors for engineering design. *Water Sci. Technol.* 62, 1821–1836.
- Boltz, J.P., Morgenroth, E., Brockmann, D., Bott, C., Gellner, W.J., Vanrolleghem, P. A., 2011. Systematic evaluation of biofilm models for engineering practice: Components and critical assumptions. *Water Sci. Technol.* 64, 930–944.
- Boyer, C., Duquenne, A.M., Wild, G., 2002. Measuring techniques in gas-liquid and gas-liquid-solid reactors. *Chem. Eng. Sci.* 57, 3185–3215. doi:10.1016/S0009-2509(02)00193-8
- Bradford, M.M., 1976. A rapid and sensitive method for the quantitation of microgram quantities of protein utilizing the principle of protein-dye binding. *Anal. Biochem.* 72, 248–254.

C

- Cense, A.W., Van Dongen, M.E.H., Gottenbos, B., Nuijs, A.M., Shulepov, S.Y., 2006. Removal of biofilms by impinging water droplets. *J. Appl. Phys.* 100. doi:10.1063/1.2374950
- Characklis, W.G., Trulear, M.G., Bryers, J.D., Zilver, N., 1982. Dynamics of biofilm processes: methods. *Water Res.* 16, 1207–1216. doi:10.1016/0043-1354(82)90139-7
- Chen, Z.D., Chen, X.D., Chen, J.J.J., 1997. Effects of an oscillating interface on heat transfer. *Chem. Eng. Sci.* 52, 3265–3275. doi:10.1016/S0009-2509(97)00136-X
- Chen, X., Stewart, P.S., 2000. Biofilm removal cause by chemical treatments. *Water Res.* 34, 4229–4233.
- Chhabra, R.P., 2010. Non-Newtonian fluids: An introduction, in: Krishnan JM, Deshpande

- AP, Kumar PBS (Ed.), *Rheology of Complex Fluids*. Springer New York, pp. 3–34. doi:10.1007/978-1-4419-6494-6_1
- Climent, J., Basiero, L., Berlanga, J.G., Chiva, S., 2018. Biological reactor retro fitting using CFD-ASM modelling. *Chem. Eng. J.* 348, 1–14. doi:10.1016/j.cej.2018.04.058
- Clussler, E.L., 1984. *Diffusion-Mass Transfer in Fluid Systems*. Cambridge University Press, Cambridge.
- Cohen, L.S., Hanratty, T.J., 1965. Generation of waves in the concurrent flow of air and a liquid. *AIChE J.* 11, 138–144. doi:10.1002/aic.690110129
- Cox, W.P., Merz, E.H., 1958. Correlation of dynamic and steady flow viscosities. *Polymer (Guildf)*. 619–622.
- Craig, K.J., Nieuwoudt, M.N., Niemand, L.J., 2013. CFD simulation of anaerobic digester with variable sewage sludge rheology. *Water Res.* 47, 4485–4497. doi:10.1016/j.watres.2013.05.011
- D**
- Da Silva, M.J., Schleicher, E., Hampel, U., 2007. A novel needle probe based on high-speed complex permittivity measurements for investigation of dynamic fluid flows. *IEEE Trans. Instrum. Meas.* 56, 1249–1256. doi:10.1109/TIM.2007.900419
- Da Silva, M.J., 2008. *Impedance sensors for fast multiphase flow measurement and imaging*. Technische Universität Dresden.
- Davey, C., Kell, D.B., Walz, D., Berg, H., Milazzo, G., 1995. The low-frequency dielectric properties of biological cells, in: Walz, D., Berg, H., Milazzo, G. (Eds.), *Bioelectrochemistry of Cells and Tissues 2*. Springer Nature Switzerland AG, pp. 159–207. doi:10.1007/978-3-0348-9063-2_5
- De Beer, D., Stoodley, P., Roe, F., Lewandowski, Z., 1994. Effects of biofilm structure on oxygen distribution and mass transport. *Biotechnol. Bioeng.* 43, 1131–1138.
- De Beer, D., Stoodley, P., Lewandowski, Z., 1996. Liquid flow and mass transport in heterogeneous biofilms. *Water Res.* 30, 2761–2765. doi:10.1016/S0043-1354(96)00141-8
- Delhoménie, M.-C., Heitz, M., 2005. Biofiltration of air: a review. *Crit. Rev. Biotechnol.* 25, 53–72. doi:10.1080/07388550590935814
- Denkhaus, E., Meisen, S., Telgheder, U., Wingender, J., 2007. Chemical and physical methods for characterisation of biofilms. *Microchim. Acta* 158, 1–27. doi:10.1007/s00604-006-0688-5
- Deshusses, M.A., Hamer, G., Dunn, I.J., 1995. Behavior of biofilters for waste air biotreatment. 2. Experimental evaluation of a dynamic model. *Environ. Sci. Technol.* 29, 1059–1068.
- Deshusses, M.A., Shareefdeen, Z., 2005. Modeling of biofilters and biotrickling filters for odor and VOC control applications, in: Shareefdeen, Z., Singh, A. (Eds.), *Biotechnology for Odor and Air Pollution Control*. Springer Berlin Heidelberg, Berlin, Heidelberg, pp. 213–231. doi:10.1007/b138434

- Deviny, J.S., Ramesh, J., 2005. A phenomenological review of biofilter models. *Chem. Eng. J.* 113, 187–196. doi:10.1016/j.cej.2005.03.005
- Di Stefano, A., D'Aurizio, E., Trubiani, O., Grande, R., Di Campli, E., Di Giulio, M., Di Bartolomeo, S., Sozio, P., Iannitelli, A., Nostro, A., Cellini, L., 2009. Viscoelastic properties of *Staphylococcus aureus* and *Staphylococcus epidermidis* mono-microbial biofilms. *Microb. Biotechnol.* 2, 634–641. doi:10.1111/j.1751-7915.2009.00120.x
- Dorado, A.D., Baquerizo, G., Maestre, J.P., Gamsans, X., Gabriel, D., Lafuente, J., 2008. Modeling of a bacterial and fungal biofilter applied to toluene abatement: Kinetic parameters estimation and model validation. *Chem. Eng. J.* 140, 52–61.
- Dolz, M., Hernández, M.J., Delegido, J., 2008. Creep and recovery experimental investigation of low oil content food emulsions. *Food Hydrocoll.* 22, 421–427. doi:10.1016/j.foodhyd.2006.12.011
- Duddu, R., Chopp, D.L., Moran, B., 2009. A two-dimensional continuum model of biofilm growth incorporating fluid flow and shear stress based detachment. *Biotechnol. Bioeng.* 103, 92–104. doi:10.1002/bit.22233

E

- Eberl, H.J., van Loosdrecht, M.C.M., Morgenroth, E., Noguera, D.R., Perez, J., Picioreanu, C., Rittmann, B.E., Schwarz, a. O., Wanner, O., 2004. Modelling a spatially heterogeneous biofilm and the bulk fluid: Selected results from benchmark problem 2 (BM2). *Water Sci. Technol.* 49, 155–162.
- Egorov, Y., Boucker, M., Martin, A., Pigny, S., Scheuerer, M., Willemsen, S., 2004. Validation of CFD codes with PTS-relevant test cases, in: 5th Euratom Framework Programme ECORA Project, CONTRACT No FIKS-CT-2001-00154. pp. 91–116.
- Eshtiaghi, N., Markis, F., Yap, S.D., Baudez, J.C., Slatter, P., 2013. Rheological characterisation of municipal sludge: A review. *Water Res.* 47, 5493–5510. doi:10.1016/j.watres.2013.07.001
- Evans, L. V., 2000. *Biofilms: recent advances in their study and control.* Harwood Academic.

F

- Fabbri, S., 2016. *Interfacial instability generation in dental biofilms by high-velocity fluid flow for biofilm removal and antimicrobial delivery.* University of Southampton.
- Fabbri, S., Johnston, D.A., Rmaile, A., Gottenbos, B., De Jager, M., Aspiras, M., Starke, E.M., Ward, M.T., Stoodley, P., 2016a. High-Velocity Microsprays Enhance Antimicrobial Activity in *Streptococcus mutans* Biofilms. *J. Dent. Res.* 95, 1494–1500. doi:10.1177/0022034516662813
- Fabbri, S., Johnston, D.A., Rmaile, A., Gottenbos, B., De Jager, M., Aspiras, M., Starke, M.E., Ward, M.T., Stoodley, P., 2016b. *Streptococcus mutans* biofilm transient viscoelastic fluid behaviour during high-velocity microsprays. *J. Mech. Behav. Biomed. Mater.* 59, 197–206. doi:10.1016/j.jmbbm.2015.12.012
- Fabbri, S., Stoodley, P., 2016. Mechanical Properties of Biofilms, in: Flemming, H.-C., Neu, T.R., and Wingender, J. (Ed.), *The Perfect Slime: Microbial Extracellular Polymeric Substances (EPS).* IWA Publishing, London, UK, pp. 153–172. doi:10.1016/B978-

012595340-5/50008-0

- Fabbri, S., Li, J., Howlin, R.P., Rmaile, A., Gottenbos, B., De Jager, M., Starke, E.M., Aspiras, M., Ward, M.T., Cogan, N.G., Stoodley, P., 2017. Fluid-driven Interfacial instabilities and turbulence in bacterial biofilms 19, 4417–4431. doi:10.1111/1462-2920.13883
- Fauvart, M., Phillips, P., Bachaspatimayum, D., Verstraeten, N., Fransaeer, J., Michiels, J., Vermant, J., 2012. Surface tension gradient control of bacterial swarming in colonies of *Pseudomonas aeruginosa*. *Soft Matter* 8, 70–76. doi:10.1039/c1sm06002c
- Feng, W., Wen, J., Liu, C., Yuan, Q., Jia, X., Sun, Y., 2007. Modeling of local dynamic behavior of phenol degradation in an internal loop airlift bioreactor by yeast *Candida tropicalis*. *Biotechnol. Bioeng.* 97, 251–264.
- Ferreira, A.P., Vieira, L.M., Cardoso, J.P., Menezes, J.C., 2005. Evaluation of a new annular capacitance probe for biomass monitoring in industrial pilot-scale fermentations. *J. Biotechnol.* 117, 403–409. doi:10.1016/j.jbiotec.2004.12.006
- Ferziger, J.H., Perić, M., 1996. *Computational Methods for Fluid Dynamics*, Third Edit. ed. Springer-Verlag, Berlin. doi:10.1002/zamm.19970770220
- Findley, W.N., Lai, J.S., Onaran, K., 1978. *Creep and relaxation of nonlinear viscoelastic materials, with an introduction to linear viscoelasticity*. Dover Publishing, Mineola, NY. doi:10.1016/0032-3861(78)90187-8
- Flemming, H.C., Neu, T.R., Wozniak, D.J., 2007. The EPS matrix: The “House of Biofilm Cells.” *J. Bacteriol.* 189, 7945–7947. doi:10.1128/JB.00858-07
- Flemming, H., Wingender, J., 2010. The biofilm matrix. *Nat. Rev. Microbiol.* 8, 623–33. doi:10.1038/nrmicro2415
- Forrester, S.E., Evans, G.M., 1997. Computational modelling study of a plane gas jet impinging onto a liquid pool, in: *1st International Conference on CFD in the Mineral & Metal Processing and Power Generation Industries*. pp. 313–320.

G

- Giboreau, A., Cuvelier, G., Launay, B., 1994. Rheological behaviour of three biopolymer/water systems, with emphasis on yield stress and viscoelastic properties. *J. Texture Stud.* 25, 119–137. doi:10.1111/j.1745-4603.1994.tb01321.x
- Glover, G.C., Printemps, C., Essemiani, K., Meinhold, J., 2006. Modelling of wastewater treatment plants - How far shall we go with sophisticated modelling tools? *Water Sci. Technol.* 53, 79–89.
- Grillet, A.M., Wyatt, N.B., Gloe, L.M., 2012. Polymer gel rheology and adhesion, in: Vicente, D.J. De (Ed.), *Rheology*. InTech, pp. 1073-1101. doi:10.5772/36. Available from: <http://www.intechopen.com/books/rheology/rheology-and-adhesion-of-polymer-gels>, Accessed on Aug. 10, 2018
- Guimerà, X., Moya, A., Dorado, A.D., Villa, R., Gabriel, D., Gabriel, G., Gamisans, X., 2015. Biofilm dynamics characterization using a novel DO-MEA sensor: mass transport and biokinetics. *Appl. Microbiol. Biotechnol.* 99, 55–66.
- Guimerà, X., 2016. Diseño, caracterización y aplicación de microelectrodos para el estudio

de biopelículas sulfuroxidantes. Univeritat Politècnica de Catalunya.

Guimerà, X., Dorado, A.D., Bonsfills, A., Gabriel, G., Gabriel, D., Gamisans, X., 2016. Dynamic characterization of external and internal mass transport in heterotrophic biofilms from microsensors measurements. doi:10.1016/j.watres.2016.07.009

H

Hall-Stoodley, L., Stoodley, P., 2002. Developmental regulation of microbial biofilms. *Curr. Opin. Biotechnol.* 13, 228–233. doi:10.1016/S0958-1669(02)00318-X

Hanratty, T.J., 1983. Interfacial instabilities caused by air flow over a thin liquid layer, in: *Waves on Fluid Interfaces*. Elsevier, pp. 221–259. doi:10.1016/B978-0-12-493220-3.50015-5

Henze, M., van Loosdrecht, M. C. M., Ekama, G., Brdjanovic, D., 2008. *Biological wastewater treatment: principles, modelling and design*. IWA Publishing.

Heydorn, A., Nielsen, A.T., Hentzer, M., Sternberg, C., Givskov, M., Ersbøll, B.K., Molin, S., 2000. Quantification of biofilm structures by the novel computer program COMSTAT. *Image Process.* 2395–2407. doi:10.1099/00221287-146-10-2395

Hirt, C., Nichols, B., 1981. Volume of fluid (VOF) method for the dynamics of free boundaries. *J. Comput. Phys.* 39, 201–225. doi:10.1016/0021-9991(81)90145-5

Hodge, D., Deviny, J., 1997. Determination of transfer rate constants and partition coefficients for air phase biofilters. *J. Environ. Eng.* 123, 577–585.

Hoehn, R.C., Ray, A.D., Hoehn, C., 1973. Effects of Thickness on Bacterial Film. *J. (Water Pollut. Control Fed.* 45, 2302–2320.

Höhne, T., Mehlhoop, J.P., 2014. Validation of closure models for interfacial drag and turbulence in numerical simulations of horizontal stratified gas-liquid flows. *Int. J. Multiph. Flow* 62, 1–16. doi:10.1016/j.ijmultiphaseflow.2014.01.012

Horn, H., Hempel, D.C., 1995. Mass transfer coefficients for an autotrophic and a heterotrophic biofilm system. *Water Sci. Technol.* 32, 199–204.

Horn, H., Hempel, D.C., 1997a. Substrate utilization and mass transfer in an autotrophic biofilm system: Experimental results and numerical simulation. *Biotechnol. Bioeng.* 53, 363–371.

Horn, H., Hempel, D.C., 1997b. Growth and decay in an auto-/heterotrophic biofilm. *Water Res.* 31, 2243–2252.

Horn, H., Lackner, S., 2014. Modeling of Biofilm Systems: A Review. *Adv Biochem Eng Biotechnol* 146, 53–76. doi:10.1007/10

Hyun, K., Kim, S.H., Ahn, K.H., Lee, S.J., 2002. Large amplitude oscillatory shear as a way to classify the complex fluids. *J. Nonnewton. Fluid Mech.* 107, 51–65. doi:10.1016/S0377-0257(02)00141-6

Hyun, K., Wilhelm, M., Klein, C.O., Cho, K.S., Nam, J.G., Ahn, K.H., Lee, S.J., Ewoldt, R.H., McKinley, G.H., 2011. A review of nonlinear oscillatory shear tests: Analysis and application of large amplitude oscillatory shear (LAOS). *Prog. Polym. Sci.* 36, 1697–1753. doi:10.1016/j.progpolymsci.2011.02.002

I

- Ikeda, S., Nishinari, K., 2001. "Weak gel"-type rheological properties of aqueous dispersions of nonaggregated kappa-carrageenan helices. *J. Agric. Food Chem.* 49, 4436–4441.
- Iliuta, I., Larachi, F., 2004. Biomass accumulation and clogging in trickle-bed bioreactors. *AIChE J.* 50, 2541–2551. doi:10.1002/aic.10201
- Iliuta, I., Larachi, F., 2005. Modeling simultaneous biological clogging and physical plugging in trickle-bed bioreactors for wastewater treatment. *Chem. Eng. Sci.* 60, 1477–1489. doi:10.1016/j.ces.2004.10.016
- IWA Task Group on Biofilm Modeling, 2006. *Mathematical Modeling of Biofilms*, Scientific. ed. IWA Publishing.

J

- Jafari, M., Desmond, P., van Loosdrecht, M.C.M., Derlon, N., Morgenroth, E., Picioreanu, C., 2018. Effect of biofilm structural deformation on hydraulic resistance during ultrafiltration: A numerical and experimental study. *Water Res.* 145, 375–387. doi:10.1016/j.watres.2018.08.036
- Janknecht, P., Melo, L., 2003. Online biofilm monitoring. *Rev. Environ. Sci. Biotechnol.* 269–283. doi:10.1023/B:RESB.0000040461.69339.04
- Jia, X., Wen, J., Wang, X., Feng, W., Jiang, Y., 2009. CFD Modeling of Immobilized Phenol Biodegradation in Three-Phase Airlift Loop Reactor. *Ind. Eng. Chem. Res.* 48, 4514–4529. doi:10.1021/ie800816d
- Jones, W.L., Sutton, M.P., McKittrick, L., Stewart, P.S., 2011. Chemical and antimicrobial treatments change the viscoelastic properties of bacterial biofilms. *Biofouling* 27, 207–215. doi:10.1080/08927014.2011.554977

K

- Kaiser, S.C., Solutions, F., Kraume, M., Eibl, D., 2014. Computational fluid dynamics as a modern tool for engineering characterization of bioreactors. *Pharm. Bioprocess.* 2, 85–99. doi:10.4155/PBP.13.60
- Karimi, A., Karig, D., Kumar, A., Ardekani, a M., 2015. Interplay of physical mechanisms and biofilm processes: review of microfluidic methods. *Lab Chip* 15, 23–42. doi:10.1039/c4lc01095g
- Karpinska, A.M., Bridgeman, J., 2016. CFD-aided modelling of activated sludge systems - A critical review. *Water Res.* 88, 861–879. doi:10.1016/j.watres.2015.11.008
- Kelly, W.J., 2008. Using computational fluid dynamics to characterize and improve bioreactor performance. *Biotechnol. Appl. Biochem.* 49, 225. doi:10.1042/BA20070177
- Kim, S., Deshusses, M.A., 2003. Development and experimental validation of a conceptual model for biotrickling filtration of H₂S. *Environ. Prog.* 119–128.
- Klapper, I., Rupp, C.J., Cargo, R., Purvedorj, B., Stoodley, P., 2002. Viscoelastic fluid description of bacterial biofilm material properties. *Biotechnol. Bioeng.* 80, 289–296. doi:10.1002/bit.10376
- Koza, A., Hallett, P.D., Moon, C.D., Spiers, A.J., 2009. Characterization of a novel air-liquid

interface biofilm of *Pseudomonas fluorescens* SBW25. *Microbiology* 155, 1397–1406. doi:10.1099/mic.0.025064-0

Kulicke, W.M., Porter, R.S., 1980. Relation between steady shear flow and dynamic rheology. *Rheol. Acta* 19, 601–605.

L

Launder, B.E., Spalding, D.B., 1972. *Lectures in Mathematical Models of Turbulence*. Academic Press, London, England.

Le Moullec, Y., Gentric, C., Potier, O., Leclerc, J.P., 2010. CFD simulation of the hydrodynamics and reactions in an activated sludge channel reactor of wastewater treatment. *Chem. Eng. Sci.* 65, 492–498.

Levenspiel, O., 1999. *Chemical reaction engineering*. Wiley.

Lewandowski, Z., Altobelli, S. A, Fukushimai, E., 1993. NMR and microelectrode studies of hydrodynamics and kinetics in biofilms. *Biotechnol. Prog.* 9, 40–45. doi:doi:10.1021/bp00019a006

Lewandowski, Z., Walser, G., Characklis, W.G., 1991. Reaction kinetics in biofilms. *Biotechnol. Bioeng.* 38, 877–882. doi:10.1002/bit.260380809

Lewandowski, Z., Beyenal, H., 2007. *Fundamentals of biofilm research*. Taylor & Francis, Boca Raton.

Lieleg, O., Caldara, M., Baumgärtel, R., Ribbeck, K., 2011. Mechanical robustness of *Pseudomonas aeruginosa* biofilms. *Soft Matter* 7, 3307–3314. doi:10.1039/c0sm01467b

Liotta, F., Chatellier, P., Esposito, G., Fabbricino, M., Van Hullebusch, E.D., Lens, P.N.L., 2014. Hydrodynamic mathematical modelling of aerobic plug flow and nonideal flow reactors: A critical and historical review. *Crit. Rev. Environ. Sci. Technol.* 44, 2642–2673.

Liu, X., Wang, H., Long, F., Qi, L., Fan, H., 2016. Optimizing and real-time control of biofilm formation, growth and renewal in denitrifying biofilter. *Bioresour. Technol.* 209, 326–332. doi:10.1016/j.biortech.2016.02.095

López, L.R., Dorado, A.D., Mora, M., Gamisans, X., Lafuente, J., Gabriel, D., 2016. Modeling an aerobic biotrickling filter for biogas desulfurization through a multi-step oxidation mechanism. *Chem. Eng. J.* 294, 447–457.

M

Ma, Y.J., Xia, C.W., Yang, H.Y., Zeng, R.J., 2014. A rheological approach to analyze aerobic granular sludge. *Water Res.* 50, 171–178. doi:10.1016/j.watres.2013.11.049

Manz, B., Volke, F., Goll, D., Horn, H., 2003. Measuring local flow velocities and biofilm structure in biofilm systems with magnetic resonance imaging (MRI). doi:10.1002/10782

Markis, F., Baudez, J.C., Parthasarathy, R., Slatter, P., Eshtiaghi, N., 2014. Rheological characterisation of primary and secondary sludge: Impact of solids concentration. *Chem. Eng. J.* 253, 526–537. doi:10.1016/j.cej.2014.05.085

Masić, A., Bengtsson, J., Christensson, M., 2010. Measuring and modeling the oxygen profile in a nitrifying Moving Bed Biofilm Reactor. *Math. Biosci.* 227, 1–11.

- Massey, B.S., Ward-Smith, J., 1998. *Mechanics of fluids*. S. Thornes. Cheltenham, England.
- Mattei, M.R., Frunzo, L., D'Acunto, B., Pechaud, Y., Pirozzi, F., Esposito, G., 2017. Continuum and discrete approach in modeling biofilm development and structure: a review. *J. Math. Biol.* doi:10.1007/s00285-017-1165-y
- Maurício, R., Dias, C.J., Santana, F., 2006. Monitoring biofilm thickness using a non-destructive, on-line, electrical capacitance technique. *Environ. Monit. Assess.* 119, 599–607. doi:10.1007/s10661-005-9045-0
- Mayer, C., Moritz, R., Kirschner, C., 1999. The role of intermolecular interactions: studies on model systems for bacterial biofilms. *Int. J. Biol. Macromol.* 26, 3–16.
- Mendoza, J.A., Prado, Ó.J., Veiga, M.C., Kennes, C., 2004. Hydrodynamic behaviour and comparison of technologies for the removal of excess biomass in gas-phase biofilters. *Water Res.* 38, 404–413. doi:10.1016/j.watres.2003.09.014
- Menter, F.R., 1994. Two-equation eddy-viscosity turbulence models for engineering applications. *AIAA J.* 32, 1598–1605. doi:10.2514/3.12149
- Meyer, B., 2003. Approaches to prevention, removal and killing of biofilms. *Int. Biodeterior. Biodegrad.* 51, 249–253. doi:10.1016/S0964-8305(03)00047-7
- Mezger, T., 2006. *The rheology handbook: for users of rotational and oscillatory rheometers*. Vincentz Verlag, Hannover, Germany.
- Milferstedt, K., Pons, M.N., Morgenroth, E., 2006. Optical Method for Long-Term and Large-Scale Monitoring of Spatial Biofilm Development. *Biotechnol. Bioeng.* 94, 773–782. doi:10.1002/bit
- Monrós-Andreu, G., Martínez-Cuenca, R., Torró, S., Escrig, J., Hewakandamby, B., Chiva, S., 2016. Multi-needle capacitance probe for non-conductive two-phase flows. *Meas. Sci. Technol.* 27, 074004. doi:10.1088/0957-0233/27/7/074004

N

- Naessens, W., Maere, T., Ratkovich, N., Vedantam, S., Nopens, I., 2012. Critical review of membrane bioreactor models – Part 2: Hydrodynamic and integrated models. *Bioresour. Technol.* 122, 107–118. doi:10.1016/j.biortech.2012.05.071
- Nguyen, M.T., Appan, A., Tan, D.S., Tan, S.K., 2014. Influence of small water surface perturbations on the reaeration process. *J. Environ. Eng.* 140.
- Noguera, D.R., Morgenroth, E., 2004. Introduction to the IWA Task Group on Biofilm Modeling. *Water Sci. Technol.* 49, 131–136.

O

- Ohashi, A., Harada, H., 1994. Adhesion strength of biofilm developed in an attached-growth reactor. *Wat Sci Technol* 29, 281–288.
- Okkerse, W.J.H., Ottengraf, S.P.P., Osinga-Kuipers, B., 2000. Biofilm thickness variability investigated with a laser triangulation sensor. *Biotechnol. Bioeng.* 70, 619–629. doi:10.1002/1097-0290(20001220)70:6<619::AID-BIT3>3.0.CO;2-4
- Osher, S., Sethian, J.A., 1988. Fronts propagating with curvature-dependent speed: Algorithms based on Hamilton-Jacobi formulations. *J. Comput. Phys.* 79, 12–49.

doi:10.1016/0021-9991(88)90002-2

P

- Paramonova, E., De Jong, E.D., Krom, B.P., Van Der Mei, H.C., Busscher, H.J., Sharma, P.K., 2007. Low-load compression testing: A novel way of measuring biofilm thickness. *Appl. Environ. Microbiol.* 73, 7023–7028. doi:10.1128/AEM.00935-07
- Patankar, S. V., 1980. Numerical heat transfer and fluid flow. Amsterdam: John Benjamins Publishing Co.
- Payne, A.R., 1962. The dynamic properties of carbon black loaded natural rubber vulcanizates. Part II. *J. Appl. Polym. Sci.* VI, 368–372.
- Perry, R.H., Green, D.W., 1997. Perry's chemical engineer's handbook, 7th edition. ed. Mc Graw-Hill.
- Peterson, B.W., Busscher, H.J., Sharma, P.K., van der Mei, H.C., 2014. Visualization of microbiological processes underlying stress relaxation in *Pseudomonas aeruginosa* biofilms. *Microsc. Microanal.* 20, 912–5. doi:10.1017/S1431927614000361
- Peterson, B.W., He, Y., Ren, Y., Zerdoum, A., Libera, M.R., Sharma, P.K., van Winkelhoff, A.J., Neut, D., Stoodley, P., van der Mei, H.C., Busscher, H.J., 2015. Viscoelasticity of biofilms and their recalcitrance to mechanical and chemical challenges. *FEMS Microbiol. Rev.* 39, 234–245. doi:10.1093/femsre/fuu008
- Picioareanu, C., 1999. Multidimensional modeling of biofilm structures. Delft University of Technology.
- Picioareanu, C., van Loosdrecht, M.C.M., Heijnen, J.J., 1998a. A new combined differential-discrete cellular automaton approach for biofilm modeling: Application for growth in gel beads. *Biotechnol. Bioeng.* 57, 718–731. doi:10.1002/(SICI)1097-0290(19980320)57:6<718::AID-BIT9>3.0.CO;2-O
- Picioareanu, C., van Loosdrecht, M.C.M., Heijnen, J., 1998b. Mathematical modeling of biofilm structure with a hybrid differential-discrete cellular automata approach. *Biotechnol. Bioeng.* 58, 101–116. doi:10.1002/(SICI)1097-0290(19980405)58
- Picioareanu, C., van Loosdrecht, M.C.M., Heijnen, J.J., 2000a. A Theoretical Study on the Effect of Surface Roughness on Mass Transport and Transformation in Biofilms. *Biotechnol. Bioeng.* 68, 355–369.
- Picioareanu, C., van Loosdrecht, M.C.M., Heijnen, J.J., 2000b. Effect of diffusive and convective substrate transport on biofilm structure formation: A two-dimensional modeling study. *Biotechnol. Bioeng.* 69, 504–515. doi:10.1002/1097-0290(20000905)69
- Picioareanu, C., van Loosdrecht, M.C.M., Heijnen, J.J., 2001. Two-dimensional model of biofilm detachment caused by internal stress from liquid flow. *Biotechnol. Bioeng.*
- Picioareanu, C., Kreft, J.-U., van Loosdrecht, M.C.M., 2004. Particle based multidimensional multispecies biofilm model. *Appl. Environ. Microbiol.* 70, 3024–3040. doi:10.1128/AEM.70.5.3024
- Picioareanu, C., Vrouwenvelder, J.S., van Loosdrecht, M.C.M., 2009. Three-dimensional modeling of biofouling and fluid dynamics in feed spacer channels of membrane devices. *J. Memb. Sci.* 345, 340–354.

- Piciooreanu, C., Blauert, F., Horn, H., Wagner, M., 2018. Determination of mechanical properties of biofilms by modelling the deformation measured using optical coherence tomography. *Water Res.* 145, 588–598. doi:10.1016/j.watres.2018.08.070
- Piciooreanu, C., 2018. Biofilm mechanics and mechanical modelling of microbial communities, in: *NSF Biofilm Mechanical Properties Workshop*. Indiana, USA.
- Potter, M.C., Wiggert, D.C., Ramadan, B.H., Shih, T.I.-P., 2012. *Mechanics of fluids*, Fourth Edition. ed. Stamford, USA.
- Prades, L., Dorado, A.D., Climent, J., Guimerà, X., Chiva, S., Gamisans, X., 2017. CFD modeling of a fixed-bed biofilm reactor coupling hydrodynamics and biokinetics. *Chem. Eng. J.* 313, 680–692. doi:10.1016/j.cej.2016.12.107

R

- Ramin, E., Wágner, D.S., Yde, L., Binning, P.J., Rasmussen, M.R., Mikkelsen, P.S., Plósz, B.G., 2014. A new settling velocity model to describe sedimentation of activated sludge. *Water Res.* 66, 447–458. doi:10.1016/j.watres.2014.08.034
- Ratkovich, N., Horn, W., Helmus, F.P., Rosenberger, S., Naessens, W., Nopens, I., Bentzen, T.R., 2013. Activated sludge rheology: A critical review on data collection and modelling. *Water Res.* 47, 463–482. doi:10.1016/j.watres.2012.11.021
- Reichert, P., 1994. AQUASIM - A tool for simulation and data-analysis of aquatic systems. *Water Sci. Technol.* 30, 21–30.
- Reichert, P., 1998. Computer program for the identification and simulation of aquatic systems (AQUASIM), Swiss Federal Institute for Environmental Science and Technology (EAWAG).
- Rittmann, B.E., Laspidou, C.S., 2001. Biofilm detachment, G. Bitton (Ed.), *The encyclopedia of environmental microbiology*. Wiley, New York, pp. 556–562.
- Rmaile, A., Carugo, D., Capretto, L., Wharton, J.A., Thurner, P.J., Aspiras, M., Ward, M., De Jager, M., Stoodley, P., 2015. An experimental and computational study of the hydrodynamics of high-velocity water microdrops for interproximal tooth cleaning. *J. Mech. Behav. Biomed. Mater.* 46, 148–157. doi:10.1016/j.jmbbm.2015.02.010
- Roberts, R.M., Chang, H.C., 2000. Wave-enhanced interfacial transfer. *Chem. Eng. Sci.* 55, 1127–1141. doi:10.1016/S0009-2509(99)00391-7
- Rodriguez, G., 2013. Eliminació de H₂S mitjançant biofiltres percoladors: Millora de la transferència d'oxigen. Univeristat Politècnica de Catalunya.
- Ross-Murphy, S.B., 1995. Structure–property relationships in food biopolymer gels and solutions. *J. Rheol. (N. Y. N. Y.)* 39, 1451. doi:10.1122/1.550610
- Rühs, P. a., Böni, L., Fuller, G.G., Inglis, R.F., Fischer, P., 2013. In-situ quantification of the interfacial rheological response of bacterial biofilms to environmental stimuli. *PLoS One* 8. doi:10.1371/journal.pone.0078524
- Rusconi, R., Lecuyer, S., Guglielmini, L., Stone, H.A., 2010. Laminar flow around corners triggers the formation of biofilm streamers. *J. R. Soc. Interface* 7, 1293–1299. doi:10.1098/rsif.2010.0096

S

- Safari, A., Tukovic, Z., Walter, M., Casey, E., Ivankovic, A., 2015. Mechanical properties of a mature biofilm from a wastewater system: from microscale to macroscale level. *Biofouling* 31, 651–664. doi:10.1080/08927014.2015.1075981
- Samstag, R.W., Ducoste, J.J., Griborio, A., Nopens, I., Batstone, D.J., Wicks, J.D., Saunders, S., Wicklein, E.A., Kenny, G., Laurent, J., 2016. CFD for wastewater treatment: An overview. *Water Sci. Technol.* 74, 549–563. doi:10.2166/wst.2016.249
- San-Valero, P., Dorado, A.D., Martínez-Soria, V., Gabaldón, C., 2018. Biotrickling filter modeling for styrene abatement. Part 1: Model development, calibration and validation on an industrial scale. *Chemosphere* 191, 1066–1074. doi:10.1016/j.chemosphere.2017.10.069
- Saramito, P., 2009. A new elastoviscoplastic model based on the Herschel-Bulkley viscoplastic model. *J. Nonnewton. Fluid Mech.* 158, 154–161. doi:10.1016/j.jnnfm.2008.12.001
- Schramm, G., 1994. *A Practical Approach to Rheology and Rheometry*. GmbH Gebrueder HAAKE, Karlsruhe, Germany.
- Shareefdeen, Z., Baltzis, B.C., Oh, Y.S., Bartha, R., 1993. Biofiltration of methanol vapor. *Biotechnol. Bioeng.* 41, 512–24.
- Sharvelle, S., McLamore, E., Banks, M.K., 2008. Hydrodynamic characteristics in biotrickling filters as affected by packing material and hydraulic loading rate. *J. Environ. Eng.* 134, 346–352.
- Shaw, T., Winston, M., Rupp, C.J., Klapper, I., Stoodley, P., 2004. Commonality of elastic relaxation times in biofilms. *Phys. Rev. Lett.* 93, 1–4. doi:10.1103/PhysRevLett.93.098102
- Sheng, G.P., Yu, H.Q., Li, X.Y., 2010. Extracellular polymeric substances (EPS) of microbial aggregates in biological wastewater treatment systems: A review. *Biotechnol. Adv.* 28, 882–894. doi:10.1016/j.biotechadv.2010.08.001
- Simões, M., Pereira, M.O., Vieira, M.J., 2005. Effect of mechanical stress on biofilms challenged by different chemicals. *Water Res.* 39, 5142–5152. doi:10.1016/j.watres.2005.09.028
- Slatter, P.T., 1997. The rheological characterisation of sludges. *Water Sci. Technol.* 36, 9–18. doi:10.1016/S0273-1223(97)00663-X
- Solórzano-López, J., Zenit, R., Ramírez-Argáez, M.A., 2011. Mathematical and physical simulation of the interaction between a gas jet and a liquid free surface. *Appl. Math. Model.* 35, 4991–5005. doi:10.1016/j.apm.2011.04.012
- Spigno, G., Zilli, M., Nicoletta, C., 2004. Mathematical modelling and simulation of phenol degradation in biofilters. *Biochem. Eng. J.* 19, 267–275.
- Srinivasan, R., Stewart, P.S., Chen, G.C., Xu, X., 1995. Biofilm parameters influencing biocide efficacy. *Biotechnol. Bioeng.* 46, 553–560.
- Stewart, P.S., 2012. Mini-review: convection around biofilms. *Biofouling* 28, 187–198.

- Stickel, J.J., Knutsen, J.S., Liberatore, M.W., 2013. Response of elastoviscoplastic materials to large amplitude oscillatory shear flow in the parallel-plate and cylindrical-Couette geometries. *J. Rheol.* (N. Y. N. Y). 57, 1569–1596. doi:10.1122/1.4820495
- Stoodley, P., Lewandowski, Z., Boyle, J.D., Lappin-Scott, H.M., 1999a. Structural deformation of bacterial biofilms caused by short-term fluctuations in fluid shear: An in situ investigation of biofilm rheology. *Biotechnol. Bioeng.* 65, 83–92. doi:10.1002/(SICI)1097-0290(19991005)65:1<83::AID-BIT10>3.0.CO;2-B
- Stoodley, P., Boyle, J.D., Lappin-scott, H.M., 1999b. Evolving Perspectives of Biofilm Structure Stages in Biofilm Development 14, 75–90.
- Stoodley, P., Lewandowski, Z., Boyle, J.D., Lappin-Scott, H.M., 1999c. The formation of migratory ripples in a mixed species bacterial biofilm growing in turbulent flow. *Environ. Microbiol.* 1, 447–455. doi:10.1046/j.1462-2920.1999.00055.x
- Stoodley, P., Cargo, R., Rupp, C.J., Wilson, S., Klapper, I., 2002. Biofilm material properties as related to shear-induced deformation and detachment phenomena. *J. Ind. Microbiol. Biotechnol.* 29, 361–367. doi:10.1038/sj/jim/7000282
- Storck, T., Picioreanu, C., Virdis, B., Batstone, D.J., 2014. Variable cell morphology approach for individual-based modeling of microbial communities. *Biophys. J.* 106, 2037–2048. doi:10.1016/j.bpj.2014.03.015
- Stotsky, J.A., Hammond, J.F., Pavlovsky, L., Stewart, E.J., Younger, J.G., Solomon, M.J., Bortz, D.M., 2014. Variable viscosity and density biofilm simulations using an immersed boundary method, part I: Numerical scheme and convergence results. *Comput. Model. Eng. Sci* 98, 295–340. doi:10.1016/j.jcp.2016.04.027
- Stotsky, J.A., Hammond, J.F., Pavlovsky, L., Stewart, E.J., Younger, J.G., Solomon, M.J., Bortz, D.M., 2016. Variable viscosity and density biofilm simulations using an immersed boundary method, part II: Experimental validation and the heterogeneous rheology-IBM. *J. Comput. Phys.* 317, 204–222. doi:10.1016/j.jcp.2016.04.027
- Sudarsan, R., Ghosh, S., Stockie, J.M., Eberl, H.J., 2016. Simulating biofilm deformation and detachment with the immersed boundary method. *Commun. Comput. Phys.* 19, 682–732. doi:10.4208/cicp.161214.021015a

T

- Taherzadeh, D., Picioreanu, C., Küttler, U., Simone, A., Wall, W.A., Horn, H., 2010. Computational study of the drag and oscillatory movement of biofilm streamers in fast flows. *Biotechnol. Bioeng.* 105, 600–610. doi:10.1002/bit.22551
- Taherzadeh, D., Picioreanu, C., Horn, H., 2012. Mass transfer enhancement in moving biofilm structures. *Biophys. J.* 102, 1483–1492. doi:10.1016/j.bpj.2012.02.033
- Thormann, K.M., Saville, R.M., Shukla, S., Spormann, A.M., 2005. Induction of rapid detachment in shewanella oneidensis MR-1 biofilms. *J. Bacteriol.* 187, 1014–1021. doi:10.1128/JB.187.3.1014-1021.2005
- Tierra, G., Pavissich, J.P., Nerenberg, R., Xu, Z., Alber, M.S., 2015. Multicomponent model of deformation and detachment of a biofilm under fluid flow. *J. R. Soc. Interface* 12, 1–13. doi:10.1098/rsif.2015.0045

- Towler, B.W., Rupp, C.J., Cunningham, A.B., Stoodley, P., 2003. Viscoelastic properties of a mixed culture biofilm from rheometer creep analysis. *Biofouling* 19, 279–285. doi:10.1080/0892701031000152470
- Towler, B.W., Cunningham, A.B., Stoodley, P., McKittrick, L., 2007. A model of fluid–biofilm interaction using a burger material law. *Biotechnol. Bioeng.* 96, 259–271. doi:10.1002/bit
- Trejo-Aguilar, G., Revah, S., Lobo-Oehmichen, R., 2005. Hydrodynamic characterization of a trickle bed air biofilter. *Chem. Eng. J.* 113, 145–152.

V

- Vallée, C., Höhne, T., Prasser, H.M., Sühnel, T., 2008. Experimental investigation and CFD simulation of horizontal stratified two-phase flow phenomena. *Nucl. Eng. Des.* 238, 637–646. doi:10.1016/j.nucengdes.2007.02.051
- Vázquez-Uña, G., Chenlo-Romero, F., Sánchez-Barral, M., Pérez-Muñuzuri, V., 2000. Mass transfer enhancement due to surface wave formation at a horizontal gas-liquid interface. *Chem. Eng. Sci.* 55, 5851–5856. doi:10.1016/S0009-2509(00)00190-1
- Versteeg, H.K., Malalasekera, W., 2007. *An Introduction to Computational Fluid Dynamics, Second ed.* ed. Essex, England. doi:10.2514/1.22547
- Vinogradov, A.M.M., Winston, M., Rupp, C.J.J., Stoodley, P., 2004. Rheology of biofilms formed from the dental plaque pathogen *Streptococcus mutans*. *Biofilms* 1, 49–56. doi:10.1017/S1479050503001078
- Vojinović, V., Cabral, J.M.S., Fonseca, L.P., 2006. Real-time bioprocess monitoring: Part I: In situ sensors. *Sensors Actuators, B Chem.* 114, 1083–1091. doi:10.1016/j.snb.2005.07.059
- Vrouwenvelder, J.S., Picioreanu, C., Kruithof, J.C., van Loosdrecht, M.C.M., 2010. Biofouling in spiral wound membrane systems: Three-dimensional CFD model based evaluation of experimental data. *J. Memb. Sci.* 346, 71–85.

W

- Wagner, M., Taherzadeh, D., Haisch, C., Horn, H., 2010. Investigation of the mesoscale structure and volumetric features of biofilms using optical coherence tomography. *Biotechnol. Bioeng.* 107, 844–853. doi:10.1002/bit.22864
- Wagner, M., Horn, H., 2017. Optical coherence tomography in biofilm research: A comprehensive review. *Biotechnol. Bioeng.* 114, 1386–1402. doi:10.1002/bit.26283
- Wang, M.-J., 1999. The role of filler networking in dynamic properties of filled rubber. *Rubber Chem. Technol.* 72, 430–448. doi:10.5254/1.3538812
- Wang, Q., Zhang, T., 2010. Review of mathematical models for biofilms. *Solid State Commun.* 150, 1009–1022. doi:10.1016/j.ssc.2010.01.021
- Wang, X., Jia, X., Wen, J., 2011. Transient CFD modeling of toluene waste gas biodegradation in a gas–liquid–solid three-phase airlift loop reactor by immobilized *Pseudomonas putida*. *Chem. Eng. J.* 172, 735–745.
- Wang, J., Gao, Q., Yu, Y., Wang, H., Jin, M., 2012. Radio-triggered power management in wireless sensor networks, in: *Matin, M. A. (Ed.), Wireless Sensor Networks -*

- Technology and Applications. IntechOpen, pp. 51-68. doi: 10.5772/39189. Available from: <http://www.intechopen.com/books/wireless-sensor-networks-technologyand-applications/radio-triggered-power-management-in-wireless-sensornetworks>, Accessed on Aug. 20, 2018
- Wang, H.-F., Hu, H., Yang, H.-Y., Zeng, R.J., 2016. Characterization of anaerobic granular sludge using a rheological approach. *Water Res.* 106, 116–125. doi:10.1016/j.watres.2016.09.045
- Wanner, O., Morgenroth, E., 2004. Biofilm modeling with AQUASIM. *Water Sci. Technol.* 49, 137–144.
- Wäsche, S., Horn, H., Hempel, D.C., 2000. Mass transfer phenomena in biofilm systems. *Water Sci. Technol.* 41, 357–360.
- Wäsche, S., Horn, H., Hempel, D.C., 2002. Influence of growth conditions on biofilm development and mass transfer at the bulk/biofilm interface. *Water Res.* 36, 4775–4784.
- Wilcox, D.C., 1998. *Turbulence Modeling for CFD*. DCW Industries, Inc, La Canada, California.
- Wilking, J.N., Angelini, T.E., Seminara, A., Brenner, M.P., Weitz, D. a., 2011. Biofilms as complex fluids. *MRS Bull.* 36, 385–391. doi:10.1557/mrs.2011.71
- Wloka, M., Rehage, H., Flemming, H.-C., Wingender, J., 2004. Rheological properties of viscoelastic biofilm extracellular polymeric substances and comparison to the behavior of calcium alginate gels. *Colloid Polym. Sci.* 282, 1067–1076. doi:10.1007/s00396-003-1033-8
- Wloka, M., Rehage, H., Flemming, H.-C., Wingender, J., 2005. Structure and rheological behaviour of the extracellular polymeric substance network of mucoid *Pseudomonas aeruginosa* biofilms. *Biofilms* 2, 275. doi:10.1017/S1479050506002031
- Worosz, T., Bernard, M., Kong, R., Toptan, A., Kim, S., Hoxie, C., 2016. Sensitivity studies on the multi-sensor conductivity probe measurement technique for two-phase flows. *Nucl. Eng. Des.* 310, 552–563. doi:10.1016/j.nucengdes.2016.10.046

X

- Xavier, J.B., Picioreanu, C., Abdul Rani, S., van Loosdrecht, M.C.M., Stewart, P.S., 2005a. Biofilm-control strategies based on enzymic disruption of the extracellular polymeric substance matrix - A modelling study. *Microbiology* 151, 3817–3832. doi:10.1099/mic.0.28165-0
- Xavier, J.B., Picioreanu, C., van Loosdrecht, M.C.M., 2005b. A general description of detachment for multidimensional modelling of biofilms. *Biotechnol. Bioeng.* 91, 651–669. doi:10.1002/bit.20544
- Xavier, J.B., Picioreanu, C., van Loosdrecht, M.C.M., 2005c. A framework for multidimensional modelling of activity and structure of multispecies biofilms. *Environ. Microbiol.* 7, 1085–1103. doi:DOI 10.1111/j.1462-2920.2005.00787.x

Y

- Yeoh, G.H., Tu, J., 2010. *Computational techniques for multiphase flows*. Butterworth-

Heinemann.

- Youngs, D.L., 1982. Time-dependent multi-material flow with large fluid distortion, in: Morton, K.W., Baines, M.J. (Eds.), *Numerical Methods for Fluid Dynamics*. Academic Press, London, pp. 273–285.
- Yu, L.M., Zeng, A.W., Yu, K.T., 2006. Effect of interfacial velocity fluctuations on the enhancement of the mass-transfer process in falling-film flow. *Ind. Eng. Chem. Res.* 45, 1201–1210. doi:10.1021/ie050855q

Z

- Zarook, S.M., Ansar, Z., 1996. Development, experimental validation and dynamic analysis of a general transient biofilter model. *Chem. Eng. Sci.* 52, 759–773.
- Zenit, R., Koch, D.L., Sangani, A.S., 2001. Measurements of the average properties of a suspension of bubbles rising in a vertical channel. *J. Fluid Mech.* 429, 307–342. doi:10.1017/S0022112000002743
- Zhang, T., Bishop, P., 1994. Experimental determination of the dissolved oxygen boundary layer and mass transfer resistance near the fluid-biofilm interface. *Water Sci. Technol.* 30, 47–58.
- Zhang, T., Cogan, N., Wang, Q., 2008. Phase-field models for biofilms II. 2-D numerical simulations of biofilm-flow interaction. *Commun. Comput. Phys.* 4, 72–101.
- Zhou, X.-H., Liu, J., Song, H.-M., Qiu, Y.-Q., Shi, H.-C., 2012. Estimation of heterotrophic biokinetic parameters in wastewater biofilms from oxygen concentration profiles by microelectrode. *Environ. Eng. Sci.* 29, 466–471.
- Zuckerman, N., Lior, N., 2006. jet impingement heat transfer: Physics, correlations, and numerical modeling. *Adv. Heat Transf.* 39, 565–631. doi:10.1016/S0065-2717(06)39006-5